Università degli Studi di Ferrara

DOCTORAL COURSE IN
ENGINEERING SCIENCE

CYCLE XXXIII

DIRECTOR Prof. TRILLO STEFANO

ON THE PROCESS-MICROSTRUCTURE-PROPERTIES RELATIONSHIP OF A LASER ADDITIVELY MANUFACTURED AlSi10Mg ALLOY

Scientific/Disciplinary Sector (SDS) ING-IND/21

Candidate
Dott. Maverick Giovagnoli

_____
(signature)

Supervisor
Prof. Merlin Mattia

_____
(signature)

Co-supervisor
Prof. Roberto Tovo

_____
(signature)

Years 2017/2020

To my family, friends and äppel,
thanks for bringing me this far...

Dedicated to the memory of Professor Gabrielli

ABSTRACT

Additive Manufacturing (AM) has become particularly attracting over the last decade since it offers several advantages as compared to traditional manufacturing technologies. Among these, the complete design freedom, light-weighted lattice structures, and minimisation of waste and raw materials consumption are noteworthy.

In light of a green and circular economy, Al alloys represent a fundamental material class for automotive, aerospace and marine fields, thanks to lighter and more eco-friendly components. To date, the AlSi10Mg alloy is the most widespread Al alloy in the industrial field, due to its excellent processability, good mechanical properties and corrosion resistance, and limited thermal expansion.

Due to the complex physic of the AM process, the choice of deposition parameters is not straightforward, and unsuitable combinations result in highly defective parts. In this light, the effect of process parameters on microstructure, faultiness and mechanical properties of the 3D printed material was investigated in-depth. Results showed that, in a narrow range, deposition parameters slightly modify the microstructure but strongly affect porosity. Additionally, methods to guide the process design are required, with the energy density-based approach being currently the most employed. The actual reliability of this method was assessed, and results did not validate it as a useful tool for the selection of deposition parameters.

Applications like crashworthy structural Al vehicles and welded Al components require suitable high-strain rate properties, like impact toughness and absorbed energy, besides static and dynamic performances. Hence, during the PhD the impact behaviour of the 3D printed AlSi10Mg alloy was studied in-depth as a function of the heat treatment state. The as-built material has a remarkable impact strength but low absorbed energy. Hot isostatic pressing prevented the growth of gas pores during heat treatment but significantly softened the material. Precipitation strengthening usually obtained by a T6 heat treatment could be achieved more conveniently using a novel high-pressure heat treatment. Finally, as a major drawback of additively manufactured parts, the anisotropic behaviour was deepened in light of microstructural features and their evolution with the heat treatment.

SOMMARIO

L'Additive Manufacturing (AM) è una tecnologia produttiva divenuta particolarmente attrattiva nell'ultimo decennio, poiché offre indiscutibili vantaggi rispetto alle tecnologie produttive tradizionali. Degni di nota risultano essere la completa flessibilità di design, l'alleggerimento tramite realizzazione di strutture reticolari, e la minimizzazione di materie prime e scarti.

In un contesto di economia circolare e "green", le leghe di Al rappresentano una classe di materiali fondamentali nei settori automobilistico, aerospaziale e marino, grazie alla realizzazione di componenti leggeri e a minor impatto ambientale. Ad oggi, la lega AlSi10Mg risulta la più utilizzata in ambito industriale, grazie all'ottima processabilità, buona resistenza meccanica e a corrosione, e ridotta dilatazione termica.

I complessi fenomeni fisici che governano il processo AM rendono complicata la scelta dei parametri di deposizione, con il rischio di produzione di parti difettose. In quest'ottica, è stato indagato l'effetto dei parametri di processo su microstruttura, difettosità e proprietà meccaniche del prodotto stampato. I risultati mostrano che, in un range ridotto, i parametri di deposizione influenzano in misura ridotta la microstruttura ma sensibilmente la porosità. In aggiunta, risulta necessario sviluppare delle metodologie per il design del processo AM e, ad oggi, il metodo basato sulla densità di energia risulta il più diffuso. L'affidabilità di tale metodo è stata valutata, e i risultati mostrano come non possa essere ritenuto efficacie per il design del processo.

Struttura resistente agli urti e componenti saldati richiedono adeguate proprietà ad impatto, come tenacità e capacità di assorbire energia. In quest'ottica, il comportamento ad impatto della lega AlSi10Mg è stato indagato in funzione dello stato di trattamento termico. Il materiale tal quale mostra una notevole resistenza all'impatto ma un ridotto assorbimento di energia. La pressatura isostatica a caldo previene l'accrescimento di porosità gassose durante il trattamento termico, ma addolcisce il materiale. L'indurimento per precipitazione tipicamente ottenuto con trattamento T6 è raggiungibile con maggior vantaggio tramite un trattamento innovativo ad elevata pressione. Infine, in quanto notevole inconveniente dei processi additivi, il comportamento anisotropo ad impatto è stato approfondito in relazione alle caratteristiche microstrutturali e relativa evoluzione con il trattamento termico.

ACKNOWLEDGEMENTS

The present doctoral research activity would not have been possible without the support of several colleagues and co-workers, to all whom I owe my sincere gratitude.

Professor Gian Luca Garagnani and Professor Mattia Merlin, for the opportunity of doctoral course on this fascinating topic, and for confirming their trust in me after Bachelor and Master theses.

All colleagues of Metallurgy and Corrosion research group: Dr Annalisa Fortini, PhD fellow Lucia Lattanzi, Dr Chiara Soffritti, Professor Vincenzo Gabrielli, Professor Cecilia Monticelli, Dr Andrea Balbo, Dr Vincenzo Grassi, Dr Federica Zanotto, PhD fellow Mahla Seyedi, and all colleagues of the Engineering Department, for creating a friendly and stimulating working atmosphere.

Professor Raffaella Rizzoni, for the exciting cooperation as teaching assistant and stimulating discussions.

Dr Maria Teresa Di Giovanni and Manuel Bertani, for the valuable collaboration that covers the first part of this thesis and good experimental cooperation.

Professor Annalisa Pola, for the precious collaboration that covers most of the present thesis, and Dr Marialaura Tocci, for dedication and precise experimental support.

Professor Matteo Ferroni, for gotting me hooked with the electron microscopy and excellent experimental cooperation, and Dr Andrea Migliori, for irreplaceable support in electron microscopy investigations.

Dr Daniele Casari and Stefano Pirletti, for the excellent collaboration in casting research activity, and for joyrides.

Gabriele Bertocchi, for skilled expertise and help with X-ray diffraction tests.

Professor Leinenbach and Professor Vedani, for accepting to review and evaluate the present thesis.

Last but not least, my deepest gratitude to my family and friends, for everyday love, trust and sustenance that pushed me this far.

PREFACE

The present doctoral thesis gathers the experimental research activity carried out at the University of Ferrara (Ferrara, Italy) from November 2017 to October 2020. Most of the experimental work was performed at the Department of Engineering in Ferrara, and a small part was carried out at the Institute for Microelectronics and Microsystems (IMM) of the National Research Council in Bologna (Bologna, Italy).

Prof Mattia Merlin and Prof Roberto Tovo at the Department of Engineering in Ferrara were the principal supervisor and the co-supervisor, respectively.

The current research activity dealt with the characterisation of an AlSi10Mg alloy processed by the laser-powder bed fusion technology. Notably, the following two main topics were investigated:

- the effect of 3D printing parameters on microstructure and static properties, in collaboration with the industrial partner AMT S.r.l. (Camposanto (MO), Italy);
- the effect of heat treatment on microstructure, impact behaviour and corresponding anisotropy, in collaboration with the University of Brescia (Brescia, Italy) and the CNR National Research Council in Bologna (Bologna, Italy).

Chapter 1 is a literature survey which covers the theoretical background about the main topics of the research activity. In particular, it introduces the powder bed fusion processes, and focuses on metallurgy and heat treatment of the AlSi10Mg alloy, providing a sound basis to the following chapters.

Chapter 2 deals with the effect of deposition parameters on density, microstructural features and static properties of the AlSi10Mg alloy. Additionally, it discusses the reliability of the energy density-based method as a design tool for additive manufacturing processes. The research activity led to the following article:

- M. Giovagnoli, G. Silvi, M. Merlin, M. T. Di Giovanni. *Optimisation of process parameters for an additively manufactured AlSi10Mg alloy: limitations of the energy density-based approach on porosity and mechanical properties estimation*. Mat. Sci. Eng. A, 802, 140613, 2021. https://doi.org/10.1016/j.msea.2020.140613

Part of the experimental results was also submitted at the following conference:

- Junior Euromat 2020. Granada (Spain), 15th-19th November 2020 - extended abstract.

Additionally, the activity resulted in the supervision of the following master thesis:

· Giacomo Silvi (March 2020). *Studio di campioni in lega AlSi10Mg ottenuti via Direct Metal Laser Sintering: influenza dei parametri di processo su proprietà meccaniche e microstrutturali*. Supervisor: M. Merlin. Co-supervisor: M. Giovagnoli.

Chapter 3 covers the preliminary studies concerning the effect of conventional (casting-derived) heat treatments on microstructure and impact behaviour of the AlSi10Mg alloy. Results provided the basis to the main activity of this doctoral thesis, and led to the publication of the following article:

· L. Girelli, M. Giovagnoli, M. Tocci, A. Pola, A. Fortini, M. Merlin, G. M. La Vecchia. *Evaluation of impact behaviour of AlSi10Mg alloy produced by laser additive manufacturing*. Mat. Sci. Eng. A, 748, 38–51, 2019. https://doi.org/10.1016/j.msea.2019.01.07

Chapter 4 deals in-depth with the effect of different heat treatment routes on microstructure and impact behaviour of the alloy. Standard T6, annealing, hot isostatic pressing and new high-pressure heat treatment were investigated. The research activity resulted in the following article:

· M. Giovagnoli, M. Tocci, A. Fortini, M. Merlin, M. Ferroni, A. Migliori, A. Pola. *Effect of different heat-treatment routes on the impact properties of an additively manufactured AlSi10Mg alloy*. Mat. Sci. Eng. A, 802, 140671, 2021. https://doi.org/10.1016/j.msea.2020.140671

Part of the experimental results was presented at the following conference:

· Euromat 2019. Stockholm (Sweden), 1st-5th September 2019 - extended abstract.

Chapter 5 covers the anisotropic impact behaviour of the alloy in different heat treatment conditions. In this light, impact specimens were realised with different orientations to the building platform to assess the anisotropy. Results were gathered in the following article that will be soon submitted to an international journal:

· M. Giovagnoli, M. Tocci, A. Fortini, M. Merlin, M. Ferroni, A. Pola. *On the anisotropic impact behaviour of an additively manufactured AlSi10Mg alloy in different heat treatment conditions*. Manuscript ready for submission.

Besides the main research topics on the additively manufactured AlSi10Mg alloy, some side projects on casting Al alloys were carried out during the doctoral course.

Within the collaboration reported above with the University of Brescia, the impact behaviour of a gravity cast AlSi10Mg alloy in different heat treatment states was investigated, and results will be soon submitted to a national journal. Moreover, the activity resulted in the supervision of the following master thesis:

- Nicolò Boschini (June 2020). *Hot Isostatic Pressing combinato con trattamento di Ageing in pressione applicato ad una lega AlSi10Mg colata per gravità in conchiglia: effetto su microstruttura e proprietà ad impatto*. Supervisor: M. Merlin. Co-supervisor: M. Giovagnoli.

In the frame of a collaboration between the University of Ferrara and the company Fonderie Mario Mazzucconi SpA (Ponte San Pietro (BG), Italy), the effect of liquid melt treatments, in particular grain refining and strontium modification, on the microstructure of an AlSi7Mg cast alloy was assessed. The research activity resulted in the publication of the following articles:

- L. Lattanzi, A. Fortini, M. Giovagnoli, M. Merlin, S. Pirletti, S. Morè Spreafico, G.L. Garagnani. *Thermal Analysis for the Prediction of Grain Refinement: An Experimental Investigation on an AlSiMg Foundry Alloy*. Materials Science Forum, Vol. 941, pp. 1029-1034, 2018.
- L. Lattanzi, A. Fortini, M. Giovagnoli, M. Merlin. *Influence of Mg and Ti on both eutectic solidification and modifying efficiency in Sr-modified Al-7Si cast alloys*. La Metallurgia Italiana, Vol. 2, pp. 5-15, 2018.

As a continuation of the master thesis, and within a collaboration among the University of Ferrara, the Norwegian University of Science and Technology (Trondheim, Norway) and the University of Parma (Parma, Italy), the effect of increasing Ni additions on an AlSi7Mg cast alloy was investigated. Results led to the publication of the following article:

- L. Lattanzi, M.T. Di Giovanni, M. Giovagnoli, A. Fortini, M. Merlin, D. Casari, M. Di Sabatino, E. Cerri, G.L. Garagnani. *Room temperature mechanical properties of A356 alloy with Ni additions from 0.5 wt to 2 wt %*. Metals, Vol. **8**, pp. 224-238, 2018.

Part of the results was also presented at the following conference:

- Metallurgy 37th National Congress. Bologna (Italy), 12th-14th September 2019 - oral presentation and extended abstract.

Additionally, the activity resulted in the supervision of the following master thesis

· Mario Lucci Manni (December 2018). *Effect of Ni addition on the impact properties of an A356 alloy: fractographic, thermal and microstructural analyses*. Supervisors: M. Merlin, M. Di Sabatino Lundberg. Co-supervisors: L. Lattanzi, M. Giovagnoli.

TABLE OF CONTENTS

CHAPTER 5

NOMENCLATURE

ACRONYMS

3D	Three-dimensional
3NND	3-Nearest Neighbours Distance [μm], [nm]
AM	Additive manufacturing
APT	Atom probe tomography
BD	Building direction
BF	Bright-field
BJ	Binder jetting
BSE	Backscattered electrons
CAD	Computer-aided drafting
CET	Columnar-to-equiaxed transition
C_{hkl}	Texture coefficient of *hkl* reflection
C_R	Cooling rate [K/s]
DF	Dark-field
DED	Direct energy deposition
DSC	Differential scanning calorimetry
EB	Electron beam
EBM	Electron beam melting
EBSD	Electron backscattered diffraction
ED	Equivalent diameter [μm]
EDX	Energy-dispersive X-ray
E_f	Elongation at failure [%]
FFT	Fast Fourier transform
GA	Gas atomisation
GMA	Gas metal arc
GP	Guinier-Preston
HAADF	High-angle annular dark-field
HAGB	High-angle grain boundary
HAGBs	High-angle grain boundaries
HAZ	Heat-affected zone
HF	Hydrofluoric acid
HIP	Hot isostatic pressing
HR	High-resolution

IHT	Intrinsic heat treatment
IPF	Inverse pole figure
LAGB	Low-angle grain boundary
LAGBs	Low-angle grain boundaries
ME	Metal extrusion
MPB	Melt pool boundary
MPBs	Melt pool boundaries
MJ	Material jetting
OM	Optical microscopy/microscope
PA	Plasma arc
PBF	Powder bed fusion
PDF	Probability density function
PRE	Plasma rotating electrode
RA	Rotary atomisation
SAED	Selected area electron diffraction
SE	Secondary electrons
SEM	Scanning electron microscopy/microscope
SHT	Solution heat treatment
SL	Sheet lamination
SLM	Selective laser melting
STEM	Scanning transmission electron microscopy
TD	Transverse direction
TEM	Transmission electron microscopy/microscope
UTS	Ultimate tensile strength [MPa]
VED	Volumetric energy density [J/mm^3]
VP	Vat photopolymerisation
WA	Water atomisation
XRD	X-ray diffraction
YS	Yield strength [MPa]

GREEK LETTERS

β	Mg_2Si compound
	Al_5SiFe compound
β′	$Mg_{1.8}Si$ compound
β′′	Mg_5Si_6 compound

γ	Building angle to the vertical direction [°]
ε	True strain
Θ	Strain hardening rate [MPa]
ϑ	Bragg angle [°]
λ	Size of cellular dendrites [μm]
	Angle between loading and slip directions [°]
σ	True stress [MPa]
	Degree of preferred orientation
τ_R	Shear stress along the slip direction [MPa]
φ	Angle between laser scan direction and growth direction [°]
	Angle between loading direction and normal to the slip plane [°]

LATIN LETTERS

A	Area of particle [μm^2]
a	Proportional constant [μm·s/K]
B′	$Mg_9Al_3Si_7$ compound
C	Circularity
E	Elastic modulus [GPa]
G	Thermal gradient [K/m]
h	Hatch spacing [mm]
L	Laser
m	Schmid factor
n	Dimensionless exponent
P	Perimeter of particle [μm]
P	Laser power [W]
R	Solidification rate [m/s]
t	Layer thickness [mm]
U1	$MgAl_2Si_2$ compound
U2	$Mg_4Al_4Si_4$ compound
v	Scan speed [mm/s]

LIST OF FIGURES

CHAPTER 1

THEORETICAL BACKGROUND

CHAPTER 3

IMPACT PROPERTIES AND HEAT TREATMENTS: PRELIMINARY STUDIES

CHAPTER 4

MICROSTRUCTURE AND IMPACT BEHAVIOUR: EFFECT OF HEAT TREATMENT

CHAPTER 5

ANISOTROPIC IMPACT BEHAVIOUR WITH DIFFERENT HEAT TREATMENTS

LIST OF TABLES

CHAPTER 1

THEORETICAL BACKGROUND

The present thesis deals with the technological, microstructural and mechanical properties of an additively manufactured AlSi10Mg alloy. Most of the work focuses on its performances during impact loading in different heat treatment conditions. A chapter is dedicated to the optimisation of building parameters.

In this light, the first chapter introduces the theoretical background that paves the fundamentals of the present research work. A brief introduction to the additive manufacturing technologies, with a focus on the powder bed fusion process, opens the chapter. The second paragraph deals with the metallurgical and mechanical aspects of the AlSi10Mg alloy processed by powder bed fusion. Despite the focus on this specific alloy, most of the notions are rather general and applicable to other alloy systems processed by powder bed fusion. The chapter ends with a comprehensive review of the current heat treatment routes of the above-mentioned alloy.

1.1 BRIEF OVERVIEW OF POWDER BED FUSION PROCESSES

The following paragraph aims at briefly introducing the additive manufacturing technologies, with particular attention devoted to the powder bed fusion processes. The main features arising during the heat source-matter (powder bed) interaction will be explained to give a panoramic view of the physical principles involved in the process. This will help to comprehend the formation mechanism of the several defects affecting the additively manufactured products. Furthermore, the main parameters which dictate the process and the corresponding final microstructure will be explained.

1.1.1 General aspects

ISO/ASTM52900 - 15 defines additive manufacturing (AM) as “a process of joining materials to make objects from 3D model data, usually layer upon layer, as opposed to subtractive manufacturing methodologies” [1]. It has gained increasing interest over the last decade within academic and industrial fields because of the several advantages it offers, which are not achievable with more traditional and well-established manufacturing technologies. Due to its working principle, it ensures complete design

freedom, enabling to realise complex parts without significantly affecting the final cost. Elements with intricated internal structures and channels [2], [3], lattice structures for light-weighted parts through topology optimisation [4]–[6] and multi-material components [7], [8] are nowadays a sound reality. Moreover, adding material just where needed, AM technologies offer the possibility to minimise waste and raw material consumption [9], [10], placing themselves in the context of a green and circular economy.

Despite these invaluable advantages, AM technologies suffer from some drawbacks. The cost-per-part is high compared to traditional manufacturing technologies, and the process is generally suitable just for small series production. Hence, AM processes cannot be imagined as a substitute to traditional processes, but rather as valuable alternatives to enlarge the horizon of possible goals.

- *Classification of AM processes*

According to the ISO/ASTM52900 – 15 standard [1], several categories fall within the definition of AM process, alphabetically *binder jetting* (BJ), *direct energy deposition* (DED), *metal extrusion* (ME), *material jetting* (MJ), *powder bed fusion* (PBF), *sheet lamination* (SL), and *vat photopolymerisation* (VP). Among these, PBF technologies are receiving considerable attention from both academic and industrial fields. Further classification divides the AM categories based on the heat source, namely laser (L), electron beam (EB), plasma arc (PA) and gas metal arc (GMA). In PBF processes, laser or electron beam are employed. The former heats the powder bed via photon absorption, whereas the latter by transferring kinetic energy from focused electrons and thus requires a vacuum chamber. Such technologies are often referred to as *selective laser melting* (SLM) and *electron beam melting* (EBM), respectively.

Despite the different heat source, they share the basic working principle, depicted in Fig. 1.1 [11]: a 3D CAD model, accurately oriented within the build chamber volume and including the eventual support structures, is sliced into planar layers. A proper combination of process parameters (§ 1.1.2) is selected for the deposition procedure. Thin powder layers (usually a few tens of μm) are deposited within the building chamber and selectively fused by the scanning laser or electron beam. The building platform is incrementally lowered along the vertical axis after each layer, allowing a new powder layer to be deposited. The operation is conducted under vacuum (L, EB) or using an inert gas (L), such as argon or nitrogen, depending on the processed powder alloy.

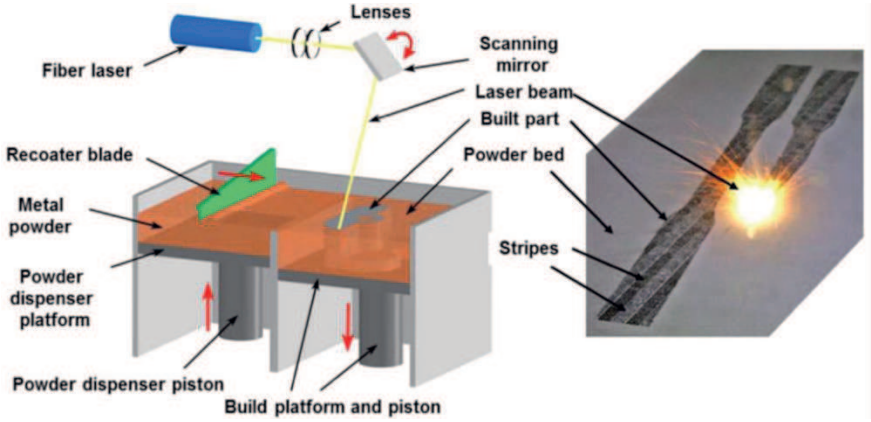

Figure 1.1. Schematic of the L-PBF process. Reprinted with permission from Ref. [11].

Compared to other AM processes like DED, PBF processes suffer from a high production time mainly due to the limited powder feeding rate and use of thin powder layers. In DED processes, metal wires are often employed, which reduces the production time. Additionally, PBF is expensive because of the high cost of fine metal powders. For these reasons, PBF processes generally are considered suitable for relatively small components and limited production series. However, they allow the production of very complex parts, usually unworkable for other AM technologies, and generally ensure a better quality of the final part, in terms of dimensional accuracy, surface finishing, defects and microstructural features [12].

- *Laser-matter interaction in L-PBF processes*

Since a laser beam is an oscillating electromagnetic radiation, it generates an oscillatory motion on charged particles (electrons and protons) when striking and propagating through a solidus. The effect of such laser-induced atomic oscillation is an increase of the solidus temperature proportional to the amplitude of the oscillation itself. Unfortunately, the incident laser radiation is never fully transmitted to the solid medium, but a given fraction is reflected and does not contribute to the increase of temperature. The fraction of reflected radiation depends on the properties of the target material and the energy (wavelength) of the incident radiation. For instance, solid aluminium absorbs less than 10 % of an incident beam being ~1 μm in wavelength, and just ~2 % of an incident beam being ~10 μm in wavelength. This fact partially accounts for the greater challenges in AM processes using Al powders compared to, for example, steels and Ti alloys [6], [13].

Even if the effect of laser radiation on a solid medium is quite simple (an increase of temperature), the dynamic evolution of the material within the melt pool is dramatically complex. A fast-moving heat source, rapid heating and cooling rates, melting and vaporisation, convective mass and heat transfers, all contribute to the time evolution of temperature distribution, affecting the resulting microstructure and its final properties. The accurate calculation of temperature fields requires the fully-coupled solution of equations of conservation of mass, momentum and energy, but such a heavy topic will not be covered in this doctoral thesis [14]–[17]. However, some phenomena inherently characterise the laser-matter interaction in AM processes, namely surface tension-driven Marangoni convection and recoil pressure due to metal vaporisation. They rule the transient dynamics of the melt pool, which determines the final microstructure as well as the formation of possible defects (§ 1.1.3). Hence, a brief description of such phenomena and their interaction will be given.

Convective Marangoni flow is a thermal phenomenon rising at the interface of a liquid-gas system due to a surface tension gradient on the top surface of the molten pool, resulting from the spatial variation of temperature. Generally, for pure metals and alloys, the surface tension decreases with temperature. Accordingly, during the AM processes a surface tension gradient forms between the high-temperature inner part of the melt pool and its colder periphery, with the hot liquid carrying heat outwards from the melt pool. The superficial flow is then transferred to the underlying liquid, and a convective flow is established, becoming the major factor controlling the flow of molten metal within the pool. Under these circumstances, the centrifugal Marangoni convection creates a wide and shallow melt pool, as found in Al alloys [12], [18], [19]. However, some alloys contain surface-active elements that, migrating at the surface of the liquid, reverse the surface tension-temperature relationship. Such a situation could occur in sulphide- or nitrogen-containing steels. The molten metal flows from the periphery downward in the middle of the melt pool, which will be narrow and deep [12], [20].

Given the intense energy of the radiating laser, the surface temperature just below the laser spot easily reaches the boiling point of the medium. As a consequence, a high pressure, called *recoil pressure*, vapour plume is generated around the laser beam, and it applies extra forces normal to the melt pool surface, accelerating the liquid. This latter escapes vertically, digging into the melt pool a depression, whose size and morphology

strongly depend on the adopted process parameters. Such an effect is depicted in Figs. 1.2a-c for a simulated laser scanning an SS316L bare plate [21]. As shown, at 150 W power and 0.5 m/s scan speed the depression is significantly deeper than at 200 W power and 1.5 m/s. Furthermore, it also modifies the resulting force direction of the vapour plume, which is almost vertical in the former case and more divergent in the latter. Spatter ejection trajectories from a powder layer in Figs. 1.2b-d complement the simulation results, highlighting that spatter directions of powder particles mirror the direction of the vapour plume [21].

After the vapour plume is created, as the heat source passes through, the decreased temperature reduces the recoil pressure, which was keeping the depression open, and increases the surface tension and the convective Marangoni flow. The restored melt recirculation under the Marangoni convection moves the liquid toward the centre of the melt pool, causing its sidewalls to collapse. The collapse likely entraps gas bubbles, retained as pores at the bottom of the melt pool, as will be highlighted in § 1.1.3. Successively, the molten metal fills the depression. Part of the flowing liquid often catches neighbouring powder particles, creating the so-called *denudation zone* along the sides of the tracks.

Recoil pressure from vapour plume and convective Marangoni flow both contribute to the depression formation. However, they also interact in the light of powder spattering. Figures 1.2e-f-g depict the effect of changing the environment pressure on the amount of hot and cold spatter of a PBF process with a stationary (not moving) laser beam [22]. As soon as the temperature of molten pool surface reaches the boiling point of the material under laser irradiation, intense vaporisation occurs, with the strong vapour plume ejecting powder particles away from the melt pool. If argon gas is absent (vacuum condition, Fig. 1.2e), the spatter is solely due to the freely expanding vapour plume, which ejects the particles far from the melt pool with the largest divergent angle. When argon is present, the environment pressure at fist confines the expanding vapour plume. As the pressure of the latter accumulates and exceeds the environment pressure, the metal vapour breaks out and forms a vapour jet. Due to the vapour jet-induced horizontal pressure difference (Bernoulli effect), an argon gas flow occurs and entrains particles in the flow path towards the melt pool. The lateral particles asportation from

the powder bed contributes to the *denudation* phenomenon and affects the effectiveness of the subsequent scan tracks.

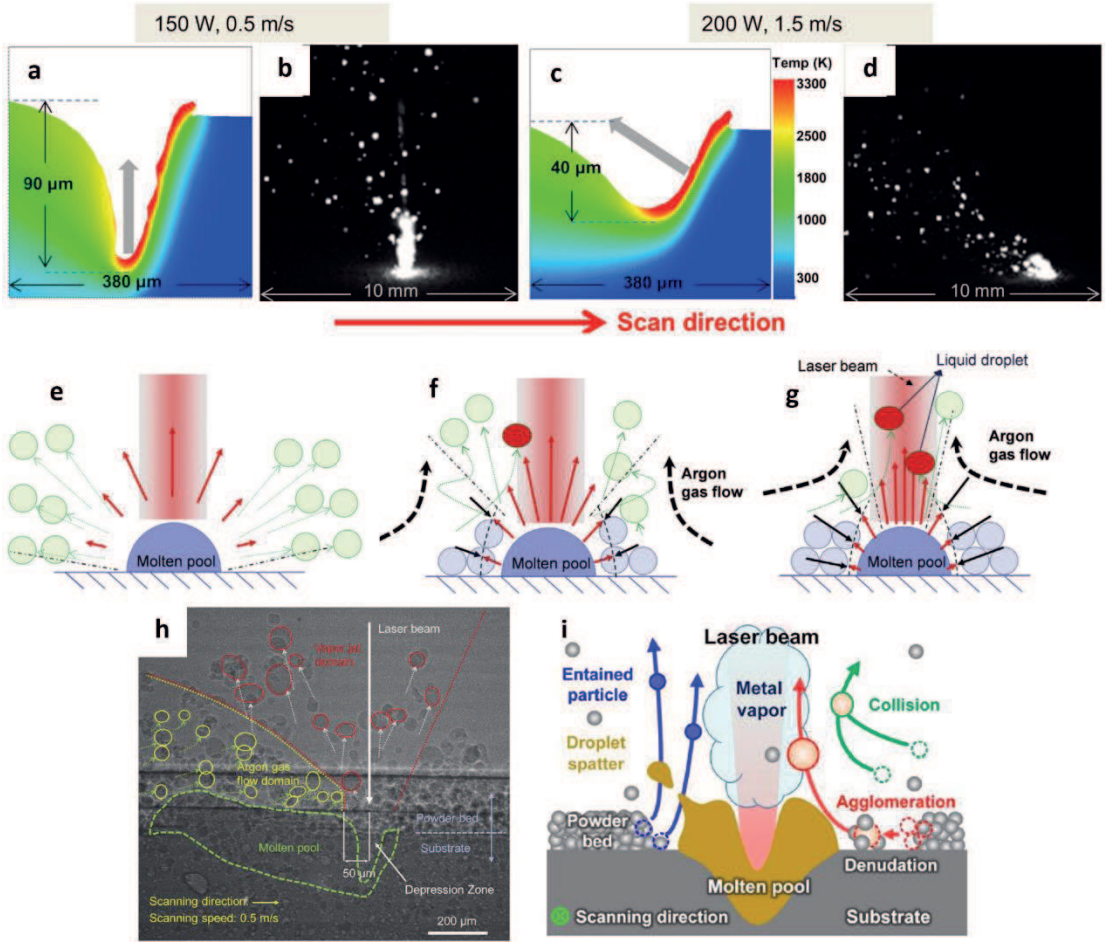

Figure 1.2. (a) to (d) Depression formation and spatter ejection for an SS316L, red arrow indicates the scanning direction. (a, b) vs (c, d) Effect of different process parameters. (a, c) Simulation of the melt pool and depression in case of a bare plate, the arrows indicate the expected direction of the vapour plume. (b, d) Experimental spatter ejection trajectories for a powder layer. Adapted with permission from Ref. [21] under the Creative Commons Attribution 4.0 license. (e) to (g) Schematic map of powder spattering behaviour as a function of environment pressure for stationary laser beam melting. (e) Vacuum (10^{-4} atm). (f) Weak environment pressure (0.05 atm). (g) Strong environment pressure (1 atm). (h) X-ray image of powder spattering during laser single track scanning under 1 atm. Adapted with permission from Ref. [22]. (i) Schematic of main physical phenomena during L-PBF. Reprinted with permission from Ref. [23].

Most of the entrained particles usually does not directly reach the area of the heat source and are ejected on the powder bed as cold spatter. However, some particles are carried to the central area just above the molten pool, where they are heated by the laser

or metal vapour and become hot spatter. The ratio between hot and cold spatter is a function of the environment pressure: the higher the pressure, the more intense the vapour jet and the corresponding pressure difference, which would generate a stronger gas flow towards the melt pool and bring more particles to hot spattering (Fig. 1.2f-g). However, besides the increment of hot spatter, the overall amount of spatter reduces as the environment pressure increases. A proper selection of the environment pressure would thus mitigate both cold and hot spatter [22].

Figures 1.2e-f-g illustrate the laser-matter interaction for a stationary laser. Besides the effect of the moving source, described basic principles also apply to the case of a scanning laser, as depicted in Figures 1.2h [22]. A depression forms under the laser irradiation and three regions characterised by a different powder motion can be identified. Red-circled particles around the laser beam raise upward, moving away from the melt pool, and are identified as vapour jet-ejected powders. Yellow-circled particles behind the laser beam mainly move towards the melt pool and are recognised as argon gas flow-entrained powders moving under the pressure difference due to the vapour jet. Their speed and acceleration are about one order of magnitude smaller than vapour jet-induced particles. Finally, particles ahead of the beam are slightly affected by the argon gas and do not move over long distances [22]. Figure 1.2i gives a comprehensive framework of all the major phenomena involved in the laser-matter interaction [23].

1.1.2 Involved process parameters

The working principle of PBF technologies is rather simple: a heat source, either laser or electron beam, scans the powder bed, ensuring an adequate horizontal overlap and bonding between adjacent scan tracks. After that, a new powder bed is deposited, and the procedure is iterated, ensuring an adequate vertical overlap with the underlying layer. Despite the simple principle, the entire process is governed by several parameters, each one possibly altering the final result. The mainly investigated in the literature include the laser power, the hatch spacing, the scan speed, the layer thickness and the scan strategy. However, their number is significantly higher, and a more comprehensive description divides them into four groups [24].

- *Beam-related process parameters*

The heat source *power* [W] primarily rules the amount of energy imparted to the powder bed, and the spot size [μm] (or *beam diameter*) defines the area over which the source irradiates it. If the heat source is not a continuous wave source but rather a pulsed one, the *pulse duration* [μs] (or *exposure time*) refers to the amount of time the spot stops over the same position. The *point distance* [μm] (or the *frequency* [μm^{-1}]) determines subsequent positions of the spot in order to ensure adequate overlap between them.

Among these, the source power is usually the most investigated parameter. Source power significantly controls thermal gradients and cooling rates [15], [25], as well as the porosity level within the consolidated material [26]. Additionally, it affects the size of microstructural features, such as scan tracks [26], [27] or cellular and grain microstructure [28], and also modifies the crystallographic texture [28], [29]. Due to its high reflectivity, Al alloys generally require high power to melt completely [30].

- *Scan-related process parameters*

Scan-related process parameters determine the way the heat source scans over the powder bed. The *scan speed* [mm/s] specifies how fast the source covers the powder bed. The slower the scan speed, the longer the heat source irradiates the underlying material, favouring its complete melting, consolidation and solidification with slower cooling rates. However, an excessive time to scan the powder bed causes the source radiation to produce undesired porosities [26], [31]. Similarly to source power, scan speed could significantly affect the microstructural features [27], [32], [33].

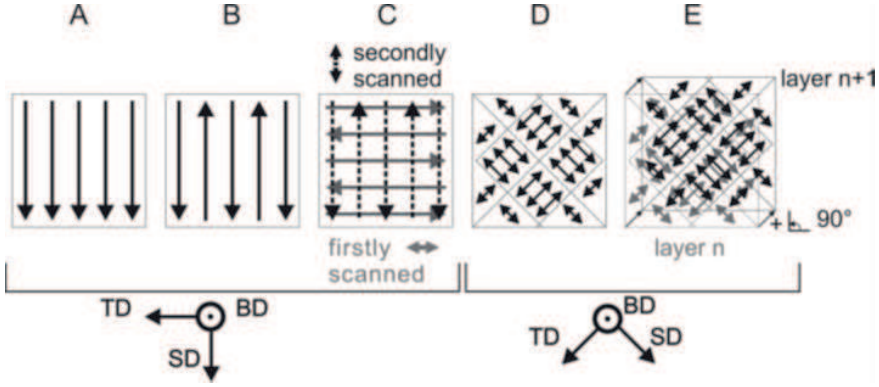

Figure 1.3. Examples of possible scan patterns. (a) Monodirectional. (b) Bidirectional. (c) Alternate bidirectional. (d) Chessboard strategy with 90° rotation. (e) Chessboard strategy with 90° rotation and shift. Reprinted with permission from Ref. [35].

The *hatch spacing* [μm] is the distance between two adjacent scan tracks and rules their mutual overlap. A high hatch spacing leads adjacent tracks to be partially separated, with a significant number of pores between them that negatively affects the final properties. A low hatch spacing ensures a better metallurgical bonding of the melt powder bed but decreases the building rate [31]. Generally, suitable hatch spacing values depend on the employed layer thickness, which also affects the building rate [34].

The *scan pattern* specifies the path of the heat source over the powder bed. Figure 1.3 depicts some possible choices, with the simplest one being the monodirectional (Figure 1.3a). In the bidirectional or meander strategy, the source moves along parallel tracks with alternate directions (Figure 1.3b), and its performance could be enhanced scanning twice and rotating the scan direction (Figure 1.3c). Figure 1.3d depicts the so-called chessboard strategy, where the region of interest is divided into several squares individually scanned by the source, usually with different mutual orientation. Again, differentiating the strategy for subsequent layers, for instance, shifting the chessboard as in Figure 1.3e, could improve the final result. Different scan strategies affect the amount of porosity [31], the microstructural features and crystallographic texture [35].

- *Powder-related process parameters*

The characteristics of alloy powder feedstock materials significantly influence the final quality of the AM part. The main features promoting a better flowability and homogenous melting include *size* and *shape distributions* of powder particles and their surface morphology. Particle size for PBF processes is typically a few tens of μm. Depending on the adopted manufacturing process, the shape varies from almost circular to significantly elongated and the surface morphology from almost smooth to very irregular. Four processes are mainly used for powder atomisation [12]. In the water atomisation (WA) process, a high-pressure water jet is used to atomise and solidify to powder a molten metal. The gas atomisation (GA) process implements a similar principle, with argon or nitrogen gas substituting water. Fine droplets of molten metal are poured on a rotary disk and flung to solidify as powders in the rotary atomisation (RA) process. In the plasma rotating electrode process (PREP) the end of a metal bar is melted through an electric arc or plasma and longitudinally rotated to eject fine droplets of solidifying metal.

Figures 1.4a-b compare an H13 tool steel powder produced by GA (Fig. 1.4a) and WA (Fig. 1.4b) processes [36]. The former is regular in shape, with a quite smooth surface showing small satellite particles. On the contrary, the WA powder exhibits an irregular and coarse surface texture that lowers flowability and causes a high surface roughness of the final part. Such features are typical of the WA process, which usually offers the worst atomisation performance. Generally, the RA process produces powder with a smooth surface but not very spherical in shape. Conversely, GA process results in a spherical morphology but a rougher surface due to satellite particles. Moreover, GA atomised powder often contains entrapped gas bubbles leading to porosity in the component, as will be shown in § 1.1.3. PREP generally offers the best result, with a powder perfectly spherical in shape and a smooth surface, but at the highest cost of fabrication process [12].

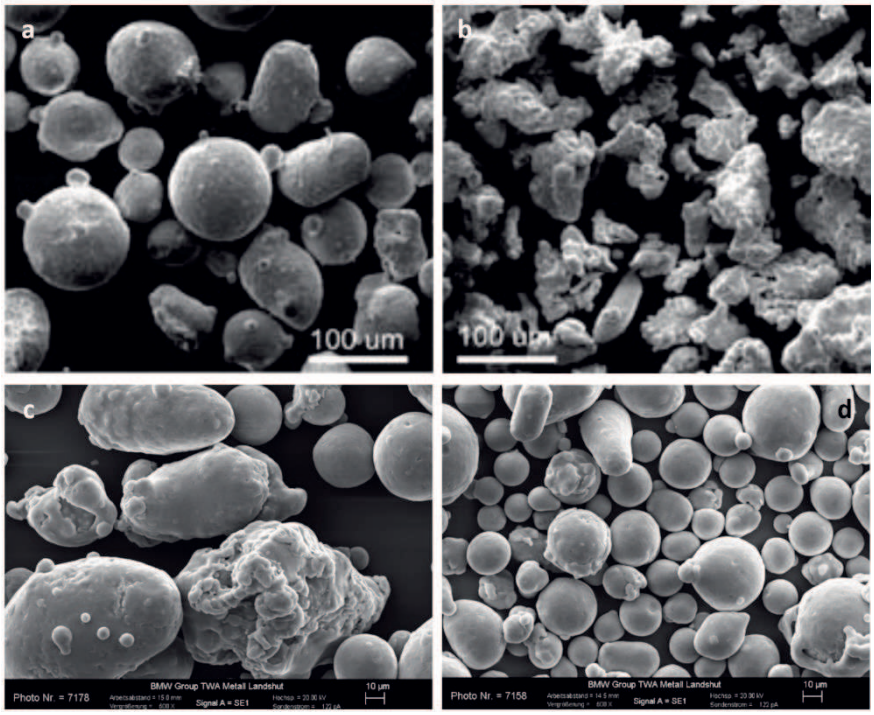

Figure 1.4. SEM images of alloy powders. (a) Gas-atomised and (b) water-atomised H13 tool steel powder. Reprinted with permission from Ref. [36]. (c)-(d) Gas atomised powder from two suppliers showing different size and shape distributions. Adapted with permission from Ref. [37].

Despite such general observations, the same atomisation process could lead to very different powder characteristics depending on the adopted process parameters. Figures

1.4c-d depict powders obtained from the GA process by two distinct suppliers, with the former being coarser in size and much more irregular in shape [37].

The high cost of atomisation processes to obtain high-quality powders often pushes for their reuse in PBF technologies [31], [38]–[40]. Nonvirgin powder affected by the heat source, e.g. heated or partially melted but not wholly fused, usually is more irregular in size and shape than the virgin powder. This fact possibly results in worse flowability and poor surface finish of the final components, limiting the number of possible reuses [13]. Conversely, the powder not affected by the process is usually comparable to the fresh one and could be reused several times without affecting the final result [38]–[40].

The *density* of the powder bed (its *packing structure*), the *layer thickness*, as well as the *chemical composition* of the alloy powder that determines its thermo-physical properties, all influence the interaction with the heat source. As a consequence, they have a role in the resulting microstructural features, defects and hence final performance of the components fabricated with a given set of building parameters. Among these, the layer thickness if usually the most investigated. A high layer thickness increases the building rate but can also lead to defects such as balling and reduces the dimensional accuracy. The maximum permissible value strongly depends on the hatch spacing to ensure the bonding between adjacent tracks [34].

- *Temperature-related process parameters*

They include the temperature field of *powder feedstock*, *powder bed* and *building platform*. Pre-heating of the powder could help to remove hydrogen absorption by moisture, reducing the appearance of gas pores [41]. It could be obtained either heating the powder feeder, scanning the powder bed with a low-power (not-melting) heat source, or using a heated building platform [41], [42]. This latter also helps in controlling thermal gradients during the AM process, reducing residual stresses [40]. It can also affect the microstructural features, as will be explained in § 1.2.2. Combined with high source power, a high powder bed temperature generally produces dense parts, which however could suffer from poor dimensional accuracy. Combinations of high source power and low powder bed temperature ensure better dimensional accuracy, but raise the risk of nonuniform shrinkage and residual stresses [24].

Besides the above-reported classification of process parameters, it is worth to note that most of them are not independent, but rather interact mutually. For instance, the required laser power depends on the thermo-physical properties of the powder, such as thermal conductivity and reflectivity. In turn, these properties are also a function of the powder bed characteristics, like size, shape and packing density of particles. Laser power also depends on the overall energy input required to melt the powder, and thus it strongly interacts with the spot size, the scan speed and the powder bed temperature. As a consequence, multiple-parameter diagrams are often experimentally determined to detect a suitable combination of process parameters to minimise defects and optimise the mechanical performance [26], [43], [44]. A more recent field of research is instead devoted to the online monitoring of AM processes through optical imaging [45], thermal imaging [46], [47], and acoustic emission [48].

1.1.3 Process-related defects

Despite the relatively simple working principle of the PBF technology, paragraph § 1.1.2 showed that several process parameters are simultaneously involved. They all contribute, to a certain extent, to the source-matter interaction briefly described in § 1.1.1, affecting the quality of the final part. Additionally, in general, their effect is not simply assessable because of their multiple mutual interactions. It follows that it is not straightforward to identify the proper combination of process parameters. Under conditions far from ideal, the final product would suffer from several deleterious defects, such as porosities, stress cracks, humping and balling phenomena. All these are mitigated, or eliminated, adjusting the building parameters. However, it is worth to note that several defects, like oxides, residual stresses and poor surface quality, struggle to be avoided even if a suitable combination of process parameters is employed.

- *Loss of alloying elements*

During PBF processes, the molten metal reaches considerably high temperatures, usually up to 2000 °C for Al alloys [15], and pronounced vaporisation of alloying elements occurs. Due to their different volatility, selective vaporisation could cause the chemical composition of the final product to change compared to the starting powder bed. Generally, the higher the temperature distribution of the molten metal, the higher would be the vaporisation rate of volatile elements. However, depletion of alloying

elements concerns the entire volume of the fused material, but they vaporise just through its external surface. Thus, the surface-to-volume ratio of the melt pool affects the overall vaporisation rate. Since a higher temperature field often means a larger melt pool, its effect on the vaporisation rate is not easily predictable.

Measuring the composition of the metal powder and the final part is the quickest way to evaluate potential vaporisation of alloying elements. Energy-dispersive X-ray (EDX) measurements by Aboulkhair *et al.* [31] detect a significant loss of Mg from an additively manufactured AlSi10Mg alloy compared to the fresh powder. Partial loss of volatile alloying elements could affect the properties of the AM product. For instance, depletion of Mg in Al alloys reduces its contribution to precipitation strengthening and corrosion resistance.

- *Humping phenomenon (or Kelvin-Helmholtz hydrodynamic instability)*

A high building rate is often easily achieved by increasing the scan speed and consequently adjusting other parameters to obtain a near fully dense part. However, increasing the scan speed could lead to instability of the melt pool, resulting in a discontinuously deposited track with nonuniform thickness.

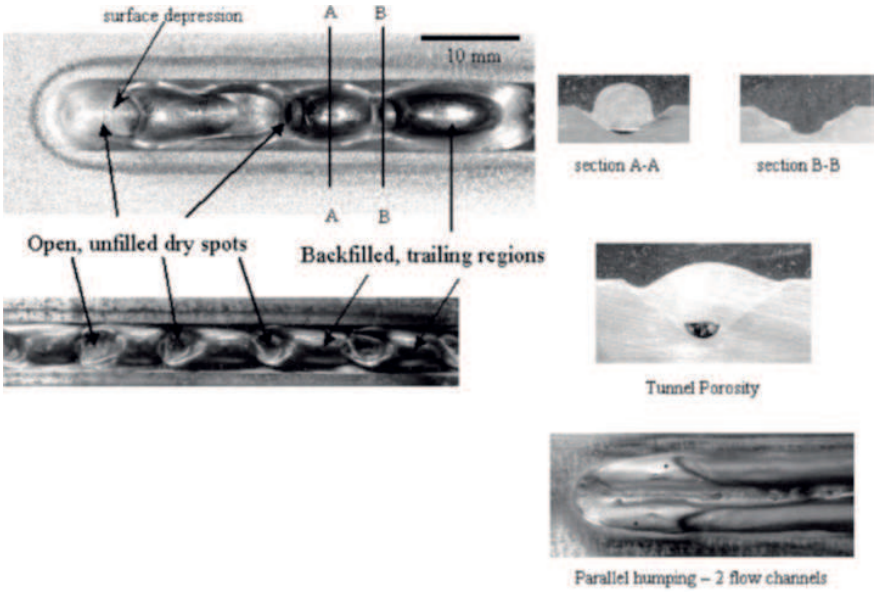

Figure 1.5. Humping phenomenon in arc welding, exhibiting the typical bead-like appearance. Reprinted with permission from Ref. [49].

One kind is the so-called Kelvin-Helmholtz hydrodynamic instability, which causes the scan track to exhibit a bead-like appearance, also known as humping. Figure 1.5 depicts such a phenomenon for a high-speed arc welding process [49]. The scan track

shows an alternation of humped bead-like features and unfilled dry spots, together with surface depressions at the front of the melt pool.

The Kelvin-Helmholtz hydrodynamic instability is usually ascribed to the velocity difference between the molten metal at the top of the melt pool and shielding gas. This latter is quicker than molten metal, destabilising the liquid metal surface. The effect is generally mitigated by higher layer thickness. However, scientific works concerning with such a phenomenon are scarce [12], and they generally deal with another kind of instability.

- *Balling phenomenon (or Plateau-Raleigh capillary instability)*

At high scan speed, the melt pool tends to elongate and thin and, depending on additional parameters such as viscosity and surface tension, becomes unstable. According to the Plateau-Raleigh capillary instability, if the width-to-length ratio of the melt pool is too small, it separates and forms small spherical balls to maintain the uniform capillary pressure inside the pool [50]. These balls then group along the scan track, increasing the surface roughness and possibly leading to an improper deposition of the following layer.

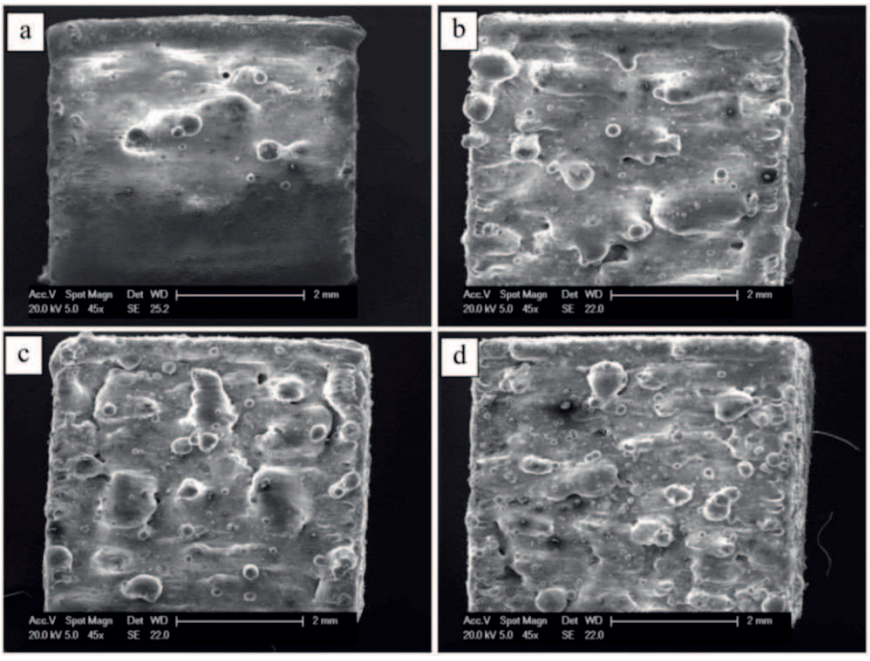

Figure 1.6. Balling phenomenon. (a) to (d) Effect of increasing scan speed. Reprinted under Creative Commons CC-BY license from Ref. [31].

The balling phenomenon is often reported in the literature of PBF produced alloys [26], [31], [51]. Figure 1.6 depicts its dependence on an increasing scan speed. According

to the Plateau-Raleigh capillary instability, as the scan speed raises from Figure 1.6a to Figure 1.6d, more and more spherical balls are formed on the scanned surface.

- *Lack-of-fusion porosity*

As suggested by the name, it stems from an incomplete fusion due to lack of the energy input from the heat source during the AM process [31], [52], [53]. It results from a not proper choice of the deposition parameters. For instance, high hatch spacing and layer thickness are often employed to increase the building rate. However, if the energy input is insufficient, the former causes incomplete melting and bonding between adjacent tracks, the latter between subsequently deposited layers [31].

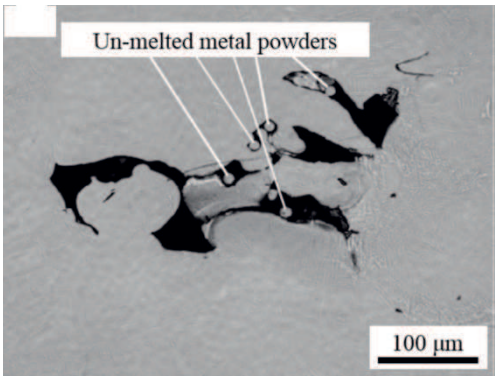

Figure 1.7. Lack-of-fusion pore, with the typical irregular morphology, hosting unmelted metal powders. Reprinted under a Creative Commons license from Ref. [52].

Therefore, lack-of-fusion pores are usually located in such positions, and often host unmelted powder particles (Fig. 1.7). Due to their inherent nature, they occur with a very irregular and sharp morphology, which promotes stress concentration. Additionally, when occurring between subsequent layers, they reduce the load-bearing section. In all cases, they deleteriously affect static and dynamic resistance [53].

- *Keyhole porosity*

Lack-of-fusion porosity occurs due to incomplete fusion and bonding of the powder alloy, suggesting a higher energy input to solve the problem. However, imparting excess energy to the molten metal would likewise be deleterious and produce a different kind of porosity. If the energy input is much higher than required, the resulting overheating, through strong metal vaporisation from the surface and recoil pressure, drives the melt pool surface deep into the material to form a keyhole-like depression [54]–[56]. Such occurrence is depicted in Figure 1.8a for an AlSi10Mg alloy [54]. Due to its inherent instability, such depression can easily collapse (Fig. 1.8b) and trap the inert shielding

gas, giving rise to the pore formation within the substrate at the bottom of melt pool (Fig. 1.8c-d). Due to entrapped gas pressure, the resulting pore is almost spherical, which makes it readily discernible from a lack-of-fusion pore.

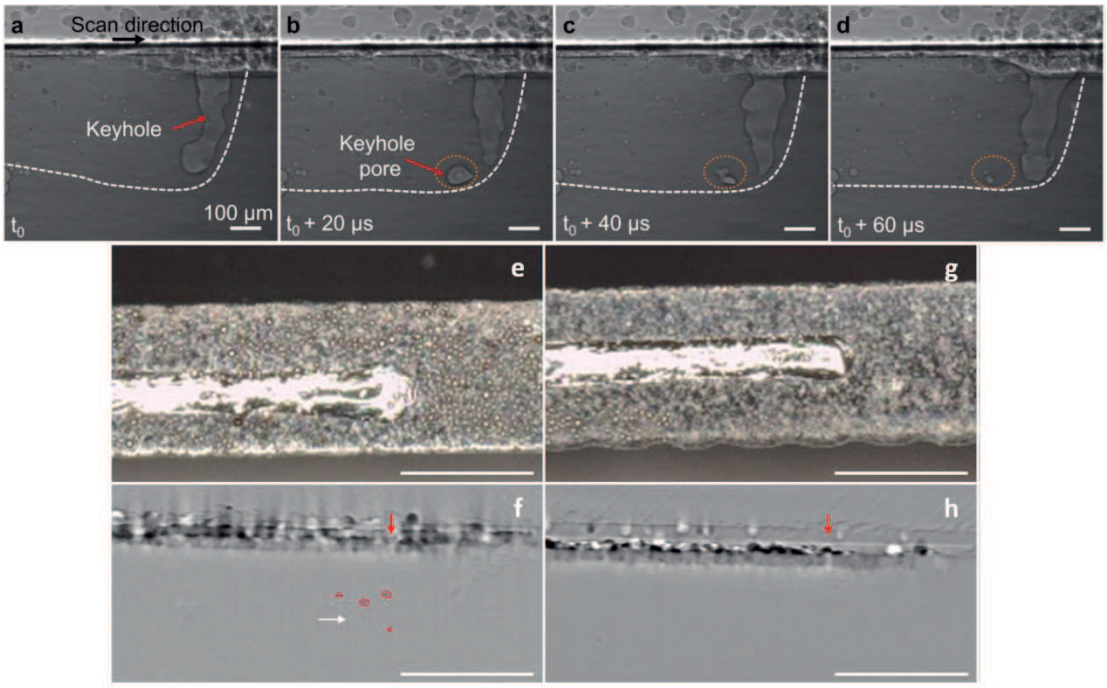

Figure 1.8. PBF process of AlSi10Mg alloy. (a) to (d) Pore formation due to keyhole collapse. Adapted with permission from Ref. [54]. PBF process of Ti–6Al–4V alloy. (e) Optical image and (f) side-on X-ray image of a scan track in the turning point region produced using a constant power of 100 W. (g) Optical image and (h) side-on X-ray image of a scan track in the turning point region produced using a 100 W peak power pore mitigation scan strategy. Reprinted under a Creative Commons Attribution 4.0 International License from Ref. [56].

Even under suitable deposition parameters, keyhole pores could occur at the source turning point at the end of a scan track. As the heat source approaches the turning point, it is decelerated and then accelerated back to the nominal scan speed immediately after the turn. As the scan speed is reduced to zero at the turning point, with all other deposition parameters being constant, the energy per unit volume instantly transferred to the material raises and leads to a keyhole depression and pores formation, as depicted in Figs. 1.8e-f. In this light, Martin *et al.* [56] implemented a mitigation strategy to prevent pore formation at laser turning points by modulating the laser power to compensate for melt pool overheating. Figures 1.8g-h depict successful results.

- *Gas porosity*

Gas pores are commonly found in PBF processes and stem from gas entrapment within the AM product. The gas is generally hydrogen, mostly coming from moisture absorption by the powder bed. The hydrogen solubility in solid aluminium is about ten-fold lower than in liquid aluminium, causing strong segregation at the solidification front as cooling occurs. As such amount exceeds the maximum solubility, hydrogen pores nucleate. Actually, given the fast solidification rate of the PBF processes [15], [35], hydrogen is often trapped within the solidified material in a metastable solute state. This latter is released, and the pore nucleates as further energy is imparted to the material, either coming from a neighbouring heat source scan or a subsequent heat treatment. Weingarten *et al.* [41] found that moisture on the surface of powder particles is the dominating hydrogen source in PBF processes. Typical methods to reduce the hydrogen content include an external drying of the powder at moderately high temperature (100-200 °C) or a pre-scanning of the powder bed with a low-power heat source [41].

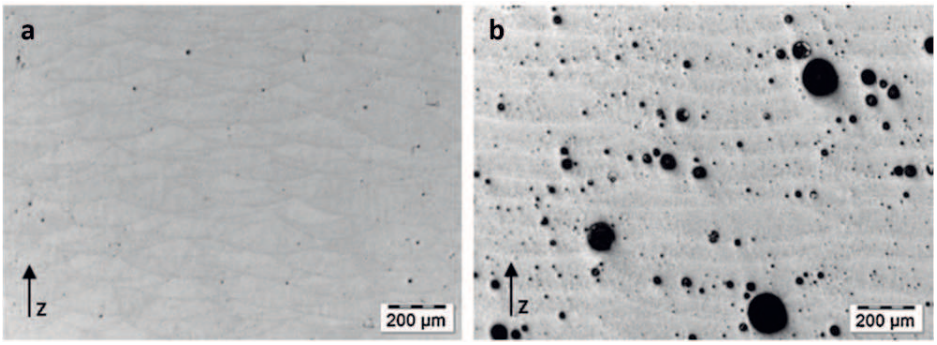

Figure 1.9. PBF process of AlSi10Mg alloy: hydrogen pores in samples built up with dried powder (T_{heat} = 90 °C) and different laser beam diameter. (a) 0.3 mm. (b) 1 mm. Reprinted with permission from Ref. [41].

Besides powder drying, deposition parameters also affect the volume of gas pores. For instance, Fig. 1.9 elucidates that, with all other parameters being constant, increasing the beam diameter worsen the porosity level significantly. Gas pores in AM products do not stem just from superficial moisture of the powder bed, but also from pre-existing gas pores within single powder particles. Figure 1.10a depicts a couple of such pores located in the powder bed obtained by the GA process. GA produced powders often contain entrapped gas bubbles, whereas using PREP process ensures a lower porosity for powders obtained under the same processing conditions [12].

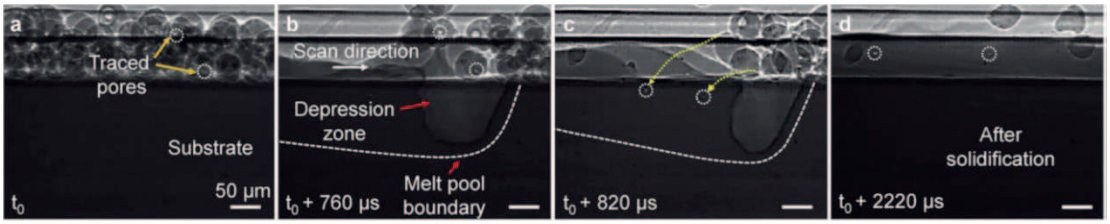

Figure 1.10. Pore formation from feedstock powders in PBF process. (a) to (d) X-ray image sequence showing the transfer of pores from the powder bed into the melt pool and, then, in the solidified track. Reprinted with permission from Ref. [54].

The sequence of X-ray images from Fig. 1.10b to Fig. 1.10d highlights the way gas bubbles entrapped within the powder particles are transferred to the melt pool, and finally to the solidified material.

- *Oxides*

Given the complex dynamic of the heat source-powder bed interaction and the high temperatures involved in AM processes, possible formation of oxides is not surprising. Two kinds of oxide could be detected in PBF processes of Al alloys, and they differ for formation mechanism and size. Large micrometric oxides originate from oxidation of metal in the gas phase or spattered powders during the interaction of heat source and powder bed. They subsequently impinge on the molten metal, preventing a successful consolidation. For such a reason, they are often in association with irregular (lack-of-fusion) pores. Figure 1.11a depicts an example of such kind of oxide [57].

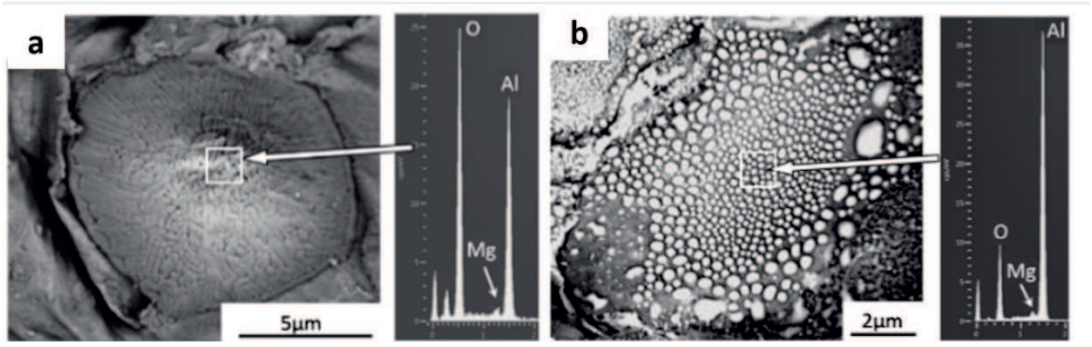

Figure 1.11. PBF process of AlSi10Mg alloy. (a) Micrometric oxide from the oxidation of metal vapour or spatter. (b) Submicrometric oxides from the native oxide film of powders. Adapted with permission from Ref. [57].

Additionally, submicrometric oxides are reported. They are believed to originate from the native nanometric oxide film of powders which, upon melting, de-wets from the Al alloy to form fine particles, possibly Al-based oxides, as reported in Fig. 1.11b [57].

- *Cracking*

AM processes suffer from two main kinds of cracking phenomena, both originating because of the fast cooling conditions. The first kind, the *solidification cracking*, is rather a thermal phenomenon. After being deposited over the substrate, a new solidifying layer tends to contract due to thermal contraction and solidification shrinkage. However, such a mechanism is hindered to a certain extent by the previously solidified layers. Since they have already reached a lower temperature, they are stiffer and resist from being pulled in tension by the new contracting layer. The result is a tension generation in the solidifying layer, which cracks if the stress value overcomes the material strength [12].

The second cracking phenomenon, often known as *liquation cracking*, is mostly dependent on the chemical composition of the alloy. It mainly concerns alloys having a significant difference between liquidus and solidus temperatures to generate a mushy zone or partially melted zone. During the cooling stage, the mushy zone, being partially solidified and able to bear external forces, suffers from tensile stresses coming from solidification shrinkage and thermal contraction. Such a mechanism often results in the formation of so-called "hot" (because of the forming temperature) cracks.

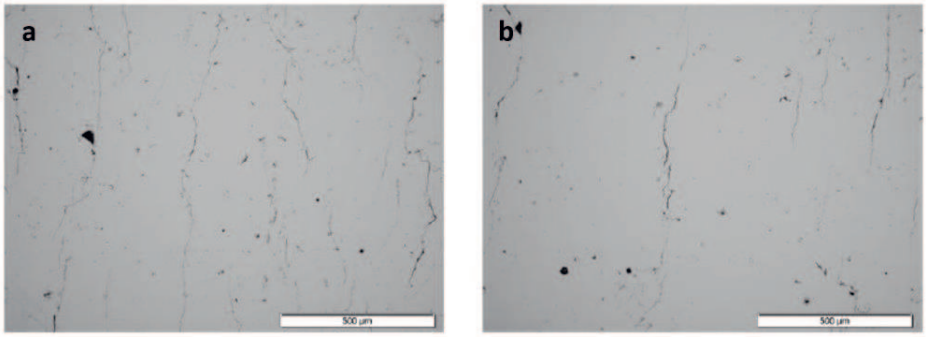

Figure 1.12. PBF process of an Al7075 alloy, cracking phenomenon at different pre-heating temperature. (a) 40 °C. (b) 200 °C. Reprinted under a Creative Commons CC-BY license from Ref. [58].

Figure 1.12 depicts the liquation cracking phenomenon for an Al7075 alloy processed with different pre-heating temperatures [58]. Even if this latter mitigates the deleterious

effect, several cracks are still observable (Fig. 1.12b). As shown, cracks could reach hundreds of μm in length, and often spread over several layers.

Alloys coupling wide mushy zone and massive thermal contraction, like most of wrought Al alloys, are the most susceptible to liquation cracking and often defined as "unprintable" [12], [58]–[60]. On the contrary, alloys with narrow mushy zone and solidification range exhibit a better printability. This reason accomplishes for the early success and spread of nearly eutectic AlSi alloys among the 3D printing technologies. However, recent developments enable also typically unprintable Al alloy to be processed successfully by PBF technologies, and Fig. 1.13 summarises the adopted strategy [59]. Typical solidification curves of printable and unprintable alloys are depicted in Fig. 1.13a. Hot tear-susceptible alloys, such as the Al7075, displays large solidification ranges and a sharp turnover in the solidification curves at high fractions of solid, this latter usually associated with an increased solute partitioning in the liquid.

Printable alloys, such as the AlSi10Mg, have a small difference between the liquidus and solidus temperatures and a mild turnover occurring at lower solid fractions. Figure 1.13b shows a schematic of solidification growth for alloys with broad and narrow solidification ranges. In the first case, columnar grains grow leaving long and empty channels of interdendritic liquid. As solidification proceeds, thermal shrinkage leads to tearing and long cracks formation. In the second case, the narrow solidification range promotes a more planar solidification front and short interdendritic channels, which are easily backfilled. As a result, hot tears do not occur. As a general solution, Martin *et al.* [59] suggest the addition of suitable nanoparticles to the standard powder feedstock. For instance, the Al7075 powder was added with hydrogen-stabilized Zr particles, which decompose during melting to form the favourable Al_3Zr nucleant phase (Fig. 1.13c-d).

Addition of Zr to Al7075 does not significantly alter the solidification behaviour, as highlighted by the almost superimposing curves in Fig. 1.13e. However, primary Al_3Zr particles form in the melt pool and act as nucleants for the Al phase, which now solidifies with an equiaxed morphology. Microstructural analyses reveal many long cracks (Fig. 1.13f) and columnar grains (Fig. 1.13g) in the standard Al7075 alloy, as expected from the solidification conditions. On the contrary, specimens built using the functionalised powder are almost crack-free (Fig. 1.13h) and composed of many fine equiaxed grains (Fig. 1.13i). Despite the solidification range is not modified by Zr addition, fine equiaxed

grains easily allow grain rotation and deformation. As a result, the grain structure accommodates strain from solidification shrinkage in the mushy zone, preventing crack initiation and growth.

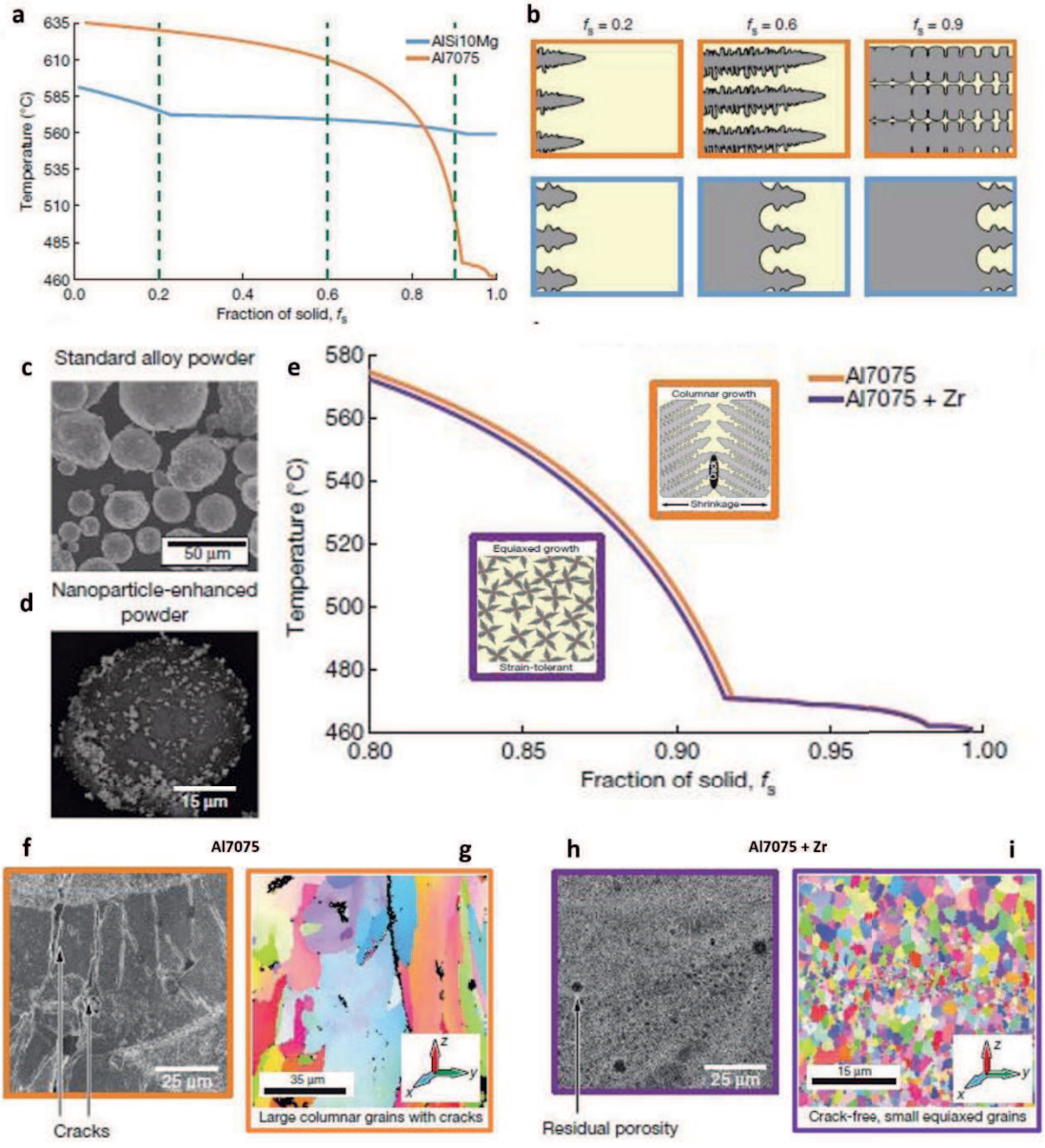

Figure 1.13. Production of high-strength and hot crack-free Al alloys by PBF. (a) Evolution of solid fraction with temperature for Al7075 and AlSi10Mg (conventional 3D-printed) alloys. (b) Schematic of solidification of alloys solidifying over a large (top, Al7075) and narrow (bottom, AlSi10Mg alloy) temperature range. (c)-(d) Al7075 alloy powder feedstock: (c) conventional; (d) functionalised with nanoparticles. (e) Effect of Zr addition on the evolution of solid fraction with temperature, insets depict columnar (Al7075) and equiaxed (Al7075 + Zr) solidification behaviour. Microstructural features of (f)-(g) Zr-free and (h)-(i) Zr-added Al7075 alloy: (f)-(h) SEM images; (g)-(i) EBSD inverse pole figures. Adapted with permission from Ref. [59].

Some alloys allow the nucleation mechanism described above without the need for nanoparticles addition to the starting powder. AlMgSc [32], [61], [62] and AlMgZr [63]–[65] alloys inherently contain solute elements (Sc and Zr) that promote the formation of primary nucleant phases, Al_3Sc and Al_3Zr, respectively. However, the nucleation efficiency is lower compared to functionalised powders. In fact, a duplex grain structure usually forms, with columnar grains located in the top part of melt pools. The increased solidification front velocity toward the melt pool surface causes solute entrapment and hinders the formation of primary nucleant phases [64]. Laser rescanning could be adopted to increase the equiaxed-to-columnar ratio of grains [64].

- *Surface roughness*

Since most of the AM products in the as-built state suffer from poor surface roughness, it is reasonable to include it among the characteristic defects. It mainly stems from two causes. The first one is related to the part design and process, and includes its orientation, the building angle, the presence of down-skin surfaces and support structures.

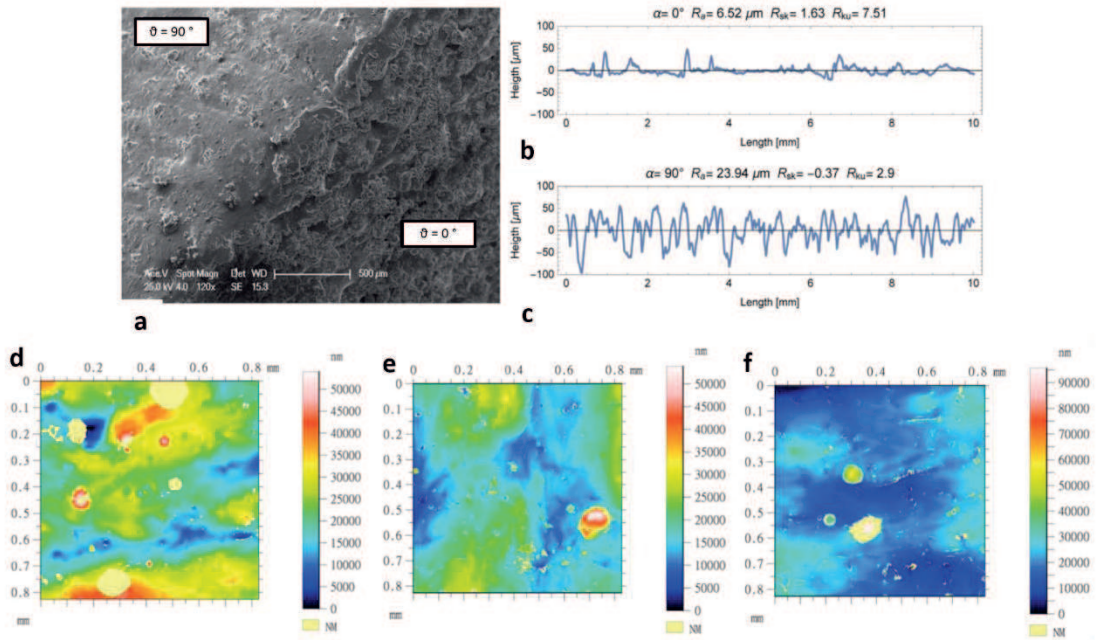

Figure 1.14. PBF of an AlSi10Mg alloy. (a) to (c) Effect of building angle on the surface roughness. (a) SEM image of the surfaces characterised by building angles γ of 0° and 90°. (b) Surface roughness for 0° building angle. (c) surface roughness for 90° building angle. Reprinted with permission from Ref. [66]. (d) to (f) Effect of increased energy input on the surface roughness. Adapted with permission from Ref. [67].

For instance, the effect of building angle to the vertical direction γ, known as "stair-step" effect, is due to the stepped stair-like approximation by layers of curved and inclined surfaces. The lower γ, the higher the resulting surface roughness for a given layer thickness. Figures 1.14a-b-c depict this effect comparing surfaces built at 0° and 90° to the vertical direction [66]. The second one exhibits a surface roughness significantly higher. The stair-step effect is the more pronounced, the larger is the layer thickness, due to a worse approximation of the inclined surface.

The second source of poor surface roughness descends from the characteristics of the material feedstock (powder size and shape distributions) as well as an improper selection of deposition parameters. In this latter case, balling phenomenon and unmelted powder particles over the surface could occur. The lack of adequate energy input from the heat source causes the powder to stick at the solidified surface, and the average surface roughness is on the same order of magnitude of the powder size. An improvement generally could be achieved adjusting the deposition parameters to increase the energy input, as highlighted comparing in the order the sequence of contour plots in Figs. 1.14d-e-f [67]. However, it is worth notice that a very high heat input could be as detrimental as a very low one for surface finish, because of induced high thermal stresses and non-uniform solidification rate [12].

- *Residual stresses*

High spatial thermal gradients develop in AM processes within the rapidly solidifying material due to the presence of a cold substrate, either the building platform or previously solidified layers. Since the new layer and the underlying material are not homogeneously heated and cooled, differential contraction occurs, leading elastic-plastic strain and thus residual stress to arise. The final result stems from a complex interaction between the time variation of the temperature field, thermal expansion and contraction of the material, and the constitutive mechanical behaviour. Cyclic deformations up to the plastic regime due to periodic heating and cooling would generate residual stresses strongly dependent on the material flow stress.

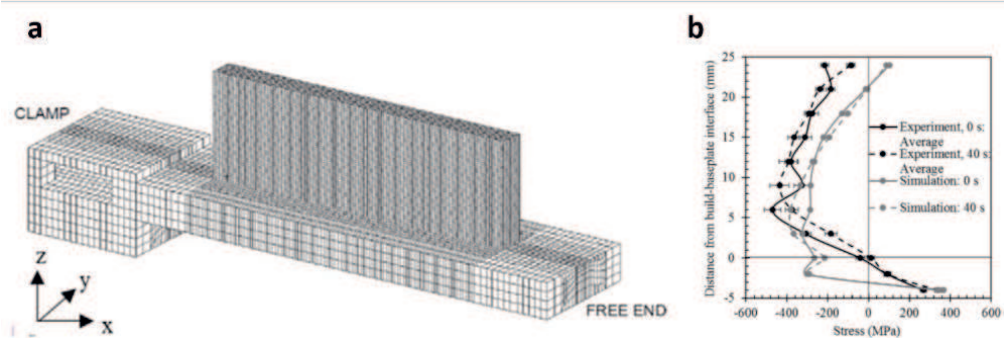

Figure 1.15. Residual stresses distribution in an Inconel 625 additively manufactured alloy. (a) Schematic of finite element mesh of the wall. (b) Comparison of simulated and experimental results. Adapted with permission from Ref. [68].

Given the complexity of the formation mechanism and the limitations of experimental methods, numerical models are often employed to estimate entity and distribution of residual stresses [69], [70]. Figure 1.15a depicts the simplified wall geometry adopted to simulate the distribution of residual stresses in an Inconel 625 alloy [68]. Simulated results are reported in Fig. 1.15b, together with the experimental ones determined by diffraction methods. Residual stresses strongly change along the wall height, reaching values as high as several hundreds of MPa, and also extending within the building platform. Some commonly adopted strategies to mitigate residual stresses include use of a pre-heated substrate, shorter deposition length and layer thickness, scan patterns with smaller scanned areas (chessboard) [12]. Besides causing part distortion and loss of the geometric tolerances, the presence of residual stresses severely affects the mechanical properties of the final product, especially regarding fatigue strength [71], [72].

1.2 METALLURGY OF AlSi10Mg ALLOY PROCESSED BY POWDER BED FUSION

Additively manufactured alloys exhibit a peculiar microstructure significantly different from the one obtained by traditional technologies. This is due to the unique process conditions characterising the AM process and briefly described in the previous paragraph. Since the AlSi10Mg alloy is the main subject of the present thesis, the following paragraph (§ 1.2.1) aims at deeply describing its microstructural features in the as-built state down to the nanometric scale. Comprehension of the microstructure is an invaluable tool to understand the corresponding mechanical properties as well as its response to heat treatments (§ 1.3). The final part of the paragraph (§ 1.2.2) is devoted to

the metastability of the as-built microstructure, which is believed to be a suitable link to the subsequent paragraph regarding heat treatments.

1.2.1 Peculiar features of the as-built microstructure

Directional heat transfer, high thermal gradients (G) and growth rates (R) characterise the manufacturing process of the AlSi10Mg alloy. The resulting microstructure displays a peculiar hierarchical arrangement, which will be described in the following.

- *Melt pools and cellular-dendritic structure*

The laser-matter interaction leads to the formation of a melt pool elongated along the scanning direction of the heat source, creating a scan track. As depicted by scanning electron microscopy (SEM) image in Fig. 1.16a [33], melt pools in a transversal section are approximately semi-circular in shape and hundreds of μm in size. Both size and shape of melt pools depend on the adopted deposition parameters [27], [73]–[75] and they, in turn, affect other microstructural features like the morphology and texture of the grain structure [12]. Within the melt pool, the high G/R ratio promotes a cellular-dendritic solidification mechanism [35], [76]. The resulting microstructure exhibits elongated cellular dendrites of the primary Al phase, surrounded by a network of eutectic Al-Si, as shown in Figs. 1.16b-c [33]. It is worth to note that the growth of the columnar structure possibly terminates with the formation of an equiaxed structure at the top of the melt pool due to the columnar-to-equiaxed transition (CET). Such behaviour will be deepened further in this section when the grain structure will be taken into account. Since eutectic and primary Al phases are barely distinguishable at microstructural observations, in the following the eutectic Al-Si will be often simplified as "Si network" or "eutectic Si network", whereas it actually indicates a mixture of both Al and Si. As well as for the melt pools, the finesse of the cellular structure is ruled by the deposition parameters, which affect the resulting cooling rate ($C_R = G \cdot R$). Due to the high C_R, estimated as 10^3-10^8 K/s [77], [78], typical size values lie in the micrometric or sub-micrometric range.

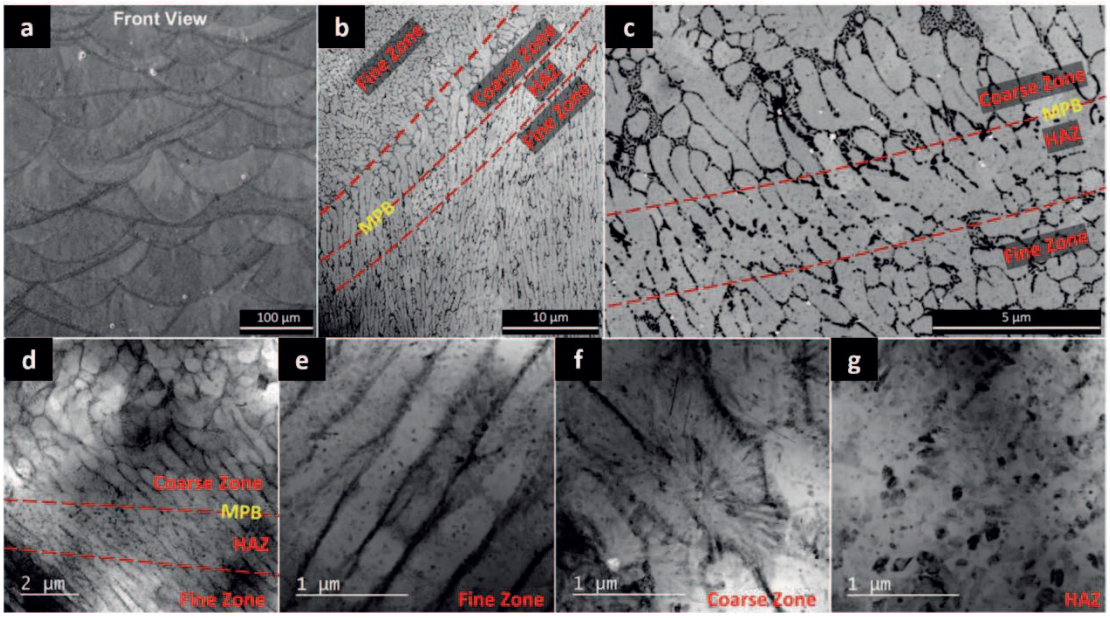

Figure 1.16. Cross sectional microstructure of a PBF produced AlSi10Mg alloy in the as-built state. (a) to (c) SEM images. (d) to (g) BF-TEM images. (a) Melt tracks. (b) to (d) Location of different areas within the melt tracks. (e) Fine zone. (f) Coarse zone. (g) HAZ. Reprinted with permission from Ref. [33].

However, the microstructure is not homogeneous across the melt pool, but three different areas could be detected, as shown in Figs. 1.16b-c [33]. The finest microstructural features lie in the inner part of the melt pool, defining the *fine zone*. Along the melt pool boundary (MPB), a reduction of C_R leads to a local coarsening of the microstructure without altering the cellular dendritic shape. Such an area is defined as the *coarse zone*. A thin stripe underlying the coarse zone displays the Si network disrupted into distinct Si particles. It represents an area of previously solidified material that does not undergo melting during the deposition of the new layer. However, since the temperature increment modifies its microstructure, such area is commonly referred to as the *heat-affected zone* (HAZ). Bright-field (BF) transmission electron microscopy (TEM) images in Figs. 1.16d-e-f-g depict the fine, coarse and heat affect zones at higher magnification [33]. Because of the different size and shape of the microstructure across the melt pool, the resulting local strength significantly differs [79]–[81]. As highlighted in Fig. 1.17, nanoindentation tests reveal that coarse zone and HAZ exhibit the lowest mechanical properties [81]. Inhomogeneous properties across the whole microstructure are often ascribed as one of the causes of the anisotropic behaviour of the AM produced components [82], [83].

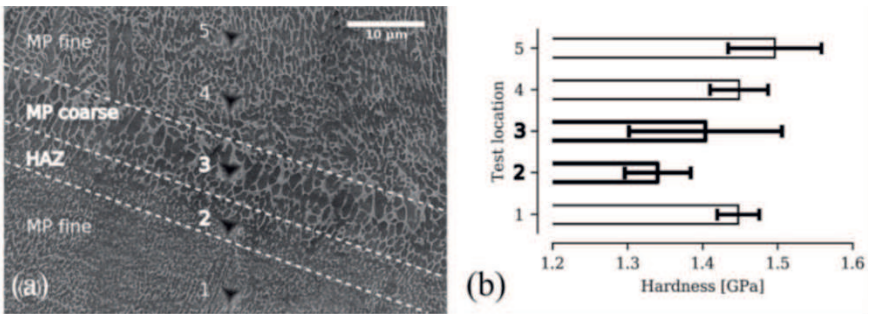

Figure. 1.17. Variation of mechanical properties along the MPB in the as-built condition. (a) Micrograph of indent prints in the MPB fine (zones 1,4 and 5), MPB coarse (zone 3) and HAZ (zone 2). (b) Nano-indentation hardness values measured in the corresponding zones. Reprinted with permission from Ref. [81].

- *Secondary phases and dislocation tangles*

Primary Al phase and eutectic Si network constitute most of the sub-micrometric microstructure. However, the AlSi10Mg alloy also contains a minor amount (< 1 wt. %) of Mg and Fe (other trace elements are not taken into account in the present discussion). According to the phase diagram and solidification sequence reported in Fig. 1.18a, and Fig. 1.18b, respectively, the formation of secondary Mg- and Fe-rich phases is expected [84]. Due to the low amount of Mg and Fe in the alloy, their corresponding phases form in the last stages of solidification within the inter-dendritic Si network. SEM imaging (Fig. 1.16) usually lacks in detecting such features because of poor compositional contrast and limited spatial resolution of EDX analysis. Conversely, they are readily identifiable by scanning transmission electron microscopy (STEM)-EDX analysis, as reported in Figs. 1.18c to Figs. 1.18g [84] and other works [6], [85], [86].

Figure 1.18c highlights a high density of dislocations (black stripes) within the Al cellular dendrites. Such microstructural feature is peculiar of the PBF produced AlSi10Mg alloy, and generally of many AM processed alloys [87]–[91]. Dislocation tangles are generally ascribed to high thermal stresses that develop during the thermal heating/cooling cycles of the material [32], [89], [92] and, for Al-Si alloys, to the difference in thermal expansion of the Al matrix and eutectic Si [79]. Dislocation strengthening (or Taylor strengthening) is one of the main reinforcing mechanisms in crystalline metals. It is usually achieved after plastic deformation and causes a reduction of ductility. However, recent works demonstrated that the dislocation network in AM produced steels could enhance both strength and ductility by a modulation of the dislocation

motion [91]. This outcome breaks a well-established trade-off of crystalline metals and suggests the possible development of high-performance alloys by tailoring the microstructure through the AM process.

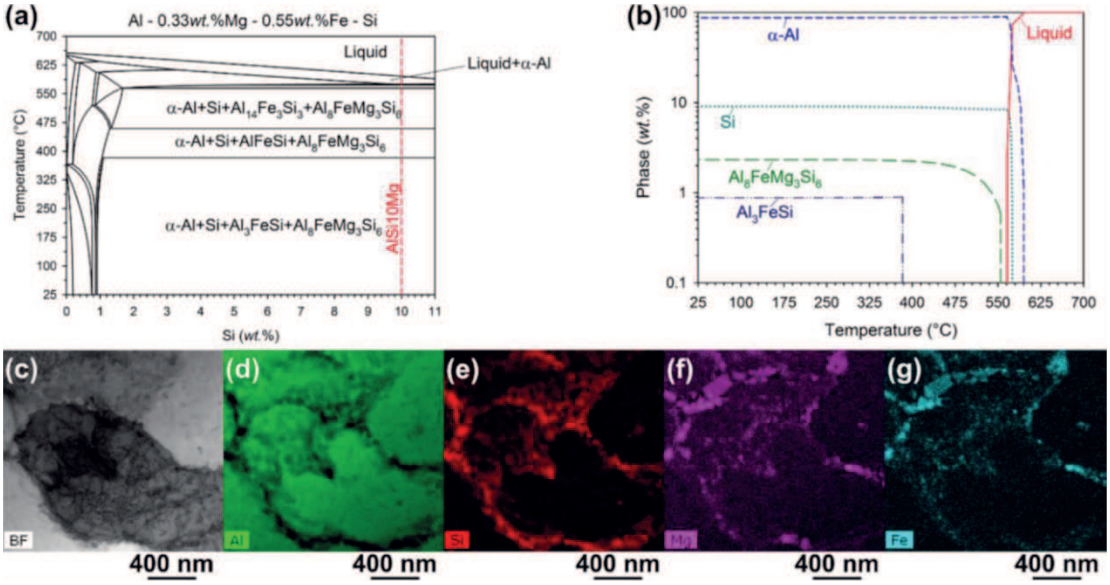

Figure 1.18. Amount and location of secondary phases of a PBF produced AlSi10Mg alloy in the as-built condition. (a) Al-Si-Mg-Fe isopleth with 0.33 wt. % Mg - 0.55 wt. % Fe at Al-rich corner. (b) Phase amount during equilibrium solidification of AlSi10Mg alloy. (c) BF-STEM image of the as-built sample with the beam direction parallel to the Al [011] zone axis. (d) to (g) Corresponding EDX mappings for Al, Si, Mg, Fe, respectively. Reprinted with permission from Ref. [84].

- *Crystal structure*

Several neighbouring Al cellular dendrites share a common crystallographic orientation and form a single large grain. In the AM processes, the grain growth direction is parallel to the maximum heat flow direction, which is normal to the solidification interface of the melt pool. The growth direction changes from almost opposite to the build direction to radial to MPBs as the width-to-depth ratio of the melt pool decreases. The high thermal conductivity of Al alloys promotes strong thermal gradients and solidification velocities, hindering constitutional undercooling to develop at tips of grains. As a consequence, they nucleate and grow with a cellular-dendritic solidification mechanism, analogously to the Al cellular dendrites. Morphological grain texture is realised, with the elongated grains developing from the MPBs in a front view section, as depicted in Fig. 1.19a by electron backscattered diffraction (EBSD) orientation

map [35]. Figure 1.19b shows equiaxed grains in a top view section. Elongated grains are generally micrometric in width but span over several tens of μm in length. Moreover, they often grow epitaxially from the underlying material, crossing several subsequent layers [35], [93], [94]. The morphological texture is often ascribed as a cause of anisotropic mechanical properties in AM produced parts [95]–[97].

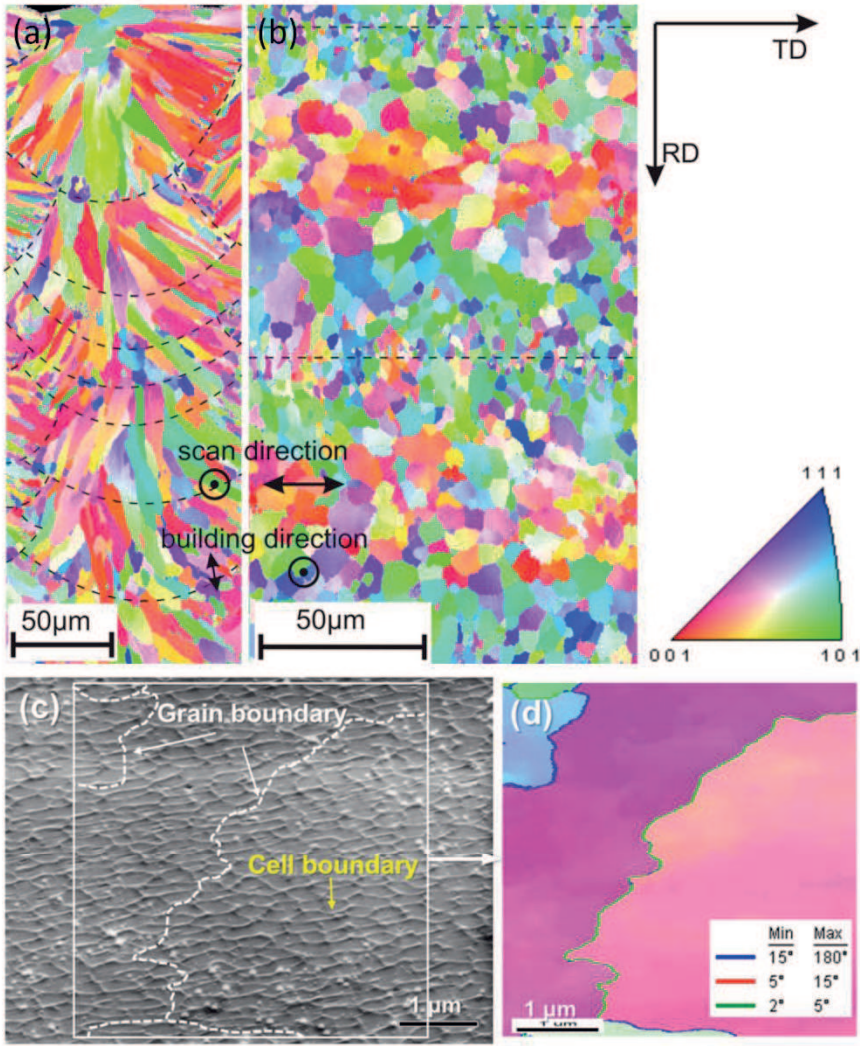

Figure 1.19. Grain structure and EBSD orientation maps of a PBF produced AlSi10Mg alloy in the as-built condition. (a) Front view. (b) Top view. Black arrows indicate the scanning and building directions, black dashed lines point out some MPB. The specimen coordination system and the crystal orientation–colour relation map referenced to the direction perpendicular to TD and RD are shown at the right. Reprinted with permission from Ref. [35]. The distinction between cell and grain boundaries. (c) SEM microstructure, white dashed lines reproduce grain boundaries. (d) Inverse pole figure. Adapted with permission from Ref. [98].

Figures 1.19c-d depict the relationship between cell and grain structures. Each grain is composed of several cells, whose boundaries sometimes coincide with a grain

boundary. According to Fig. 1.19d, grain boundaries could be either low- angle grain boundaries (LAGBs), with typical misorientation < 15°, or high-angle grain boundaries (HAGBs).

Elongated grains represent a common feature of AM processes, but a small fraction of equiaxed grains usually forms at the top of each layer. Local thermal conditions rapidly change during solidification, with the thermal gradients reduced by the release of latent heat and the growth velocity increasing from a low value at the bottom of the melt pool to a maximum value at the surface of the layer [99]. The reduction of the G/R ratio changes the solidification mechanism from cellular-dendritic to equiaxed-dendritic, leading to the so-called columnar-to-equiaxed transition (CET) phenomenon (see also page 26). A thin layer of equiaxed grains thus forms at the top of the solidifying melt pool [100], [101]. However, during the AM processes, the top of each layer is remelted and, depending on the adopted deposition parameters, the remelting may completely dissolve the equiaxed grains. For this reason, their presence is seldom reported in the literature. Besides controlling the local thermal history by the modulation of deposition parameters, it was shown in § 1.1.3 that equiaxed grain structures could be achieved adjusting the chemical composition [32], [61]–[65] or through the addition of nucleating nano-particles to the starting powder [59], [78], [102].

In addition to morphological texture, the grain structure of PBF produced AlSi10Mg alloy usually displays crystallographic texture [28], [35], [80], [92], [102], [103]. During the solidification process, competitive growth occurs between grains with different crystallographic orientations. Grains whose preferred growth direction is closely aligned to the thermal gradient direction, which is normal at any point to the solidification interface, require a limited undercooling to growth compared to misoriented grains. As a consequence, these latter are rapidly out-grown by the favourably oriented grains, which achieved competitive growth. For cubic materials such as Al alloys, {100} represents the preferred or easy-growth direction, and the PBF produced AlSi10Mg alloy often shows typical {100} cube [35] or fibre [28], [35], [80], [92], [102], [103] crystallographic texture along the major heat flow direction. This latter usually almost coincides with the building direction [80], [92], [102], [103], but can also shift to the scanning direction depending on the adopted deposition parameters [28], [35]. Grain orientation also varies across the scan track width. For instance, as depicted in Fig. 1.19b,

the orientation along the building direction is {100} for grains at the centreline and between {110} and {111} for the remaining ones.

- *Supersaturated solid solution*

Unique solidification conditions in AM processes promote a cooling rate as high as 10^3-10^8 K/s [77], [78], which produces fine and metastable microstructural features. According to the Al-Si phase diagram, Si reaches a maximum solubility in Al of 1.6 wt. % at the eutectic temperature and it becomes negligible at room temperature. However, high cooling rates extend the solubility of Si in Al, resulting in a supersaturated solid solution. Several studies report such a feature, even if a large scatter characterises the published data. Depending on the measurement method and location, Si in solid solution is estimated in the 2-7 wt. % range [77], [81], [104], [105], considerably higher than the equilibrium one. For instance, Fig. 1.20a shows the Si in solid solution measured by EDX point analyses within the Al cellular dendrites (Fig. 1.20b). Monte Carlo simulations (Fig. 1.20c) enabled to distinguish between Si layer (eutectic Si), Si precipitates and actual solid solution Si. This latter exhibits an average value of ~4 wt. % regardless of the measurement location across the melt pool (Fig. 1.20d) [81].

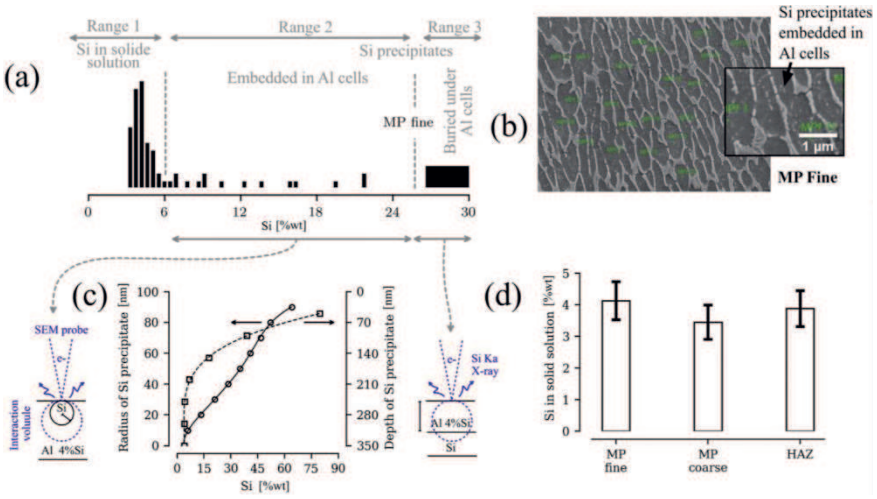

Figure 1.20. Supersaturated solid solution of a PBF produced AlSi10Mg alloy in the as-built condition. (a) Amount of Si in solid solution in the Al cell measured by EDX point analyses. (b) Areas used for EDX analyses. (c) Influence of the size of a Si precipitate and the depth of a Si layer embedded in an Al matrix with 4 % of Si in solution on the amount of total Si measured by EDX. Results obtained by Monte Carlo simulations. (d) Si in solid solution inside the fine, coarse and HAZ areas of the MPB. Adapted with permission from Ref. [81].

Besides strengthening the as-built material by the solid solution reinforce mechanism, supersaturated Si enables the precipitation strengthening after direct ageing (without solution heat treatment) of the AlSi10Mg alloy (§ 1.3.2).

- *Clustering*

Given the strong cooling rates of the AM processes, part of the secondary elements is retained in solid solution. However, during the manufacturing process, the heat stored in the previously built layers as well as in the surrounding powder bed could trigger the diffusion process and enable atoms clustering. In the AlSi10Mg alloy typical clustering phenomenon regards Si and Mg [105], [106] atoms. Figures 1.21a-b-c represent the spatial distribution of Mg, Si and Mg + Si atoms, respectively, obtained by atom probe tomography (APT). By selecting a 3 at. % threshold for the Mg content (Fig. 1.21d) or measuring the local chemical composition (Fig. 1.21e), clustering is revealed.

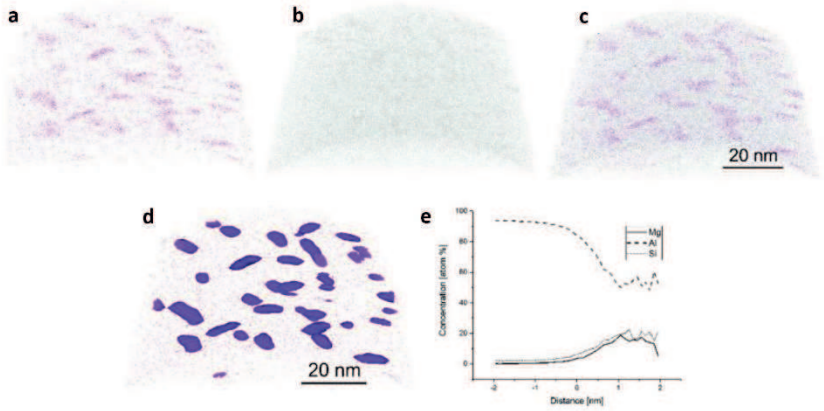

Figure. 1.21. Nanometric Mg-based precipitates of a PBF produced AlSi10Mg alloy in the as-built condition. (a) Mg atom distribution. (b) Si atom distribution. (c) Superimposed Mg and Si atom distributions. (d) Distribution of the Mg atoms with 3 at. % iso-surface. (e) Proxigram showing the chemical composition for the precipitates, the x-axis indicates the distance relative to the interface/iso-surface; zero indicates the interface itself, negative x-values the chemical composition outside (matrix) and positive x-values inside (cluster) the interface. Reprinted under a Creative Commons Attribution CC-BY license from Ref. [106].

Although there is some debate about the actual strengthening contribution from clusters [105], [106], it is well-accepted that they would act as nuclei for the accelerated precipitation of Mg_2Si or Si compounds by subsequent laser scans and during low temperature or short-time heat treatments.

- *Nanometric precipitates*

In the previous sections, it was stated that a significant amount of Si is often retained in solid solution within the Al phase. Additionally, clustering of Mg and Si atoms could also occur. The actual amount at which both phenomena take place depends on the employed deposition parameters. When the heat flow from neighbouring solidifying melt pools strongly triggers the diffusion processes, no clustering occurs. Instead, nanometric Si precipitation within the Al cellular dendrites is promoted. As depicted in Fig. 1.22 combining high-angle annular dark-field (HAADF)-STEM imaging and EDX analysis, Si compounds precipitate with different morphologies, from globular to plate- and needle-like [33]. Their size lies in the nanometric range up to a few tens of nm. Diffraction analyses highlight that Si precipitates grow alongside the preferred crystallographic directions of the Al matrix (Fig. 1.22c-f). For instance, needle-like precipitates are usually oriented alongside $\{100\}_{Al}$ directions [33].

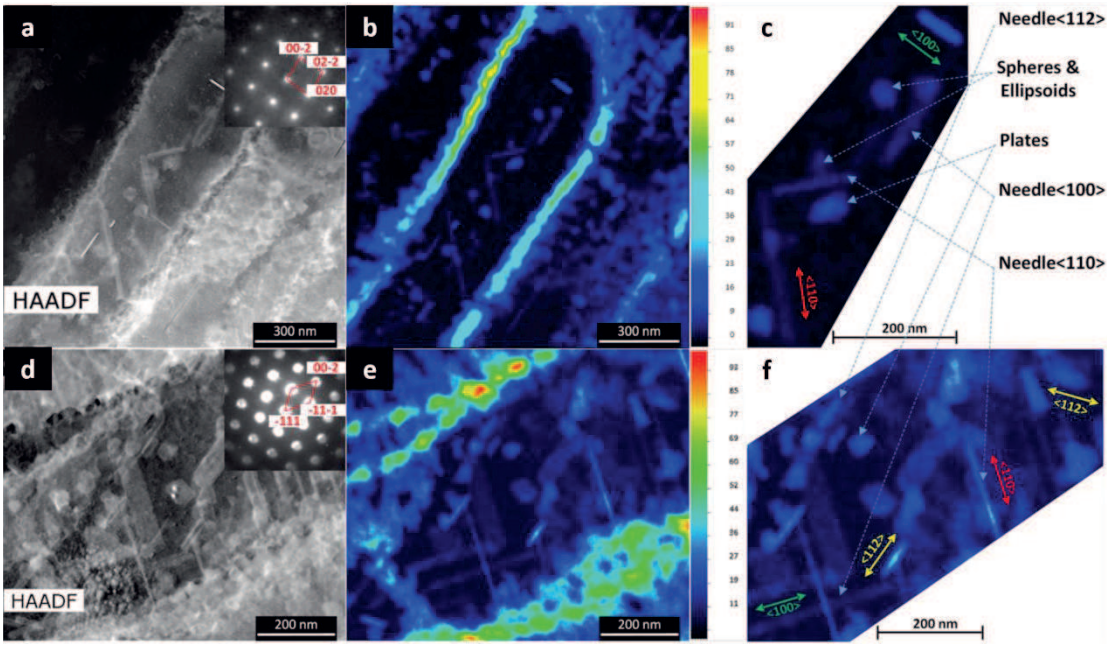

Figure. 1.22. Nanometric Si precipitates of a PBF processed AlSi10Mg alloy in the as-built state. (a)-(d) HAADF-STEM images. (b)-(e) EDX Si concentration maps. (a)-(b) Obtained in $[100]_{Al}$ zone axis. (d)-(e) Obtained in $[110]_{Al}$ zone axis. (c)-(f) Si precipitates labelled according to their morphology and crystallographic orientation. Reprinted with permission from Ref. [33].

Si precipitation during the solidification process does not merely depend on the deposition parameter. Takata *et al.* [107] highlight the influence of the sample size, with the smaller samples showing a higher density of Si precipitates. The authors suggest that small samples suffer from a reduced cooling rate, due to the more inefficient heat

conduction with the powder surrounding the specimens. As a consequence, retainment of Si in solid solution is just partially achieved, and it forms a higher fraction of nanometric precipitates.

- *Residual stresses*

In section § 1.1.3, it was shown that residual stresses commonly arise in AM realised products. Periodic heating and cooling lead to cyclic deformations up to the plastic regime and generate residual stresses. Several works report residual stresses to affect the PBF processed AlSi10Mg alloy, and their values strongly depend on the measurement location. Compressive stress is often found at the top surface layer [108], whereas tensile stress in the building direction characterises the underlying layers [109]. In both cases, the residual stress could reach ~100 MPa, which is anything but negligible, since it equals ~20-25 % of the typical tensile strength. Using a pre-heated building platform during the process was proven to be a reliable method to reduce residual stresses [40].

- *Deformation behaviour and sudden failure*

All the previous sections highlight the hierarchical microstructure of the AlSi10Mg alloy. Melt pools and grain structure represent the outer level, followed by the Al cellular dendrites and the Al-Si eutectic network. Within the Al phase, dislocation tangles, nanometric precipitates, Mg/Si atom clusters and supersaturated Si atoms could be present. Such different microstructural features span from the micrometric to the atomic scale and accomplish for almost all the possible strengthening mechanisms in metal alloys [92]. As a consequence, AM processed AlSi10Mg alloy displays exceptional mechanical properties. The yield strength (YS) lies in the range of 200-300 MPa and the tensile strength (UTS) reaches about 300-450 MPa [26], [27], [44], [98], [108], [110]–[114].

Some authors investigate the deformation behaviour of the AM produced AlSi10Mg alloy to reveal the role of the hierarchical microstructure [115], [116]. Images from Fig. 1.23a to Fig. 1.23d depict the microstructure of a tensile fractured specimen, with a focus on the role of the Si network and Al cellular structure [115]. Figure 1.23a shows a Si particle alongside the network, with the corresponding selected area electron diffraction (SAED) pattern in the inset displaying characteristic streaks and twin spots. DF-TEM image in Fig. 1.23b shows pile-up dislocations within the Al matrix and in proximity of the Si network. High-resolution (HR)-TEM images in Figs. 1.23c-d highlight several stacking faults and twin boundaries in the Si phase. Comprehensively, it is suggested

that the intensified stress from pile-up dislocations in the Al matrix causes the shearing mechanism of Si network.

Lattice strain of main constituent phases (Al and Si) was measured by neutron diffraction. The results (Fig. 1.23e) reveal that, along the applied stress direction, the lattice strain of the Si phase is higher than that of the Al phase. Such strain partitioning causes microscopic deformation heterogeneity throughout the microstructure. Simulated and measured stress-strain relationships are depicted in Fig. 1.23f. Similar observations were drawn by Wu *et al.* by in-situ TEM compression tests [117]. They verify that dislocations movement is blocked by the Si precipitates within the Al matrix and by the Si network, which also explains the high strength of the as-built material.

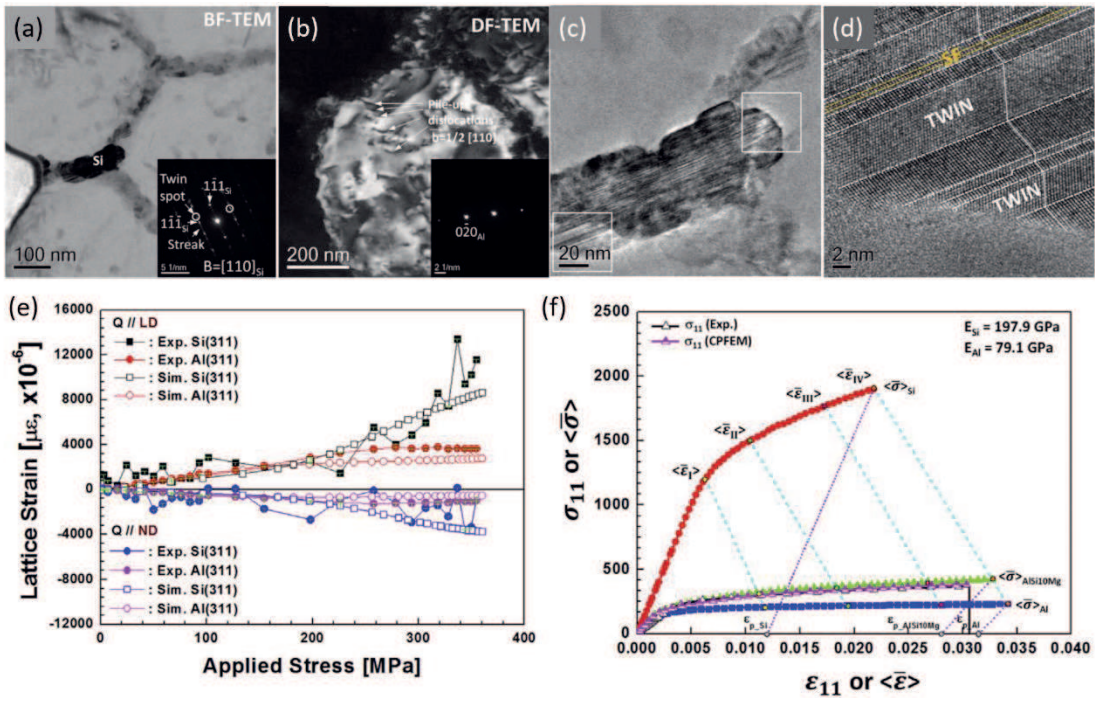

Figure. 1.23. Deformation behaviour of the AlSi10Mg alloy in the as-built state. (a) BF-TEM image and SAED pattern (inset) of a Si particle at grain boundary along the $[110]_{Si}$ zone axis. (b) DF-TEM image and SAED pattern (inset) of an Al cell. (c) BF-TEM image, higher magnification of the same particle shown in (a), the white square highlights the area analysed in (d). (d) HR-TEM image of the Si particle. (e) Lattice strains simulated and measured by neutron diffraction as a function of macroscopic stress. (f) Simulated microscopic effective stress, ⟨s⟩, of constituent phases and AlSi10Mg alloy as a function of microscopic effective strain, ⟨ε⟩, and measured macroscopic stress, s11, as a function of macroscopic strain, ε11. Adapted with permission from Ref. [115].

Despite the remarkable mechanical strength, PBF processed AlSi10Mg alloy generally suffers from a reduced ductility. The maximum achievable elongation at failure (E_f) is ~6-8 % [27], [108], [113], [114], but much lower values between ~1-3 % are often reported [26], [44], [110], [111]. Moreover, the alloy in the as-built state typically prematurely fails, even when processed with optimised process parameters. During tensile tests, the incipient necking and the consequent stress reduction in the engineering stress-strain curves are not reached [98], [111], [118]. Figure 1.24a depicts such behaviour, showing the limited strain hardening behaviour of the PBF produced AlSi10Mg alloy in comparison with the same alloy produced by powder metallurgy [98].

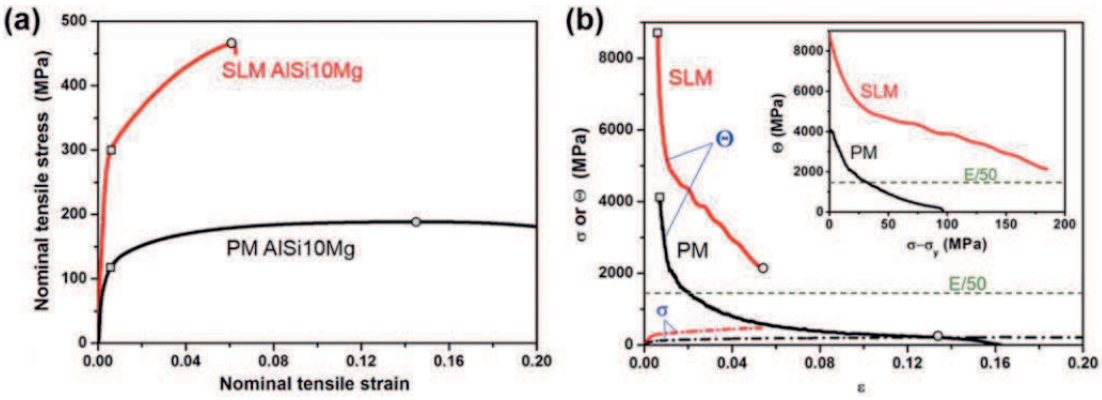

Figure. 1.24. Tensile behaviour and premature failure of a PBF produced AlSi10Mg alloy in the as-built state. (a) Nominal tensile stress-strain curves, comparison with the same alloy produced by powder metallurgy (PM). (b) True tensile stress-strain (σ-ε) and strain hardening rate (Θ-ε) curves, yield strength and ultimate tensile strength points are marked by white squares and circles, respectively. Inset of (b) shows Θ as a function of net flow stress (σ-σ_y), where σ_y is true yield strength. Reprinted with permission form Ref. [98].

The onset of necking in tensile tests is usually detected at the intersection between the true stress-strain and the strain hardening rate curves (Considère's criterion [119]). PBF processed AlSi10Mg alloy misses this condition, as highlighted in Fig. 1.24b, elucidating its sudden failure. It is worth to note that such behaviour was recently assessed in detail by Wang *et al.* [90] for an Ag-Cu-Ge alloy. The authors recognise the premature failure of many AM produced metal alloys as a drawback of the adopted manufacturing process, with common causes identified as unmelted powder particles, residual stresses, micro-cracks, small pores, and other residual defects. Such phenomenon severely limits the applicability of most AM produced parts in the as-built state and paved to the study of dedicated heat treatments.

1.2.2 Metastability of the as-built microstructure

Section § 1.2.1 depicts the non-equilibrium solidification conditions and resulting metastable microstructure of the PBF processed AlSi10Mg alloy. Under an appropriate external input, such microstructure tends to restore the thermodynamic equilibrium, with the driving force typically being a heat flow. Such a situation could be achieved on purpose during the manufacturing process (§ 1.3.1) or with dedicated heat treatments (§ 1.3.2, § 1.3.3). However, recovery from the metastable state could occur with time during high-temperature applications (150-200 °C) of the as-built material [86].

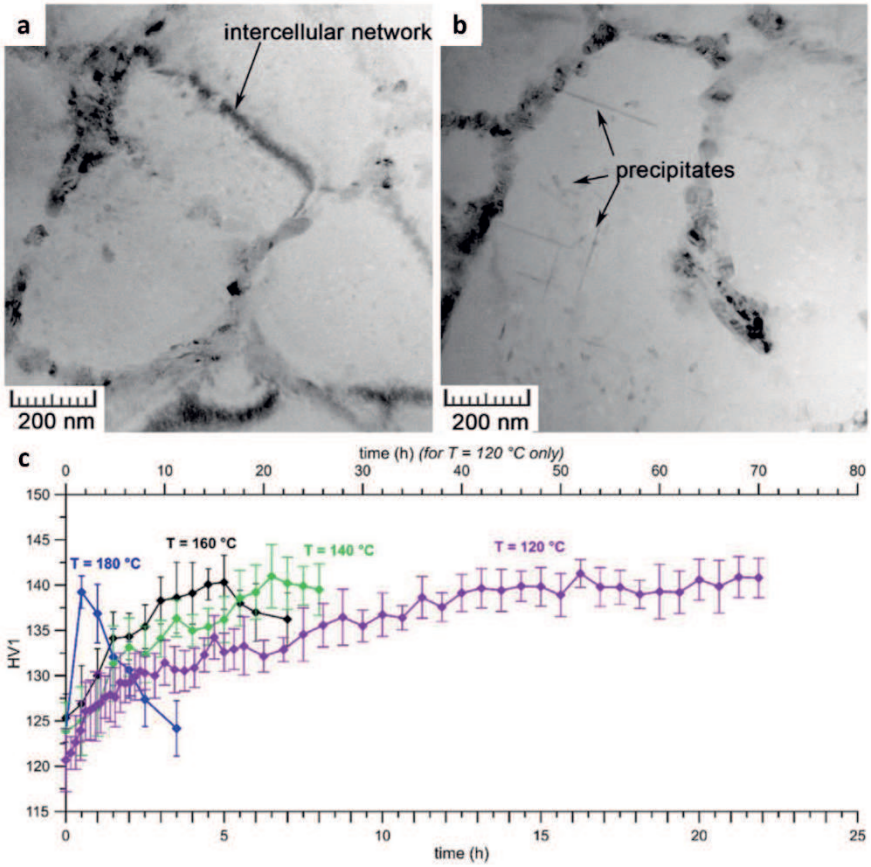

Figure 1.25. Direct age-hardenability of a PBF produced AlSi10Mg alloy in the as-built state. BF-TEM image of the cellular microstructure: (a) before ageing, and (b) after ageing at 160 °C. (c) Curves showing the time evolution of hardness when exposed to elevated temperatures in the range 120 to 180 °C. Reprinted with permission from Ref. [86].

TEM images in Fig. 1.25a-b highlight that prolonged exposure to high temperatures leads to nanometric acicular Si precipitates in the Al cellular structure. Such precipitation stems from the supersaturated solid solution of Si in the as-built state. Figure 1.25c shows

that the material stability and kinetic evolution significantly depend on the exposure temperature, and the effect is a material strengthening.

Together with the increase in hardness, the authors additionally report a decrease in elongation during tensile tests [86]. The instability of mechanical properties over time makes the as-built AlSi10Mg alloy not suitable for high-temperature applications before its complete recovery from the metastable state. It is worth notice that the susceptibility of the alloy to Si precipitation depends on the amount of available Si in solid solution. As previously underlined, this strongly descends from the adopted deposition parameters and, therefore, such behaviour cannot be generalised.

The instability of the as-built material could be reduced during the manufacturing process adopting a pre-heated platform instead of a cold one [118]. The differential scanning calorimetry (DSC) curve of the as-built alloy in Fig. 1.26a shows two characteristic peaks between 200 °C and 300 °C. The precise nature of such peaks will be underlined furtherly (§ 1.3.2). However, they represent solid-state transformations during heating and prove the metastable condition of the as-built alloy. As further proof, the DSC curve of the supersaturated alloy after solution heat treatment and quench displays the same peaks (Fig. 1.26a). Conversely, when a pre-heated platform is used, the DSC curve does not show appreciable peaks. The heat flow promoted by the hot platform triggers diffusion processes and restores the equilibrium state during the manufacturing process.

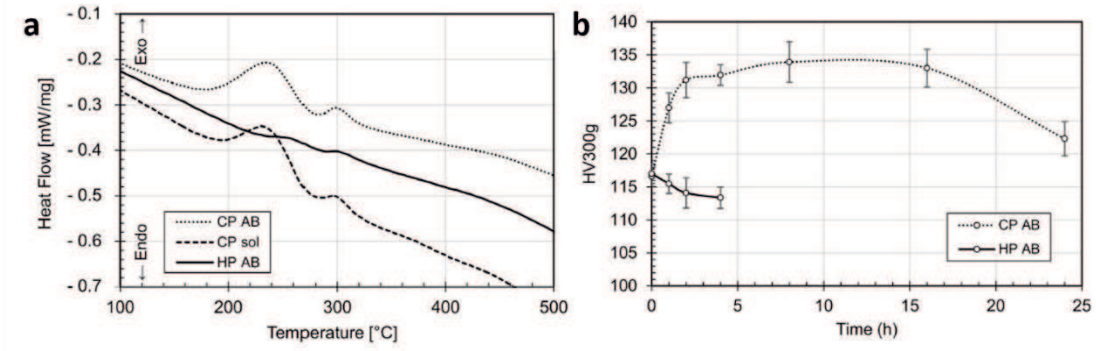

Figure 1.26. Solid-state transformations of a PBF produced AlSi10Mg alloy in the as-built condition. (a) DSC scan profiles collected on heating of the cold-platform produced as-built (CP AB), hot platform produced as-built (HP AB) and cold platform produced solution heat-treated (CP sol) alloys. (b) Ageing curves at 160 °C of cold- and heat-platform produced alloys. Reprinted under a Creative Commons Attribution License from Ref. [118].

Ageing curves of the alloy manufactured with hot and cold platforms are depicted in Fig. 1.26b [118]. Analogously to Fig. 1.26c, the alloy processed with the cold platform is susceptible to age-hardenability due to Si compounds precipitation, as highlighted by the hardness increment. Conversely, the exposure to a high temperature just slightly softens the alloy produced using the hot platform, which is more thermally stable. Such behaviour confirms the disappearance of the supersaturated solid solution and the restoration of the equilibrium state.

In conclusion, the AM process conditions determine the peculiar hierarchical microstructure of the as-built AlSi10Mg alloy, which is characterised by outstanding mechanical properties. Metastability of the resulting microstructure causes such properties to change significantly over time during exposure to high temperatures. This drawback could be avoided during the manufacturing process using a pre-heated platform. Even in vthis latter case, the as-built material generally suffers from limited ductility and premature failure during the strain hardening process. In light of this, to date, the application of dedicated heat treatments is an undeniable step of the whole production process of the AlSi10Mg alloy.

1.3 HEAT TREATMENTS FOR 3D-PRINTED AlSi10Mg ALLOY

Despite its remarkable mechanical properties, the PBF produced AlSi10Mg alloy usually requires heat treatment to improve ductility and mitigate residual defects and anisotropy. Moreover, heat-treated alloys reach equilibrium conditions and thus are more thermally stable. As a drawback, the heat treatment profoundly alters the starting microstructure and often decreases mechanical properties. The following paragraph aims at introducing the heat treatment routes of the AlSi10Mg alloy, even if the basic principles are quite general and applicable also to other alloy systems. The first part of the paragraph (§ 1.3.1) briefly deals with the possibility of inducing heat treatment during the manufacturing process. Then the treatment routes of the AlSi10Mg alloy, typically divided into low- (§ 1.3.2) and high-temperature (§ 1.3.3) heat treatments, will be described.

1.3.1 Intrinsic heat treatment

The inherent nature of the AM process, with the heat source repetitively scanning the powder bed or the deposition plate, determines heating and cooling cycles of the previously solidified material. Figures 1.27a-b depict the simulated temperature evolution during the L-PBF process at various deposition parameters [15]. The peak temperature reached at a given laser scan increases with the power of the laser (Fig. 1.27a) and decreases with the scan speed of the moving source (Fig. 1.27b). In this latter case, the time between subsequent peaks is also reduced. Such thermal cycles, so-called *intrinsic heat treatment* (IHT), potentially trigger precipitation reaction in age-hardenable alloys as well as phase transformations in materials like Ti alloys and steels [116], [120], [121]. In both cases, the following post-process heat treatments could be avoided. Moreover, the local induced heat treatment and the corresponding effect on the microstructure are tunable by adjusting the deposition parameter, as suggest by Fig. 1.27.

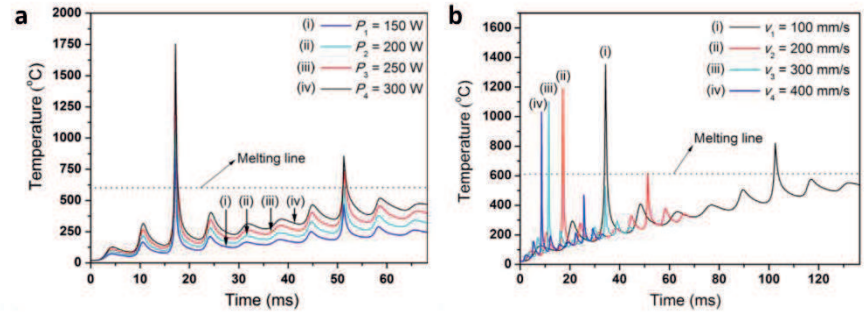

Figure 1.27. Intrinsic heat treatment of a PBF produced AlSi10Mg alloy, temperature variation with time. (a) At different laser powers in the range 150 to 300 W, scan speed 200 mm/s. (b) At different scan speeds in the range 100 to 400 mm/s, laser power 200 W. Reprinted with permission from Ref. [15].

Kürnsteiner *et al.* [120], [122] exploit the IHT to tailor the local microstructure of Fe19Ni5Ti Maraging steel strengthened by a precipitation reaction. Fig. 1.28a shows the experimental time-temperature profiles obtained with different pause times after each fourth layer. Without pause time (0 s), the temperature of the deposited material continuously increases, without the possibility of the quench-induced martensitic transformation from the austenite phase. Conversely, a pause time of 180 s provides the alloy enough time to cool down to room temperature and, subsequently, to be precipitation hardened. Soft and hard regions are identified as bright and dark bands in

Fig. 1.28b. After being cooled down to room temperature, the first temperature peak of the following scan sequence induces the IHT and triggers the precipitation of nanometric Ti-Ni compounds within a thin strip of the deposited material. APT reconstructions of different precipitates distribution within soft and hard regions and their chemical composition are depicted in Fig. 1.28c.

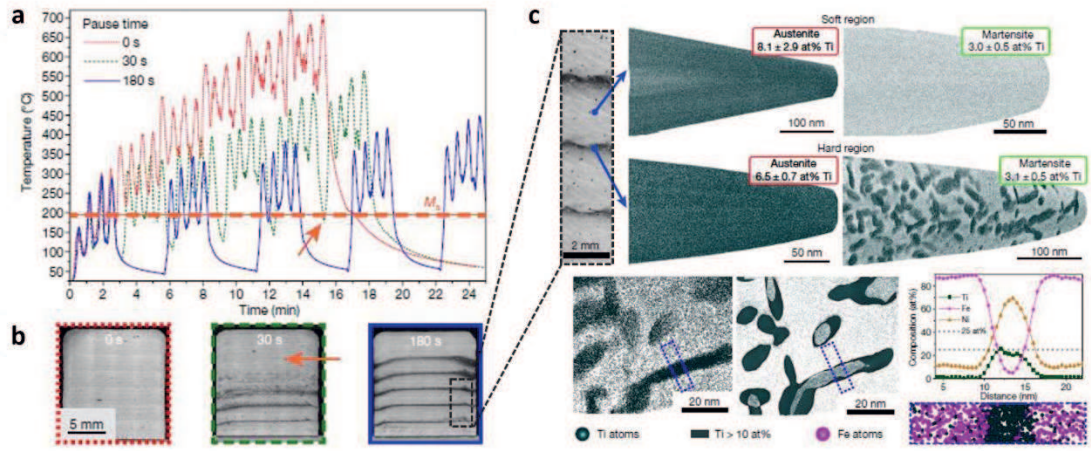

Figure 1.28. Effect of thermal history of a DED produced Fe19Ni5Ti steel. (a) Experimental time-temperature profiles of samples built at different pause times after each fourth layer, the dashed orange line corresponds to martensite-start (Ms). The orange arrow points at a temperature drop that barely drops below Ms. (b) Optical micrographs of the samples built with the corresponding pause times, bright and dark stripes correspond to soft and hard regions, respectively. (c) APT analysis of martensite and austenite in the soft region precipitates-free region and hard region, with precipitates highlighted by iso-composition surfaces encompassing regions containing more than 10 at. % Ti. Adapted with permission from Ref. [122].

However, the IHT could also exert a detrimental effect on the previously solidified material, for example, in the case of Al-Sc-Zr alloy system, as summarised in Fig. 1.29 [123]. Figure 1.29a depicts the reconstructed volume from APT analyses taken from the last solidified layer of a DED produced AlScZr alloy, showing a high density of precipitates. The IHT of the material in the top layer is only due to the deposition of neighbouring tracks, which however triggers the precipitation of several nanometric compounds. These are identified as $Al_3(Sc,Zr)$ precipitates from the proxigram in Fig. 1.29b, with the BF-TEM imaging in Fig. 1.29c confirming the high volumetric density. Conversely to the top layer, underlying layers undergo IHT from both neighbouring and above-deposited tracks. The result of such intense IHT is shown in Figs. 1.29d-e, where

the reconstructed volume from the APT measurement highlights a single coarse $Al_3(Sc,Zr)$ precipitate. The coarsening of nanometric precipitates causes the mechanical properties of the alloy to change strongly with the building height [123].

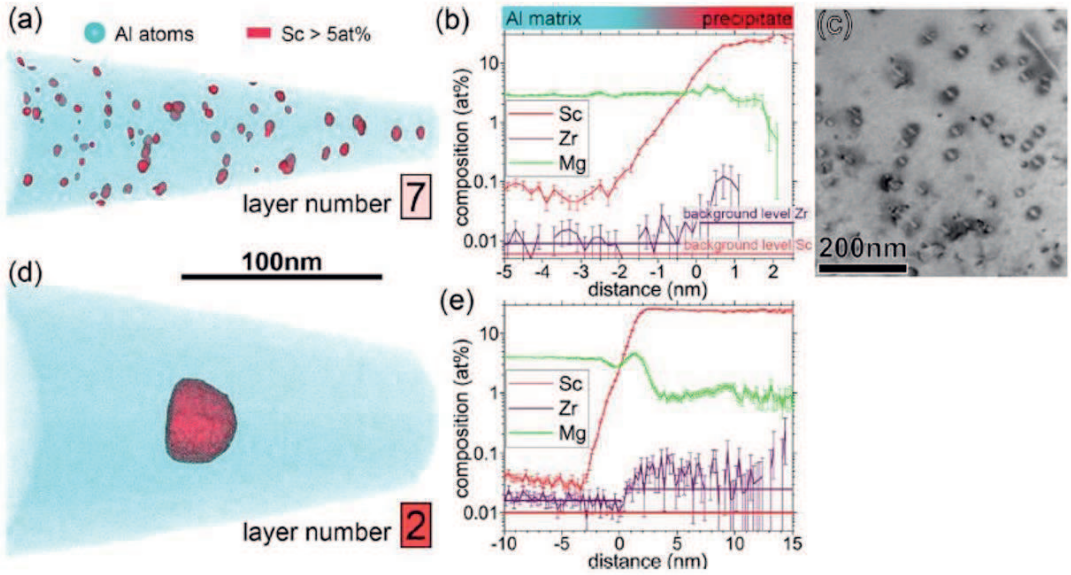

Figure 1.29. Effect of thermal history of a DED produced AlScZr alloy. (a)-(d) Reconstructed volumes from APT measurements taken from the last (without intrinsic heat treatment) and 2nd (with intrinsic heat treatment) deposited layers, different size of $Al_3(Sc,Zr)$ precipitates highlighted in red by iso-concentration surfaces at 5 at. % Sc. (b)-(e) Proximity histogram of the chemical composition as a function of the distance to the iso-concentration surface, zero correspond to the surface itself, negative and positive values correspond to matrix and precipitates, respectively. (c) BF-TEM image showing coherent nanometric precipitates. Reprinted with permission from Ref. [123].

The authors successfully implemented alternative solidification conditions and slightly modified the chemical composition of the alloy to realise a Zr-rich shell around the $Al_3(Sc,Zr)$ precipitates that prevents their coarsening.

The IHT does not merely induce precipitation reactions in age-hardenable alloys but also triggers phase transformations. Haubrich *et al.* [121] investigated the effect of the IHT on the phase transformations of a Ti-6Al-4V alloy, showing that different intrinsic heat inputs modify the mutual amount of α' martensite and β phase. Despite its great potentiality, no works in the literature deal with the IHT of Al-Si alloys. However, nanometric Si precipitation of the AlSi10Mg alloy described in § 1.2.1 likely could be ascribed to the IHT. Hence, there is room for further tailoring of the final microstructure.

1.3.2 Low-temperature heat treatments

The as-built microstructure of the PBF processed AlSi10Mg alloy leads to outstanding mechanical properties, but also limited ductility and high thermal instability. In this light, a heat treatment is often required. As will be revised in the next section (§ 1.3.3), earlier works generally concerned high-temperature heat treatments, often derived from standard routes of Al casting and wrought counterparts [111], [124]. However, it was quickly realised that such heat treatments are not optimised for AM produced parts, since they usually soften the material in comparison to the starting condition (§ 1.3.3). New low-temperature heat treatment routes, defined as annealing or stress-relieving treatments, were investigated in order to find a compromise between strength loss, mitigation of residual defects and enhancement of ductility [108], [109], [125], [126].

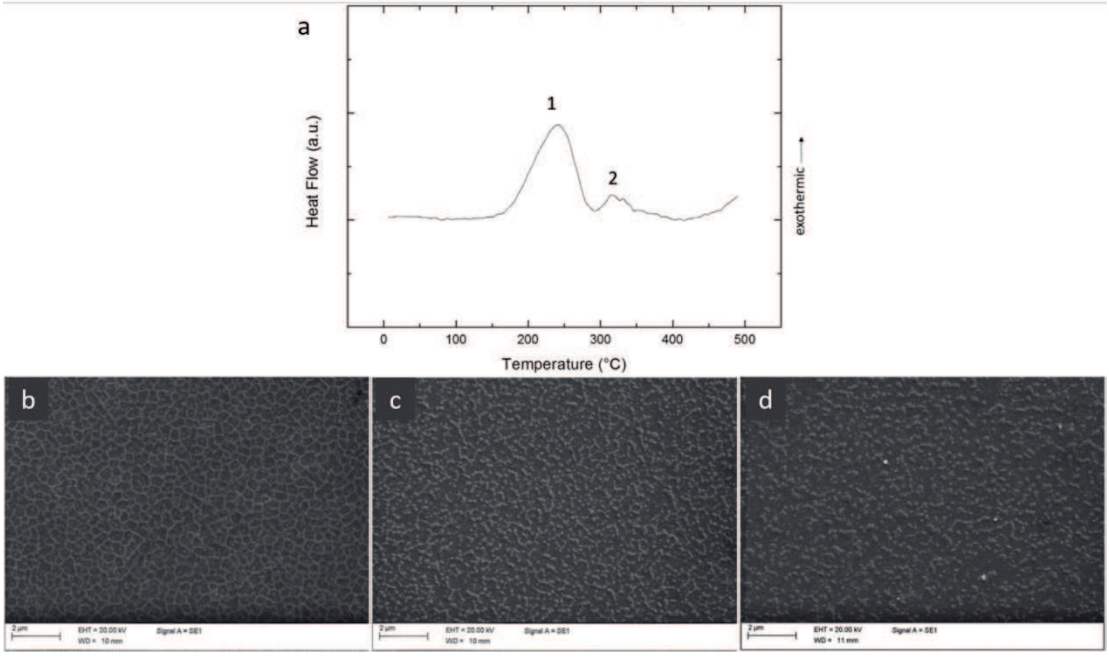

Figure 1.30. Effect of low-temperature annealing on microstructure and solid-state transformations of a PBF produced AlSi10Mg alloy. (a) DSC curves recorded at 10 C/min of as-built sample. (b) to (d) SEM images after heat treatment for 2 h. (b) 263 °C. (c) 294 °C. (d) 320 °C. Adapted with permission from Ref. [125].

The definition of proper annealing temperatures stems from the observation of available solid-state transformations in the as-built alloy. Figure 1.30a displays the DSC curve of the as-built AlSi10Mg alloy recorded during the heating stage [125]. Two distinct peaks are detected at about 250 °C and 300 °C respectively, whereas just the

former is present in the DSC curve of the starting powder. Hence, while the first peak is intrinsic of the AlSi10Mg alloy, the second one is related to the manufacturing process.

The authors [125] ascribe the first peak to the precipitation of the β-Mg_2Si phase in the metastable β''-Mg_5Si_6 form, according to the corresponding activation energy and temperature range. Based on the available literature, the activation energy of the second peak makes it ascribable to diffusional processes of Si in the Al phase. Different heat treatments were performed at temperatures below and above the second peak, and Figs. 1.30b-c-d depict the corresponding microstructures. The alloy treated below the second peak (Fig. 1.30b) exhibit the same microstructural features of the as-built alloy, even if a slight hardness decrease was measured. Above the peak (Fig. 1.30b-c), the Si network breaks into distinct particles, and the mechanical response significantly falls.

Although the presence of the two peaks in the DSC heating curve of the as-built alloy is also reported by other authors [104], [118], [127], [128], their assignment introduces some debate. Marola *et al.* [104] observed that, given the enthalpy of formation of β-Mg_2Si, the maximum heat flow per unit mass releasable by an AlSi10Mg alloy containing 0.35 wt. % Mg is ~8 J/g. Such value is much lower than the measured heat flow of the first peak (~20-30 J/g [104], [125]), and it is comparable to the heat measured of the second one. Moreover, they verify the first peak to be present in the DSC curve of a melt-spun ribbon produced from an AlSi10 master alloy not containing Mg. The final assignment agrees with Yang *et al.* [127], but it is precisely the opposite compared to [118], [125], [128].

Young *et al.* [126] evaluated by in-situ X-ray diffraction the effect of continuous heating in the annealing range on the microstructural evolution of the AlSi10Mg alloy. Figure 1.31 depicts the evolution of the diffraction pattern as the temperature increases up to 450 °C. The change in the peak intensity chromatically follows the visible light spectrum, with purple being the background. As the temperature increases, all peaks shift to lower 2ϑ angles, but the displacement is greater for the Al phase. Such a phenomenon is partially due to the higher coefficient of thermal expansion of Al, but also to the rejection of smaller Si atoms from the supersaturated Al lattice of the as-built state. From room temperature up to ~275 °C, just a few Si reflections are visible and appear rather diffuse, suggesting that Si crystallite size is in the order of tens of nm. This observation is consistent with the fine size of both Si network and Si precipitates

described in § 1.2.1. Above ~275 °C, other Si reflections become noticeable, and all of them increases in intensity and sharpens. These findings suggest the increment of the Si volume fraction after its rejection from the Al lattice and a gradual coarsening of the crystallites.

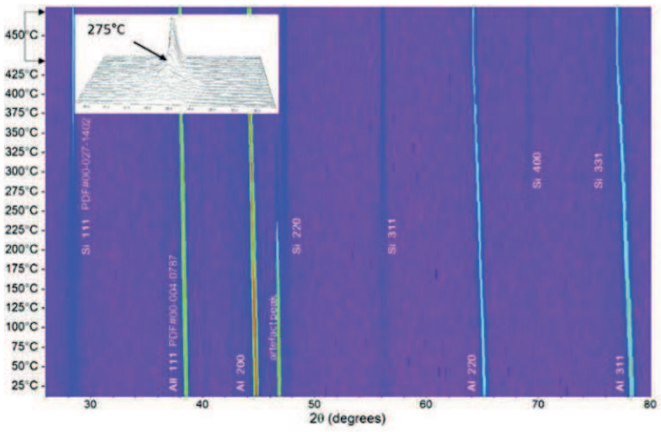

Figure 1.31. Evolution of in-situ X-ray diffraction pattern of a PBF produced AlSi10Mg alloy during heating from room temperature up to 450 °C, inset in the top-left illustrates the emerging and sharpening of the $[111]_{Si}$ peak. Reprinted under a Creative Commons Attribution 4.0 licence from Ref. [126].

The low-temperature annealing does not significantly alter the grain structure [126], [129]. However, given the metastability of the as-built AlSi10Mg alloy, it affects the inner levels of its hierarchical microstructure. It breaks the eutectic Si network, triggers the precipitation of Si particles and Mg-based compounds and reduces residual stresses [109], [126]. Hence, the choice of the proper temperature is a fundamental aspect.

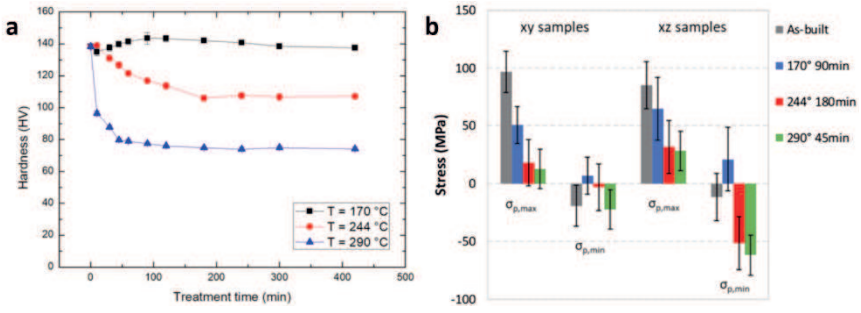

Figure 1.32. Effect of tailored low-temperature heat treatments at 170 °C, 244 °C and 290 °C on: (a) tensile properties, (b) residual stresses of a PBF produced AlSi10Mg alloy. Reprinted with permission from Ref. [109].

Figures 1.32a-b report the time-hardness profiles and residual stresses of the AlSi10Mg alloy subjected to three different heat treatments. The T5-like heat treatment (170 °C) does not alter the microstructure and slightly increases hardness compared to the starting condition. It also partially reduces residual stresses, although these are still several tens of MPa in magnitude.

The heat treatment performed at 290 °C considerably softens the material, due to the rupture of the Si network and reduction of residual stresses. On the other hand, ductility significantly increases. Middle-temperature annealing (244 °C) reliefs residual stresses preserving the continuity of the Si network, thus mitigating the strength loss. Depending on the given application, the time and temperature of the annealing treatment could be modulated to achieve the required properties. Despite this, more traditional high-temperature heat treatments are still often performed.

1.3.3 High-temperature heat treatments

Conventionally manufactured (for instance, wrought and casting) Al alloys generally reach optimised properties just after heat treatment. Therefore, in the early days of AM of Al alloys, it was quite natural to test the effectiveness of previously established heat treatments. In the following paragraph, the effect of conventional high-temperature heat treatments on the microstructural features of the PBF processed AlSi10Mg alloy will be explained. The resulting mechanical properties will be discussed and compared to the as-built alloy, underlying advantages and disadvantages.

Figure 1.33 summarises the effect of the exposure to high temperature on the Al cellular structure and eutectic Si network [130]. As previously observed in § 1.3.2, heating above 300 °C causes the rupture of the Si network into nanometric particles, as depicted in Fig. 1.33a. At higher temperatures (Fig. 1.33b), the enhanced diffusion of Si leads to particle coarsening to the micrometric size range. Increasing the treatment temperature just below the Al-Si eutectic temperature (Fig. 1.33c) further coarsens the Si particles. Boundaries of melt pools and Al cellular structure are no longer visible, indicating that the heat treatment homogenises the segregation along such boundaries. The result is an Al matrix with isolated Si particles located at grain boundaries or within them [111], [112], [131]. An additional ageing treatment (Figs. 1.33e-f) does not alter the microstructural features at the micrometric scale [130].

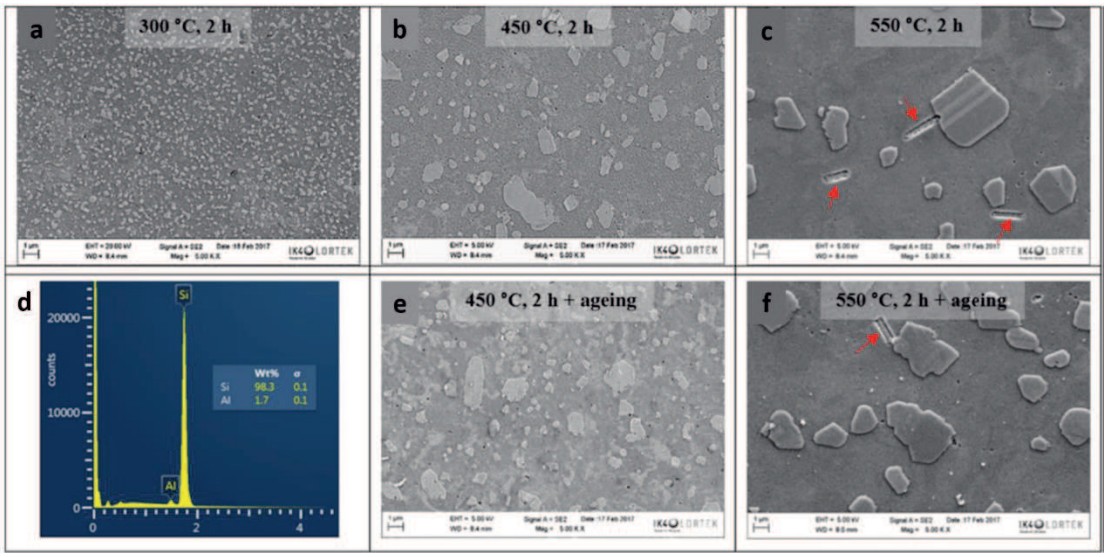

Figure 1.33. SEM observations showing the effect of different heat treatments on the microstructure of a PBF produced AlSi10Mg alloy. (a) Annealing/stress-relieving. (b)-(e) Heat-treated at 450 °C. (c)-(f) Heat-treated at 550 °C. (b)-(c) Solution heat-treated. (e)-(f) Solution heat-treated and age-hardened. (d) EDX spectrum of a Si particle. Adapted with permission from Ref. [130].

Red arrows in Figs. 1.33c-f [130] point out that additional secondary phases appear during exposure to high temperature [40], [103], [128], [129]. The corresponding EDX analysis (Figs. 1.33d) reveal them to be Fe-rich compounds. BF-TEM images in Figs. 1.34a-d show a similar feature exhibiting a plate-like shape, and EDX analysis suggests a stoichiometric composition close to Al_5SiFe [103]. SAED pattern in Fig. 1.34e reveals a monoclinic crystal structure which matches with the β-Al_5SiFe phase. In § 1.2.1, it was shown that Fe-based secondary phases precipitate in a nanometric form at the Al cell boundaries during solidification. β-Al_5SiFe compounds likely originate by coarsening of such metastable phases due to enhanced motion of Si and Fe atoms. While most of the Si particles and Fe-rich compounds display a large micrometric size, some of them nucleate in a globular nanometric form, as depicted in Fig. 1.34b and confirmed by EDX spectra in Figs. 1.34c-f.

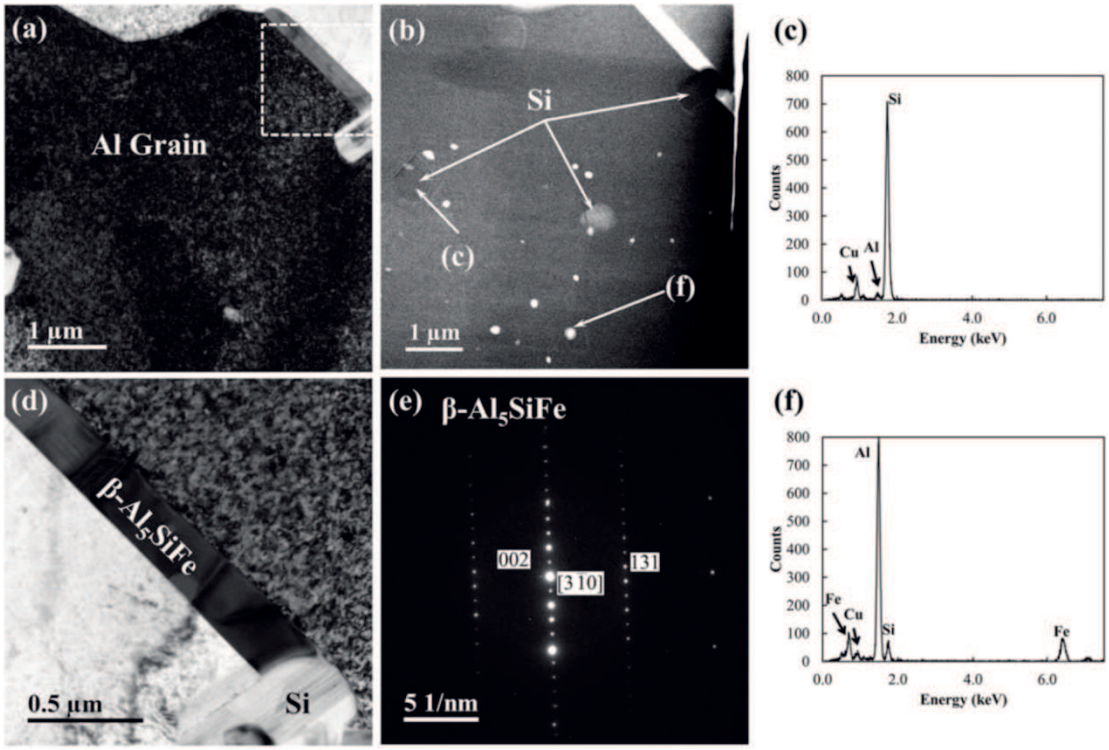

Figure 1.34. TEM observation showing the effect of high-temperature heat treatment on precipitation of Fe-based secondary phases of a PBF produced AlSi10Mg alloy. (a) BF-TEM of an Al grain. (b) HAADF-STEM highlighting bright nanometric particles. (c) EDX spectra of Si particles within the Al cells. (d) BF-TEM of a lamellar Fe-based compound taken from the dashed square in (a). (e) SAEDP and (f) EDX spectrum of the Fe-bearing compound. Reprinted with permission from Ref. [103].

Figure 1.35 depicts the effect of high temperatures on the morphological and crystallographic textures of the grain structure [129]. Figure 1.35a shows the AlSi10Mg alloy in the as-built state, which displays a strong morphological texture with grains elongated towards the building direction. Additionally, Fig. 1.35b highlights that a large fraction of grains has a [001] orientation, resulting in a {001} texture along the scan direction (Fig. 1.35c), as previously reported [35]. Such features remain unchanged after annealing at 300 °C (Figs. 1.35d-e-f) [126], [129]. The high-temperature heat treatment slightly coarsens the grain structure (Figs. 1.35g) but alter neither the morphological nor the crystallographic textures (Figs. 1.35h-i). Similar outcomes are reported in the literature [131].

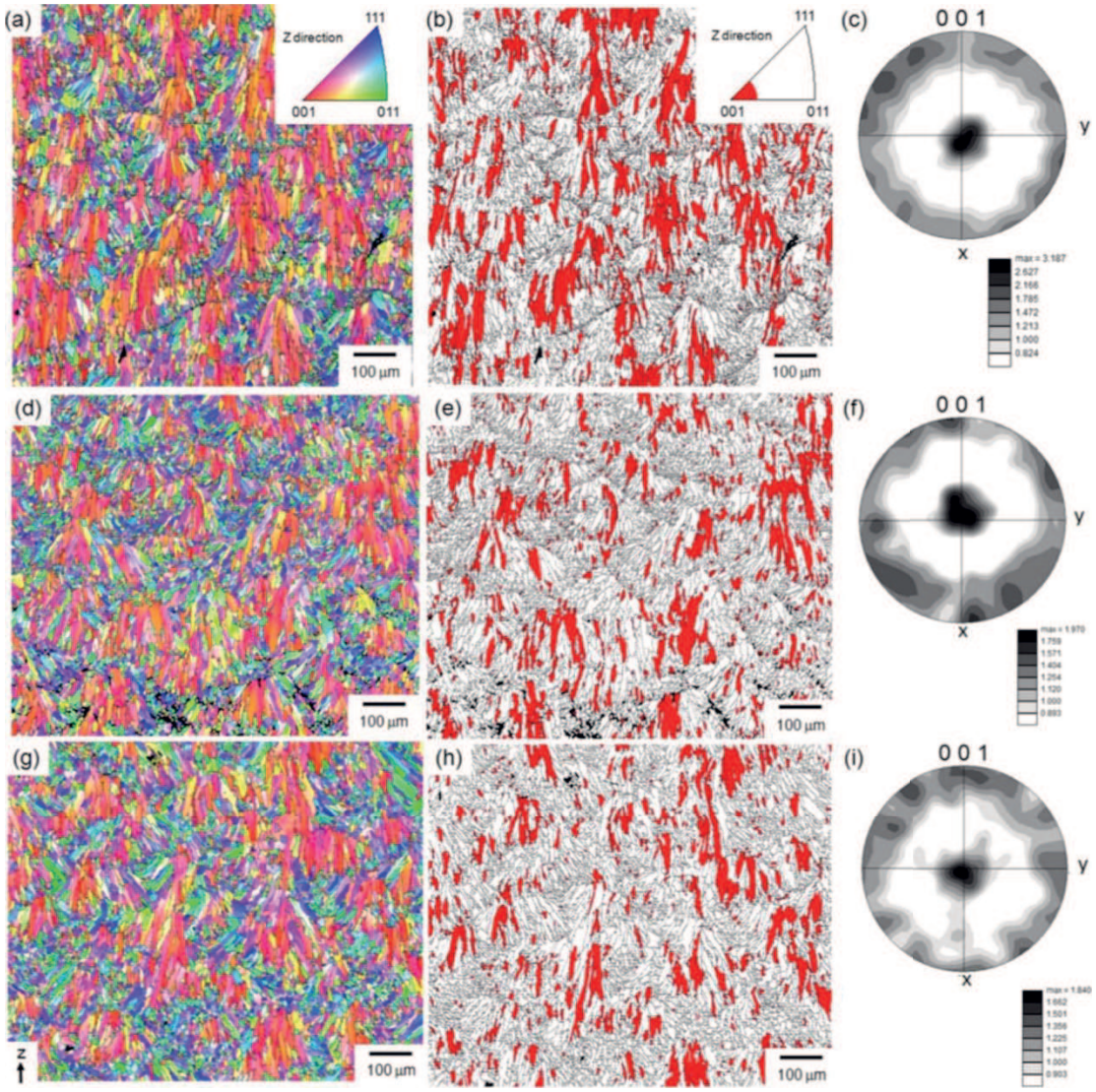

Figure 1.35. Effect of heat treatment on the grain structure of the AlSi10Mg alloy. (a)-(d)-(g) EBSD orientation colour maps. (b)-(d)-(f) Distribution maps of $[001]_{Al}$ oriented regions, with a deviation tolerance of 15° from the Z direction. (c)-(f)-(i) $[001]_{Al}$ pole figures. (a)-(b)-(c) As-built samples. (d)-(e)-(f) Annealed at 300 °C for 2 h. (g)-(h)-(i) Heat treated at 530 °C for 6 h. Reprinted with permission from Ref. [129].

Besides Al cellular and grain structures, eutectic Si network and secondary phases, the exposure to high temperature also affects the remaining microstructural features. Section § 1.3.2 previously introduced that heating the as-built alloy to low temperatures (up to 300 °C) triggers Si precipitation from the supersaturated Al lattice, mitigates residual stresses and coarsens pre-existing Si- and Mg-based nanometric precipitates [109], [126]. Hence, similar behaviour is expected during high-temperature heat treatments, with an accelerated kinetic. Furthermore, the annihilation of the dislocation tangles is suggested [129].

The most widespread heat treatment for age-hardenable Al alloys firstly requires the solution heat treatment (SHT) at high temperature. Section § 1.3.3 until now has covered the effect of such first step on the main microstructural features of the AlSi10Mg alloy. Most of them disappear, some increase in size, with the effect of softening the material. Hence, the ageing treatment is mandatory to recover the mechanical performance by precipitation strengthening. Figure 1.36 depicts relevant features of the age-hardened AlSi10Mg alloy. At the micrometric scale, coarse Si particles are embedded in the Al matrix (Fig. 1.36a). Within the Al grains, nanometric β-Mg_2Si compounds appear in the metastable β'' (Fig. 1.36b) or Guinier-Preston (GP)-zone (Fig. 1.36c) forms.

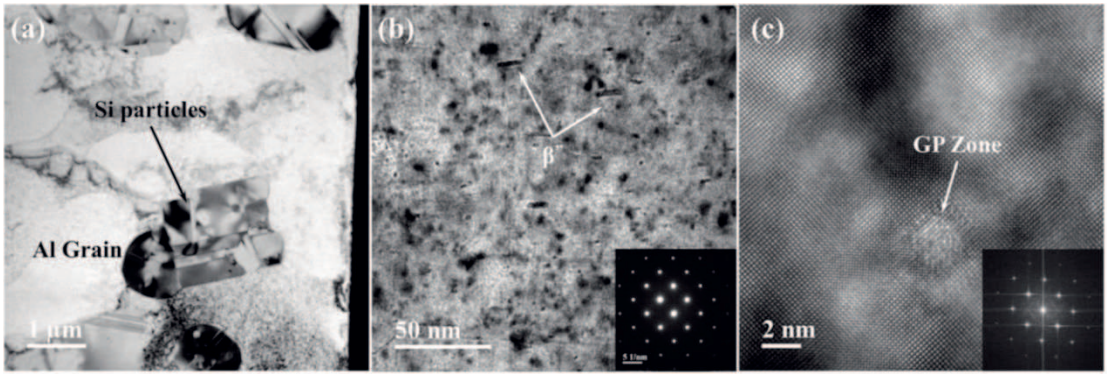

Figure 1.36. Age-hardening behaviour of a PBF produced AlSi10Mg alloy. (a) Panoramic BF-TEM image showing Al grains and Si particles. (b) BF-TEM image at $[001]_{Al}$ zone axis showing the GP-zones and β″ precipitates. (c) HR-TEM image of a GP zone. Reprinted with permission from Ref. [103].

The formation of metastable β'' compounds and GP-zones after ageing resembles that observed in casting and wrought Al-Si-Mg alloys [132]–[134]. However, the actual kinetic during both the quench and ageing stages in PBF produced Al-Si-Mg alloys could significantly differ from their wrought/casting counterparts. The main reason lies in the much fine and highly defective microstructure of PBF processes alloys, which fastens the precipitation kinetic. Milkereit *et al.* [135] observed that the drop in hardness after ageing is much faster for alloys with a fine microstructure before quenching. The cause is the accelerated quench-induced precipitation which depletes the available solute, preventing its controlled precipitation during ageing. The upper critical cooling rate to avoid deleterious quench-induced precipitation is estimated above 10^3 °C/s for an ultrafine microstructure. Quench-induced precipitates in Al-Si-Mg alloys likely consist of Si, β-Mg_2Si, β'-$Mg_{1.8}Si$ or B'-$Mg_9Al_3Si_7$ compounds [135]. Fine and defective

microstructures additionally affect ageing treatment. Rao *et al.* [136] found the B' compound to be the main strengthening phase in a peak-hardened AlSi7Mg alloy, instead of the β'' precipitate, as typically observed in casting alloys [132], [133]. They proved the β'' phase to be the prevalent precipitate in under-aged samples, with the precipitation sequence of Al-Si-Mg alloy being maintained. However, the fine, highly defecting starting microstructure accelerates the precipitation phenomena. In this light, a long (6-8 h) high-temperature heat treatment coarsens or annihilate most of the microstructural features, mitigating the accelerated precipitation [136]. Different precipitation phenomena in ultrafine and coarse-grained Al alloys were previously assessed in the literature [137], [138].

Figure 1.37 summarises the effect of the most common heat treatments on the tensile properties of the PBF produced AlSi10Mg alloy [130]. The as-built material exhibits the highest strength, but suffers from very low ductility, as previously observed in § 1.2.1. The low-temperature annealing (300 °C) softens the material and leads to the highest elongation at failure, due to relief of residual stresses and rupture of the Si network. Solution heat treatments at 450 and 550 °C behave similarly, reducing the starting strength and promoting a high ductility, due to the coarsening of the microstructural features. A compromise is achieved after the ageing treatment, which strengthens the alloy by precipitation of nanometric compounds, without deleteriously affecting the ductility [130]. Similar results could be found in several published studies [108], [111], [112], [128], [129], [139].

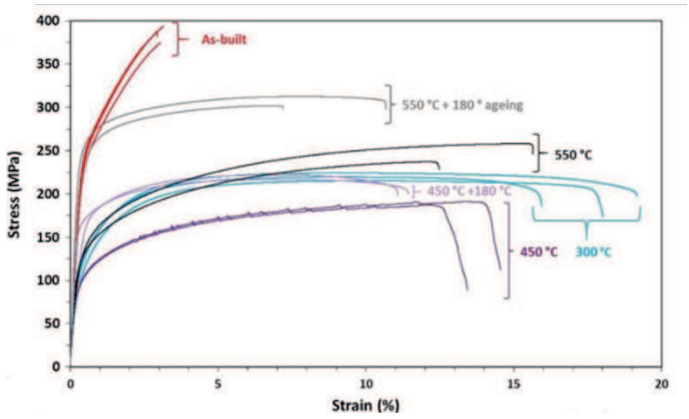

Figure 1.37. Effect of different heat treatments on the tensile behaviour of a PBF produced AlSi10Mg alloy. Considered heat treatment routes comprehend: as-built, annealing (300 °C), solution heat treatment (450-550 °C), solution heat treatment and ageing (450-550 °C + 180 °C). Adapted with permission from Ref. [130].

Almost regardless of the applied temperature, the heat treatment alters the microstructure of the starting alloy, affecting its mechanical properties (Fig. 1.37), together with the deformation and fracture behaviour. This latter is depicted in Fig. 1.38 for the as-built AlSi10Mg alloy compared to different heat treatment conditions [140]. In the as-built material (Fig. 1.38a), the Si network plays a fundamental role during the deformation stage (§ 1.2.1). Accordingly, failure starts in multiple sites next to the network, where excess stress due to the pile-up of dislocation occurs. Fracture then easily propagates following the interface between the Al cellular structure and the Si network. After direct ageing (Fig. 1.38b), microstructural features are just slightly affected. Most of the damage still nucleates at the Si network, where the fracture than propagates connecting the previously formed voids.

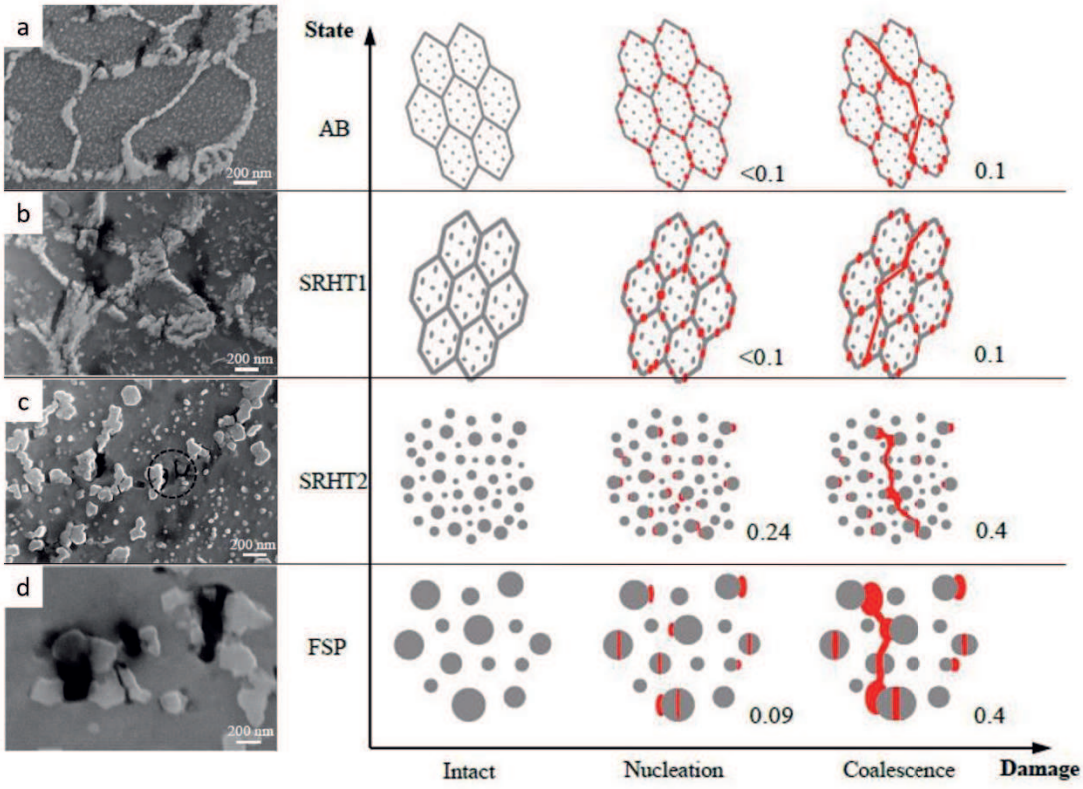

Figure 1.38. Effect of heat treatment on deformation and fracture behaviour of a PBF produced AlSi10Mg alloy. (a) As-built. (b) 250 °C for 2 h. (c) 300 °C for 2 h. (d) friction stir processed (comparable to a solution heat treatment in terms of microstructural evolution). The schematic on the right depicts in a simplified way the microstructure, the sites of starting failure and the crack propagation behaviour of the alloy, the loading is in the horizontal direction. Adapted with permission from Ref. [140].

Annealing (Fig. 1.3.8c) and high-temperature (Fig. 1.38d) heat treatments break the network into distinct Si particles. Damage still involves the Si phase, and nucleates within the particles or at their interface with the Al matrix. Conversely to the as-built and aged alloys, the fracture cannot merely connect the voids through propagation along the interconnected network. Instead, the coalescence of voids wide apart takes place through the formation of shear bands within the Al matrix, resulting in a better ductility. A small particle statistically contains less internal defects, and its failure stress is higher compared to a coarse particle. Hence, failure starts at a larger macroscopic strain in the annealed alloy. However, the large spacing between coarse particles in high-temperature heat-treated alloys enables a major void growth before coalescence. These opposite phenomena balance each other, and the net result is a similar elongation at failure of annealed and high-temperature heat-treated alloys [140].

A particular kind of heat treatment involving high pressures is the *hot isostatic pressing* (HIP). Initially devoted to material consolidation in powder metallurgy alloys [141]–[143] and removal of porosity in casting parts [144]–[146], it is attaining an increasing appeal in the AM field [147]–[149]. AM parts often suffer from residual internal porosity (§ 1.1.3), which could be eliminated by the HIP treatment. Moreover, the component shape is retained after pressing, which is notable since one of the main advantages of the AM processes is the possible building of very complex parts. Typically, HIP temperatures of Al parts are above 500 °C. Therefore, apart from the mechanical effect of hydrostatic pressure, the HIP alters the starting as-built microstructure similarly to a high-temperature heat treatment [113], [150]–[153]. Figure 1.39 depicts the effect of the HIP on the microstructural features of AlSi10Mg specimens [152]. After a stress-relieving, the circular sections of melt pools are still discernible (Figs. 1.39a-c-e), and the amount of porosity depends on the powder type, with the stored and reused ones being the most detrimental (Figs. 1.39c-e). The HIP successfully eliminates pores, regardless of the powder type (Figs. 1.39b-d-f). It also breaks the Si network and coarsens the resulting Si particles, similarly to Fig. 1.33.

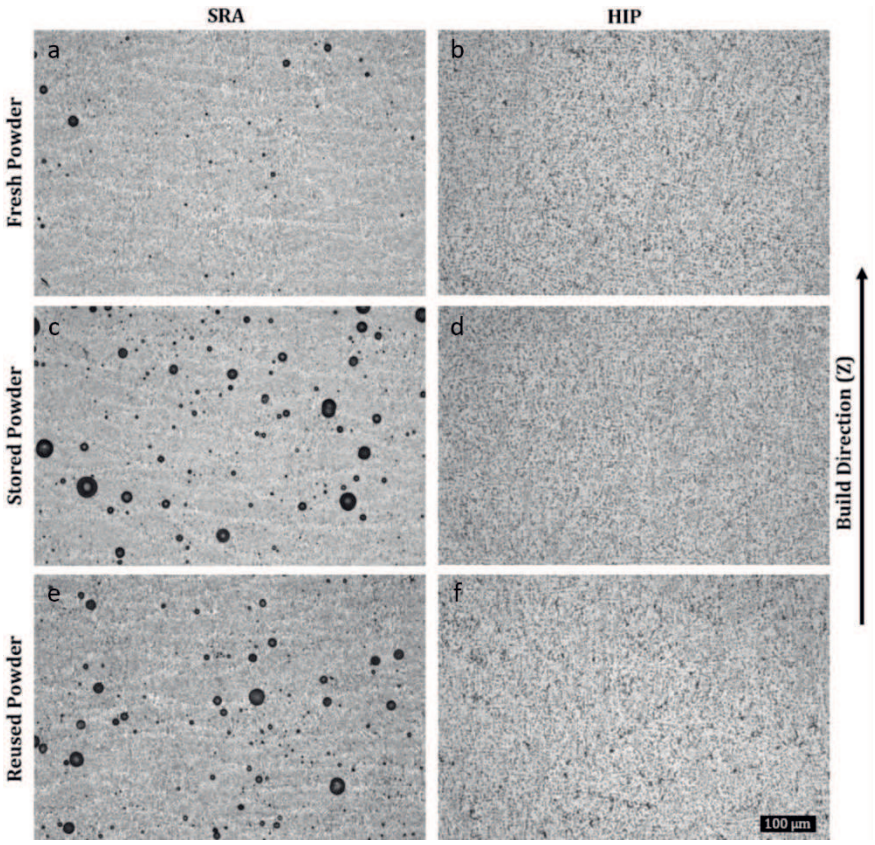

Figure 1.39. Effect of different powder type (fresh, stored and reused), stress-relief annealing (SRA) and hot isostatic pressing (HIP) on microstructure and amount of pores of a PBF produced AlSi10Mg alloy. Reprinted with permission from Ref. [152].

Figure 1.40 summarises the effect of porosity and HIP on the tensile properties of a PBF produced AlSi10Mg alloy [151]. Figure 1.40a highlights that, increasing the porosity fraction of the almost dense part (99.96 % relative density) up to 2 % (97.99 % relative density), significantly reduces its static properties (Fig. 1.40a). The HIP leads to the enclosure of pores but softens the material by altering the microstructure as reported in Fig. 1.39. Accordingly, the tensile strength is strongly reduced after HIP, and the elongation at failure increases due to the fostered ductility (Figure 1.40b). Similar results are also reported in [113], [150]. Comparable microstructural features make the static strength not more dependent on the starting condition, whereas the elongation at failure after HIP changes for specimens with different initial porosity level. In particular, specimens with a higher amount of porosity in the as-built state reach a lower elongation at failure compared to the almost dense ones. Elimination of internal pores during HIP is generally ascribed to diffusion bonding, which is hindered when stable oxides develop on the surface of pores. Therefore, differences in tensile properties after HIP could be

ascribed to oxides layers that prevent the successful bonding of internal pores and negatively affect the deformation behaviour [151]. A significant scatter in ductility after HIP is additionally reported [152].

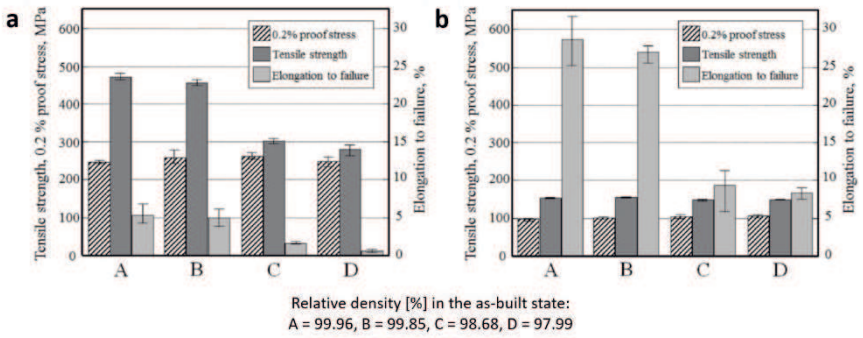

Figure 1.40. Tensile properties of a PBF produced AlSi10Mg alloy with an increasing porosity (from A to C). (a) As-built state. (b) After hot isostatic pressing. Adapted with permission from Ref. [151].

According to the results reported above, a proper selection of deposition parameters still remains the best way to reduce the porosity in AM produced parts. However, swelling of gas pores occurs at high temperatures [41], [154], which makes the HIP an invaluable step of AM produced Al components needing for high-temperature heat treatment. Since the application of HIP softens the material, the recovery of adequate strength is usually achieved by a solution heat treatment followed by the ageing treatment [150].

In conclusion, heat treatments profoundly alter the starting microstructure of the as-built AlSi10Mg alloy. A first category comprehends the low-temperature heat treatments, which usually aim at stress-relieving the material and breaking the eutectic Si network to increase ductility. Direct ageing is also possible to further strengthen the as-built alloy, provided that a supersaturated solid solution is retained during the manufacturing process. The second class comprehends the high-temperature heat treatments, which affect almost all the microstructural features, coarsening some of them and eliminating some others. The hot isostatic pressing behaves similarly and, additionally, it leads to the enclosure of pores descending from the manufacturing process. In both cases, the result is a significant softening of the material, usually recovered by the precipitation strengthening during the ageing treatment. Finally, a deep control and tailoring of the as-built microstructure of PBF produced alloys are

possible through the intrinsic heat treatment, which potentially avoids the need for further heat treatment.

REFERENCES

[1] *ISO / ASTM52900-15, Standard Terminology for Additive Manufacturing – General Principles – Terminology*. ASTM International, West Conshohocken, PA, 2015

[2] G. J. Gibbons and R. G. Hansell, *Direct tool steel injection mould inserts through the Arcam EBM free-form fabrication process*, Assem. Autom., vol. **25**, no. 4, pp. 300–305, 2005

[3] M. Pietropaoli, R. Ahlfeld, F. Montomoli, A. Ciani, and M. D'Ercole, *Design for Additive Manufacturing: Internal Channel Optimization*, J. Eng. Gas Turbines Power, vol. **139**, no. 10, pp. 1–8, 2017

[4] Y. Saadlaoui, J. L. Milan, J. M. Rossi, and P. Chabrand, *Topology optimization and additive manufacturing: Comparison of conception methods using industrial codes*, J. Manuf. Syst., vol. **43**, pp. 178–186, 2017

[5] M. Orme, I. Madera, M. Gschweitl, and M. Ferrari, *Topology Optimization for Additive Manufacturing as an Enabler for Light Weight Flight Hardware*, Designs, vol. **2**, no. 4, p. 51, 2018

[6] C. Yan, L. Hao, A. Hussein, P. Young, J. Huang, and W. Zhu, *Microstructure and mechanical properties of aluminium alloy cellular lattice structures manufactured by direct metal laser sintering*, Mater. Sci. Eng. A, vol. **628**, pp. 238–246, 2015

[7] A. Hadadzadeh, B. S. Amirkhiz, S. Shakerin, J. Kelly, J. Li, and M. Mohammadi, *Microstructural investigation and mechanical behavior of a two-material component fabricated through selective laser melting of AlSi10Mg on an Al-Cu-Ni-Fe-Mg cast alloy substrate*, Addit. Manuf., vol. **31**, no. October 2019, p. 100937, 2020

[8] M. H. Ghoncheh *et al.*, *On the solidification characteristics, deformation, and functionally graded interfaces in additively manufactured hybrid aluminum alloys*, Int. J. Plast., vol. **133**, no. August, p. 102840, 2020

[9] S. Ford and M. Despeisse, *Additive manufacturing and sustainability: an exploratory study of the advantages and challenges*, J. Clean. Prod., vol. **137**, pp. 1573–1587, 2016

[10] A. E. O. Daraban *et al.*, *A deep look at metal additive manufacturing recycling and use tools for sustainability performance*, Sustain., vol. **11**, no. 19, 2019

[11] L. E. Criales, Y. M. Arısoy, B. Lane, S. Moylan, A. Donmez, and T. Özel, *Laser powder bed fusion of nickel alloy 625: Experimental investigations of effects of process parameters on melt pool size and shape with spatter analysis*, Int. J. Mach. Tools Manuf., vol. **121**, no. March, pp. 22–36, 2017

[12] T. DebRoy *et al.*, *Additive manufacturing of metallic components – Process, structure and properties*, Prog. Mater. Sci., vol. **92**, pp. 112–224, 2018

[13] N. T. Aboulkhair, M. Simonelli, L. Parry, I. Ashcroft, C. Tuck, and R. Hague, *3D printing of Aluminium alloys: Additive Manufacturing of Aluminium alloys using selective laser melting*, Prog. Mater. Sci., vol. **106**, no. August 2018, p. 100578, 2019

[14] A. Raghavan, H. L. Wei, T. A. Palmer, and T. DebRoy, *Heat transfer and fluid flow in additive manufacturing*, J. Laser Appl., vol. **25**, no. 5, p. 052006, 2013

[15] Y. Li and D. Gu, *Parametric analysis of thermal behavior during selective laser melting additive manufacturing of aluminum alloy powder*, Mater. Des., vol. **63**, pp. 856–867, 2014

[16] V. Manvatkar, A. De, and T. Debroy, *Heat transfer and material flow during laser assisted multi-layer additive manufacturing*, J. Appl. Phys., vol. **116**, no. 12, pp. 1–8, 2014

[17] S. A. Khairallah, A. T. Anderson, A. Rubenchik, and W. E. King, *Laser powder-bed fusion additive manufacturing: Physics of complex melt flow and formation mechanisms of pores, spatter, and denudation zones*, Acta Mater., vol. **108**, pp. 36–45, 2016

[18] L. Thijs, M. L. Montero Sistiaga, R. Wauthle, Q. Xie, J. P. Kruth, and J. Van Humbeeck, *Strong morphological and crystallographic texture and resulting yield strength anisotropy in selective laser melted tantalum*, Acta Mater., vol. **61**, no. 12, pp. 4657–4668, 2013

[19] I. Rosenthal, A. Stern, and N. Frage, *Microstructure and Mechanical Properties of AlSi10Mg Parts Produced by the Laser Beam Additive Manufacturing (AM) Technology*, Metallogr. Microstruct. Anal., vol. **3**, no. 6, pp. 448–453, 2014

[20] S. Mishra, T. J. Lienert, M. Q. Johnson, and T. DebRoy, *An experimental and theoretical study of gas tungsten arc welding of stainless steel plates with different sulfur concentrations*, Acta Mater., vol. **56**, no. 9, pp. 2133–2146, 2008

[21] S. Ly, A. M. Rubenchik, S. A. Khairallah, G. Guss, and M. J. Matthews, *Metal vapor micro-jet controls material redistribution in laser powder bed fusion additive manufacturing*, Sci. Rep., vol. **7**, no. 1, pp. 1–12, 2017

[22] Q. Guo *et al.*, *Transient dynamics of powder spattering in laser powder bed fusion additive manufacturing process revealed by in-situ high-speed high-energy x-ray imaging*, Acta Mater., vol. **151**, pp. 169–180, 2018

[23] J. Yin *et al.*, *High-power laser-matter interaction during laser powder bed fusion*, Addit. Manuf., vol. **29**, no. July, p. 100778, 2019

[24] O. Diegel, A. Nordin, and D. Motte, *Additive Manufacturing Technologies*. 2015

[25] H. Hu, X. Ding, and L. Wang, *Numerical analysis of heat transfer during multi-layer selective laser melting of AlSi10Mg*, Optik (Stuttg)., vol. **127**, no. 20, pp. 8883–8891, 2016

[26] K. Kempen, L. Thijs, J. Van Humbeeck, and J. P. Kruth, *Processing AlSi10Mg by selective laser melting: Parameter optimisation and material characterisation*, Mater. Sci. Technol. (United Kingdom), vol. **31**, no. 8, pp. 917–923, 2015

[27] P. Wei *et al.*, *The AlSi10Mg samples produced by selective laser melting: single track, densification, microstructure and mechanical behavior*, Appl. Surf. Sci., vol. **408**, pp. 38–50, 2017

[28] X. Liu, C. Zhao, X. Zhou, Z. Shen, and W. Liu, *Microstructure of selective laser melted AlSi10Mg alloy*, Mater. Des., vol. **168**, p. 107677, 2019

[29] Z. Sun, X. Tan, S. B. Tor, and C. K. Chua, *Simultaneously enhanced strength and ductility for 3D-printed stainless steel 316L by selective laser melting*, NPG Asia Mater., vol. **10**, no. 4, pp. 127–136, 2018

[30] D. Buchbinder, H. Schleifenbaum, S. Heidrich, W. Meiners, and J. Bültmann, *High power Selective*

Laser Melting (HP SLM) of aluminum parts, Phys. Procedia, vol. **12**, no. PART 1, pp. 271–278, 2011

[31] N. T. Aboulkhair, N. M. Everitt, I. Ashcroft, and C. Tuck, *Reducing porosity in AlSi10Mg parts processed by selective laser melting*, Addit. Manuf., vol. **1**, pp. 77–86, 2014

[32] A. B. Spierings, K. Dawson, P. J. Uggowitzer, and K. Wegener, *Influence of SLM scan-speed on microstructure, precipitation of Al3Sc particles and mechanical properties in Sc- and Zr-modified Al-Mg alloys*, Mater. Des., vol. **140**, pp. 134–143, 2018

[33] H. Qin, Q. Dong, V. Fallah, and M. R. Daymond, *Rapid Solidification and Non-equilibrium Phase Constitution in Laser Powder Bed Fusion (LPBF) of AlSi10Mg Alloy: Analysis of Nano-precipitates, Eutectic Phases, and Hardness Evolution*, Metall. Mater. Trans. A Phys. Metall. Mater. Sci., vol. **51**, no. 1, pp. 448–466, 2020

[34] X. Su and Y. Yang, *Research on track overlapping during Selective Laser Melting of powders*, J. Mater. Process. Technol., vol. **212**, pp. 2074–2079, 2012

[35] L. Thijs, K. Kempen, J. P. Kruth, and J. Van Humbeeck, *Fine-structured aluminium products with controllable texture by selective laser melting of pre-alloyed AlSi10Mg powder*, Acta Mater., vol. **61**, no. 5, pp. 1809–1819, 2013

[36] A. J. Pinkerton and L. Li, *Direct additive laser manufacturing using gas- and water-atomised H13 tool steel powders*, Int. J. Adv. Manuf. Technol., vol. **25**, no. 5–6, pp. 471–479, 2005

[37] K. Riener *et al.*, *Influence of particle size distribution and morphology on the properties of the powder feedstock as well as of AlSi10Mg parts produced by laser powder bed fusion (LPBF)*, Addit. Manuf., vol. **34**, no. November 2019, p. 101286, 2020

[38] H. P. Tang, M. Qian, N. Liu, X. Z. Zhang, G. Y. Yang, and J. Wang, *Effect of Powder Reuse Times on Additive Manufacturing of Ti-6Al-4V by Selective Electron Beam Melting*, Jom, vol. **67**, no. 3, pp. 555–563, 2015

[39] H. Asgari, C. Baxter, K. Hosseinkhani, and M. Mohammadi, *On microstructure and mechanical properties of additively manufactured AlSi10Mg_200C using recycled powder*, Mater. Sci. Eng. A, vol. **707**, no. September, pp. 148–158, 2017

[40] A. H. Maamoun, M. Elbestawi, G. K. Dosbaeva, and S. C. Veldhuis, *Thermal post-processing of AlSi10Mg parts produced by Selective Laser Melting using recycled powder*, Addit. Manuf., vol. **21**, no. March, pp. 234–247, 2018

[41] C. Weingarten, D. Buchbinder, N. Pirch, W. Meiners, K. Wissenbach, and R. Poprawe, *Formation and reduction of hydrogen porosity during selective laser melting of AlSi10Mg*, J. Mater. Process. Technol., vol. **221**, pp. 112–120, 2015

[42] A. G. Demir and B. Previtali, *Investigation of remelting and preheating in SLM of 18Ni300 maraging steel as corrective and preventive measures for porosity reduction*, Int. J. Adv. Manuf. Technol., vol. **93**, no. 5–8, pp. 2697–2709, 2017

[43] E. Louvis, P. Fox, and C. J. Sutcliffe, *Selective laser melting of aluminium components*, J. Mater. Process. Technol., vol. **211**, no. 2, pp. 275–284, 2011

[44] N. Read, W. Wang, K. Essa, and M. M. Attallah, *Selective laser melting of AlSi10Mg alloy: Process optimisation and mechanical properties development*, Mater. Des., vol. **65**, pp. 417–424, 2015

[45] S. K. Everton, M. Hirsch, P. I. Stavroulakis, R. K. Leach, and A. T. Clare, *Review of in-situ process monitoring and in-situ metrology for metal additive manufacturing*, Mater. Des., vol. **95**, pp. 431–445, 2016

[46] M. Khanzadeh, W. Tian, A. Yadollahi, H. R. Doude, M. A. Tschopp, and L. Bian, *Dual process monitoring of metal-based additive manufacturing using tensor decomposition of thermal image streams*, Addit. Manuf., vol. **23**, no. July, pp. 443–456, 2018

[47] J. L. Bartlett, F. M. Heim, Y. V. Murty, and X. Li, *In situ defect detection in selective laser melting via full-field infrared thermography*, Addit. Manuf., vol. **24**, no. July, pp. 595–605, 2018

[48] S. A. Shevchik, C. Kenel, C. Leinenbach, and K. Wasmer, *Acoustic emission for in situ quality monitoring in additive manufacturing using spectral convolutional neural networks*, Addit. Manuf., vol. **21**, pp. 598–604, 2018

[49] E. Soderstrom and P. Mendez, *Humping mechanisms present in high speed welding*, Sci. Technol. Weld. Join., vol. **11**, no. 5, pp. 572–579, 2006

[50] A. Gusarov and I. Smurov, *Modeling the interaction of laser radiation with powder bed at selective laser melting*, Phys. Procedia, vol. **5**, pp. 381–394, 2010

[51] P. Bajaj, J. Wright, I. Todd, and E. A. Jägle, *Predictive process parameter selection for Selective Laser Melting Manufacturing: Applications to high thermal conductivity alloys*, Addit. Manuf., vol. **27**, no. April 2019, pp. 246–258, 2019

[52] B. Zhang, Y. Li, and Q. Bai, *Defect Formation Mechanisms in Selective Laser Melting: A Review*, Chinese J. Mech. Eng. (English Ed., vol. **30**, no. 3, pp. 515–527, 2017

[53] G. Kasperovich, J. Haubrich, J. Gussone, and G. Requena, *Correlation between porosity and processing parameters in TiAl6V4 produced by selective laser melting*, Mater. Des., vol. **105**, pp. 160–170, 2016

[54] S. M. H. Hojjatzadeh *et al.*, *Direct observation of pore formation mechanisms during LPBF additive manufacturing process and high energy density laser welding*, Int. J. Mach. Tools Manuf., vol. **153**, no. March, p. 103555, 2020

[55] M. Bayat *et al.*, *Keyhole-induced porosities in Laser-based Powder Bed Fusion (L-PBF) of Ti6Al4V: High-fidelity modelling and experimental validation*, Addit. Manuf., vol. **30**, no. April, p. 100835, 2019

[56] A. A. Martin *et al.*, *Dynamics of pore formation during laser powder bed fusion additive manufacturing*, Nat. Commun., vol. **10**, no. 1, 2019

[57] M. Tang and P. C. Pistorius, *Oxides, porosity and fatigue performance of AlSi10Mg parts produced by selective laser melting*, Int. J. Fatigue, vol. **94**, no. April, pp. 192–201, 2017

[58] N. Kaufmann, M. Imran, T. M. Wischeropp, C. Emmelmann, S. Siddique, and F. Walther, *Influence of process parameters on the quality of aluminium alloy en AW 7075 using Selective Laser Melting (SLM)*, Phys. Procedia, vol. **83**, pp. 918–926, 2016

[59] J. H. Martin, B. D. Yahata, J. M. Hundley, J. A. Mayer, T. A. Schaedler, and T. M. Pollock, *3D printing of high-strength aluminium alloys*, Nature, vol. **549**, no. 7672, pp. 365–369, 2017

[60] T. Qi, H. Zhu, H. Zhang, J. Yin, L. Ke, and X. Zeng, *Selective laser melting of Al7050 powder: Melting mode transition and comparison of the characteristics between the keyhole and conduction mode*, Mater. Des., vol. **135**, pp. 257–266, 2017

[61] A. B. Spierings *et al.*, *Microstructural features of Sc- and Zr-modified Al-Mg alloys processed by selective laser melting*, Mater. Des., vol. **115**, pp. 52–63, 2017

[62] J. P. Best, X. Maeder, J. Michler, and A. B. Spierings, *Mechanical Anisotropy Investigated in the Complex SLM-Processed Sc- and Zr-Modified Al–Mg Alloy Microstructure*, Adv. Eng. Mater., vol. **21**, no. 3, pp. 1–6, 2019

[63] J. R. Croteau *et al.*, *Microstructure and mechanical properties of Al-Mg-Zr alloys processed by selective laser melting*, Acta Mater., vol. **153**, pp. 35–44, 2018

[64] S. Griffiths, M. D. Rossell, J. Croteau, N. Q. Vo, D. C. Dunand, and C. Leinenbach, *Effect of laser rescanning on the grain microstructure of a selective laser melted Al-Mg-Zr alloy*, Mater. Charact., vol. **143**, no. March, pp. 34–42, 2018

[65] S. Griffiths *et al.*, *Coarsening- and creep resistance of precipitation-strengthened Al–Mg–Zr alloys processed by selective laser melting*, Acta Mater., vol. **188**, pp. 192–202, 2020

[66] A. Boschetto, L. Bottini, and F. Veniali, *Roughness modeling of AlSi10Mg parts fabricated by selective laser melting*, J. Mater. Process. Technol., vol. **241**, no. November 2016, pp. 154–163, 2017

[67] L. zhi Wang, S. Wang, and J. jiao Wu, *Experimental investigation on densification behavior and surface roughness of AlSi10Mg powders produced by selective laser melting*, Opt. Laser Technol., vol. **96**, pp. 88–96, 2017

[68] Z. Wang, E. Denlinger, P. Michaleris, A. D. Stoica, D. Ma, and A. M. Beese, *Residual stress mapping in Inconel 625 fabricated through additive manufacturing: Method for neutron diffraction measurements to validate thermomechanical model predictions*, Mater. Des., vol. **113**, pp. 169–177, 2017

[69] J. Wu, L. Wang, and X. An, *Numerical analysis of residual stress evolution of AlSi10Mg manufactured by selective laser melting*, Optik (Stuttg)., vol. **137**, pp. 65–78, 2017

[70] B. K. Panda and S. Sahoo, *Thermo-mechanical modeling and validation of stress field during laser powder bed fusion of AlSi10Mg built part*, Results Phys., vol. **12**, no. January, pp. 1372–1381, 2019

[71] S. Siddique, M. Imran, E. Wycisk, C. Emmelmann, and F. Walther, *Influence of process-induced microstructure and imperfections on mechanical properties of AlSi12 processed by selective laser melting*, J. Mater. Process. Technol., vol. **221**, pp. 205–213, 2015

[72] N. T. Aboulkhair, I. Maskery, C. Tuck, I. Ashcroft, and N. M. Everitt, *Improving the fatigue behaviour of a selectively laser melted aluminium alloy: Influence of heat treatment and surface quality*, Mater. Des., vol. **104**, pp. 174–182, 2016

[73] I. Yadroitsev, A. Gusarov, I. Yadroitsava, and I. Smurov, *Single track formation in selective laser melting of metal powders*, J. Mater. Process. Technol., vol. **210**, no. 12, pp. 1624–1631, 2010

[74] I. Yadroitsev, P. Krakhmalev, I. Yadroitsava, S. Johansson, and I. Smurov, *Energy input effect on morphology and microstructure of selective laser melting single track from metallic powder*, J. Mater. Process. Technol., vol. **213**, no. 4, pp. 606–613, 2013

[75] N. T. Aboulkhair, I. Maskery, C. Tuck, I. Ashcroft, and N. M. Everitt, *On the formation of AlSi10Mg single tracks and layers in selective laser melting: Microstructure and nano-mechanical properties*, J. Mater. Process. Technol., vol. **230**, pp. 88–98, 2016

[76] A. Hadadzadeh, B. S. Amirkhiz, J. Li, and M. Mohammadi, *Columnar to equiaxed transition during*

direct metal laser sintering of AlSi10Mg alloy: Effect of building direction, Addit. Manuf., vol. **23**, no. July, pp. 121–131, 2018

[77] X. P. Li *et al.*, *A selective laser melting and solution heat treatment refined Al-12Si alloy with a controllable ultrafine eutectic microstructure and 25% tensile ductility*, Acta Mater., vol. **95**, no. October, pp. 74–82, 2015

[78] X. P. Li *et al.*, *Selective laser melting of nano-TiB2decorated AlSi10Mg alloy with high fracture strength and ductility*, Acta Mater., vol. **129**, pp. 183–193, 2017

[79] M. Tang and P. C. Pistorius, *Anisotropic Mechanical Behavior of AlSi10Mg Parts Produced by Selective Laser Melting*, Jom, vol. **69**, no. 3, pp. 516–522, 2017

[80] Y. J. Liu, Z. Liu, Y. Jiang, G. W. Wang, Y. Yang, and L. C. Zhang, *Gradient in microstructure and mechanical property of selective laser melted AlSi10Mg*, J. Alloys Compd., vol. **735**, pp. 1414–1421, 2018

[81] J. Delahaye, J. T. Tchuindjang, J. Lecomte-Beckers, O. Rigo, A. M. Habraken, and A. Mertens, *Influence of Si precipitates on fracture mechanisms of AlSi10Mg parts processed by Selective Laser Melting*, Acta Mater., vol. **175**, pp. 160–170, 2019

[82] J. T. Oliveira de Menezes, E. M. Castrodeza, and R. Casati, *Effect of build orientation on fracture and tensile behavior of A357 Al alloy processed by Selective Laser Melting*, Mater. Sci. Eng. A, vol. **766**, no. September, p. 138392, 2019

[83] M. T. Di Giovanni, J. T. O. de Menezes, G. Bolelli, E. Cerri, and E. M. Castrodeza, *Fatigue crack growth behavior of a selective laser melted AlSi10Mg*, Eng. Fract. Mech., vol. **217**, no. March, p. 106564, 2019

[84] A. Hadadzadeh, B. S. Amirkhiz, J. Li, A. Odeshi, and M. Mohammadi, *Deformation mechanism during dynamic loading of an additively manufactured AlSi10Mg_200C*, Mater. Sci. Eng. A, vol. **722**, no. March, pp. 263–268, 2018

[85] T. G. Holesinger *et al.*, *Characterization of an Aluminum Alloy Hemispherical Shell Fabricated via Direct Metal Laser Melting*, Jom, vol. **68**, no. 3, pp. 1000–1011, 2016

[86] M. Fousová, D. Dvorský, A. Michalcová, and D. Vojtěch, *Changes in the microstructure and mechanical properties of additively manufactured AlSi10Mg alloy after exposure to elevated temperatures*, Mater. Charact., vol. **137**, no. December 2017, pp. 119–126, 2018

[87] Y. M. Wang *et al.*, *Additively manufactured hierarchical stainless steels with high strength and ductility*, Nat. Mater., vol. **17**, no. 1, pp. 63–70, 2018

[88] R. Li, M. Wang, Z. Li, P. Cao, T. Yuan, and H. Zhu, *Developing a high-strength Al-Mg-Si-Sc-Zr alloy for selective laser melting: crack-inhibiting and multiple strengthening mechanisms*, Acta Mater., vol. **193**, pp. 83–98, 2020

[89] G. Wang *et al.*, *The origin of high-density dislocations in additively manufactured metals*, Mater. Res. Lett., vol. **8**, no. 8, pp. 283–290, 2020

[90] Z. Wang *et al.*, *Premature failure of an additively manufactured material*, NPG Asia Mater., vol. **12**, no. 1, 2020

[91] L. Liu *et al.*, *Dislocation network in additive manufactured steel breaks strength–ductility trade-off*, Mater. Today, vol. **21**, no. 4, pp. 354–361, 2018

[92] A. Hadadzadeh, B. Shalchi Amirkhiz, A. Odeshi, J. Li, and M. Mohammadi, *Role of hierarchical microstructure of additively manufactured AlSi10Mg on dynamic loading behavior*, Addit. Manuf., vol. **28**, no. November 2018, pp. 1–13, 2019

[93] A. Hadadzadeh, B. S. Amirkhiz, B. Langelier, J. Li, and M. Mohammadi, *Evolution of a Gradient Microstructure in Direct Metal Laser Sintered AlSi10Mg*, in *TMS 2019 148th Annual Meeting & Exhibition Supplemental Proceedings*, 2019, pp. 331–338

[94] W. H. Kan, Y. Nadot, M. Foley, L. Ridosz, G. Proust, and J. M. Cairney, *Factors that affect the properties of additively-manufactured AlSi10Mg: Porosity versus microstructure*, Addit. Manuf., vol. **29**, no. April, p. 100805, 2019

[95] B. E. Carroll, T. A. Palmer, and A. M. Beese, *Anisotropic tensile behavior of Ti-6Al-4V components fabricated with directed energy deposition additive manufacturing*, Acta Mater., vol. **87**, pp. 309–320, 2015

[96] M. Simonelli, Y. Y. Tse, and C. Tuck, *Effect of the build orientation on the mechanical properties and fracture modes of SLM Ti-6Al-4V*, Mater. Sci. Eng. A, vol. **616**, pp. 1–11, 2014

[97] A. Takaichi *et al.*, *Effect of heat treatment on the anisotropic microstructural and mechanical properties of Co–Cr–Mo alloys produced by selective laser melting*, J. Mech. Behav. Biomed. Mater., vol. **102**, no. October 2019, p. 103496, 2020

[98] B. Chen *et al.*, *Strength and strain hardening of a selective laser melted AlSi10Mg alloy*, Scr. Mater., vol. **141**, pp. 45–49, 2017

[99] X. Lin, T. M. Yue, H. O. Yang, and W. D. Huang, *Solidification behavior and the evolution of phase in laser rapid forming of graded Ti6Al4V-Rene88DT alloy*, Metall. Mater. Trans. A Phys. Metall. Mater. Sci., vol. **38**, no. 1, pp. 127–137, 2007

[100] Q. Jia *et al.*, *Precipitation kinetics, microstructure evolution and mechanical behavior of a developed Al–Mn–Sc alloy fabricated by selective laser melting*, Acta Mater., vol. **193**, pp. 239–251, 2020

[101] M. Bermingham, D. StJohn, M. Easton, L. Yuan, and M. Dargusch, *Revealing the Mechanisms of Grain Nucleation and Formation During Additive Manufacturing*, Jom, vol. **72**, no. 3, pp. 1065–1073, 2020

[102] Y. K. Xiao *et al.*, *Effect of nano-TiB2 particles on the anisotropy in an AlSi10Mg alloy processed by selective laser melting*, J. Alloys Compd., vol. **798**, pp. 644–655, 2019

[103] L. Zhou, A. Mehta, E. Schulz, B. McWilliams, K. Cho, and Y. Sohn, *Microstructure, precipitates and hardness of selectively laser melted AlSi10Mg alloy before and after heat treatment*, Mater. Charact., vol. **143**, no. March, pp. 5–17, 2018

[104] S. Marola *et al.*, *A comparison of Selective Laser Melting with bulk rapid solidification of AlSi10Mg alloy*, J. Alloys Compd., vol. **742**, pp. 271–279, 2018

[105] T. Maeshima and K. Oh-ishi, *Solute clustering and supersaturated solid solution of AlSi10Mg alloy fabricated by selective laser melting*, Heliyon, vol. **5**, no. 2, p. e01186, 2019

[106] L. Hitzler *et al.*, *Heat treatments and critical quenching rates in additively manufactured Al-Si-Mg alloys*, Materials (Basel)., vol. **13**, no. 3, pp. 1–17, 2020

[107] N. Takata, H. Kodaira, A. Suzuki, and M. Kobashi, *Size dependence of microstructure of AlSi10Mg*

alloy fabricated by selective laser melting, Mater. Charact., vol. **143**, no. October, pp. 18–26, 2018

[108] L. Zhuo *et al.*, *Effect of post-process heat treatment on microstructure and properties of selective laser melted AlSi10Mg alloy*, Mater. Lett., vol. **234**, pp. 196–200, 2019

[109] J. Fiocchi, C. A. Biffi, C. Colombo, L. M. Vergani, and A. Tuissi, *Ad Hoc Heat Treatments for Selective Laser Melted Alsi10mg Alloy Aimed at Stress-Relieving and Enhancing Mechanical Performances*, Jom, vol. **72**, no. 3, pp. 1118–1127, 2020

[110] E. Brandl, U. Heckenberger, V. Holzinger, and D. Buchbinder, *Additive manufactured AlSi10Mg samples using Selective Laser Melting (SLM): Microstructure, high cycle fatigue, and fracture behavior*, Mater. Des., vol. **34**, pp. 159–169, 2012

[111] N. T. Aboulkhair, I. Maskery, C. Tuck, I. Ashcroft, and N. M. Everitt, *The microstructure and mechanical properties of selectively laser melted AlSi10Mg: The effect of a conventional T6-like heat treatment*, Mater. Sci. Eng. A, vol. **667**, pp. 139–146, 2016

[112] W. Li *et al.*, *Effect of heat treatment on AlSi10Mg alloy fabricated by selective laser melting: Microstructure evolution, mechanical properties and fracture mechanism*, Mater. Sci. Eng. A, vol. **663**, pp. 116–125, 2016

[113] N. E. Uzan, R. Shneck, O. Yeheskel, and N. Frage, *Fatigue of AlSi10Mg specimens fabricated by additive manufacturing selective laser melting (AM-SLM)*, Mater. Sci. Eng. A, vol. **704**, no. August, pp. 229–237, 2017

[114] Z. H. Xiong, S. L. Liu, S. F. Li, Y. Shi, Y. F. Yang, and R. D. K. Misra, *Role of melt pool boundary condition in determining the mechanical properties of selective laser melting AlSi10Mg alloy*, Mater. Sci. Eng. A, vol. **740–741**, no. April 2018, pp. 148–156, 2019

[115] D. K. Kim, J. H. Hwang, E. Y. Kim, Y. U. Heo, W. Woo, and S. H. Choi, *Evaluation of the stress-strain relationship of constituent phases in AlSi10Mg alloy produced by selective laser melting using crystal plasticity FEM*, J. Alloys Compd., vol. **714**, no. August, pp. 687–697, 2017

[116] E. A. Jägle *et al.*, *Precipitation Reactions in Age-Hardenable Alloys During Laser Additive Manufacturing*, Jom, vol. **68**, no. 3, pp. 943–949, 2016

[117] J. Wu, X. Q. Wang, W. Wang, M. M. Attallah, and M. H. Loretto, *Microstructure and strength of selectively laser melted AlSi10Mg*, Acta Mater., vol. **117**, pp. 311–320, 2016

[118] R. Casati, M. H. Nasab, M. Coduri, V. Tirelli, and M. Vedani, *Effects of platform pre-heating and thermal-treatment strategies on properties of alsi10mg alloy processed by selective laser melting*, Metals (Basel)., vol. **8**, no. 11, p. 954, 2018

[119] G. E. Dieter and D. J. Bacon, *Mechanical Metallurgy*. 1986

[120] P. Kürnsteiner, M. B. Wilms, A. Weisheit, P. Barriobero-Vila, E. A. Jägle, and D. Raabe, *Massive nanoprecipitation in an Fe-19Ni-xAl maraging steel triggered by the intrinsic heat treatment during laser metal deposition*, Acta Mater., vol. **129**, no. August, pp. 52–60, 2017

[121] J. Haubrich *et al.*, *The role of lattice defects, element partitioning and intrinsic heat effects on the microstructure in selective laser melted Ti-6Al-4V*, Acta Mater., vol. **167**, pp. 136–148, 2019

[122] P. Kürnsteiner, M. B. Wilms, A. Weisheit, B. Gault, E. A. Jägle, and D. Raabe, *High-strength Damascus steel by additive manufacturing*, Nature, vol. **582**, no. 7813, pp. 515–519, 2020

[123] P. Kürnsteiner *et al.*, *Control of thermally stable core-shell nano-precipitates in additively manufactured*

Al-Sc-Zr alloys, Addit. Manuf., vol. **32**, no. October 2019, p. 100910, 2020

[124] K. G. Prashanth *et al.*, *Microstructure and mechanical properties of Al-12Si produced by selective laser melting: Effect of heat treatment*, Mater. Sci. Eng. A, vol. **590**, pp. 153–160, 2014

[125] J. Fiocchi, A. Tuissi, P. Bassani, and C. A. Biffi, *Low temperature annealing dedicated to AlSi10Mg selective laser melting products*, J. Alloys Compd., vol. **695**, pp. 3402–3409, 2017

[126] P. Yang *et al.*, *Effect of thermal annealing on microstructure evolution and mechanical behavior of an additive manufactured AlSi10Mg part*, J. Mater. Res., vol. **33**, no. 12, pp. 1701–1712, 2018

[127] P. Yang, L. A. Deibler, D. R. Bradley, D. K. Stefan, and J. D. Carroll, *Microstructure evolution and thermal properties of an additively manufactured, solution treatable AlSi10Mg part*, J. Mater. Res., vol. **33**, no. 23, pp. 4040–4052, 2018

[128] E. Padovano, C. Badini, A. Pantarelli, F. Gili, and F. D'Aiuto, *A comparative study of the effects of thermal treatments on AlSi10Mg produced by laser powder bed fusion*, J. Alloys Compd., vol. **831**, p. 154822, 2020

[129] N. Takata, H. Kodaira, K. Sekizawa, A. Suzuki, and M. Kobashi, *Change in microstructure of selectively laser melted AlSi10Mg alloy with heat treatments*, Mater. Sci. Eng. A, vol. **704**, no. August, pp. 218–228, 2017

[130] A. Iturrioz, E. Gil, M. M. Petite, F. Garciandia, A. M. Mancisidor, and M. San Sebastian, *Selective laser melting of AlSi10Mg alloy: influence of heat treatment condition on mechanical properties and microstructure*, Weld. World, vol. **62**, no. 4, pp. 885–892, 2018

[131] F. Alghamdi, X. Song, A. Hadadzadeh, B. Shalchi-Amirkhiz, M. Mohammadi, and M. Haghshenas, *Post heat treatment of additive manufactured AlSi10Mg: On silicon morphology, texture and small-scale properties*, Mater. Sci. Eng. A, vol. **783**, no. March, p. 139296, 2020

[132] H. W. Zandbergen, S. J. Andersen, and J. Jansen, *Structure determination of Mg5Si6:particles in Al by dynamic electron diffraction studies*, Science (80-.)., vol. **277**, no. 5330, pp. 1221–1225, 1997

[133] S. J. Andersen, H. W. Zandbergen, J. Jansen, C. Træholt, U. Tundal, and O. Reiso, *The crystal structure of the β" phase in Al-Mg-Si Alloys*, Acta Mater., vol. **46**, no. 9, pp. 3283–3298, 1998

[134] C. D. Marioara, S. J. Andersen, J. Jansen, and H. W. Zandbergen, *Atomic model for GP-zones in a 6082 Al-Mg-Si system*, Acta Mater., vol. **49**, no. 2, pp. 321–328, 2001

[135] B. Milkereit, M. J. Starink, P. A. Rometsch, C. Schick, and O. Kessler, *Review of the quench sensitivity of aluminium alloys: Analysis of the kinetics and nature of quench-induced precipitation*, Materials (Basel)., vol. **12**, no. 24, 2019

[136] J. H. Rao, Y. Zhang, K. Zhang, A. Huang, C. H. J. Davies, and X. Wu, *Multiple precipitation pathways in an Al-7Si-0.6Mg alloy fabricated by selective laser melting*, Scr. Mater., vol. **160**, pp. 66–69, 2019

[137] T. Hu, K. Ma, T. D. Topping, J. M. Schoenung, and E. J. Lavernia, *Precipitation phenomena in an ultrafine-grained Al alloy*, Acta Mater., vol. **61**, no. 6, pp. 2163–2178, 2013

[138] W. Chrominski and M. Lewandowska, *Precipitation phenomena in ultrafine grained Al-Mg-Si alloy with heterogeneous microstructure*, Acta Mater., vol. **103**, pp. 547–557, 2016

[139] I. Rosenthal, R. Shneck, and A. Stern, *Heat treatment effect on the mechanical properties and fracture mechanism in AlSi10Mg fabricated by additive manufacturing selective laser melting process*, Mater. Sci.

Eng. A, vol. **729**, no. May, pp. 310–322, 2018

[140] L. Zhao, J. G. Santos Macías, L. Ding, H. Idrissi, and A. Simar, *Damage mechanisms in selective laser melted AlSi10Mg under as built and different post-treatment conditions*, Mater. Sci. Eng. A, vol. **764**, pp. 1–25, 2019

[141] F. Erdemir, A. Canakci, T. Varol, and S. Ozkaya, *Corrosion and wear behavior of functionally graded Al2024/SiC composites produced by hot pressing and consolidation*, J. Alloys Compd., vol. **644**, pp. 589–596, 2015

[142] A. J. Knowles, X. Jiang, M. Galano, and F. Audebert, *Microstructure and mechanical properties of 6061 Al alloy based composites with SiC nanoparticles*, J. Alloys Compd., vol. **615**, no. S1, pp. S401–S405, 2015

[143] T. J. Harrell, T. D. Topping, H. Wen, T. Hu, J. M. Schoenung, and E. J. Lavernia, *Microstructure and Strengthening Mechanisms in an Ultrafine Grained Al-Mg-Sc Alloy Produced by Powder Metallurgy*, Metall. Mater. Trans. A Phys. Metall. Mater. Sci., vol. **45**, no. 13, pp. 6329–6343, 2014

[144] L. Ceschini, A. Morri, and G. Sambogna, *The effect of hot isostatic pressing on the fatigue behaviour of sand-cast A356-T6 and A204-T6 aluminum alloys*, J. Mater. Process. Technol., vol. **204**, no. 1–3, pp. 231–238, 2008

[145] M. Ostermeier, H. Hoffmann, and E. Werner, *The Effects of Hot Isostatic Pressing on Aluminium Castings*, Key Eng. Mater., vol. **345–346**, no. November, pp. 1545–1548, 2007

[146] J. T. Staley, M. Tiryakioğlu, and J. Campbell, *The effect of hot isostatic pressing (HIP) on the fatigue life of A206-T71 aluminum castings*, Mater. Sci. Eng. A, vol. **465**, no. 1–2, pp. 136–145, 2007

[147] S. Siddique *et al.*, *Computed tomography for characterization of fatigue performance of selective laser melted parts*, Mater. Des., vol. **83**, pp. 661–669, 2015

[148] J. Benzing, N. Hrabe, T. Quinn, R. White, R. Rentz, and M. Ahlfors, *Hot isostatic pressing (HIP) to achieve isotropic microstructure and retain as-built strength in an additive manufacturing titanium alloy (Ti-6Al-4V)*, Mater. Lett., vol. **257**, p. 126690, 2019

[149] L. N. Carter, C. Martin, P. J. Withers, and M. M. Attallah, *The influence of the laser scan strategy on grain structure and cracking behaviour in SLM powder-bed fabricated nickel superalloy*, J. Alloys Compd., vol. **615**, pp. 338–347, 2014

[150] U. Tradowsky, J. White, R. M. Ward, N. Read, W. Reimers, and M. M. Attallah, *Selective laser melting of AlSi10Mg: Influence of post-processing on the microstructural and tensile properties development*, Mater. Des., vol. **105**, pp. 212–222, 2016

[151] T. Hirata, T. Kimura, and T. Nakamoto, *Effects of hot isostatic pressing and internal porosity on the performance of selective laser melted AlSi10Mg alloys*, Mater. Sci. Eng. A, vol. **772**, no. June 2019, p. 138713, 2020

[152] C. B. Finfrock, A. Exil, J. D. Carroll, and L. Deibler, *Effect of Hot Isostatic Pressing and Powder Feedstock on Porosity, Microstructure, and Mechanical Properties of Selective Laser Melted AlSi10Mg*, Metallogr. Microstruct. Anal., vol. **7**, no. 4, pp. 443–456, 2018

[153] W. Schneller, M. Leitner, S. Springer, F. Grün, and M. Taschauer, *Effect of hip treatment on microstructure and fatigue strength of selectively laser melted AlSi10Mg*, J. Manuf. Mater. Process., vol.

3, no. 1, 2019

[154] K. V. Yang *et al.*, *Porosity formation mechanisms and fatigue response in Al-Si-Mg alloys made by selective laser melting*, Mater. Sci. Eng. A, vol. **712**, no. September 2017, pp. 166–174, 2018

CHAPTER 2

RELIABILITY OF DESIGN BY THE ENERGY DENSITY-BASED APPROACH

The present chapter deals with the effect of building parameters on microstructure, mechanical properties and fracture behaviour of an L-PBF produced AlSi10Mg alloy. Scan speed and hatch spacing are progressively varied to achieve a well-defined range of volumetric energy density (VED) values. The results of density and tensile measurements are compared to literature studies that employ the same energy density range. The aim is to assess the reliability of the energy density-based approach in defining a suitable process window to realise defect-free parts.

2.1 USE OF VED AS A PROCESS DESIGN PARAMETER

2.1.1 Additional background and purpose of the work

The mechanical performance of AM produced Al alloys components can be severely affected by process-related defects, with porosity being the most deleterious one [1]–[3]. Porosity stems from a non-optimised process, and hence a proper choice of building parameters is mandatory. However, the complexity of AM processes hinders to assess the effect of individual deposition parameters unambiguously. An energy density-based approach is often suggested in the literature to overcome such complexity. The minimum porosity is achieved within a specific range of energy density, whereas too low or too high values lead to lack-of-fusion and keyhole porosities, respectively [4]–[6]. Kempen *et al*. [7] optimised the deposition of an AlSi10Mg alloy based on an energy per unit length parameter E' [J/mm], defined as the ratio of laser power and scan speed. With the same alloy Krishnan *et al*. [8] adopted a superficial energy density parameter E_d [J/mm^2] to minimise the porosity. However, the suitable process window is generally identified using a volumetric energy density [J/mm^3] parameter [2], [9]–[11], defined as in equation (1):

$$VED = \frac{P}{v \cdot h \cdot t} \tag{1}$$

where P [W] is the laser power, v [mm/s] is the scan speed, h [mm] is the hatch spacing, and t [mm] is the layer thickness. Read *et al*. [11] found that a VED of ~60 J/mm^3 is suitable to achieve a dense AlSi10Mg alloy. A similar optimum value was determined by Kimura *et al*. [10] processing an AlSi7Mg alloy. Despite such agreement, data in the literature are somewhat scattered. Figure 2.1 depicts the optimum density obtained for several AlSi alloys (Si ≥ 7 wt.%) and the correspondent VED range or value [1], [3], [7]–[17]. In the case of studies not directly referring to the energy density, VED was calculated using the optimised building parameters accordingly to equation (1).

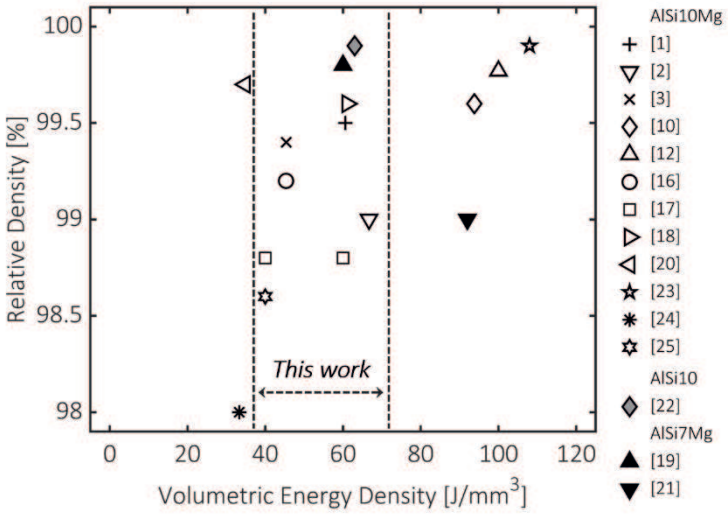

Figure 2.1. Comparison of literature data of different AlSi alloys: VED values that achieved fully dense components (relative density in the 98-99.9 % range).

VED values in the 30-110 J/mm^3 range were found to be suitable to achieve fully dense parts (relative density in the 98-99.9 % range), with most of the data lying between 40 and 70 J/mm^3.

The current research activity stems from an actual industrial need of the AMT S.r.l. industrial partner. The final goal is to determine a suitable combination of printing parameters to optimise density and tensile performance of the AlSi10Mg alloy. In this light, specimens were produced in the above-mentioned VED range (40-70 J/mm^3) according to literature data. The research activity aims to evaluate the reliability of the energy density-based approach to define the optimum process window of deposition parameters. Additionally, it seeks to assess the reproducibility of the tensile properties of specimens produced within a given energy density range.

2.2 MATERIALS AND EXPERIMENTAL PROCEDURE

2.2.1 L-PBF of samples

The samples were produced with an EOS M290 system using L-PBF technology. A commercially available AlSi10Mg powder, with the measured chemical composition by optical emission spectroscopy (OES) reported in Table 2.1, was processed in a protective argon atmosphere on a cold-building platform.

Table 2.1. Chemical composition (wt.%) of the AlSi10Mg alloy samples produced by L-PBF.

Si	**Mg**	**Fe**	**Mn**	**Cu**	**Al**
9.6	0.36	0.16	0.02	< 0.01	balance

All the specimens were realised at constant laser power (P) and layer thickness (t). Different combinations of scan speed (v) and hatch spacing (h) are listed in Table 2.2, together with the corresponding VED. Absolute values of process parameters cannot be disclosed, and they are reported normalised with respect to the minimum value.

Table 2.2. Combinations of building parameters - scan speed and hatch spacing - and the corresponding VED.

v [mm/s]	v	1.18 v	1.36 v	1.55 v	v	1.18 v	1.36 v	1.55 v
h [mm]	h	h	h	h	1.12 h	1.12 h	1.12 h	1.12 h
VED [J/mm^3]	66	56	48	42	59	50	43	38

For each condition, three cylindrical tensile specimens were produced vertically to the building platform, as reported in Fig. 2.2, and then machined to the final size (diameter d_0 = 4 mm, gage length L_0 = 20 mm).

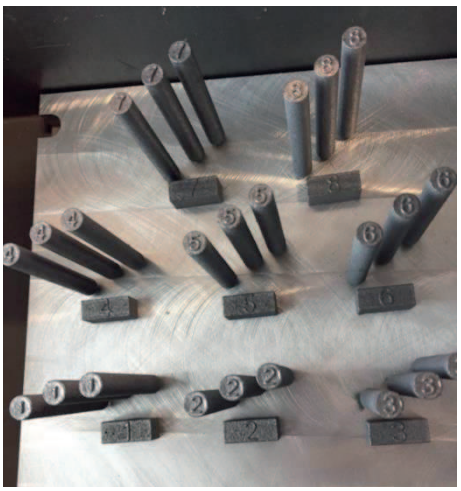

Figure 2.2. Building platform with the L-PBF produced cuboid and tensile specimens.

An additional 10 x 10 x 25 mm^3 cuboid sample was realised with the long side parallel to the building platform for each condition (Fig. 2.2). Microstructural and mechanical characterisations were performed on the specimens in the as-built state.

2.2.2 Density tests and mechanical characterization

Density measurements were conducted on the cuboid samples with the hydrostatic weighing method using a METTLER AE240 analytical balance. Samples were firstly weighed in air and then in distilled water. Absolute density was obtained, averaging five measurements. A pure Al specimen was used as a standard, giving a measured density of 2.699 g/cm^3. Relative density was calculated, dividing by the nominal alloy density, assumed as 2.67 g/cm^3 [18]. Tensile tests were performed using an Instron 5982 testing machine, according to the ISO 6892-1: 2016 standard. Brinell hardness tests were carried out on the lateral sides of the cuboid samples. The measurements were conducted using an ERNST AT130 DR hardness tester, with a load of 62.5 kg_f and a 2.5 mm diameter spherical indenter, according to the UNI EN ISO 6505-1: 2015 standard.

2.2.3 Microstructural characterization

Sections parallel and perpendicular to the building direction were cut from the cuboid samples and subjected to standard metallographic preparations. The porosity was investigated with a Leica DMI 5000M optical microscope (OM) and measured by image analysis using the software ImageJ [19]. The relative density was calculated as the

percentage of the analysed surface not occupied by the porosity. Size and morphology of the pores were evaluated respectively by Equivalent Diameter (ED) [μm] and Circularity (C) parameters, accordingly to the following expressions:

$$ED = \left(\frac{4 \cdot A}{\pi}\right)^{1/2} \tag{2}$$

$$C = \frac{4 \cdot \pi \cdot A}{P^2} \tag{3}$$

where A [μm²] is the area of the pore and P [μm] its perimeter. Samples were subsequently etched for 10 s with a 1% HF distilled water solution. Microstructural and fractographic observations were performed with a Zeiss EVO MA 15 scanning electron microscope (SEM) on cuboid and fractured tensile samples, respectively. Size and spacing of microstructural and fractographic features were measured with the software ImageJ. The width of grains and Al dendrites and the ED of Si particles were assumed as representative size parameters, whereas the spacing of Si particles and dimples was measured with the 3-Nearest Neighbours Distance (3NND) method. X-ray diffraction (XRD) tests were performed on the polished top surface of cuboid samples in a Bragg-Brentano geometry with a Bruker D8 Advance diffractometer equipped with a Cu filament (Kα, 1.5406 Å). Data were acquired in the 2ϑ range from 20° to 110°, with a step-size of 0.02° and a step-time of 1 s. Quantitative measurements were computed with the Rietveld refinement method using the software Maud [20]. A 3-parameter harmonic function was used to account for the presence of texture and reduce the error in quantitative measurements of phases amount.

2.3 RESULTS AND ANALYSES

2.3.1 Effect of process parameters on the porosity level

Figure 2.3 depicts representative OM images of samples produced at a different VED. Sections parallel to the building direction (Figs. 2.3a-b-c) show the semi-circular shape of the melt pools, whereas sections perpendicular to the building direction (Figs. 2.3d-e-f) display elongated scan tracks.

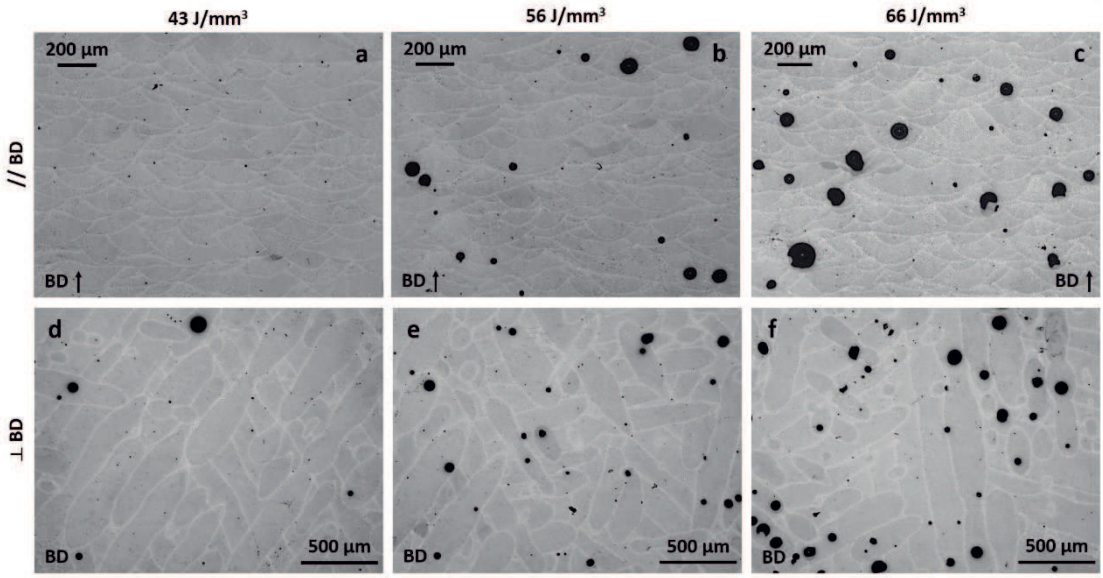

Figure 2.3. OM images in complementary sections of samples produced with different VED. (a-d) 43 J/mm³. (b-e) 56 J/mm³. (c-f) 66 J/mm³. (a-b-c) section parallel to the building direction. (d-e-f) section perpendicular to the building direction. Black vertical arrows and dots point out the building direction (BD).

At 43 J/mm³ (Figs. 2.3a-d) the alloy exhibits a low number of pores, most being a few tens of µm in size. At 56 J/mm³ (Figs. 2.3b-e) large circular pores, several tens of µm wide, appear. Several large pores up to 100-200 µm in size and mainly located at the bottom of the melt pools characterise the alloy processed with 66 J/mm³ (Figs. 2.3c-f).

In addition to porosity, other defects were detected in the as-built material, namely small shrinkage voids, as depicted in Figs. 2.4a-b, and Mg-based oxides (see § 2.3.3). A limited amount of such defects was found in all the investigated samples, with a size generally smaller than large pores in Fig 2.3. Accordingly, their effect on the final properties was assumed as negligible and will not be furtherly discussed.

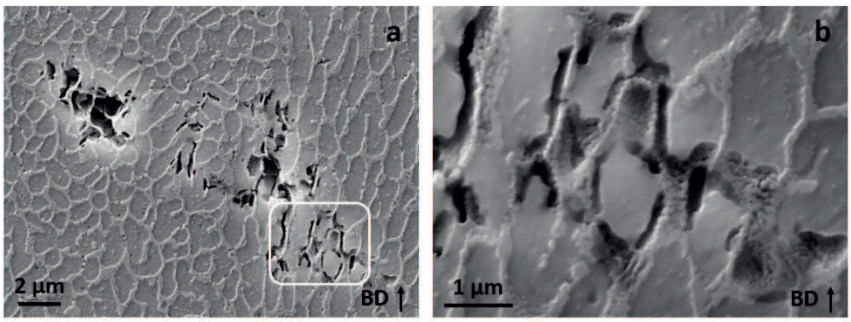

Figure 2.4. SEM images of process defects. (a) Micro-void. (b) Detailed image taken from the area marked by the solid line in (a), high magnification of shrinkage at the Al/Si interface. Black vertical arrows point out the building direction (BD).

Image analysis was carried out to determine ED and C of the pores. Figure 2.5a reports their probability density functions (PDF) of samples in Fig. 2.3. At low VED, the ED statistical distribution is narrow and located in the range of a few tens of µm. As the VED raises, the distributions gradually become flattered and broaden to higher ED values. Such behaviour mirrors the appearance of the larger pores detected by microstructural observations. Conversely to ED, the C statistical distributions slightly narrow as VED increases. Most of the pores in each sample range between 0.7-0.9 of C, indicating a nearly circular morphology.

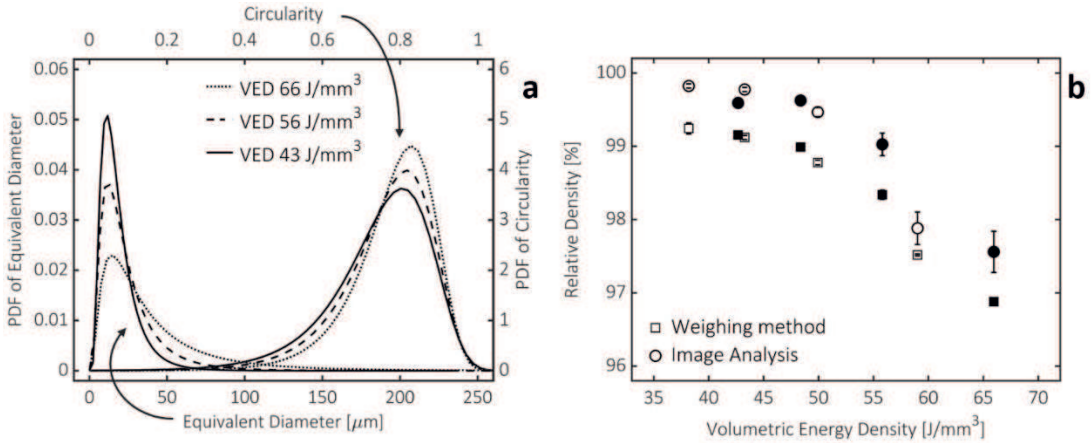

Figure 2.5. (a) ED and C statistical distributions of porosities in a transverse section of the specimens in Figure 5. (b) Relationship between VED and relative density; filled and open markers correspond to hatch spacing h and 1.12h, respectively. Standard deviation is reported as error bar.

Figure 2.5b reports the relationship between VED and relative density. Measurements by the weighing method are always ~0.5% lower than by image analysis. A lower size threshold of 70 μm² (ED ~10 μm) was applied to pores with a low resolution at the employed magnification during image analysis. Additionally, the corresponding relative density stems from an areal measurement, whereas the weighing method is a volumetric one. These observations could justify the difference mentioned above. However, both methods provide the same trend, with the relative density progressively reducing as the VED increases. The highest value of 99.8-99.3 was reached with a VED of 38 J/mm³, whereas it falls to 97.5-96.5 as the energy density reaches 66 J/mm³. The distinction between filled and open markers in Fig. 2.5b is related to the two employed *h*. It appears that the progressively deteriorating effect of building parameters (*v* and *h*) on the relative density can be described with a univocal function of the energy density.

2.3.2 Metastable microstructure of the as-built alloy

Although the VED considerably affects the porosity level, its effect on the microstructure is much less evident. Accordingly, Fig. 2.6 depicts the typical features of the alloy processed with parameters 1.55 v-h, taken as the reference. The AlSi10Mg alloy exhibits a hierarchical microstructure, with the semi-circular melt pools shown in Fig. 2.6a as the outer level. They are delimited by melt pool boundaries (MPBs), coarse zones produced with a low local cooling rate during the solidification process, highlighted with black arrows in Fig. 2.6a. Inside the melt pools, the BSE channelling contrast reveals columnar grains elongated radially to the MPBs (Fig. 2.6b). They are a few tens of μm wide and up to 200 μm long, and often epitaxially grow across several melt pools. Equiaxed grains are sometimes detected along the MPBs, as marked by the black arrow in Fig. 2.6c. They likely form due to the columnar-to-equiaxed transition phenomenon, and are not remelted by the deposition of the overhead layer. Each grain is made up of a continuous network of fibrous eutectic Si that surrounds small Al cellular dendrites, pointed out respectively with black and white arrows in Fig. 2.6d. These micrometric dendrites are about one order of magnitude smaller than grains depicted in Figs. 2.6b-c, with which they share the same elongation direction. The amount of eutectic phase, calculated as ~20 ± 4% by image analysis, is far distant from the one expected for an AlSi10 alloy (~75%).

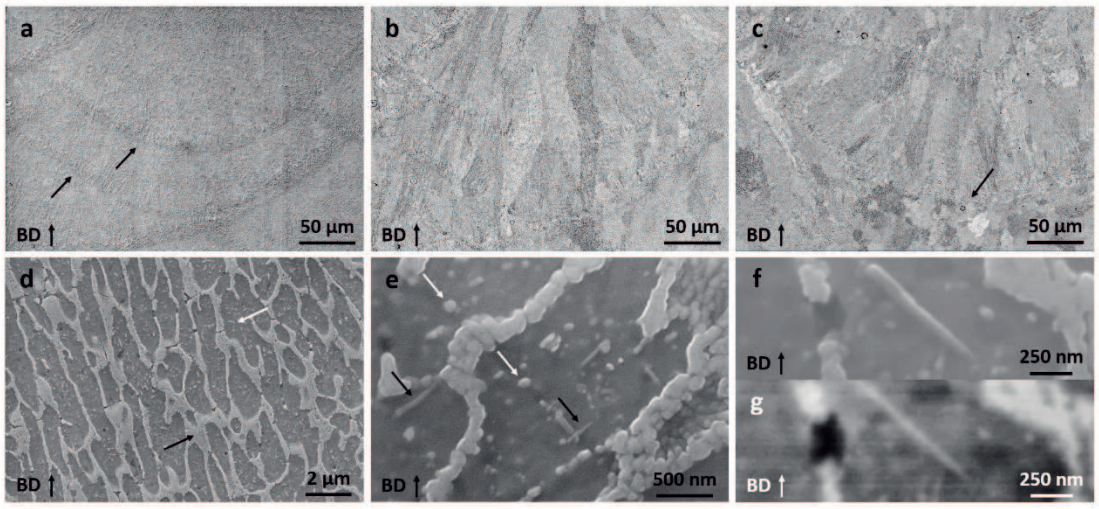

Figure 2.6. SEM images in a transverse section of the AlSi10Mg alloy. (a) SE image of the semi-circular melt pools, black arrows mark the melt pool boundaries. (b) Same area as (a), BSE image of epitaxial columnar grains. (c) Columnar grain within the melt pool and equiaxed grains (black arrow) at the melt pool boundary. (d) Al cellular dendrites (white arrow) and eutectic network (black arrow). (e) Nano-sized Si precipitates with globular (white arrow) and acicular (black arrow) morphology. (f) Acicular Si precipitate at high magnification. (g) Same area as (a), BSE image providing compositional contrast. In all images, vertical arrows in the bottom-left corner mark the building direction (BD).

Nano-sized precipitates, hosted inside the Al dendrites, occupy the inner level of the hierarchical microstructure. They exhibit both globular and needle-like morphologies, as highlighted respectively by white and black arrows in Fig. 2.6e. Figure 2.6f shows a detailed image of a needle-like precipitate. The complementary BSE image in Fig. 2.6g provides the compositional contrast and clarifies such features as Si precipitates. They could either result from a reduced solubility of Si inside the Al phase during the cooling process or precipitation-induced phenomena caused by the neighbouring laser scans. The lack of Mg-containing phases suggests the element to be retained in solid solution inside the Al phase. Alternatively, nanometric Mg-bearing compounds could form along the Si network and not being resolvable with the SEM. Both situations result from the high solidification rate in the AM process.

The existence of a non-equilibrium microstructure suggested by SEM investigations calls for confirmation by quantitative XRD analyses. As an example, Fig. 2.7 reports the experimental (dotted) and simulated (solid) diffraction patterns of the 1.55v-h sample. Following SEM observations, none of the experimental peaks matched with an Mg-

bearing constituent. Therefore, the simulated pattern accounts only for the Al and Si phases. The difference curve lies around the zero value and shows the excellent match between the observed and simulated patterns. Instead of the $[111]_{Al}$ being the strongest peak in the diffraction pattern, a pronounced crystallographic texture is present, with the $[200]_{Al}$ reflection being the most intense.

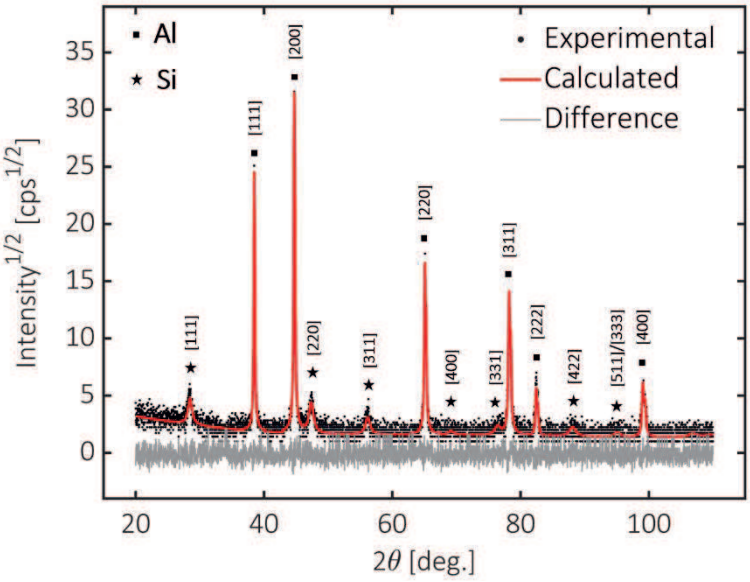

Figure 2.7. XRD analysis of the AlSi10Mg alloy: experimental and calculated patterns.

Quantitative calculations pointed out some deviations from the equilibrium conditions. A lattice parameter of 4.0498 ± 0.0040 Å was measured for the Al phase, which is slightly lower than the equilibrium one (4.0515 Å) of the AlSi10Mg alloy [21]. Additionally, Si reflections barely stand out from the background in Fig. 2.7, suggesting a reduced amount of crystalline Si with a nanometric size. Indeed, a Si weight fraction of ~8.0 ± 0.3% was calculated by full-pattern analysis. From the mass balance of the alloy with a calculated amount of Si of 9.6 wt.% (Tab. 2.1), the residual Si retained in solid solution in the α-Al phase was estimated as ~1.85 wt.%.

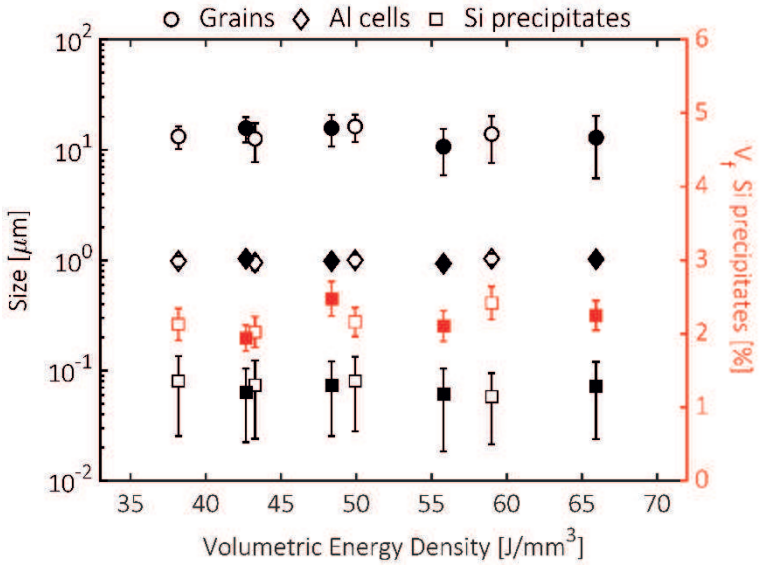

Figure 2.8. Microstructural features with different VED values. Filled and open markers correspond to hatch spacing h and 1.12h, respectively. Standard deviation is reported as error bar. The reduced standard deviation is not visible in size measurements of Al cells.

Microstructural features were quantitatively evaluated by image analysis to confirm the negligible effect of VED, and results are reported in Fig. 2.8. The logarithmic Y-axis shows that the size of microstructural features extends over two orders of magnitude, but it does not appreciably change with VED. The mean width of elongated grains and cellular dendrites is 14 ± 2 μm and 1 ± 0.05 μm, respectively. Mean ED and volumetric fraction of Si precipitates are 72 ± 8 nm and 2.2 ± 0.2 %, respectively, similarly to [22].

2.3.3 Effect of process parameters on mechanical and fracture behaviour

Figure 2.9 shows the relationship between VED and Brinell hardness, which mirrors the relationship in Fig. 2.5b. As the energy density increases, porosity significantly raises and affect the material macro-hardness. Data in Fig. 2.9 are plotted into two series (filled and open markers) as a function of *h*. At a given *h*, hardness decreases with a reduction of the *v*. Similarly, at constant *v*, hardness lowers with a reduction of *h*. As in Fig. 2.5b, the separate effect of deposition parameters can be described incorporating them in a single energy parameter, that is in a univocal relationship with the hardness.

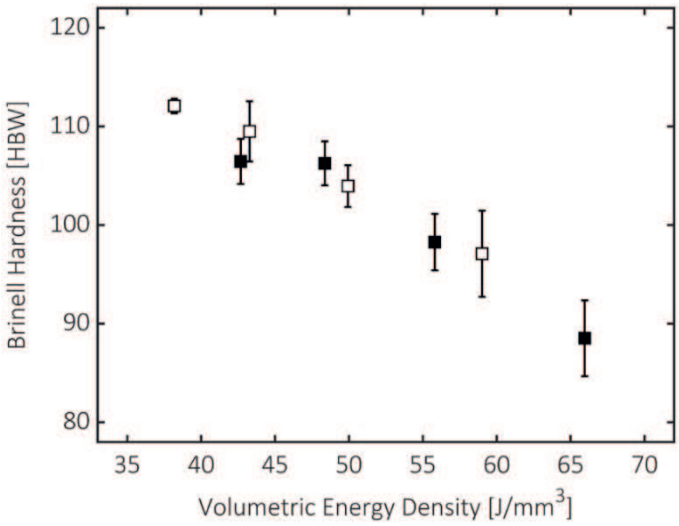

Figure 2.9. Brinell hardness of samples produced with different VED values. Filled and open markers correspond to hatch spacing h and 1.12h, respectively. Standard deviation is reported as error bar.

Figure 2.10 depicts engineering stress-strain curves of each investigated condition. Specimens produced with low v and h (v-h, v-1.12h), and thus with the highest energy density, display the worst mechanical properties. As the energy density reduces, strength and ductility progressively raise, reaching the outstanding tensile strength of ~ 500-550 MPa, and a relevant elongation of ~6 %, at the highest values of v and h (1.55v-h, 1.55v-1.12h). Similar performances were achieved just for specifically designed high-strength Al alloys [22]–[24], whereas in the literature the resistance of the AlSi10Mg alloy ranges between 350-450 MPa [1], [7], [11], [18].

Despite the different final properties, the stress-strain curves display all a similar shape. The applied stress reaches a maximum, and then abruptly falls during the strain-hardening stage, without any evidence of stress reduction. The necking stage is absent, and the alloy fails before the potential UTS is reached. True stress (σ) and strain hardening rate (Θ) are plotted as a function of the true strain (ε) in the insets in Fig. 2.10 to assess such behaviour furtherly. According to Considère's criterion [25], the necking stage starts when $\Theta = d\sigma/d\varepsilon = \sigma$, at the intersection of σ and Θ curves. Insets in Fig. 2.10 show that in almost all cases such a condition is not satisfied, even if σ and Θ values at failure are generally quite close. Similar behaviour is reported in the literature of AM produced parts [12], [26], [27], and it is generally ascribed to the high density of microstructural defects, like tangled dislocations, residual stresses and sub-micrometric

pores. However, in the current study, abrupt failure is more likely determined by keyhole pores, which overtake the effect of features mentioned above.

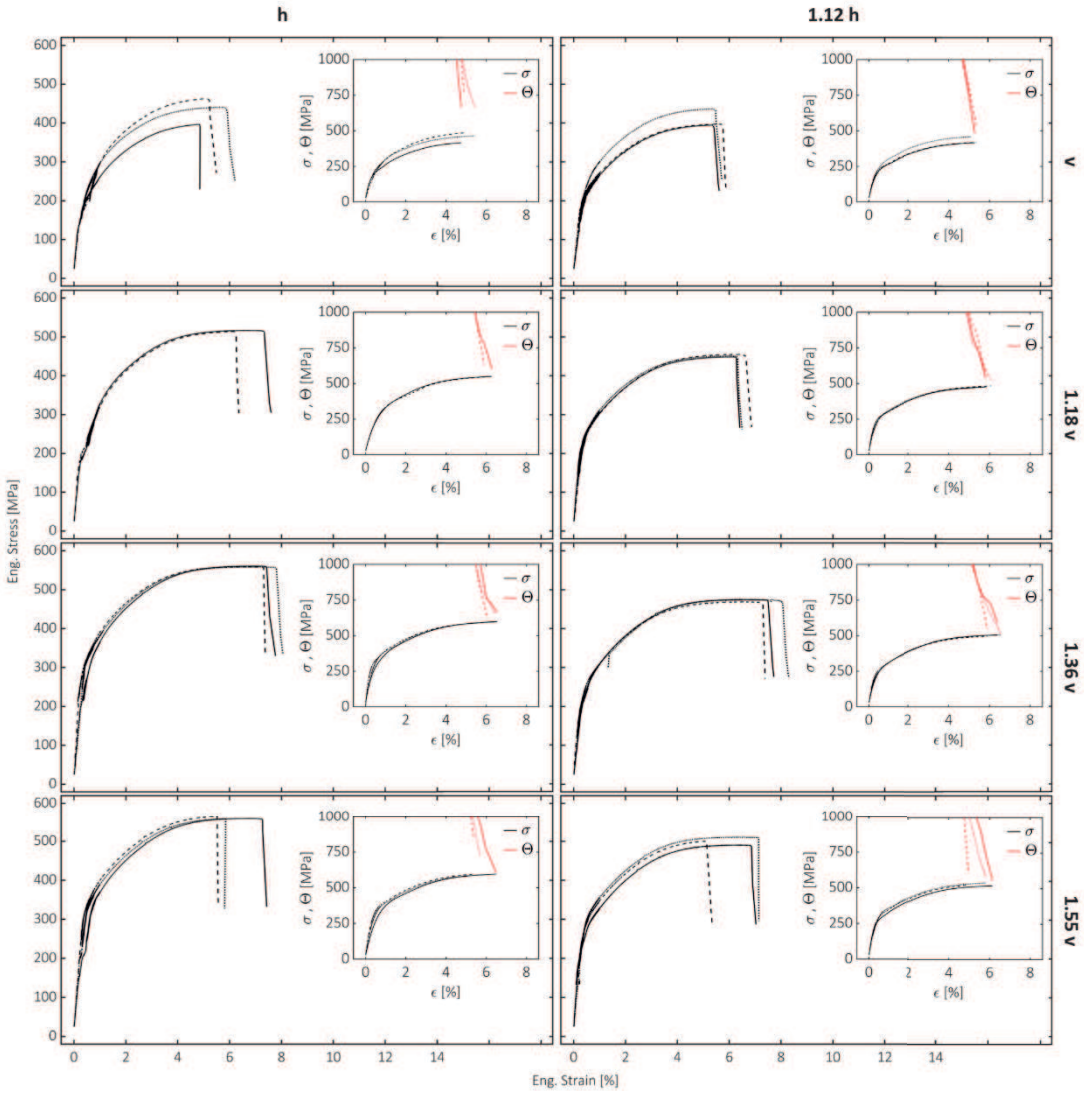

Figure 2.10. Engineering stress-strain of samples produced with different deposition parameters; insets depict the correspondent true stress-strain curve (σ) together with the strain hardening rate curve (Θ).

Figure 2.11 reports the tensile parameters as a function of adopted *v*-*h* combinations and the corresponding VED. The elastic modulus (E) reaches its maximum value of 78 ± 9 GPa at the lowest energy density of 38 J/mm^3. Similar E values are reported for a fully dense AlSi10Mg alloy [18]. It then falls about linearly to 57 ± 6 GPa as the VED increases to the maximum value of 66 J/mm^3. Other tensile parameters, yield strength (YS), ultimate tensile strength (UTS) and elongation at failure (E_f), also decrease with the energy density. Each one is reduced by ~20-25% of its maximum value. YS falls from 300-

320 MPa to 220-240 MPa and UTS from 500-550 MPa to 410-430 MPa, whereas E_f decreases from 6-6.5 % to ~5 %.

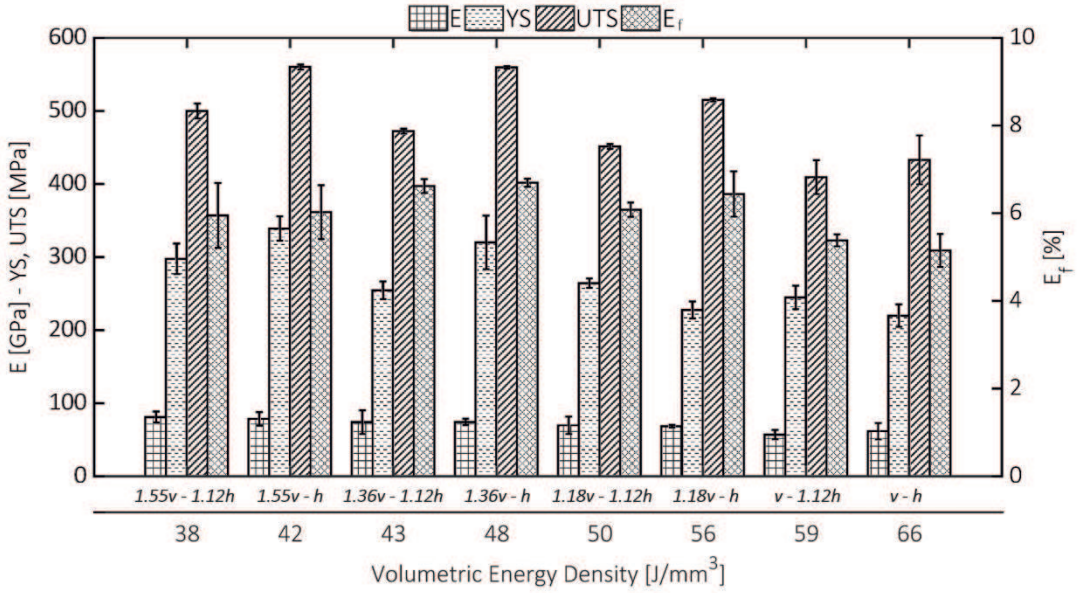

Figure 2.11. Tensile parameters of samples produced with different VED values. Standard deviation is reported as error bar.

Figure 2.11 shows that, conversely to E and hardness, specimens produced at constant v with the lowest h (h) exhibit higher properties than their counterparts (1.12 h). UTS more clearly shows such an effect, because of the higher deviations that YS and E_f suffer. A further comparison concerns samples produced with very close VED values. The 1.55v-h and 1.36v-1.12h specimens were produced with almost the same energy density (42 and 43 J/mm^3 respectively), but the former display better mechanical properties than the latter. The same observation rules for the 1.36v-h and 1.18v-1.12h specimens, realised with a VED of 48 and 50 J/mm^3, respectively.

Results of image analysis in Fig. 2.5 shows that the porosity increases as VED raises. A complementary analysis was performed on the fracture surface of tensile specimens, and results are reported in Fig. 2.12. Probability histograms depict the size distribution of pores on the fracture surfaces and confirm the results in Fig. 2.5a. At low VED, most of the pores are a few tens of μm wide, with the probability of finding large pores (ED > 100 μm) being near zero. At intermediate VED, the appearance of pores several tens of μm wide became more probable. These latter are the most probable at high VED, together with additional large pores ranging between 100-200 μm.

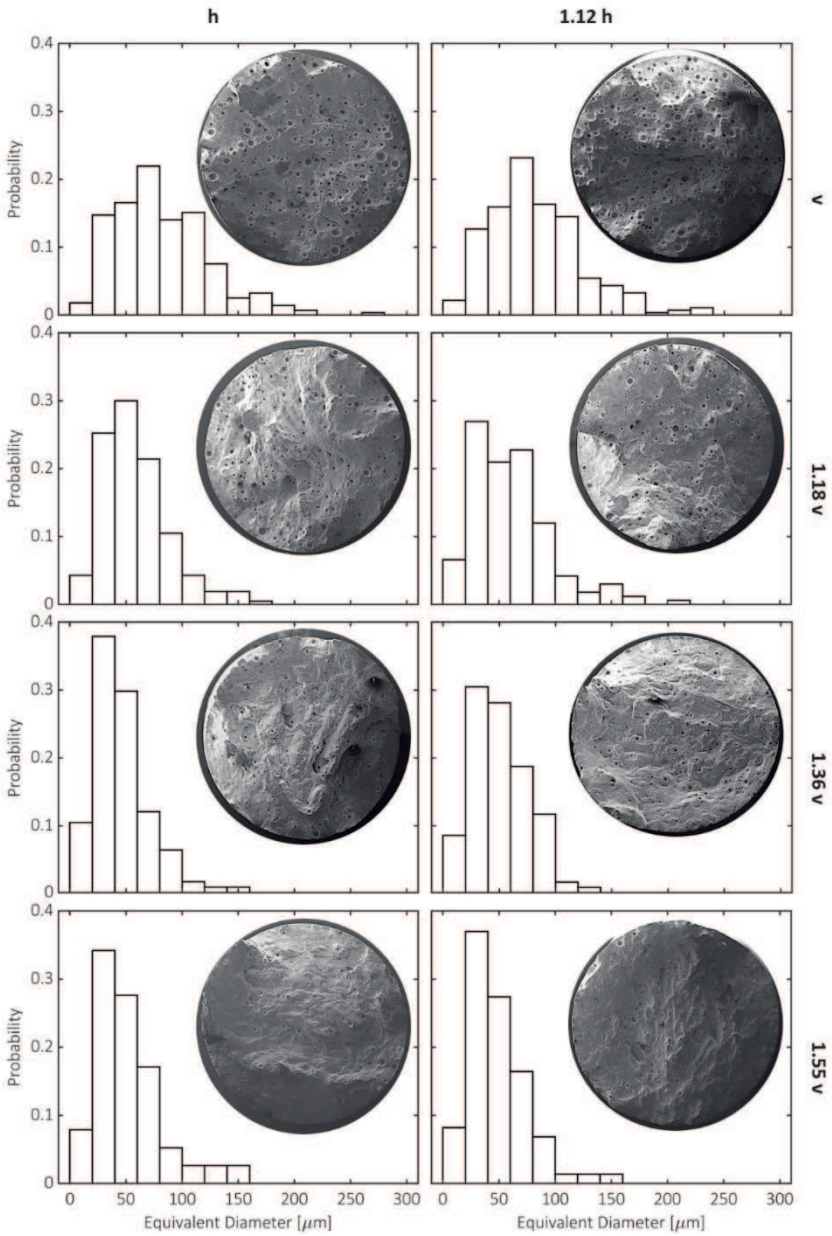

Figure 2.12. Quantitative analysis of pores on the fracture surfaces of samples produced with different VED values: probability histograms.

A comparison between Fig. 2.12 and Fig. 2.5a shows that the size range of pores on fracture surfaces and metallographic sections closely corresponds. This result suggests that tensile specimens experienced limited plasticity before failure, with the pores on the fracture surfaces otherwise being somewhat deformed. In turn, this observation matches the tensile behaviour and premature failure shown in Fig. 2.10.

A more in-depth analysis of fracture surfaces is proposed in Fig. 2.13, considering specimens produced with the lowest (Figs. 2.13a-b-c) and highest (Figs. 2.13d-e-f) energy density, respectively.

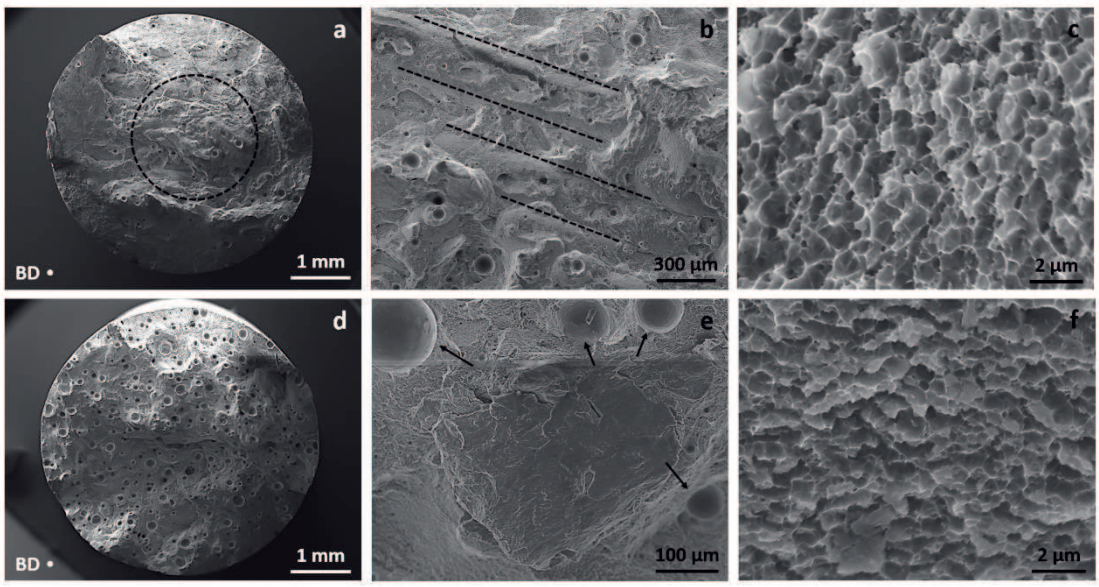

Figure 2.13. Fracture surfaces of samples process with different energy density. (a-b-c) Low and (d-e-f) high energy density. (a) Low magnification, circled area highlights elongated features. (b) Particular of the scan tracks, marked with black dotted lines. (c) High magnification, fine dimples. (d) Low magnification. (e) Particular of the pores, pointed out by black arrows. (f) High magnification, fine dimples. In (a-d), white dots on the bottom-left corner point out the building direction (BD).

Samples processed with a low VED show a limited number of small pores and several elongated features, these latter marked by a dashed circular line in Fig. 2.13a. Figure 2.13b clarifies these features to be traces of the scan tracks. Previous studies report the MPBs to be a weak microstructural feature and an easy fracture path because of the coarse and heat-affected microstructure [28]. Such a statement explains the presence of scan tracks on the fracture surface. Figure 2.13c points out that, at high magnification, the fracture surface consists of very fine dimples.

Samples produced with a high energy density show a copious number of coarse pores on the surface (Fig. 2.13d). Differently than in Figs. 2.13b, traces of scan tracks are not distinguishable in Fig. 2.13e. Pores represent a weaker feature than MPBs, and they mainly guide the fracture at a macroscopic level, making the scan track no longer detectable. Conversely, Fig. 2.13f depicts fine dimples similar to Fig. 2.13c, elucidating the same fracture mechanism at the microscale.

Fracture surfaces exhibit additional defects other than pores. These latter are typically Mg-based oxides, as reported in Figs. 2.14a-b and confirmed by the EDX spectrum in

Fig. 2.14c. Similarly to shrinkage voids (§ 2.3.1), all fracture surfaces exhibit a limited number of oxides, regardless of the adopted deposition parameters. In this light, their effect, even if deleterious, is assumed to be similar in all the investigated conditions and will not be furtherly discussed.

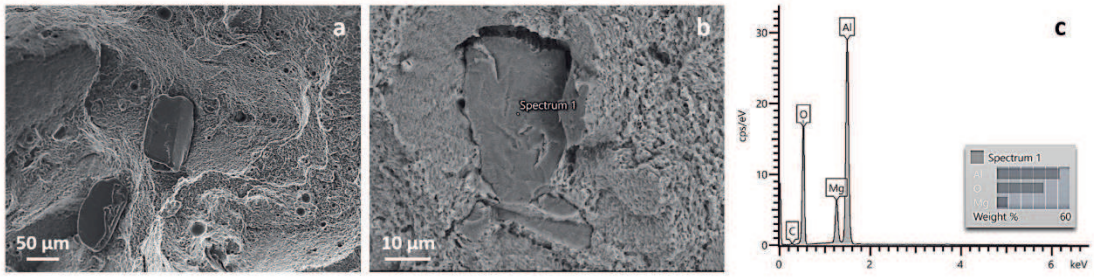

Figure 2.14. SEM images of process defects on the fracture surfaces. (a) Oxide layers. (b) Embedded oxide particle. (c) EDX spectrum of the feature showed in (b).

The fracture behaviour at the microscale was deepened analysing and comparing the fine dimples (Figs. 2.13 c-f) and the smallest microstructural features (Figs. 2.6d-e). Results are averaged among all the investigated conditions since no significant differences in the microstructural features were detected (Fig. 2.8). From Fig. 2.8, the spacing of Al cellular dendrites matches their width, and it is ~1 µm, whereas the mutual distance of Si precipitates was measured as ~210 ± 75 nm. For the ease of analysis, no distinction was made between globular and acicular precipitates, which accounts for the scatter of measurements. The mean spacing of dimples on the fracture surfaces was measured as ~270 ± 65 nm, which more closely resembles that of Si particles rather than Al cells, suggesting the formers to mainly rule the deformation behaviour at the microscale.

2.4 DISCUSSION

2.4.1 Process parameters and porosity level

OM images in Fig. 2.3 show that, in the range reported in Tab. 2.2, a decrease of either v or h promotes the formation of large round pores up to 100-200 µm wide. Density measurements (Fig. 2.5b) confirm OM observations, showing that the relative density falls from 99.3 % to ~96.5 %. Moreover, Fig. 2.5b shows that the effect of deposition parameters on density is representable as a univocal function of VED.

The L-PBF process of Al components could suffer from different kinds of porosity, usually classified in lack-of-fusion and keyhole porosity. The former depends on the incomplete powder melting, caused by a poor overlap of melting pools or by insufficient laser power. Due to their inherent nature, lack-of-fusion pores are usually irregularly-shaped [6], and do not fit with the current OM observations. Conversely, the keyhole porosity is determined by an excess of energy that the laser imparts to the powder. The resulting overheating, metal vaporisation and recoil pressure, drive the melt pool surface deep into the material to form a keyhole depression. Due to its inherent instability, it easily collapses, trapping the inert shielding gas. The resulting pore is almost spherical and located at the bottom of the melt pool [4], [5]. Pores in Fig. 2.3 are quite circular, as confirmed by Fig. 2.5b, and located in the low part of the melt pools, strongly suggesting them to be keyhole pores.

King *et al.* [29] proposed a geometrical criterion to assess the heat transfer mode during the deposition of an AISI 316L alloy. A depth-to-width ratio of the melt pool of 0.5 is the threshold between conduction (< 0.5) and keyhole (> 0.5) modes. The same criterion was adopted for Al alloys [30]. The depth-to-width ratio of melt pools of the top layer was evaluated to avoid multiple overlaps and accurately measure their size.

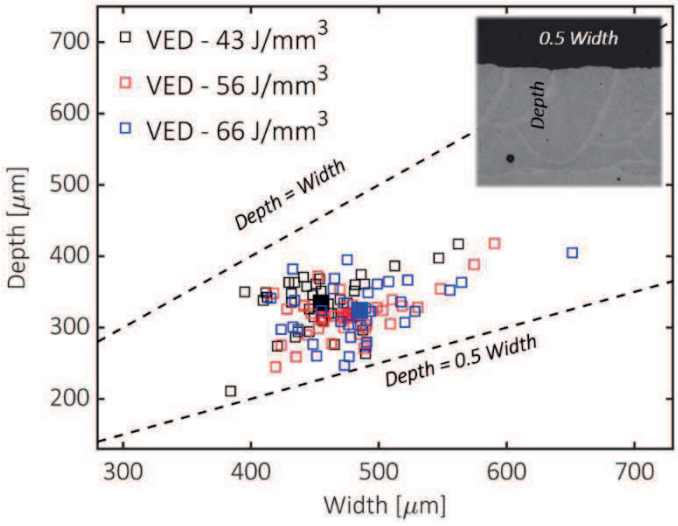

Figure 2.15. The aspect ratio of the melt pools in the top building layer of specimens produced with different VED.

Figure 2.15 summarises the results of the samples in Fig. 2.3. Data range between 0.5 and 1, with no significant effect of the VED, confirming the keyhole heat conduction mode.

Due to its inherent nature, the keyhole phenomenon mainly depends on the energy density. Such observation perfectly matches the univocal relationship in Fig. 2.5b between density and VED. In the adopted range of v and h, a VED of ~40 J/mm^3 is suitable to minimise the porosity. Any variation of v and h that increases VED just imparts an excess of energy to the material, deteriorating its properties.

2.4.2 Process parameters and microstructural features

SEM observations show the microstructure of the L-PBF produced AlSi10Mg alloy to have a hierarchical ordering (Fig. 2.6). Columnar grains grow radially and epitaxially through the melt pools (Fig. 2.6b), with their cubic {100} orientation along the building direction (Fig. 2.7). Epitaxy and strong crystallographic texture can be ascribed to the strong thermal gradients that develop during the L-PBF process [31].

Inside the grains, a fibrous Si network surrounds micrometric Al cellular dendrites (Fig. 2.6d). An estimated high cooling rate of ~10^3-10^5 K/s [22] accounts for their micrometric size, and determines the fibrous morphology of Si, accordingly to the quench modification phenomenon [32]. The high cooling rate also extends the solubility of Si inside the Al phase during the solidification. XRD analyses (Fig. 2.7) confirm such a statement measuring ~1.85 wt.% of Si retained in solid solution. A similar value was recently assessed by the 3D APT technique [33]. As the cooling proceeds, the solubility of Si falls and it is partially ejected from the Al matrix to form nanometric features (Fig. 2.6e-f-g), even if they also likely precipitate and coarsen due to the heating produced by neighbouring laser scans.

Besides the peculiar microstructure, a change of deposition parameters does not significantly affect the microstructural features. Size and morphology of these latter depend on thermal gradient G and growth rate R. The G/R ratio determines the stability of the solid/liquid front and the resulting solidification mode, while the G·R product, *i.e.* the cooling rate C_R, rules the final size of the microstructure. In steady-state conditions:

$$R = v \cdot \cos\varphi \tag{4}$$

where v is the scan speed, and φ is the angle between the growth and laser scan directions [31]. Nominally, G depends on alloy properties and energy imparted to the material, thus on building parameters. However, numerical simulations proved that P is a slightly influencing variable, whereas v has a neglecting effect [34]. Therefore, a

constant G value of 10^6 K/m is often reported [35]. The maximum *h* variation in this work is 12 % (Tab. 2.2, h - 1.12 h), and it reasonably just slightly modifies the total heat input from neighbouring scan tracks [36]. Therefore, the effect of *h* on microstructural features will be neglected in the following discussion, with G/R and G·R mainly depending on v.

Increasing v and reducing G/R, planar, cellular and dendritic structures are progressively expected. Nevertheless, the Al phase of samples produced at different v always exhibits a cellular structure (Fig. 2.6d). Likely, the high G prevents the increasing v from changing the solidification mode. Similarly, the size of microstructural features does not change significantly with v, and G·R. A typical relationship between the size of cellular dendrites and C_R is:

$$\lambda = a \cdot (C_R)^{-n} = a \cdot (G \cdot R)^{-n} \quad (5)$$

where λ [μm] is the cell size for cellular growth, a [μm·s/K] is a proportional constant, C_R [K/s] is the cooling rate, and n is a dimensionless exponent ranging between 0.32-0.38, often assumed as 0.33 [37]. The maximum v variation in this work is 55 % (Tab. 2.2, v-1.55 v). Applying (5), the maximum size difference of Al dendrites is ~13 %, which reasonably falls in the experimental uncertainty of the size measurement. Similar considerations extend to the other microstructural features, like elongated grains and Si precipitates, and explain why no significant differences were found among the investigated alloys.

Summarising, small variations of v and *h* do not alter the microstructural features but remarkably affects the alloy density. This trend is advantageous for engineering purposes because where the process is to be optimised for defect reduction (as in the present study) or productivity maximisation, deposition parameters can be changed without affecting the microstructural features. Clearly, out of a proper process window defined by VED, mechanical properties suffer from the increasing porosity. However, some relevant considerations hide behind this somewhat trivial result, as will be elucidated in the following discussion.

2.4.3 Limitations of VED as a reliable design parameter

In this work, a VED of ~40 J/mm^3 is suitable to minimise the porosity level. Additionally, the density reduction with any variation of v and *h* is fully described by VED (Fig. 2.5b). In this light, the energy density-based approach seems a valuable tool

to define a proper process window of deposition parameters. However, Fig. 2.16a highlights a different situation. According to literature data, the relative density of the AlSi10Mg alloy uniformly distributes between 98-100 % with VED ranging between 30-110 J/mm^3. In this work (red markers in Fig. 2.16a), porosity steeply increases within the VED range of 40-70 J/mm^3. Even if not available, any additional increment beyond 70 J/mm^3 likely would further deteriorate density. Thus, a significantly different amount of porosity is achievable at the same VED, which severely limits its applicability in the industrial field to determine suitable deposition parameters. Such an outcome stems from the simplicity of equation (1): it comprehends just a few of the assessable process parameters, it does not account for the material properties and for the physical events that characterise the kinetic of solidifying melt pools. Therefore, a mere energy density-based approach cannot capture the complexity of the L-PBF process, with the effect of individual deposition parameters that cannot be neglected.

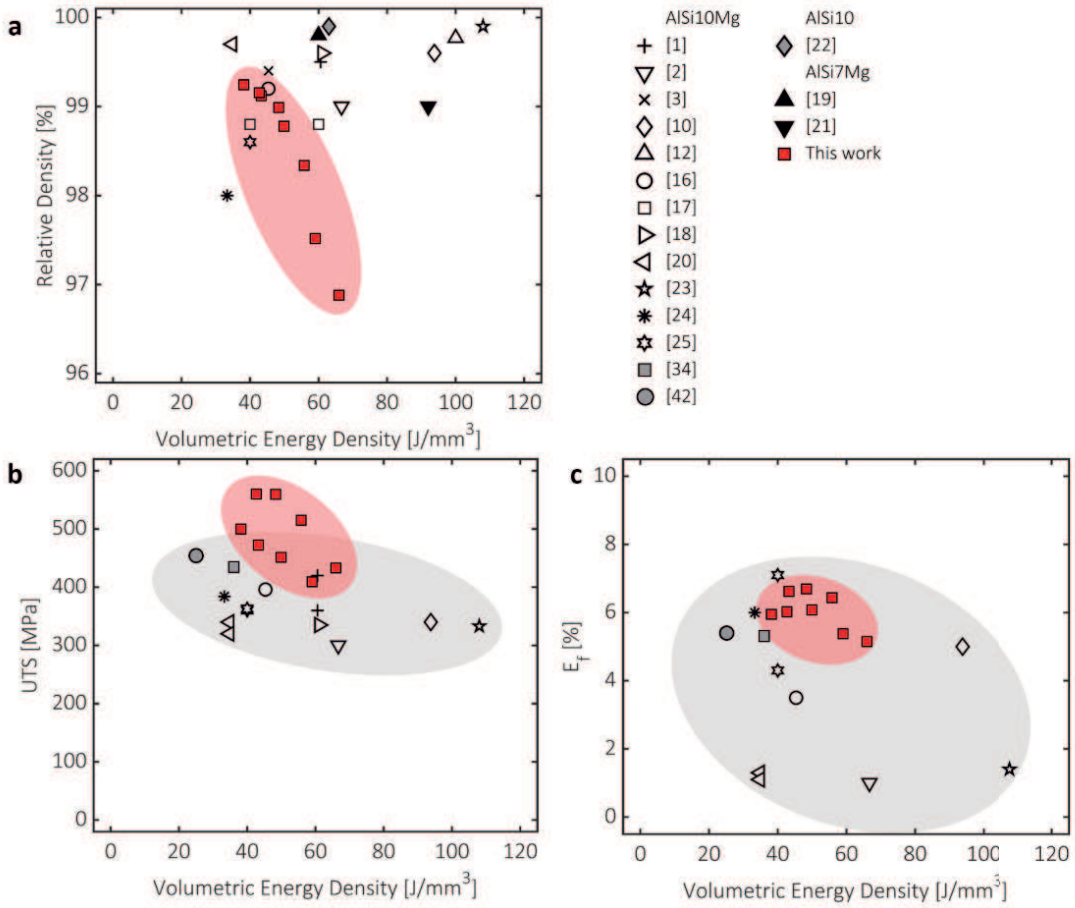

Figure 2.16. Comparison of literature data for the AlSi10Mg alloy (grey clouds) with results from this work (red clouds) as a function of VED. (a) Relative density. (b) UTS. (c) E_f.

Figures 2.9-2.10 show that tensile properties decrease as VED increases, according to the raised amount of porosity. However, samples produced at almost equal VED have a close porosity (Fig. 2.5b) and different mechanical response. For instance, comparing 1.55v-h and 1.36v-1.12h specimens (42 and 43 J/mm^3, respectively) and 1.36v-h and 1.18v-1.12h specimens (48 and 50 J/mm^3, respectively), porosity differs less than 0.2 %, whereas UTS differs ~100 MPa. In both cases, the specimen realised with the lowest h shows superior mechanical properties, in agreement with [38]. Such an effect is ascribed to the higher geometrical overlapping between adjacent tracks, which provides a better material consolidation. This finding suggests that process parameters exert additional effects not taken into account by the energy density-based approach. For industrial purposes, this limitation possibly leads to define the best combination of deposition parameters erroneously.

Figures 2.16b-c compare the present tensile results with available literature data. In the 30-110 J/mm^3 range of VED, UTS of the AlSi10Mg alloy lies between 300-400 MPa, with few exceptions up to 450 MPa [26], [39], whereas E_f ranges between 1-6 %. As highlighted by red markers in Figs. 2.16b-c, samples in this work show a systematically higher UTS (400-500 MPa), preserving a considerable E_f (5-6.5%). These latter values are surprising, given the significant amount of porosity of investigated samples (up to 3.5%) and their vertical building orientation. Vertically built specimens generally show worse tensile properties, particularly E_f, than horizontally built ones [1], [11], [15]. The corresponding values occupy the bottom part of Fig. 2.16c.

The outstanding strength reached in this study could be ascribed to the hierarchical structure of the alloy (Fig. 2.6). It exploits all the strengthening mechanisms of metallic materials, namely internal friction, Hall-Petch, Orowan, Taylor, solid solution and load-bearing mechanisms, with the corresponding relationships reported, in this order, as follows:

$$YS_{est.} = [\sigma_0] + \left[\frac{k}{\sqrt{d_{cell}}} + \frac{k}{\sqrt{d_{grain}}}\right] + \left[\frac{\varphi G b}{d_{Si.p}}\left(\frac{6V_{Si.p}}{\pi}\right)^{1/3}\right] + \left[\beta M G b\sqrt{\rho_d}\right] + \left[HC_{Si}{}^{N}\right] + [1.5\sigma_i V_{Si.eu}] \quad (6)$$

where σ_0 is the internal friction (72 MPa, [40]), k (40 MPa·μm$^{0.5}$, [22]), φ (~2, [22]), β (0.16, [41]), H (~13 MPa·at.%$^{-1}$, [42]), N (1, [42]) are a material constants, d_{cell} (1 ± 0.05 μm) and d_{grain} (14 ± 2 μm) are widths of Al cells and elongated grains, G (27000 MPa) and b

(0.286 nm) are shear modulus and Burger vector of the Al phase, $d_{Si.p}$ (72 ± 8 nm) and $V_{Si.p}$ (0.022 ± 0.002) are size and volumetric fraction of Si precipitates, M is the Taylor factor of FCC crystals (3.06, [26]), ρ_d is the dislocation density ($3.05 \cdot 10^{14}$ m^{-2}, [43]), C_{Si} is the solid solution Si (~1.8 ± 0.3 at.%), σ_i is the bonding strength of the Al/Si interface (240 MPa, [44]), and $V_{Si.eu}$ is the volumetric fraction of eutectic Si. This latter value is calculated as the difference between total crystalline Si (0.091 ± 0.004, from XRD results) and Si precipitates. Applying (6), individual reinforcement contributions are calculated as 72, 63, 75, 66, 23 and 25 MPa, which shows the relevant role of Al cells and Si precipitates to the alloy strength. The estimated yield strength $YS_{est.}$ is 325 ± 10 MPa, which very well matches YS of 1.55v-h and 1.55v-1.12h samples, and thus correspond to the strength of the almost dense material. In this light, the contribution of porosity Φ [%] to strength loss can be estimated as ~40 MPa· Φ^{-1} from data in Fig. 6. The harmful effect of pores is much pronounced compared to the strengthening effect of microstructural features, which suggest the importance of using optimised process parameters.

Preservation of a high E_f despite the increasing porosity stems from the microscale fracture behaviour. In dense specimens, MPBs represent the weakest fracture path (Figs. 2.12a-b), whereas keyhole pores substitute them in porous specimens (Figs. 2.12d-e). Despite such difference at the macroscale, similar fine dimples form during the deformation stage at the microscale (Fig. 2.12c-f). Quantitative analyses show that they are ~270 nm spaced (Fig. 2.14) similarly to Si precipitates (210 nm), from which they likely nucleate and grow. During the deformation stage, they provide plenty of additional sites for strain localisation other than large keyhole pores, avoiding these latter to cause an excessive damage accumulation and enhancing a ductile behaviour [45]. As a consequence, E_f limitedly suffers from the increased porosity, and moderately falls from 6.5 % to 5 %. A further reason of the relevant ductility is the lack of defects other than pores, like unmelted powder particles, shrinkage voids (Fig. 2.4) and oxides (Fig. 2.13). Such features are sometimes reported in L-PBF produced Al alloys [1], [2], [11] and would remarkably reduce tensile properties. It is worth to note that, despite the relevant ductility, tensile curves in Fig. 2.9 show that all samples prematurely fail before the necking stage. Keyhole pores and possible additional defects, such as densely tangled dislocations and residual stresses, likely explain such behaviour.

The analysis above-reported shows that VED is not a reliable parameter to estimate the tensile properties of the L-PBF produced AlSi10Mg alloy. The energy density-based approach accounts for the effect of deposition parameters on porosity but lacks in considering their impact on the microstructural features, which also determine the final mechanical performance.

2.5 CONCLUSION

The present research starts from the industrial purpose of determining a suitable combination of printing parameters of the L-PBF produced AlSi10Mg alloy. In light of density and tensile properties optimisation, the energy density-based design approach was tested, producing specimens within a literature-suggested VED range. Results highlight some significant limitations of such an approach and enable to draw the following conclusions:

- A limited variation of process parameters remarkably affects the alloy density but has a negligible effect on the microstructural features. This is an advantage where the process is to be optimised for defect reduction or productivity maximisation.
- The VED range suggested in the literature does not necessarily lead to dense parts, with the present specimens showing up to 3.5 % of porosity. VED cannot predict the final density of L-PBF produced parts, and the effect of individual deposition parameters is to be taken into account.
- The almost dense material shows outstanding tensile properties. The strengthening contribution of each microstructural feature was estimated to assess its individual effect on material strength. Results well match experimental tensile properties and show that Al cells and Si precipitates provide the primary reinforcement. However, even a limited porosity dramatically reduces material strength and overtakes the contribution of microstructure.
- VED just roughly estimates the effect of deposition parameters on the amount of energy imparted to the powder bed. Conversely, it does not account for their effect on the microstructural features and fails in predicting the final properties of the alloy.
- As currently defined, the use of VED guarantees neither the selection of suitable deposition parameters nor the optimisation of material properties. Hence, it cannot be intended as a reliable design parameter.

REFERENCES

[1] P. Wei *et al.*, *The AlSi10Mg samples produced by selective laser melting: single track, densification, microstructure and mechanical behavior*, Appl. Surf. Sci., vol. **408**, pp. 38–50, 2017

[2] S. Siddique, M. Imran, E. Wycisk, C. Emmelmann, and F. Walther, *Influence of process-induced microstructure and imperfections on mechanical properties of AlSi12 processed by selective laser melting*, J. Mater. Process. Technol., vol. **221**, pp. 205–213, 2015

[3] N. T. Aboulkhair, N. M. Everitt, I. Ashcroft, and C. Tuck, *Reducing porosity in AlSi10Mg parts processed by selective laser melting*, Addit. Manuf., vol. **1**, pp. 77–86, 2014

[4] A. A. Martin *et al.*, *Dynamics of pore formation during laser powder bed fusion additive manufacturing*, Nat. Commun., vol. **10**, no. 1, 2019

[5] M. Bayat *et al.*, *Keyhole-induced porosities in Laser-based Powder Bed Fusion (L-PBF) of Ti6Al4V: High-fidelity modelling and experimental validation*, Addit. Manuf., vol. **30**, no. April, p. 100835, 2019

[6] G. Kasperovich, J. Haubrich, J. Gussone, and G. Requena, *Correlation between porosity and processing parameters in TiAl6V4 produced by selective laser melting*, Mater. Des., vol. **105**, pp. 160–170, 2016

[7] K. Kempen, L. Thijs, J. Van Humbeeck, and J. P. Kruth, *Processing AlSi10Mg by selective laser melting: Parameter optimisation and material characterisation*, Mater. Sci. Technol. (United Kingdom), vol. **31**, no. 8, pp. 917–923, 2015

[8] M. Krishnan *et al.*, *On the effect of process parameters on properties of AlSi10Mg parts produced by DMLS*, Rapid Prototyp. J., vol. **20**, no. 6, pp. 449–458, 2014

[9] R. K. Shah and P. P. Dey, *Process parameter optimization of dmls process to produce AlSi10Mg components*, J. Phys. Conf. Ser., vol. **1240**, no. 1, pp. 1–9, 2019

[10] T. Kimura and T. Nakamoto, *Microstructures and mechanical properties of A356 (AlSi7Mg0.3) aluminum alloy fabricated by selective laser melting*, Mater. Des., vol. **89**, pp. 1294–1301, 2016

[11] N. Read, W. Wang, K. Essa, and M. M. Attallah, *Selective laser melting of AlSi10Mg alloy: Process optimisation and mechanical properties development*, Mater. Des., vol. **65**, pp. 417–424, 2015

[12] N. T. Aboulkhair, I. Maskery, C. Tuck, I. Ashcroft, and N. M. Everitt, *The microstructure and mechanical properties of selectively laser melted AlSi10Mg: The effect of a conventional T6-like heat treatment*, Mater. Sci. Eng. A, vol. **667**, pp. 139–146, 2016

[13] N. E. Uzan, R. Shneck, O. Yeheskel, and N. Frage, *Fatigue of AlSi10Mg specimens fabricated by additive manufacturing selective laser melting (AM-SLM)*, Mater. Sci. Eng. A, vol. **704**, no. August, pp. 229–237, 2017

[14] Z. H. Xiong, S. L. Liu, S. F. Li, Y. Shi, Y. F. Yang, and R. D. K. Misra, *Role of melt pool boundary condition in determining the mechanical properties of selective laser melting AlSi10Mg alloy*, Mater. Sci. Eng. A, vol. **740–741**, no. April 2018, pp. 148–156, 2019

[15] E. Brandl, U. Heckenberger, V. Holzinger, and D. Buchbinder, *Additive manufactured AlSi10Mg samples using Selective Laser Melting (SLM): Microstructure, high cycle fatigue, and fracture behavior*,

Mater. Des., vol. **34**, pp. 159–169, 2012

[16] Y. Bai, Y. Yang, Z. Xiao, M. Zhang, and D. Wang, *Process optimization and mechanical property evolution of AlSiMg0.75 by selective laser melting*, Mater. Des., vol. **140**, pp. 257–266, 2018

[17] T. Kimura, T. Nakamoto, M. Mizuno, and H. Araki, *Effect of silicon content on densification, mechanical and thermal properties of Al-xSi binary alloys fabricated using selective laser melting*, Mater. Sci. Eng. A, vol. **682**, no. November 2016, pp. 593–602, 2017

[18] *Material Data Sheet: EOS Aluminium AlSi10Mg*, 2014

[19] C. A. Schneider, W. S. Rasband, and K. W. Eliceiri, *NIH Image to ImageJ: 25 years of image analysis*, Nat. Methods, vol. **9**, pp. 671–675, 2012

[20] L. Lutterotti, H. R. Wenk, and S. Matthies, *MAUD (Material Analysis Using Diffraction): a user friendly Java program for Rietveld Texture Analysis and more*, in *ICOTOM-12.*, 1999, pp. 1599–1604

[21] S. Marola *et al.*, *A comparison of Selective Laser Melting with bulk rapid solidification of AlSi10Mg alloy*, J. Alloys Compd., vol. **742**, pp. 271–279, 2018

[22] X. P. Li *et al.*, *Selective laser melting of nano-TiB2decorated AlSi10Mg alloy with high fracture strength and ductility*, Acta Mater., vol. **129**, pp. 183–193, 2017

[23] R. Casati, M. Coduri, M. Riccio, A. Rizzi, and M. Vedani, *Development of a high strength Al–Zn–Si–Mg–Cu alloy for selective laser melting*, J. Alloys Compd., vol. **801**, pp. 243–253, 2019

[24] Q. Jia, P. Rometsch, S. Cao, K. Zhang, and X. Wu, *Towards a high strength aluminium alloy development methodology for selective laser melting*, Mater. Des., vol. **174**, p. 107775, 2019

[25] G. E. Dieter and D. J. Bacon, *Mechanical Metallurgy*. 1986

[26] B. Chen *et al.*, *Strength and strain hardening of a selective laser melted AlSi10Mg alloy*, Scr. Mater., vol. **141**, pp. 45–49, 2017

[27] Z. Wang *et al.*, *Premature failure of an additively manufactured material*, NPG Asia Mater., vol. **12**, no. 1, 2020

[28] I. Rosenthal, A. Stern, and N. Frage, *Strain rate sensitivity and fracture mechanism of AlSi10Mg parts produced by Selective Laser Melting*, Mater. Sci. Eng. A, vol. **682**, no. November 2016, pp. 509–517, 2017

[29] W. E. King *et al.*, *Observation of keyhole-mode laser melting in laser powder-bed fusion additive manufacturing*, J. Mater. Process. Technol., vol. **214**, no. 12, pp. 2915–2925, 2014

[30] N. T. Aboulkhair, I. Maskery, C. Tuck, I. Ashcroft, and N. M. Everitt, *On the formation of AlSi10Mg single tracks and layers in selective laser melting: Microstructure and nano-mechanical properties*, J. Mater. Process. Technol., vol. **230**, pp. 88–98, 2016

[31] L. Thijs, K. Kempen, J. P. Kruth, and J. Van Humbeeck, *Fine-structured aluminium products with controllable texture by selective laser melting of pre-alloyed AlSi10Mg powder*, Acta Mater., vol. **61**, no. 5, pp. 1809–1819, 2013

[32] S. Khan and R. Elliott, *Quench modification of aluminium-silicon eutectic alloys*, J. Mater. Sci., vol. **31**, no. 14, pp. 3731–3737, 1996

[33] T. Maeshima and K. Oh-ishi, *Solute clustering and supersaturated solid solution of AlSi10Mg alloy fabricated by selective laser melting*, Heliyon, vol. **5**, no. 2, p. e01186, 2019

[34] Y. Li and D. Gu, *Parametric analysis of thermal behavior during selective laser melting additive manufacturing of aluminum alloy powder*, Mater. Des., vol. **63**, pp. 856–867, 2014

[35] H. Qin, Q. Dong, V. Fallah, and M. R. Daymond, *Rapid Solidification and Non-equilibrium Phase Constitution in Laser Powder Bed Fusion (LPBF) of AlSi10Mg Alloy: Analysis of Nano-precipitates, Eutectic Phases, and Hardness Evolution*, Metall. Mater. Trans. A Phys. Metall. Mater. Sci., vol. **51**, no. 1, pp. 448–466, 2020

[36] A. B. Spierings, K. Dawson, P. J. Uggowitzer, and K. Wegener, *Influence of SLM scan-speed on microstructure, precipitation of Al3Sc particles and mechanical properties in Sc- and Zr-modified Al-Mg alloys*, Mater. Des., vol. **140**, pp. 134–143, 2018

[37] D. Bouchard and J. S. Kirkaldy, *Scaling of intragranular dendritic microstructure in ingot solidification*, Metall. Mater. Trans. B Process Metall. Mater. Process. Sci., vol. **27**, no. 1, pp. 101–113, 1996

[38] M. Tang and P. C. Pistorius, *Anisotropic Mechanical Behavior of AlSi10Mg Parts Produced by Selective Laser Melting*, Jom, vol. **69**, no. 3, pp. 516–522, 2017

[39] W. Li *et al.*, *Effect of heat treatment on AlSi10Mg alloy fabricated by selective laser melting: Microstructure evolution, mechanical properties and fracture mechanism*, Mater. Sci. Eng. A, vol. **663**, pp. 116–125, 2016

[40] E. Ghassemali, M. Riestra, T. Bogdanoff, B. S. Kumar, and S. Seifeddine, *Hall-Petch equation in a hypoeutectic Al-Si cast alloy: Grain size vs. secondary dendrite arm spacing*, Procedia Eng., vol. **207**, pp. 19–24, 2017

[41] A. Hadadzadeh, B. S. Amirkhiz, and M. Mohammadi, *Contribution of Mg2Si precipitates to the strength of direct metal laser sintered AlSi10Mg*, Mater. Sci. Eng. A, vol. **739**, no. August 2018, pp. 295–300, 2019

[42] Q. Zhao and B. Holmedal, *The effect of silicon on the strengthening and work hardening of aluminum at room temperature*, Mater. Sci. Eng. A, vol. **563**, no. October 2017, pp. 147–151, 2013

[43] A. Hadadzadeh, B. S. Amirkhiz, A. Odeshi, and M. Mohammadi, *Dynamic loading of direct metal laser sintered AlSi10Mg alloy: Strengthening behavior in different building directions*, Mater. Des., vol. **159**, pp. 201–211, 2018

[44] S. Xia, Y. Qi, T. Perry, and K. S. Kim, *Strength characterization of Al/Si interfaces: A hybrid method of nanoindentation and finite element analysis*, Acta Mater., vol. **57**, no. 3, pp. 695–707, 2009

[45] L. Zhao, J. G. Santos Macías, L. Ding, H. Idrissi, and A. Simar, *Damage mechanisms in selective laser melted AlSi10Mg under as built and different post-treatment conditions*, Mater. Sci. Eng. A, vol. **764**, pp. 1–25, 2019

CHAPTER 3

IMPACT PROPERTIES AND HEAT TREATMENTS: PRELIMINARY STUDIES

The present chapter deals with preliminary studies covering the effect of heat treatments on microstructure and impact behaviour of an L-PBF produced AlSi10Mg alloy. Samples were subjected to standard T6-like heat treatments with different holding times, with and without the hot isostatic pressing, and compared to the as-built samples. The aim is to assess the efficacy of casting-derived heat treatment routes on the high-strain rate mechanical behaviour and provide insights to optimise further the heat treatment.

3.1 HIGH-STRAIN RATE BEHAVIOUR OF L-PBF PRODUCED Al ALLOYS

3.1.1 Additional background and purpose of the work

AM produced Al components mainly find application in the automotive, aerospace and marine fields. Accordingly, besides static properties reported in Chapter 1, the published literature of AM produced Al alloys is plentiful of studies concerning the fatigue behaviour [1]–[4]. However, additional properties such as impact toughness and absorbed energy are fundamental material requirements. A few examples comprehend vehicles requiring structural crashworthiness as well as welded Al components. In this light, a brief overview of the high-strain rate deformation behaviour restricted to the AlSi10Mg alloy will be given.

Rosenthal *et al.* [5] performed tensile tests at different strain rates between 10^{-6} s^{-1} (quasi-static test) and 10^{-1} s^{-1}. The tensile strength and strain hardening exponent linearly increase, and elongation to failure reduces, respectively, as the strain rate raises, whereas the yield strength appears rather insensitive. Zaretsky *et al.* [6] extended the results of [5] using planar impact experiments to cover strain rates between 10^{4} s^{-1} and 10^{5} s^{-1}. They found that the flow stress dependence on the strain rate increases at very high strain rates compared to [5], identifying two regimes of plastic deformation. An inherent brittle fracture behaviour characterises the alloy at very high (> 10^{4} s^{-1}) strain rates. High-strain rate (750 s^{-1}) in-situ tensile tests were performed by Parab *et al.* [7] by synchrotron X-ray

phase-contrast imaging. They revealed a crack speed of the L-PBF produced specimen three times larger than its casting counterpart and ascribed it to the high porosity level, metastable microstructure and residual stresses [7].

Available studies typically lack in assessing the role of microstructure in high-strain rate experiments. Hadadzadeh *et al.* [8]–[11] filled this gap using a Split Hopkinson Pressure Bar apparatus. Figure 3.1 summarizes the evolution of grain structure at 1400 s^{-1} and 3200 s^{-1} strain rates [8].

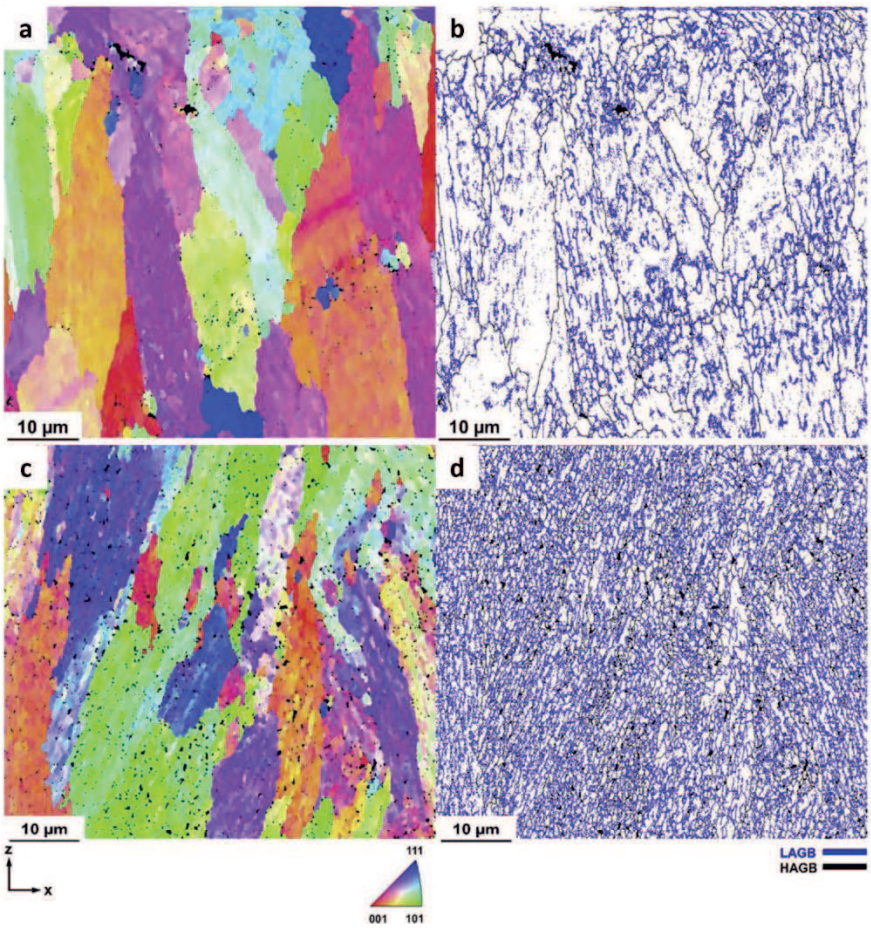

Figure 3.1. Evolution of grain structure at high strain rates of an L-PBF produced AlSi10Mg alloy, EBSD images. (a)-(c) Inverse pole figure-Z (IPF-Z) colour maps. (b)-(d) Grain boundary (GB) maps showing low- and high-angle grain boundaries (LAGBs and HAGBs, respectively). (a)-(b) Specimen deformed at 1400 s^{-1}. (c)-(d) Specimen deformed at 3200 s^{-1}. Adapted with permission from Ref. [8].

Black and blue lines indicate high- and low-angle grain boundaries (HAGBs, LAGBs), respectively, with the threshold being a misorientation angle of 15°. HAGBs in the grain boundary maps (Figs. 3.1b-d) delimit coloured elongated grains in the inverse pole

figure (IPF) maps (Figs. 3.1a-c). Regardless of the strain rate, micrometric grains are not affected by the impact loading, and the starting morphological and crystallographic textures are retained.

Conversely, an intricated substructure of LAGBs evolves. The subgrain structure is just partial developed at 1400 s^{-1} (Fig. 3.1b) and well developed at 3200 s^{-1} (Fig. 3.1d), with the fraction of LAGBs being higher in the second case. During dynamic loading, the higher the strain rate, the more dislocations are developed and arranged into dislocation networks, leading to greater stored deformation energy. This latter, together with the heat generation that increases the specimen temperature, accomplishes for the dynamic recovery. Rearrangement of dislocation into LAGBs and dynamic recovery induce nanometric subgrains within the micrometric grains [8], which contributes to materials strength by the Hall-Petch effect.

Beside interacting together, dislocations interact with the eutectic Si network and Si precipitates, as illustrated in Fig. 3.2 [9]. BF-STEM image in Figs. 3.2a depicts the microstructure deformed at 1680 s^{-1}, with LAGBs and dislocation network forming the subgrain structure described in Fig. 3.1. EDX maps (Fig. 3.2b to Fig. 3.2e) show that dislocation motion is hindered by cell boundaries and pinned by Si precipitates through Hall-Petch and Orowan mechanisms, respectively. Hindered dislocations pile-up at Si walls and Si precipitates, forming irregular and hexagonal dislocation networks [8].

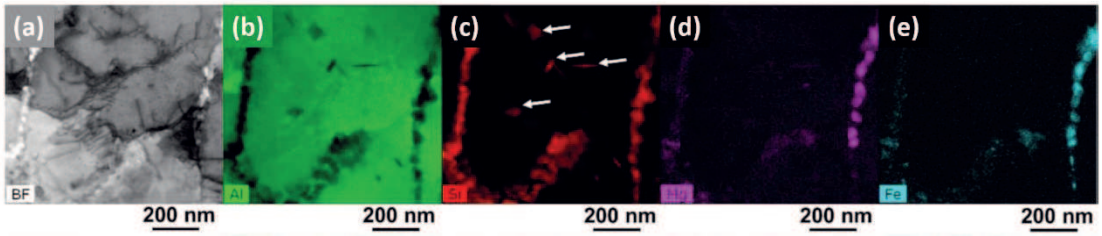

Figure 3.2. Microstructural evolution and contribution of nanometric precipitates of an L-PBF produced AlSi10Mg alloy deformed at 1680 s^{-1}. (a) BF-STEM image. (b) to (e) EDX elemental mapping. All images were taken with the beam direction along the Al [011] zone axis. Adapted with permission from Ref. [9].

In agreement with [5], the compressive strength of the as-built alloy increases with the strain rate [8]. However, complex microstructural phenomena occur varying the strain rates. Up to 1400 s^{-1} of strain rate, the dynamic loading leads to new dislocations, the evolution of accumulated dislocation networks and just a limited dynamic recovery.

As a result, the material monotonously strain hardens up to the peak flow stress. Above 1600 s^{-1}, the excess of generated dislocation promotes dynamic recovery. Stored energy is released by dislocations annihilation and rearrangement to form a LAGBs network, resulting in a material softening. As the dynamic recovery is completed, new dislocations form and the alloy again strain hardens. The resulting stress-strain curve displays more than one peak flow stress [8].

Beside notions reported above, scientific studies regarding high-strain rate properties of L-PBF processed Al alloys are limited, and none of them concerns heat treatments. In this light, the current Chapter 3 and the following Chapter 4 deal with the impact properties of the AlSi10Mg alloy in different heat treatment conditions. In particular, the present chapter covers the preliminary studies of a research collaboration activity with the University of Brescia. The aim is to assess the effect of casting-derived heat treatment routes on microstructure and Charpy impact properties of an L-PBF produced AlSi10Mg alloy. The present results pave the way to the next Chapter 4.

3.2 MATERIALS AND EXPERIMENTAL PROCEDURE

3.2.1 Samples production and heat treatments

Impact strength specimens (12 × 12 × 57 mm^3) were produced by the L-PBF technology using an EOS M290 system (400 W, Yb laser fibre; F-theta lens; 30 A and 400 V power supply; 7000 hPa, 20 m^3/h inert gas supply; 100 μm focus diameter; EOS GmbH Electro-Optical System; other parameters cannot be disclosed). They were realised both vertically (Z) and horizontally (XY) to the building platform, as depicted in Fig. 3.3a.

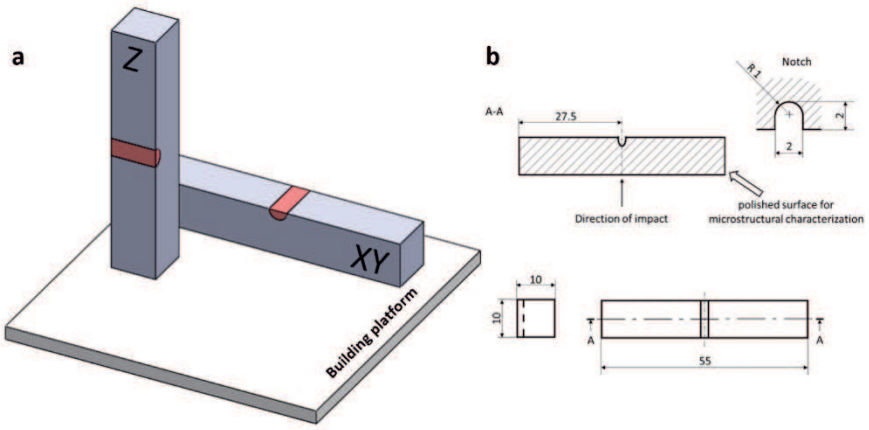

Figure 3.3. (a) The orientation of Charpy samples to the building platform and corresponding U-notch. (b) Diagram of Charpy sample geometry.

A commercial EOS Aluminium AlSi10Mg powder was processed in a protective Ar atmosphere. The chemical composition of samples measured by optical emission spectrometry is reported in Tab. 3.1.

Table 3.1. Chemical composition (wt. %) of the AlSi10Mg alloy samples produced by L-PBF.

Si	**Mg**	**Fe**	**Mn**	**Cu**	**Al**
10.245 ± 0.091	0.396 ± 0.001	0.213 ± 0.002	< 0.002	< 0.002	balance

Specimens were tested in as-built and T6 heat-treated conditions, with short and long solution times, and the corresponding parameters were selected based on previous studies [12], [13]. During solution and ageing treatments, the temperature was monitored by a Delta Hom HD 2128.1 thermocouple. Quenching was performed in water at 65 °C. Additionally, some specimens were subjected to HIP before long time solution heat treatment (SHT) to reduce the porosity. Designation and parameters of the heat treatment conditions are listed in Tab. 3.2.

Table 3.2. Designation and details of the heat treatment routes.

Designation	HIP	Solution heat treatment (+ water quench at 65 °C)	Ageing
as-built	-	-	-
$T6_{short}$	-	540 °C, 1 h	180 °C, 2 h
$T6_{long}$	-	540 °C, 9h	160 °C, 4 h
HIP + $T6_{long}$	520 °C, 2 h, 100 MPa	540 °C, 9h	160 °C, 4 h

After heat treatment, impact strength specimens were machined to the standard size of U-notched Charpy samples (10 × 10 × 55 mm^3) reported in Fig. 3.3b, in accordance with the ASTM E23 standard. In Fig. 3.3a, the position of the U-notch is also shown for both horizontal and vertical samples.

3.2.2 Density and impact tests

The density of machined Charpy specimens was measured using the hydrostatic weighing (Archimedes') method on three different samples for each investigated condition. Samples were weighed in air and, subsequently, in distilled water, using a Gibertini Europe 500 analytical digital balance. Relative density was calculated as a percentage of the nominal alloy density (2.68 g/cm^3).

Charpy impact tests were performed at room temperature (25 °C) on four samples for each investigated condition. A CEAST instrumented pendulum with available energy of 50 J was used, and the force-displacement curves were calculated according to the ISO 14556:2015 standard. The experimental apparatus is depicted in Fig. 3.4a. The pendulum initially forms an angle of 150° to the specimen, providing an impact velocity of 3.46 m/s during the test. A strain-gauge sensor bridge is placed near the edge of the instrumented pendulum to acquire the force signal. The deformation acting on the pendulum during impact is acquired by a CEAST DAS 64 K acquisition system as an electric signal, which is directly converted into a force value. The specimen displacement is automatically calculated by double integration of the force curve [14] according to:

$$x_i = \iint_0^{t_i} \frac{F(t) - gM_{tot}}{M_{tot}} d^2t \quad (1)$$

where x_i [mm] is the specimen displacement up to time t_i, $F(t)$ [N] is the acquired force as a function of time, g [m^2/s] is the gravity acceleration, M_{tot} [kg] is the total impact mass, and t [ms] is time. Data were furtherly analysed using a tailored Matlab® code. Three relevant parameters were calculated:

- Peak force F_P [kN]: the maximum force value recorded during the test;
- Initiation energy E_I [J]: the energy absorbed by the specimen before crack initiates, calculated as the area under the force-displacement curve up to peak force;
- Propagation energy E_P [J]: the energy absorbed by the specimen during crack propagation, calculated as the area under the force-displacement after the peak force.

A schematic of the force-displacement curve and the corresponding impact parameters is reported in Fig. 3.4b.

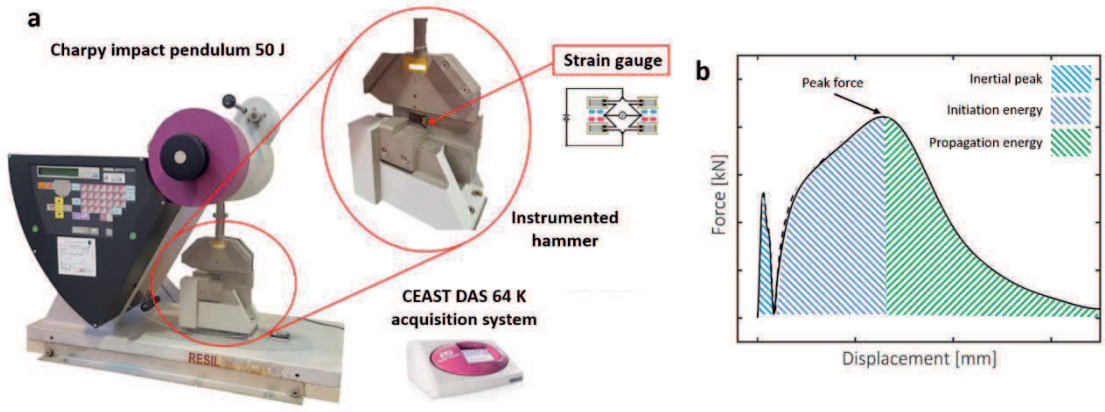

Figure 3.4. (a) Instrumented Charpy impact pendulum used for impact tests. (b) Schematic of the force-displacement curve and impact parameters.

During the impact test, as the pendulum strikes the specimen, this latter is instantly accelerated to a higher velocity than the pendulum. The shortly interrupted contact produces a first oscillation, known as "inertial peak" (Fig. 3.4b). Its subtended area is summed up to the initiation energy. It is worth to notice that, whereas the Charpy test is known as a high-strain rate test, the actual strain rate cannot be measured directly using the adopted apparatus. Additionally, calculation of an equivalent uniaxial strain rate for Charpy tests is quite troublesome as it is material-dependent and changes with distance from the notch [15]. As a reference value, 3D finite element analyses estimate the strain rate at notch as ~10^3 s^{-1} [16].

3.2.3 Microstructural characterisation

Metallographic sections were cut perpendicularly to the U-notch of Charpy specimens, as reported in Fig. 3.3b. Specimens were polished up to mirror finishing and etched for 10 s with a 0.5 wt. % HF aqueous solution. Microstructural investigations were carried out using a Leica DMI 5000M optical microscope (OM). Fracture surfaces were investigated by a Zeiss EVO MA 15 scanning electron microscope (SEM).

3.3 RESULTS AND ANALYSES

3.3.1 Microstructural investigations and density tests

Figure 3.5 couples the results of density measurements and OM images of the corresponding samples. The as-built alloy is almost fully dense, with a relative density

close to 100 %. OM images confirm this result, with the microstructure consisting of semi-circular melt pools, and just small pores detected. The $T6_{short}$ heat treatment affects the starting microstructure, with coarse Si particles that substitute the cellular structure. Additionally, several pores 5-10 μm wide appear, accordingly with the reduced relative density of 98 %. A similar microstructure characterises the $T6_{long}$ samples, although both Si particles and pores coarsen, with these ones ranging between 10-20 μm. In line with OM observations, relative density falls to 96 %. The HIP significantly reduces the porosity of HIP + $T6_{long}$ samples, and the relative density raises to ~99.5 %, although not reaching the starting value of as-built samples.

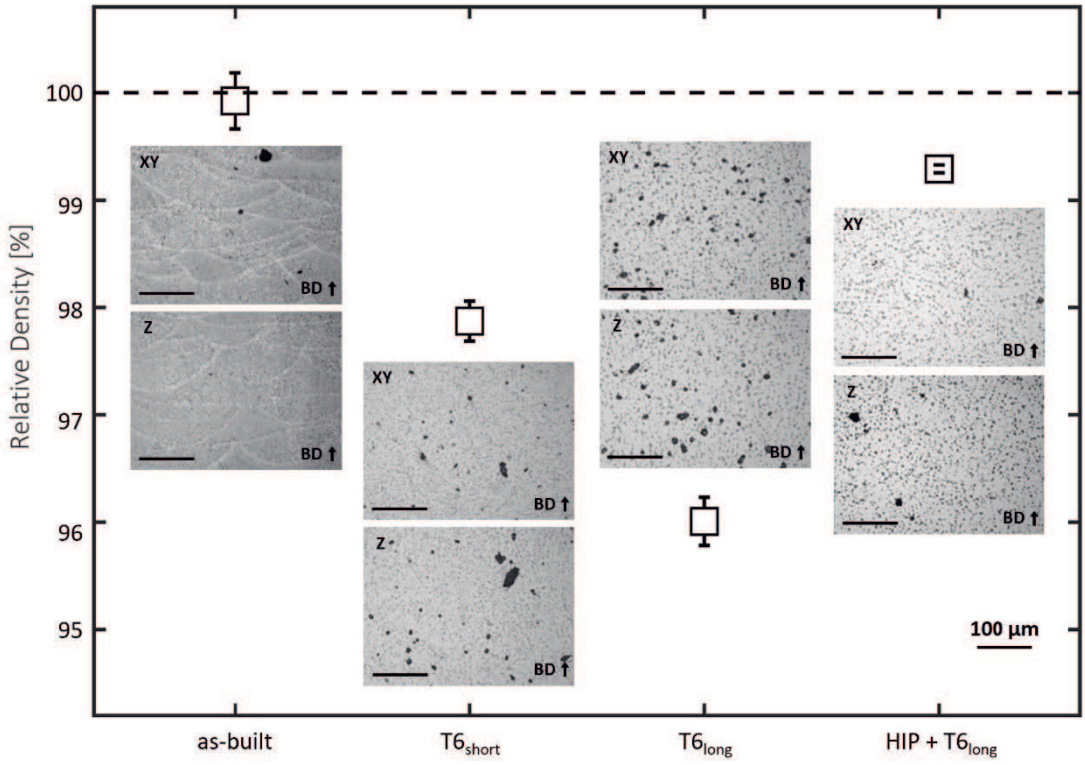

Figure 3.5. Density results and corresponding microstructural OM images of samples in different orientations and heat treatment conditions. The black vertical arrow in each image points out the building direction (BD). The marker size is reported in the bottom-right corner.

3.3.2 Impact properties

Force values of as-built samples quickly increase to F_P, elucidating a significant strain hardening. Then they moderately decay during the propagation stage, with the total absorbed energy being similarly divided into the E_I and E_P contributions (2.2-2.5 J and 1.5-2 J, respectively). The F_P of 7 kN is similar for XY and Z samples, whereas these ones have lower absorbed energy, especially E_P. Similarly to the as-built samples, $T6_{short}$

specimens rapidly strain hardens to an F_P of 7 kN, and absorb a similar E_I (2-2.5 J). Conversely, force values steeply fall after F_P, and E_P is lower than 0.5 J. $T6_{long}$ samples show the same behaviour, whereas the corresponding impact parameters reduce of 15-25 %. The HIP improves material strength (F_P 7.5 kN) and E_I (2.7-3.3 J) compared to the as-built and other heat treatment conditions but slightly affects E_P (0.5 J). All heat-treated samples share a similar behaviour regardless of orientation, whereas the Z specimens generally have a slightly higher absorbed energy.

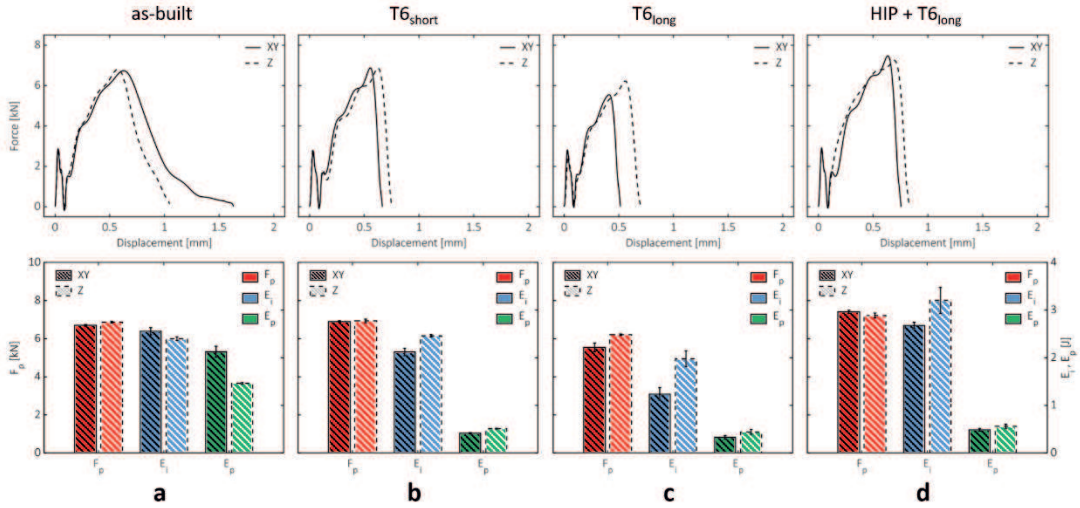

Figure 3.6. Force-displacement curves from Charpy impact tests and corresponding impact parameters of samples in different orientations and heat treatment conditions. (a) as-built. (b) $T6_{short}$. (c) $T6_{long}$. (d) HIP + $T6_{long}$.

3.3.3 Fractographic investigations

Figure 3.7 depicts the fracture surfaces of samples with different orientations and heat treatment conditions. Fracture surfaces of as-built samples are relatively flat and recall typical OM microstructural features. XY specimens show semi-circular traces of melt pools (Fig. 3.7a), whereas elongated scan tracks are visible in Z specimens (Fig. 3.7b). Fracture surfaces of heat-treated samples strongly differ, showing mainly micrometric dimples which host isolated Si particles. Some pores are detectable on the fracture surface of $T6_{short}$ samples (Fig. 3.7c-d). Pores increase in number and coarsen, reaching a few tens of μm in size, in $T6_{long}$ specimens (Fig. 3.7e-f). Although the HIP successfully encloses most of the pores, some are still detectable on the fracture surfaces of HIP + $T6_{long}$ samples (Fig. 3.7g-h). Differently from the as-built condition, relevant differences between fracture surfaces of XY and Z specimens cannot be clearly assessed.

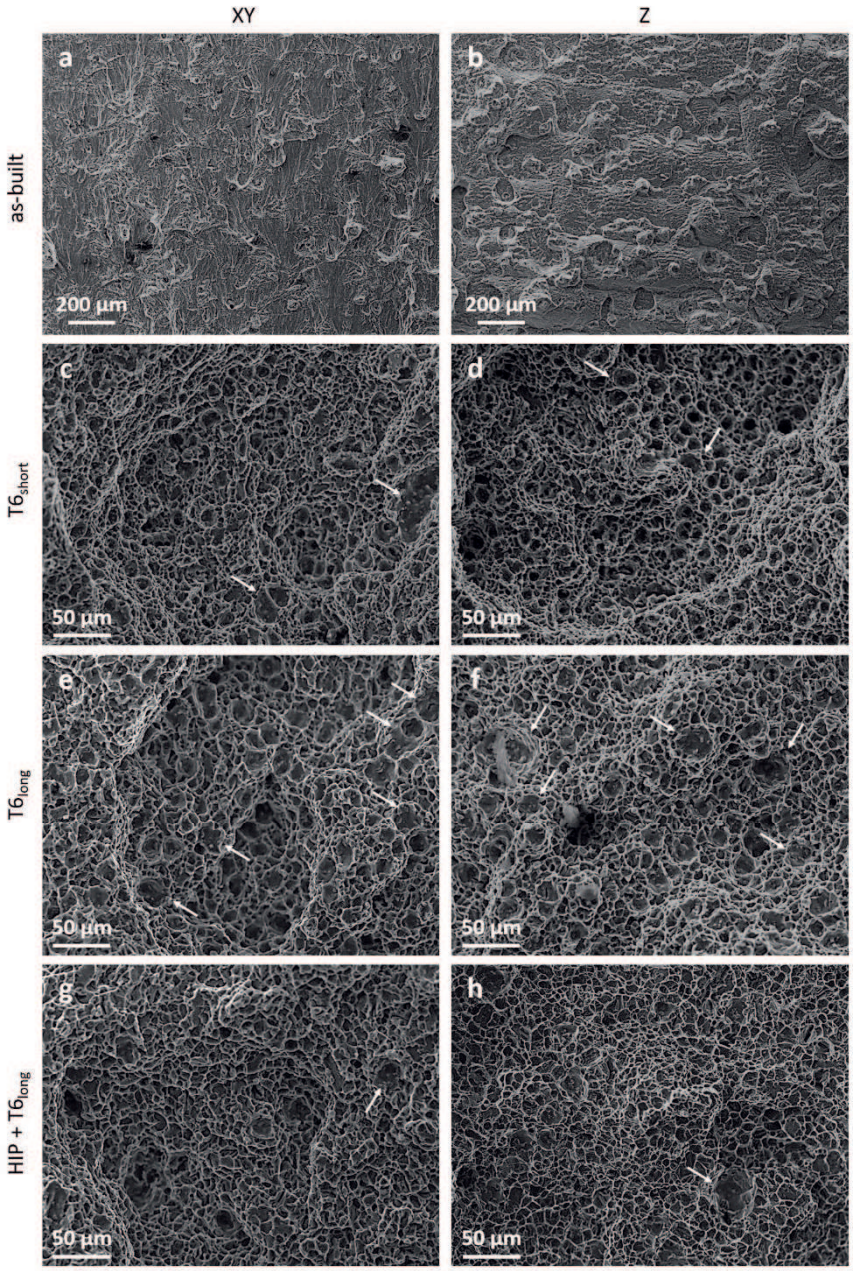

Figure 3.7. Fracture surfaces of fractured Charpy samples in different orientations and heat treatment conditions. (a-c-e-g) XY. (b-d-f-h) Z. (a-b) as-built. (c-d) $T6_{short}$. (e-f) $T6_{long}$. (g-h) HIP + $T6_{long}$. White arrows point out pores.

3.4 DISCUSSION

3.4.1 Effect of heat treatments on microstructure and impact properties

The as-built material shows a relevant impact strength but limited absorbed energy. The microstructure of the L-PBF manufactured AlSi10Mg alloy displays unique features, such as micrometric Al cellular dendrites and a network of eutectic Si [17], [18]. Moreover, high cooling rates promotes solid solution strengthening by Si [19], [20]. All

these features contribute to the high strain hardening and resulting impact strength of the as-built samples. Nevertheless, even using suitable deposition parameters, several undesired features remain, such as residual stresses, a high density of tangled dislocations and sub-micrometric pores [21]–[23]. Such residual defects affect ductility, causing the premature failure of as-built samples and enabling low energy absorption.

Whereas developed to strengthen casting products [24], [25], casting-derived heat treatments $T6_{short}$ and $T6_{long}$ do not improve the impact properties of the L-PBF produced AlSi10Mg alloy. High temperatures of SHT profoundly modify the starting microstructure. High cooling rate and thermal gradients in the L-PBF process of Al alloys produce a metastable microstructure. This latter rapidly evolves towards the equilibrium state as soon as a driving force like heating is applied. As a result, coarse Si particles embedded in the Al matrix replace the starting cellular structure, and melt pools are no longer visible. Precipitation strengthening during the ageing treatment recovers the otherwise softening effect of microstructural coarsening. However, at best, it matches the performance of the as-built material ($T6_{short}$), whereas the application of an extended solution time damages the impact properties significantly ($T6_{long}$).

Such an effect is reasonably ascribed to porosity, accordingly to density measurements, OM observations (Fig. 3.5) and SEM investigation of fracture surfaces (Fig. 3.7). The relative density of the as-built material is near 100 %, but some micrometric circular pores are present. The use of optimised deposition parameters (§ 3.2.1) rules out the possibility of lack-of-fusion pores, which additionally have an irregular morphology [26], [27]. Similarly, keyhole pores form out of the optimum process window and are up to several tens of μm wide [27], [28]. Owing to the small size and circular morphology, detected pores likely are gas pores entrapped during fast solidification. During the heat treatment, gas pressure increases with temperature, and it deforms the surrounding material when temperature sufficiently reduces its yield strength [29]. As a consequence, the longer the permanence at high temperatures, the more pre-existing pores coarsen. This statement is in line with insets in Fig. 3.5 and fracture surfaces in Fig. 3.7c-d-e-f and accounts for the reduced impact properties of $T6_{long}$ samples (Fig. 3.6).

Since porosity mainly rules the impact properties of current heat-treated samples, the HIP has a remarkably beneficial effect. Microstructural observations reveal that most of the pores are enclosed in HIP + $T6_{long}$ samples. Accordingly, a high relative density is

preserved (99.5 %), and just a few pores are visible on the fracture surfaces (Fig. 3.7 g-h). Material strength and E_I overcome the measured values of the as-built state (Fig. 3.6). E_P settles below 1 J, analogously to other heat-treated samples. Reduced energy absorption during fracture propagation relates to the local strain field induced in the Al matrix by ageing-induced strengthening compounds [30].

3.5 CONCLUSION

The present preliminary research activity aims to evaluate the effectiveness of casting-derived heat treatment routes on the high-strain rate mechanical behaviour of an L-PBF manufactured AlSi10Mg alloy. Charpy impact tests were conducted on T6-like heat-treated samples with short and long solution times and compared with the as-built material. Additionally, the effect of the HIP before long SHT was investigated. Results enable to draw the following conclusions:

- High-temperature casting-derived heat treatments alter the starting as-built microstructure and cause a significant growth of residual gas pores. This latter phenomenon worsens as the solution time increases ($T6_{long}$) and is particularly detrimental to impact properties.
- Using optimised heat treatment parameters ($T6_{short}$) porosity just partially increases. However, the impact properties of the as-built material are matched at best, with no further benefit. This outcome limits the applicability of T6-like heat treatments only.
- The HIP significantly neutralises the adverse effect of porosity, and moderately improves the impact properties of the HIP + $T6_{long}$ samples as compared to the as-built material. Such an outcome highlights the importance of HIP when the as-built material is to be heat-treated to high temperatures.

REFERENCES

[1] K. V. Yang *et al.*, *Porosity formation mechanisms and fatigue response in Al-Si-Mg alloys made by selective laser melting*, Mater. Sci. Eng. A, vol. **712**, no. September 2017, pp. 166–174, 2018

[2] M. Tang and P. C. Pistorius, *Oxides, porosity and fatigue performance of AlSi10Mg parts produced by selective laser melting*, Int. J. Fatigue, vol. **94**, no. April, pp. 192–201, 2017

[3] N. T. Aboulkhair, I. Maskery, C. Tuck, I. Ashcroft, and N. M. Everitt, *Improving the fatigue behaviour of a selectively laser melted aluminium alloy: Influence of heat treatment and surface quality*, Mater. Des., vol. **104**, pp. 174–182, 2016

[4] E. Brandl, U. Heckenberger, V. Holzinger, and D. Buchbinder, *Additive manufactured AlSi10Mg samples using Selective Laser Melting (SLM): Microstructure, high cycle fatigue, and fracture behavior*, Mater. Des., vol. **34**, pp. 159–169, 2012

[5] I. Rosenthal, A. Stern, and N. Frage, *Strain rate sensitivity and fracture mechanism of AlSi10Mg parts produced by Selective Laser Melting*, Mater. Sci. Eng. A, vol. **682**, no. November 2016, pp. 509–517, 2017

[6] E. Zaretsky, A. Stern, and N. Frage, *Dynamic response of AlSi10Mg alloy fabricated by selective laser melting*, Mater. Sci. Eng. A, vol. **688**, no. December 2016, pp. 364–370, 2017

[7] N. D. Parab *et al.*, *Investigation of dynamic fracture behavior of additively manufactured Al-10Si-Mg using high-speed synchrotron X-ray imaging*, Addit. Manuf., vol. **30**, no. September, 2019

[8] A. Hadadzadeh, B. Shalchi Amirkhiz, A. Odeshi, J. Li, and M. Mohammadi, *Role of hierarchical microstructure of additively manufactured AlSi10Mg on dynamic loading behavior*, Addit. Manuf., vol. **28**, no. November 2018, pp. 1–13, 2019

[9] A. Hadadzadeh, B. S. Amirkhiz, J. Li, A. Odeshi, and M. Mohammadi, *Deformation mechanism during dynamic loading of an additively manufactured AlSi10Mg_200C*, Mater. Sci. Eng. A, vol. **722**, no. March, pp. 263–268, 2018

[10] A. Hadadzadeh, B. S. Amirkhiz, A. Odeshi, and M. Mohammadi, *Dynamic loading of direct metal laser sintered AlSi10Mg alloy: Strengthening behavior in different building directions*, Mater. Des., vol. **159**, pp. 201–211, 2018

[11] A. Hadadzadeh, B. S. Amirkhiz, and M. Mohammadi, *Contribution of Mg2Si precipitates to the strength of direct metal laser sintered AlSi10Mg*, Mater. Sci. Eng. A, vol. **739**, no. August 2018, pp. 295–300, 2019

[12] L. Girelli, M. Tocci, L. Montesano, M. Gelfi, and A. Pola, *Optimization of heat treatment parameters for additive manufacturing and gravity casting AlSi10Mg alloy*, IOP Conf. Ser. Mater. Sci. Eng., vol. **264**, no. 1, 2017

[13] L. Girelli, M. Tocci, L. Montesano, M. Gelfi, and A. Pola, *Investigation of cavitation erosion resistance of AlSi10Mg alloy for additive manufacturing*, Wear, vol. **402–403**, no. February, pp. 124–136, 2018

[14] D. Barkley and M. Akay, *The design and evaluation of an instrumented impact tester*, Polym. Test., vol. **11**, no. 4, pp. 249–270, 1992

[15] E. Lucon, *Experimental assessment of the equivalent strain rate for an instrumented charpy test*, J. Res. Natl. Inst. Stand. Technol., vol. **121**, pp. 165–179, 2016

[16] N. Liang, Y. Zhao, J. Wang, and Y. Zhu, *Effect of grain structure on Charpy impact behavior of copper*, Sci. Rep., vol. **7**, pp. 1–11, 2017

[17] H. Qin, Q. Dong, V. Fallah, and M. R. Daymond, *Rapid Solidification and Non-equilibrium Phase Constitution in Laser Powder Bed Fusion (LPBF) of AlSi10Mg Alloy: Analysis of Nano-precipitates, Eutectic Phases, and Hardness Evolution*, Metall. Mater. Trans. A Phys. Metall. Mater. Sci., vol. **51**, no. 1, pp. 448–466, 2020

[18] L. Thijs, K. Kempen, J. P. Kruth, and J. Van Humbeeck, *Fine-structured aluminium products with controllable texture by selective laser melting of pre-alloyed AlSi10Mg powder*, Acta Mater., vol. **61**, no. 5,

pp. 1809–1819, 2013

[19] J. Delahaye, J. T. Tchuindjang, J. Lecomte-Beckers, O. Rigo, A. M. Habraken, and A. Mertens, *Influence of Si precipitates on fracture mechanisms of AlSi10Mg parts processed by Selective Laser Melting*, Acta Mater., vol. **175**, pp. 160–170, 2019

[20] T. Maeshima and K. Oh-ishi, *Solute clustering and supersaturated solid solution of AlSi10Mg alloy fabricated by selective laser melting*, Heliyon, vol. **5**, no. 2, p. e01186, 2019

[21] L. Zhuo *et al.*, *Effect of post-process heat treatment on microstructure and properties of selective laser melted AlSi10Mg alloy*, Mater. Lett., vol. **234**, pp. 196–200, 2019

[22] G. Wang *et al.*, *The origin of high-density dislocations in additively manufactured metals*, Mater. Res. Lett., vol. **8**, no. 8, pp. 283–290, 2020

[23] Z. Wang *et al.*, *Premature failure of an additively manufactured material*, NPG Asia Mater., vol. **12**, no. 1, 2020

[24] E. Sjölander and S. Seifeddine, *The heat treatment of Al-Si-Cu-Mg casting alloys*, J. Mater. Process. Technol., vol. **210**, no. 10, pp. 1249–1259, 2010

[25] L. Pedersen and L. Arnberg, *The Effect of Solution Heat Treatment and Quenching Rates.pdf*, Metall. Mater. Trans. A, vol. **32A**, no. March, p. 525, 2001

[26] N. T. Aboulkhair, N. M. Everitt, I. Ashcroft, and C. Tuck, *Reducing porosity in AlSi10Mg parts processed by selective laser melting*, Addit. Manuf., vol. **1**, pp. 77–86, 2014

[27] G. Kasperovich, J. Haubrich, J. Gussone, and G. Requena, *Correlation between porosity and processing parameters in TiAl6V4 produced by selective laser melting*, Mater. Des., vol. **105**, pp. 160–170, 2016

[28] M. Bayat *et al.*, *Keyhole-induced porosities in Laser-based Powder Bed Fusion (L-PBF) of Ti6Al4V: High-fidelity modelling and experimental validation*, Addit. Manuf., vol. **30**, no. April, p. 100835, 2019

[29] C. Weingarten, D. Buchbinder, N. Pirch, W. Meiners, K. Wissenbach, and R. Poprawe, *Formation and reduction of hydrogen porosity during selective laser melting of AlSi10Mg*, J. Mater. Process. Technol., vol. **221**, pp. 112–120, 2015

[30] H. W. Zandbergen, S. J. Andersen, and J. Jansen, *Structure determination of Mg5Si6:particles in Al by dynamic electron diffraction studies*, Science (80-.)., vol. **277**, no. 5330, pp. 1221–1225, 1997

CHAPTER 4

MICROSTRUCTURE AND IMPACT BEHAVIOUR: EFFECT OF HEAT TREATMENT

The present chapter aims at investigating the effect of different heat treatment routes on microstructure and high-strain rate behaviour of an L-PBF produced AlSi10Mg alloy. The as-built, stress-relieved/annealed and T6 conditions were considered. All the remaining samples were subjected to the hot isostatic pressing to prevent porosity growth during exposure to high temperatures. Some samples were subsequently heat-treated according to a standard T6 route, and a new heat treatment combining hot isostatic pressing and ageing at high pressure was also tested. The main goal is to identify potential candidates to substitute standard heat treatment routes with significant technological advantages.

4.1. DEFINITION OF PROPER HEAT TREATMENT ROUTES

4.1.1 Additional background and purpose of the work

Heat treatment is a fundamental post-processing step of Al alloys to ensure an adequate material performance in light of the considered application. In this regard, many researchers investigated the effect of heat treatment parameters on the microstructural and mechanical properties of the L-PBF produced AlSi10Mg alloy. Two main heat treatment paths can be identified. The first one is a low-temperature treatment (annealing or stress-relieving; typically performed at 300 °C for 2 h) to remove internal residual stresses [1]. Recently, it was shown that a decrease of the stress-relieving/annealing temperature could minimize microstructural coarsening [2], [3].

The second approach relates to T6 treatment, which is the most traditional heat treatment route for Al-Si-Mg alloys [4]–[6], to remove internal residual stresses and mitigate material anisotropy. However, the high temperatures involved in solution treatment coarsen the fine microstructure obtained after solidification in the L-PBF process, leading to a loss in material strength. An additional drawback of this method is the growth of gas pores at high temperatures, as previously assessed in Chapter 3. Such a phenomenon severely limits the applicability of the T6 treatment.

In this regards, hot isostatic pressing (HIP) is frequently performed before T6 treatment [7]–[9] to counteract gas porosity development. The beneficial effects of HIP in terms of pore closure, densification and improvement of the corresponding tensile and fatigue properties were discussed in several studies [7], [8]. Additionally, in Chapter 3 it was shown that also impact properties benefit from the application of HIP. However, it should be noted that HIP is not very useful with a low-density as-built material, which stems from non-optimised process parameters [10], [11].

Interestingly, HIP and solution heat treatment share a similar temperature range. Therefore, their combination in a single high-pressure treatment process may be viable. Furthermore, pore regrowth has been reported during heat treatment after HIP [12], which is an additional reason to maintain high pressures during the entire treatment cycle. Accordingly, in this research activity, a novel high-pressure T6 heat treatment is proposed, which involves rapid gas quenching and ageing at high pressure. A similar treatment was performed on an A356 casting alloy [13], with positive results in terms of strength and fatigue resistance. The effectiveness of this method on an L-PBF produced AlSi10Mg alloy was recently explored in light of its tensile properties [14].

Therefore, in the present research activity, the effect of various heat-treatment routes is studied, including annealing, T6, HIP only, HIP followed by T6, and HIP followed by ageing at high pressure. The aim is to compare the results of the most used heat-treatment routes with those obtained using the innovative high-pressure T6 heat-treatment. Material densification was measured, and the mechanical response of the heat-treated alloys was studied by Charpy impact testing. Impact loading is particularly sensitive to material porosity, which decreases its ability to absorb energy. Therefore, impact behaviour is particularly suitable to evaluate the effectiveness of the proposed post-processing routes. Additionally, although the high-strain rate behaviour represents a fundamental property for the design of components, few studies were performed on the Charpy impact behaviour of L-PBF AlSi10Mg alloys [11], [15], [16]. Furthermore, just a few of them involved heat-treated samples, whereas none focused on the effect of the innovative high-pressure T6 heat-treatment.

4.2 MATERIALS AND EXPERIMENTAL PROCEDURE

4.2.1 L-PBF and heat treatment

Details regarding the production of the AM impact specimens using an AlSi10Mg alloy powder and their chemical composition are reported in the previous Chapter 3 (§ 3.2.1). Just specimens with their long sides parallel to the building platform (XY, § 3.2.1) are considered in the present Chapter 4, whereas the effect of different building orientations will be the topic of next Chapter 5.

The specimens were subjected to HIP treatment at different pressures on a Quintus Technologies instrument. HIP_{50} and HIP_{150} refer to HIP treatment at pressures of 50 and 150 MPa, respectively. In addition, some samples were subsequently heat-treated (T6), as shown in Tab. 4.1 to yield HIP_{50} + T6 and HIP_{150} +T6 specimens. In the new HPT6 route, the samples were directly quenched inside the HIP vessel using a cooling gas and then reheated to the ageing temperature while maintaining high-pressure conditions. The cooling rate provided by the Uniform Rapid Quenching (URQ) unit was ~7 K/s between 540 °C and 200 °C, whereas a typical cooling rate of HIP systems is ~0.2 K/s [13]. Additional details on the working principle of the Uniform Rapid Quenching unit can be found elsewhere [13]. $HPT6_{50}$ and $HPT6_{150}$ refer to high-pressure T6 treatment at 50 and 150 MPa, respectively. For comparison, specimens in the as-built, annealed, and conventional T6 heat-treated (without HIP) conditions were also tested. Annealing and T6 treatments were performed in laboratory furnaces at atmospheric pressure using time and temperature values listed in Tab. 4.1.

Table 4.1. Designation and details of the heat treatment routes.

Designation	HIP (+ argon quench)	SHT (+ water quench)	Ageing	Annealing
as-built	-	-	-	-
annealed	-	-	-	300 °C, 2 h
T6	-	520 °C, 2 h	180 °C, 4 h	-
HIP_{50}	520 °C, 2 h, 50 MPa	-	-	-
$HPT6_{50}$	520 °C, 2 h, 50 MPa	-	180 °C, 4 h, 50 MPa	-
HIP_{50} + T6	520 °C, 2 h, 50 MPa	520 °C, 2 h	180 °C, 4 h	-
HIP_{150}	520 °C, 2 h, 150 MPa	-	-	-
$HPT6_{150}$	520 °C, 2 h, 150 MPa	-	180 °C, 4 h, 150 MPa	-
HIP_{150} + T6	520 °C, 2 h, 150 MPa	520 °C, 2 h	180 °C, 4 h	-

After heat treatment, the impact specimens were machined as reported in § 3.2.1.

4.2.2 Density measurement and mechanical properties

Procedures regarding density measurements and Charpy impact tests are reported in detail § 3.2.2 and, for short, will not be repeated here. Hardness measurements were performed on one Charpy specimen for each heat-treatment route. An LTF Galileo Ergotest Comp 25 hardness machine with a 2.5 mm diameter spherical indenter was used for hardness testing using a 613 N load (62.5 kg_f), which was applied on the specimen for 15 s. Four indentations were performed on each sample, and their average and standard deviation values were calculated.

4.2.3 Microstructural characterisation

Transversal sections for microstructural investigation were cut from the tested Charpy specimens perpendicular to the U-notch. Samples were prepared according to standard metallographic protocols and finished using an oxide polish suspension. Image analysis was conducted using the software ImageJ [17] on ten micrographs of the as-polished samples to avoid artefacts resulting from etching. The width and area fraction of Fe-based compounds were measured, whereas the equivalent diameter (ED) was selected as a representative parameter of Si particle size. The dimensional features of Si particles were reported to follow a 3-parameter log-normal distribution [18]. The mean ED value was calculated as follows:

$$ED = \tau + e^{(\mu + 0.5 \cdot \sigma^2)} \quad (1)$$

where μ, σ, and τ are the mean, standard deviation, and threshold of the logarithmic ED values, respectively. μ, σ, and τ were obtained by an image-analysis fitting procedure using a tailored Matlab® code. Samples were then etched for 10 s with a 0.5 wt. % HF aqueous solution. Fractographic and microstructural characterisation was conducted using a Zeiss EVO MA 15 scanning electron microscope (SEM) equipped with an Oxford X-Max 50 energy-dispersive X-ray (EDX) probe.

Precipitation strengthening after the novel HPT6 treatment was verified by transmission electron microscopy (TEM). The alloy treated at 150 MPa was chosen as the reference. 3 mm-diameter disk samples were first mechanically thinned and polished to

a thickness of ~25 μm. Final thinning was performed by low-energy Ar^+ ion beam milling on a GATAN precision ion polishing system. TEM images were recorded on an FEI Tecnai F20 TEM operating at 200 keV. Bright-field (BF) imaging, selected area electron diffraction (SAED), and high-resolution transmission electron microscopy (HRTEM) were conducted to analyse the presence of hardening compounds. The analysis of electron diffraction patterns and high-resolution images were conducted using the software Gatan Microscopy Suite® (GMS) 3.

Table 4.2. Relevant precipitate phases of Al-Mg-Si alloys.

Phase	**Formula**	**Crystal system and space group**	**Lattice parameters [Å]/[°]**	**Orientation relationship**
β'' [19]	Mg_5Si_6	Monoclinic C2/m	a = 15.16, b = 4.05, c = 6.74 $\alpha = \gamma = 90$, $\beta = 105.3$	$\{001\}_{Al} \parallel \{010\}_{\beta''}$ $[200]_{Al} \sim [4\underline{3}0]_{\beta''}$ $[020]_{Al} \sim [601]_{\beta''}$
β' [20]	$Mg_{1.8}Si$	Hexagonal $P6_3$	a = b = 7.15, c = 12.15 $\alpha = \beta = 90$, $\gamma = 120$	$\{001\}_{Al} \parallel \{001\}_{\beta'}$ $[200]_{Al} \times [100]_{\beta'} \sim 49°$
B' [21]	$Mg_9Al_3Si_7$	Hexagonal P_{-6}	a = b = 10.35, c = 4.058 $\alpha = \beta = 90$, $\gamma = 120$	$\{001\}_{Al} \parallel \{001\}_{B'}$ $[200]_{Al} \times [2\underline{1}0]_{B'} \sim 10°$
U1 [22]	$MgAl_2Si_2$	Trigonal P_{-3m1}	a = b = 4.05, c = 6.74 $\alpha = \beta = 90$, $\gamma = 120$	$\{001\}_{Al} \parallel \{100\}_{U1}$ $[200]_{Al} \times [001]_{U1} \sim 19°$ or $[200]_{Al} \times [001]_{U1} \sim 51°$
U2 [23]	$Mg_4Al_4Si_4$	Orthorhombic P_{nma}	a = 6.75, b = 4.05, c = 7.94 $\alpha = \beta = \gamma = 90$	$\{001\}_{Al} \parallel \{010\}_{U2}$ $[200]_{Al} \sim [10\ 0\underline{4}]_{U2}$ $[220]_{Al} = [\underline{2}0\underline{5}]_{U2}$
β [24]	Mg_2Si	Cubic F_{m-3m}	a = b = c = 6.354 $\alpha = \beta = \gamma = 90$	$\{001\}_{Al} \parallel \{100\}_{\beta}$ $[220]_{Al} \parallel [200]_{\beta}$
Si [22]	Si	Cubic F_{d3m}	a = b = c = 5.4309 $\alpha = \beta = \gamma = 90$	$\{001\}_{Al} \parallel \{110\}_{Si}$ $[010]_{Al} \parallel [\underline{1}11]_{Si}$ $[3\underline{1}0]_{Al} \parallel [1\underline{1}1]_{Si}$

Several strengthening precipitates form during ageing of Al-Mg-Si alloys, with the precipitation sequence generally being reported as [20], [22], [23]:

$$\text{supersaturated solid solution} \rightarrow \text{Mg/Si clusters} \rightarrow \text{GP-I} \rightarrow \beta'' \text{ (GP-II)} \rightarrow \beta' + B' + U1 + U2 \rightarrow \beta$$

Simulation of the corresponding electron diffraction patterns to match experimental SAED patterns or Fast Fourier Transform (FFT) of HRTEM images was performed by the STEM_CELL software [25], [26]. Lattice parameters of such compounds and their orientation relationship with the hosting Al matrix were obtained from the published literature, and are listed in Tab. 4.2. For short, individual X, Y, Z atomic coordinates and temperature (B) factors are not reported. However, they could be found in the references.

X-ray diffraction (XRD) tests were conducted using the Bragg-Brentano geometry on a Bruker D8 Advance diffractometer equipped with a Cu filament (Kα, 1.5406 Å). All patterns were acquired in the 2θ range of 20° to 110° with 0.02° of step-size and 1 s of step time. Full-pattern Rietveld refinement analysis was conducted using the software Maud [27] to evaluate the volume fraction of the Si phase and the lattice parameter of the Al phase. This latter was additionally calculated using the $\cos^2(\theta)/\sin(\theta)$ method on the full pattern.

4.3 RESULTS AND ANALYSES

4.3.1 Evolution of microstructure with heat treatment

The SEM images in Fig. 4.1 show the microstructural features of the as-built alloy. In the SE image (Fig. 4.1a), a dotted line highlights the typical semi-circular shape of melt pools, which range between 100-150 and 60-80 μm in width and depth, respectively. In Fig. 4.1b, the BSE image complements the observations in Fig. 4.1a providing a crystallographic contrast. Elongated grains, 5-10 μm wide and several tens of μm long are present inside the melt pool. Smaller equiaxed grains, 10 μm in size, are sometimes located along the MPBs. Figure 4.1c shows that the melt pools consist of a network of eutectic Si surrounding Al cellular dendrites. These, similarly to grains, are elongated inside the melt pool and mainly equiaxed at the MPB. The detailed image in 4.1d shows that Al dendrites inside the melt pool are 300-500 wide and a few μm long. Differently from some literature studies [28], [29], the Al dendrites appear free of Si precipitates.

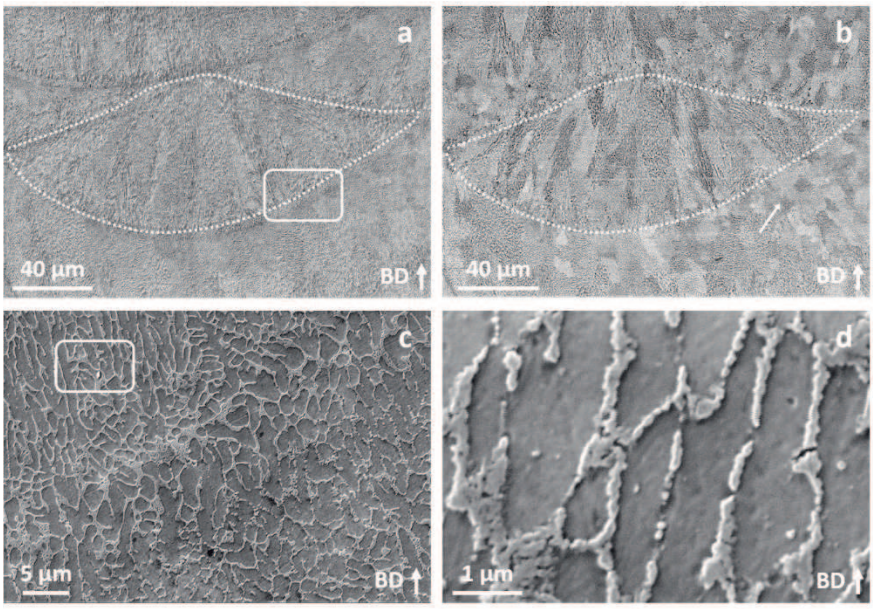

Figure 4.1. SEM images in the transverse section of the as-built sample. (a) SE image revealing the semi-circular shape of the melt pool, with MPBs marked by the dotted line. (b) BSE image highlights the grain structure in the melt pool, and the dotted line underlines the MPBs of the same area as (a). (c)-(d) Detailed images taken from the area marked by the solid line in (a)-(c), respectively. (c) Heterogeneous microstructure at the MPB. (d) Al dendrites and Si network. In all images, the arrow in the bottom-right corner shows the building direction (BD).

In the annealed alloy in Fig. 4.2a, scan tracks are not easily discernible because the Si network breaks up during the annealing treatment [2]. Fig. 4.2b, providing a crystallographic contrast, shows that grains maintain a columnar shape inside melt pools and that the low-temperature annealing does not significantly increase their size [30]. Figure 4.2c highlights that the microstructure consists of separated Si particles embedded in the Al matrix. Additionally, Si particles are slightly coarser at the MPB than in the inner region. As a consequence, the melt pool is still discernible after annealing, as highlighted by the dotted line in Fig. 4.2a. The detailed BSE image in Fig. 4.2d shows that Si particles lie in the nanometric range. Accordingly, image analysis provides a mean ED of 92 nm.

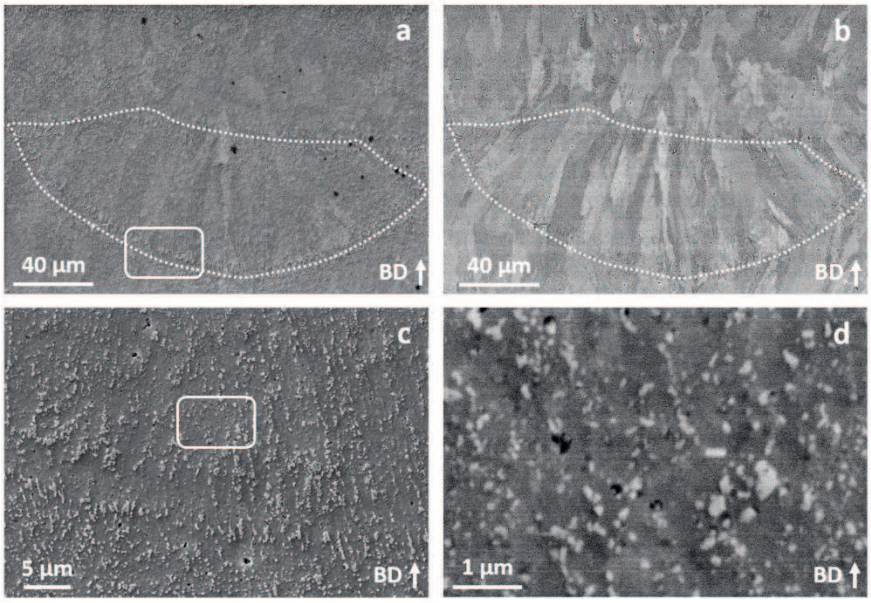

Figure 4.2. SEM images in the transverse section of the annealed sample. (a) SE image revealing the semi-circular shape of the melt pool, with MPBs marked by the dotted line. (b) BSE image highlights the grain structure in the melt pool, and the dotted line underlines the MPBs of the same area as (a). (c)-(d) Detailed images taken from the area marked by the solid line in (a)-(c), respectively. (c) Heterogeneous microstructure at the MPB. (d) Nanometric Si particles. In all images, the arrow in the bottom-right corner shows the building direction (BD).

Figures 4.3a-b show the microstructure of the HIP_{150} sample, chosen as a representative of the HIP_{50}, HPT6, and HIP + T6 conditions. Figure 4.3a highlights that Si particles significantly coarsen when compared to those in the annealed alloy. On the contrary, Fig. 4.3b elucidates that elongated grains do not show remarkable differences in size when compared to Fig. 4.1b and Fig. 4.2b [30]. The inset of Fig. 4.3a shows that large Si particles mainly originate from the breaking up of the Si network and are mostly located at boundaries of Al grains. In addition, the nucleation of nanometric Si particles was observed inside Al grains, likely originating from the supersaturated Si solid solution of the as-built state [31]. Figures 4.3c-d depict the microstructure of alloy after the T6 treatment, which mirrors the microstructural features observed in the other high-temperature heat-treated samples. Coarse micrometric Si particles are embedded in the Al matrix (Fig. 4.3c), which is made up of elongated grains (Fig. 4.3d). However, additional features appear in Fig. 4.3c-d, namely coarse pores, 10-20 µm wide.

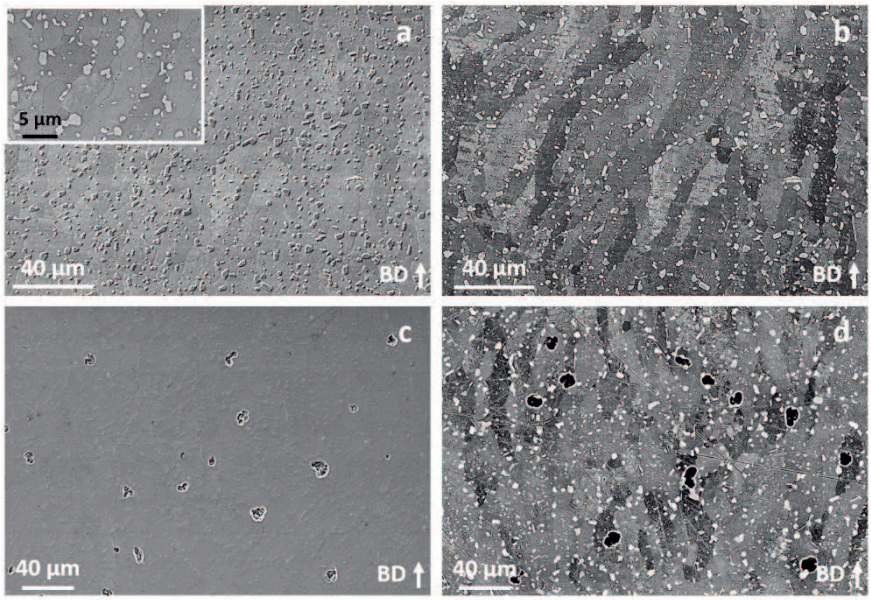

Figure 4.3. SEM images in the transverse section of the: (a-b) HIP_{150} and (c-d) T6 samples. (a) SE image shows micrometric Si particles in the Al matrix; the inset depicts the distribution of Si particles in the grains and along the grain boundaries. (b) BSE image of the same area as (a) shows elongated grains by crystallographic contrast. (c) SE image shows micrometric Si particles in the Al matrix and several pores. (d) BSE image of the same area as (a) shows elongated grains by crystallographic contrast. In all images, the white arrow in the bottom-right corner shows the building direction (BD).

Besides Si particles and Al grains, additional secondary phases, reported in Fig. 4.4, can be detected in all of the considered heat-treatment conditions. Many acicular features, a few hundreds of nm in width and up to several µm in length, could be observed (Fig. 4.4a). EDX analysis reveals them to be Fe-rich compounds (Fig. 4.4b), with $Al_{4.5}Si_{1.5}Fe_{1.5}$ as the likely stoichiometric composition. This latter is quite similar to the β-Al_5SiFe phase, a plate-shaped Fe-bearing intermetallic compound reported in Al-Si-Mg-(Fe) cast [32] and AM [4] alloys. Permanence at high temperatures reasonably coarsens the β-Al_5SiFe compounds formed at the boundaries of Al cellular dendrites during solidification as fine particles due to high cooling rates [33], [34].

Some features with a blocky morphology are sometimes detected, mainly in the proximity of Si particles (Fig. 4.4c). EDX analysis (Fig. 4.4d) reveals them to host both Mg and Fe atoms, with the atomic Mg/Fe ratio of ~1.8. Secondary sub-micrometric Mg- and Fe-based compounds form at boundaries of Al dendrites during solidification.

Similarly to β-Al_5SiFe compounds, they reasonably coarsen to the micrometric size during heat treatment, assuming a blocky shape.

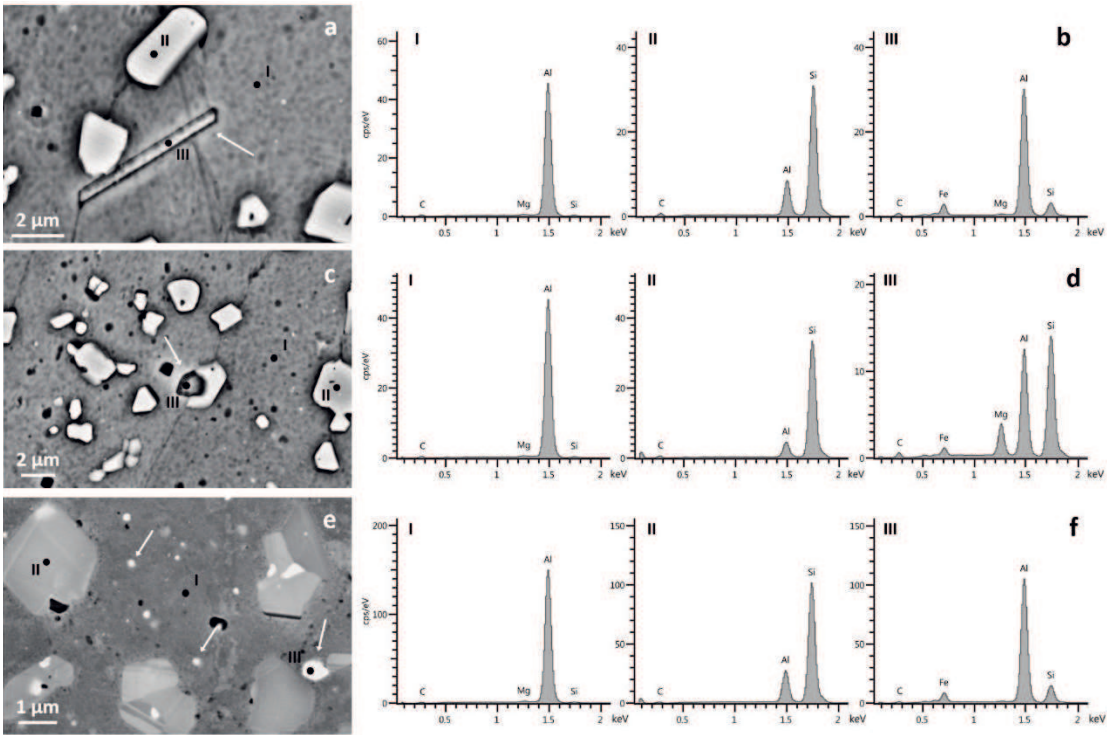

Figure 4.4. Secondary phases in the heat-treated samples. (a-c-e) SEM images. (b-d-f) EDX spectra of different features marked by white arrows in (a-c-e), respectively. EDX spectra of the Al matrix and Si particles are provided for comparison. (a-b) Micrometric needle-like Fe-rich compounds. (c-d) Blocky Mg- and Fe-rich compounds. (e-f) Nanometric Fe-rich particles.

Finally, several bright nanometric features are observable within the Al grains (Fig. 4.4e). Chemical analysis performed by SEM does not provide an adequate spatial resolution to assess their composition unambiguously. However, the EDX spectrum in Fig. 4.4f shows that they are Fe-bearing phases and do not host Mg, thus they are reasonably newly nucleated β-Al_5SiFe precipitates.

As previously stated, no significant differences could be found during the SEM investigation of T6, HIP, HPT6, and HIP + T6 alloys treated at different pressures (50 and 150 MPa). Figure 4.5 compares the SEM images of all samples heat-treated at high temperatures to support the statement reported above. Additionally, Table 4.3 complements microstructural observations with the results of image analysis of Si particles and needle-like Fe-rich compounds. These latter were chosen among the Fe-bearing compounds reported in Fig. 4.4 since they are more easily detectable as compares to features depicted in Fig. 4.4c-e.

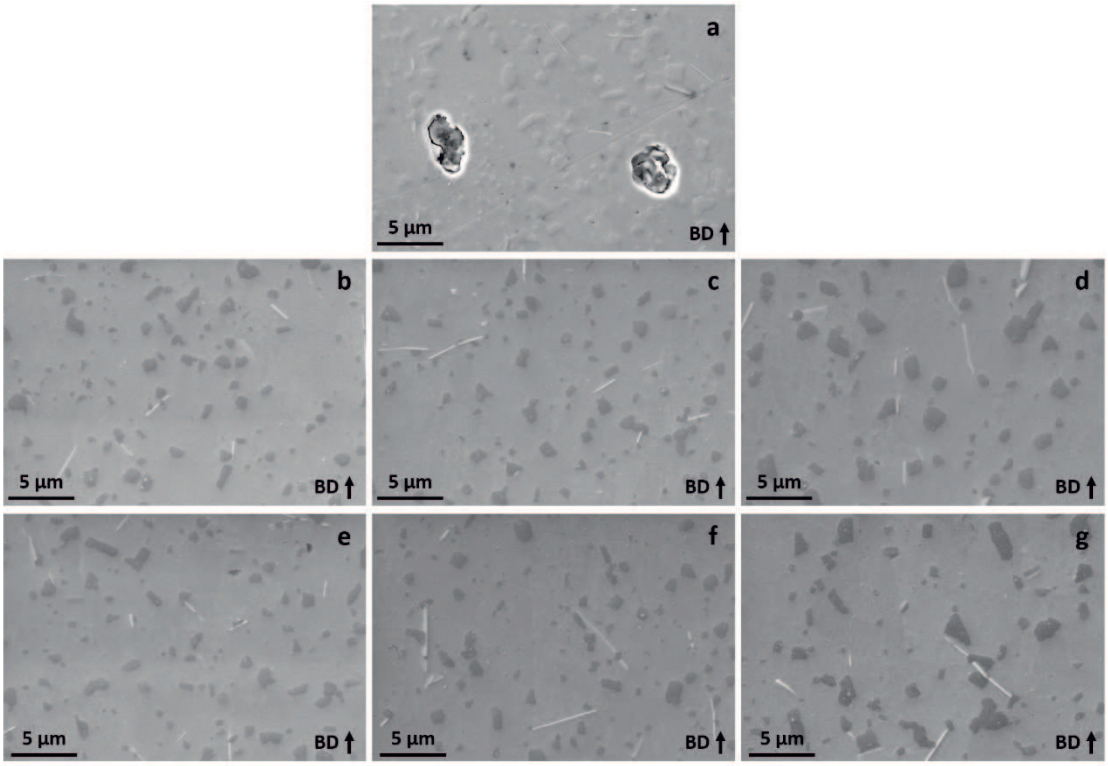

Figure 4.5. A comparison of SEM images in the transverse section of samples heat-treated at high temperatures. (a) T6. (b) HIP_{50}. (c) $HPT6_{50}$. (d) HIP_{50}+T6. (e) HIP_{150}. (f) $HPT6_{150}$. (g) HIP_{150}+T6. In all images, the vertical arrow shows the building direction (BD).

Table 4.3. Results from image analysis of sample heat-treated at high temperatures.

	Si particles		Needle-like Fe-based compounds		
	ED [µm]	AR	Width [µm]	AR	A_F [%]
T6	1.14 ± 0.77	1.60 ± 0.45	0.51 ± 0.2	9.2 ± 4.4	0.76 ± 0.18
HIP_{50}	1.21 ± 1.00	1.65 ± 0.64	0.58 ± 0.32	8.0 ± 4.3	0.77 ± 0.08
$HPT6_{50}$	1.10 ± 0.86	1.71 ± 0.72	0.52 ± 0.19	8.8 ± 3.6	0.66 ± 0.15
HIP_{50}+T6	1.38 ± 0.93	1.75 ± 0.75	0.69 ± 0.29	9.8 ± 3.7	0.82 ± 0.19
HIP_{150}	1.18 ± 0.83	1.68 ± 0.71	0.57 ± 0.18	10.3 ± 4.9	0.67 ± 0.26
$HPT6_{150}$	1.19 ± 0.88	1.53 ± 0.62	0.56 ± 0.24	10.7 ± 4.3	0.81 ± 0.16
HIP_{150}+T6	1.56 ± 0.92	1.64 ± 0.61	0.74 ± 0.31	12.2 ± 5.1	0.83 ± 0.11

The calculated ED of Si particles by image analysis ranged between 1.1-1.2 µm for T6, HIP, and HPT6 alloys. This elucidates the negligible effect of the ageing treatment on coarsening of micrometric features owing to its low temperature [35], although it promotes the precipitation of nanometric compounds not visible in SEM images. The longer permanence at high temperatures slightly coarsened the Si particles of HIP_{50} + T6

and HIP_{150} + T6 samples up to the range of 1.38-1.56 μm. Even if a reduced atomic diffusivity could be expected as the applied pressure increases (0.1, 50 and 150 MPa), results of image analysis indicated that pressure does not appreciably affect the microstructure at the micrometric scale [14]. Likely, the increased diffusivity at high temperatures overcomes such a drawback, which makes the total exposure at high temperatures the main parameter affecting the microstructural evolution of the alloy.

Regarding the Fe-bearing compounds, they had a comparable width for T6, HIP, and HPT6 samples, whereas they slightly coarsened in HIP+T6 samples, matching the observation of Si particles. Their area fraction ranged between 0.66-0.83% for all investigated samples, suggesting that the equilibrium condition was achieved

4.3.2 Precipitation strengthening by HPT6 treatment

A few recent research studies dealt with the high-pressure T6 heat treatment [13], [14], but none of them deeply investigated its effect on the microstructure. In this light, TEM investigations were performed to evaluate precipitation strengthening after $HPT6_{150}$ treatment, and results will be reported in the present paragraph. BF TEM images in Fig. 4.6 depict some relevant microstructural features at different magnifications. Figure 4.6a shows coarse features like Si particles and needle-like Fe-rich compounds embedded in the Al matrix, which present a dark contrast due to crystallographic diffraction. SEM images elucidate that coarse elongated grains of the starting as-built material are retained after heat treatment (Fig. 4.3). However, Fig. 4.6b shows a local modulation in the BF contrast of the Al phase, revealing much smaller features in the sub-micrometric range. TEM investigation suggests that the Al matrix is composed of several sub-domains, ranging between few tens and few hundreds of nm in size. Additionally, such domains appear highly defective, as elucidated by local dark contrast modulations in Fig. 4.6c likely due to a disordered structure.

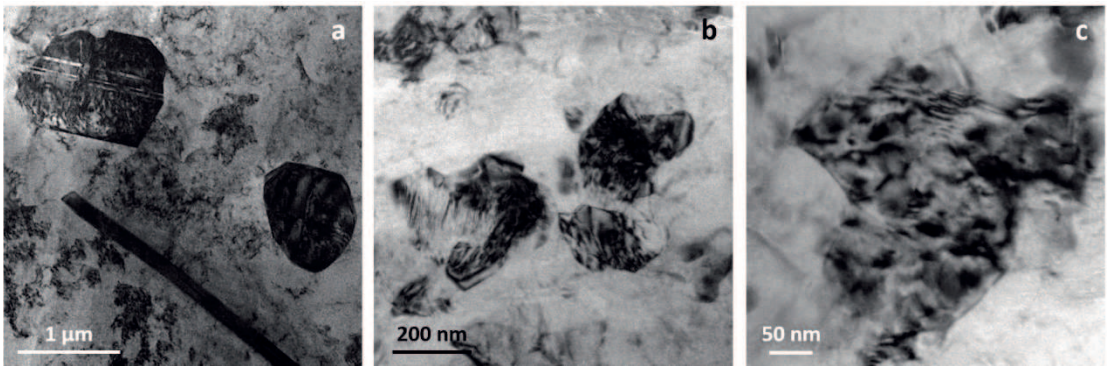

Figure 4.6. TEM observations of the HPT6$_{150}$ alloy. (a) BF TEM micrograph of Si particles and acicular Fe-rich compound. (b) Sub-micrometric Al grains. (c) Detailed image of a sub-grain showing a defective structure.

Figure 4.7a shows features similar to Fig. 4.6. According to the literature [36]–[38], the brighter areas in Fig. 4.7a represent dislocation-free Al sub-grains or cells, and these are separated by darker areas that represent heavily defective zones. As depicted in Fig. 4.7b, these ones may represent Al sub-grains with a high density of dislocations or dislocation tangles, which form dense dislocation walls along the boundaries of neighbouring sub-grains. Figure 4.7c shows the SAED pattern corresponding to the area in Fig. 4.7a. The squared pattern of intense spots corresponds to the Al crystal structure aligned along the $[001]_{Al}$ zone axis. The circular shape of $[020]_{Al}$ Bragg reflections appear slightly distorted, indicating that dislocation tangles gathered and had a small angular misorientation between boundaries [37], [38].

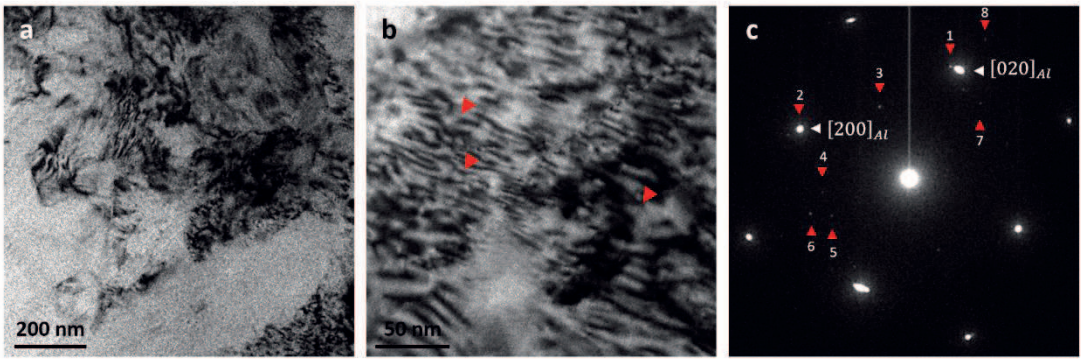

Figure 4.7. TEM observations of the HPT6$_{150}$ alloy. (a) Al domains with dislocation tangles in their interior. (b) Dense dislocation tangle pointed out by red markers, which separates adjacent Al domains. (c) SAED pattern of (b), red markers show reflections matching with the ageing-induced precipitates.

The red markers in Fig. 4.7c highlight additional weak spots in the squared Al pattern. Some investigators reported that nanometric Si particles precipitate during ageing of AM produced Al-Si alloys, given the high degree of supersaturation in the as-built state [4], [30]. Additionally, several Mg-bearing compounds are reported in the precipitation sequence of aged Al-Mg-Si alloys [19], [21], [22] (Tab. 4.2). The analysis of these additional spots, summarised in Tab. 4.4, was conducted considering the associated d-spacing and their mutual orientation. The results do not agree with the Si phase but, among the considered compounds, show a good match with the hexagonal B′-$Mg_9Al_3Si_7$ [21] and monoclinic β′′-Mg_5Si_6 [19], [39] phases. This latter is commonly associated with peak-aged Al-Mg-Si alloys, whereas the former is usually reported in over-aged alloys and AM produced A357 alloys subjected to ageing after a short (1 h) solution heat treatment [40].

Table 4.4. Analysis and match of diffraction spots marked in Fig. 4.7c.

Spot	d_{exp} [Å]	η_{exp} [deg.]	Match	h	k	l	d_{sim} [Å]	η_{sim} [deg.]	$\lvert\Delta d\rvert$ [Å]	$\lvert\Delta\eta\rvert$ [deg.]
1	2.067	3.7	β′′	6	0	1	2.107	0.0	0.041	3.7
			B′	5	-4	0	1.956	8.1	0.111	4.4
2	2.024	90.8	β′′	-4	0	3	2.126	91.2	0.102	0.4
			B′	-1	-4	0	1.956	90	0.068	0.8
3	3.149	47.6	β′′	0	0	2	3.251	57.1	0.102	9.5
4	2.732	122.8	B′	-3	-1	0	2.486	125.1	0.246	2.2
5	2.814	139.2	B′	-3	0	0	2.988	139	0.173	0.2
6	2.320	133.2	B′	-4	0	0	2.241	139	0.079	5.8
7	2.377	18.5	β′′	6	0	0	2.437	17.6	0.06	0.9
8	1.550	4.0	β′′	8	0	1	1.650	3.4	0.099	0.5

η = angle to $[020]_{Al}$; ^{exp} = experimental; ^{sim} = simulated

Crystallographic interpretation of the SAED pattern suggests the formation of precipitates within Al crystals, with a coherent orientation to the matrix, and this requires further observations of the Al lattice at high magnification. The HRTEM image

in Fig. 4.8a shows a set of contrast fringes superimposed on the [100]-oriented Al lattice. Based on the FFT of the HRTEM image (Fig. 4.8b), the analysis of spatial frequencies shows that these fringes correspond to a lattice with a 2.21 Å spacing oriented at 23° along the $[020]_{Al}$ direction. The spatial frequencies circled in white in Fig. 4.8b represent sets of planes with spacing in the range of 2.21-4.81 Å, and they do not correspond to the Al fringe pattern or possible Si reflections. In agreement with the SAED pattern in Fig. 4.7c, such spatial frequencies well match with the B'-$Mg_9Al_3Si_7$ and β''-Mg_5Si_6 phases. Figure 4.8c shows the inverse masked FFT generated using the frequency pointed at by an arrow in Fig. 4.8b, showing the presence of a small compound 4-5 nm in size.

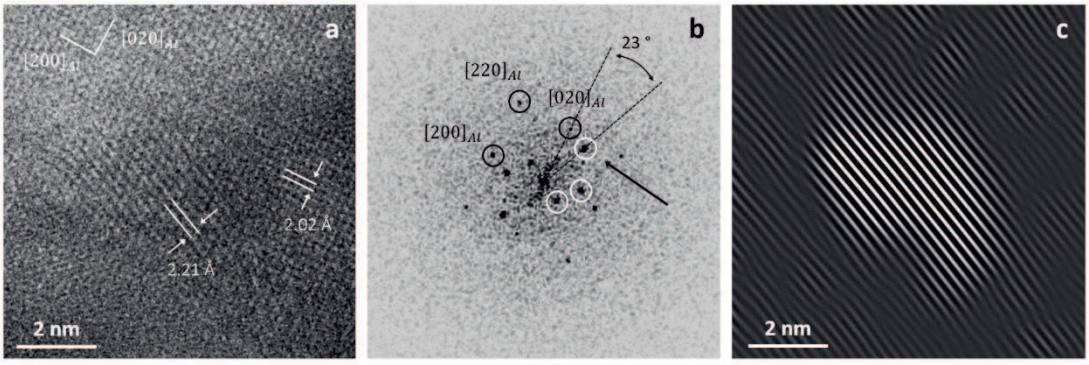

Figure 4.8. TEM observations of the $HPT6_{150}$ alloy. (a) HREM micrograph showing a fringe pattern tilted to the Al matrix. (b) FFT of (b) showing spatial frequencies (white circles) in the Al squared pattern (black circles). (c) Inverse FFT using the frequency pointed at by an arrow in (b) showing the presence of a nanometric precipitate.

TEM investigation reveals other similar features, all with sizes in the range 4-10 nm and closely matching either B'-$Mg_9Al_3Si_7$ or β''-Mg_5Si_6 phases. The HRTEM image in Fig. 4.9a shows a set of broad contrast fringes that indicates a lattice with a 4.52 Å spacing oriented at 21° along the $[200]_{Al}$ direction, which corresponds to the frequency pointed at by an arrow in the FFT (Fig. 4.9b). The inverse masked FFT in Fig. 4.9c is produced using the same frequency and highlights a nanometric compound. Figure 4.9d shows that the simulated pattern of the [010] zone axis-oriented β'' phase satisfactorily matches the experimental "digital" FFT pattern. Accordingly, the marked frequency in Fig. 4.9b likely correspond to the $[201]_{\beta''}$ reflection.

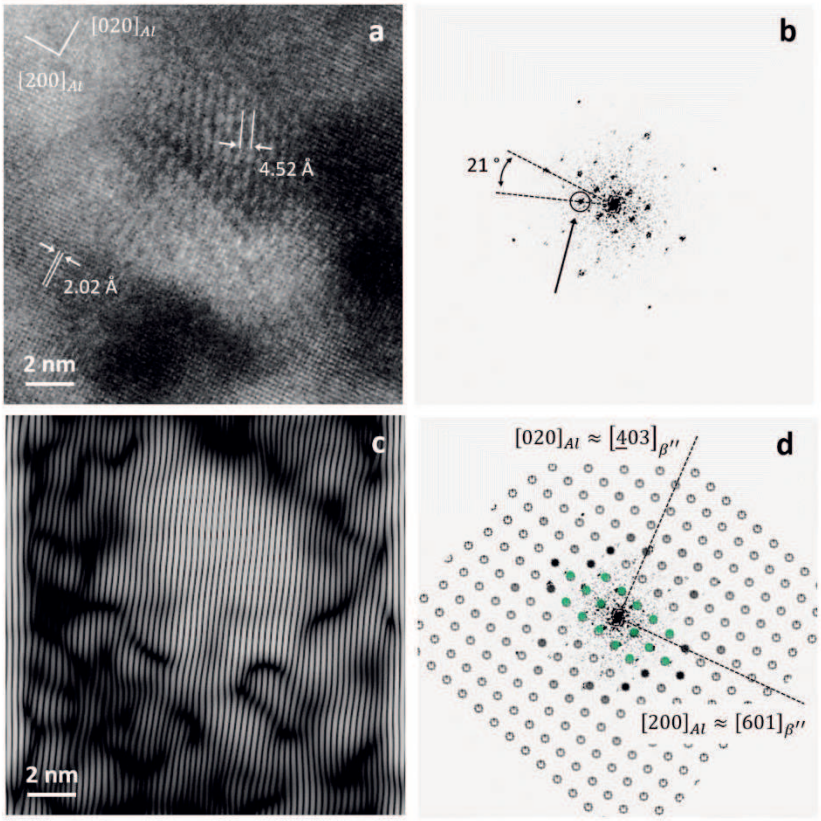

Figure 4.9. TEM observations of the HPT6150 alloy. (a) HREM micrograph showing a fringe pattern tilted to the Al matrix. (b) FFT of (b) showing spatial frequencies in the Al squared pattern. (c) Inverse FFT using the frequency pointed at by an arrow in (b) showing the presence of a nanometric precipitate. (d) Match between FFT and simulated pattern of the β'' phase. Simulated β'' and experimental Al patterns are superimposed according to Tab. 4.2.

An additional example is reported in Fig. 4.10a, where multiple sets of fringes are visible superimposed to the Al lattice. The spatial frequency marked by an arrow in the FFT image (Fig. 4.10b) corresponds to a set of fringes 2.34 Å spaced and tilted at 34° to the $[020]_{Al}$ direction. The compound revealed by the inverse masked FFT image in Fig. 4.10c using the same spatial frequency is about 10 nm in size. The experimental FFT pattern, which displays several frequencies inside the squared Al pattern, reasonably agrees with the simulated one of the [001] zone axis-oriented B'-$Mg_9Al_3Si_7$ phase (Fig. 4.10d).

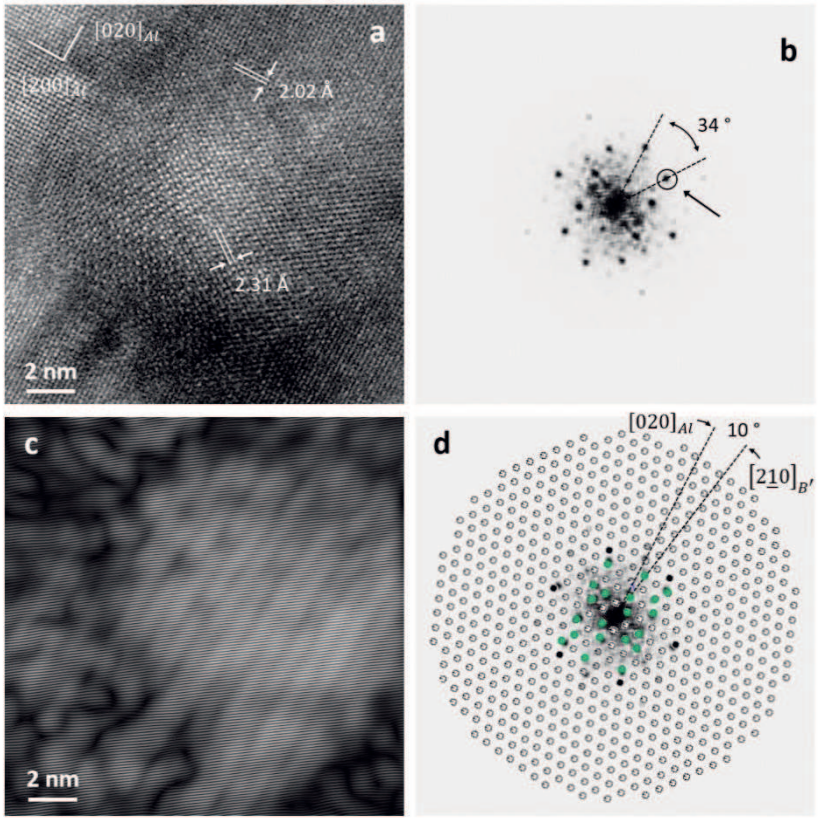

Figure 4.10. TEM observations of the HPT6150 alloy. (a) HREM micrograph showing a fringe pattern tilted to the Al matrix. (b) FFT of (b) showing spatial frequencies in the Al squared pattern. (c) Inverse FFT using the frequency pointed at by an arrow in (b) showing the presence of a nanometric precipitate. (d) Match between FFT and simulated patterns of the B′ phase. Simulated B′ and experimental Al patterns are superimposed according to Tab. 4.2.

Finally, nanometric Si particles sometimes could be detected, as reported in Fig. 4.11. The HRTEM image in Fig. 4.11a shows a set of broad fringes, whereas the corresponding FFT (Fig. 4.11b) displays four distinct spots. The analysis of measured d-spacings and mutual angles elucidates that spatial frequencies circled in white correspond to a lattice with a 3.13 Å spacing, and thus to $\{111\}_{Si}$ Si reflections. The frequency circled in black matches the $[111]_{Al}$ direction, whereas the one marked in red, corresponds to a Moiré set of fringes due to the superimposition of the Si and Al lattices. This latter mainly dominates the amplitude contrast in the HRTEM image Fig. 4.11a. The inverse masked FFT image reveals the nanometric size of the Si compound (Fig. 4.11c).

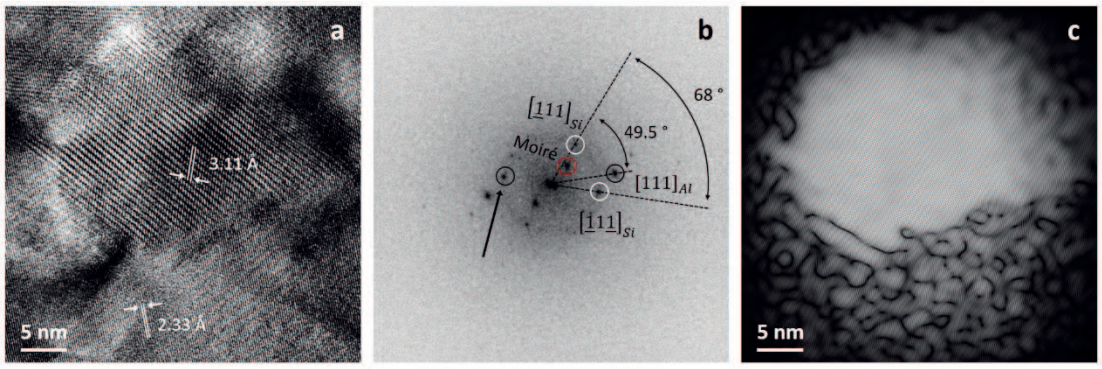

Figure 4.11. TEM observations of the HPT6150 alloy. (a) HREM micrograph showing a fringe pattern tilted to the Al matrix. (b) FFT of (b) showing four main spatial frequencies; white, black and red circles correspond to Si, Al and Moiré fringes, respectively. (c) Inverse FFT using the frequency pointed at by an arrow in (b), showing the presence of a nanometric Si particle.

It is worth noting that, despite the generally good match between experimental and simulated data, the TEM results reported in this section do not permit to determine the nature of the ageing-induced precipitates unambiguously. However, this aspect is beyond the scope of this study, since it successfully demonstrates that the novel combination of HIP and ageing treatment under pressure is capable of inducing precipitation strengthening in AlSi10Mg alloys.

4.3.3 Quantitative X-ray diffraction analyses

Figure 4.12 shows the full XRD patterns of samples in each investigated condition. In these patterns, only reflections of Al and Si phases could be detected. Mg-based compounds are expected to precipitate after ageing treatment in AlSi10Mg alloys, as suggested by TEM investigation in the previous section for the HPT6150 sample. However, none of the aged specimens shows the reflections of possible strengthening precipitates. Accordingly, just the Al and Si phases were included in the pattern simulations by the Rietveld refinement.

Inset I in Fig. 4.12 illustrates that Si reflections of the as-built and annealed samples display a broadened peak with reduced intensity when compared to patterns of high-temperature heat-treated specimens. The former feature indicates that crystalline Si domains gradually increase in size during the heat treatment, starting from the as-built state. Instead, the increased intensity of Si reflections after heat treatment suggests a gradual increase of the amount of crystalline Si.

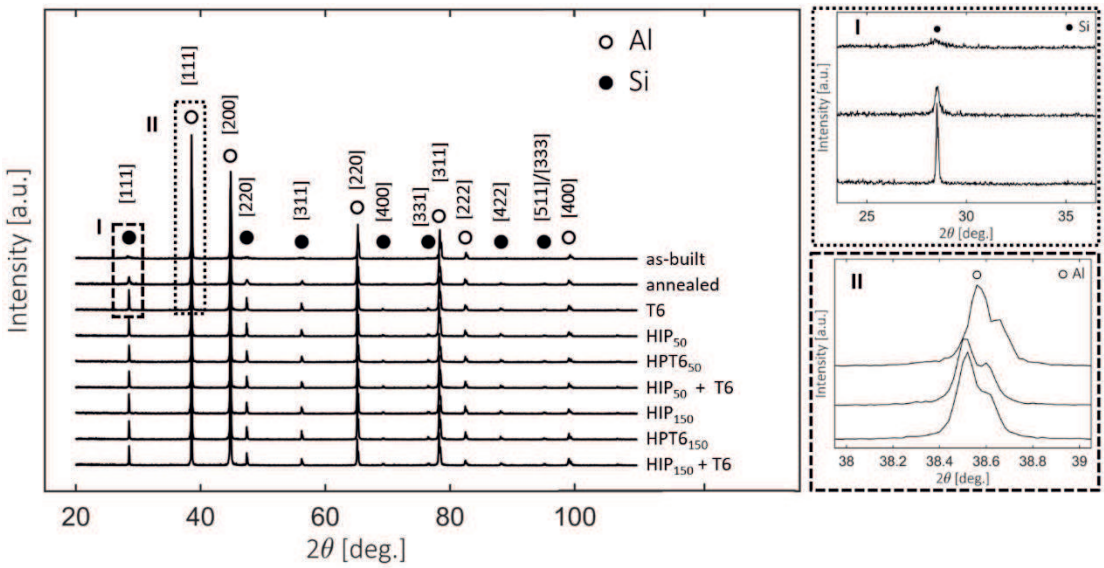

Figure 4.12. Full XRD pattern of samples in different heat-treatment conditions; inset I shows the broadening of Si peaks; inset II shows the shift of Al peaks.

In the as-built condition, Al reflections shift to higher 2θ angles, which means a lower Al lattice parameter as described by the Bragg equation. Inset II in Fig. 4.12 displays such feature, for instance, for the $[111]_{Al}$ reflection. Distortion in the phase lattice produces a shift in the corresponding reflections due to either microstructural (*e.g.*, altered solid solution) or mechanical (*e.g.*, residual stresses) effects.

Figure 4.13 shows the lattice parameters of the Al phase for each investigated condition. The results obtained from Rietveld refinement and the $\cos^2(\theta)/\sin(\theta)$ method are in agreement with each other. Both confirm that the as-built alloy exhibits the lowest lattice parameter of 4.0459 and 4.0458 Å for the two methods, respectively. After each heat treatment, this value increases more or less to the equilibrium value, which for Al in AlSi10Mg alloys is reported to be 4.0515 Å [29]. The disappearance of Al lattice distortions suggests it to be a process-related alteration quickly recovered after heat treatment, even with low-temperature annealing.

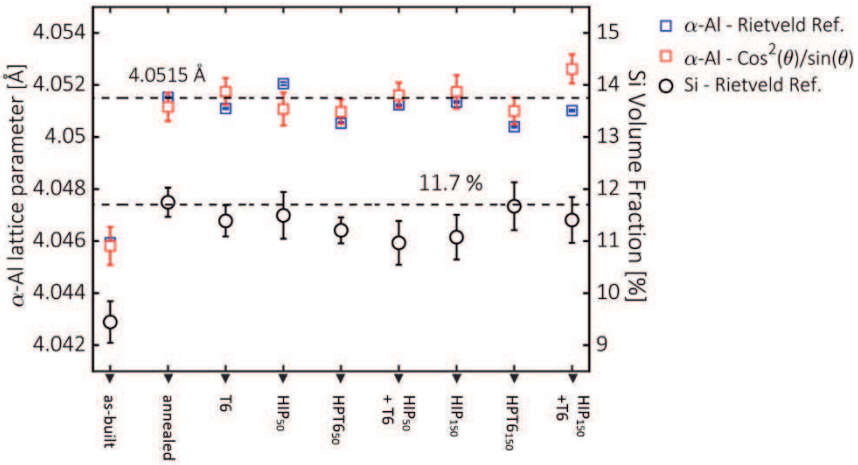

Figure 4.13. Quantitative results from XRD pattern of samples in different heat-treatment conditions: lattice parameter of the Al phase and volume fraction of the Si phase; the error is presented as the estimated standard deviation.

Figure 4.13 also reports the Si volume fraction calculated using the Rietveld method. In agreement with the analysis of the Al lattice parameter, the as-built alloy shows the lowest Si volume fraction of ~9.4 %, which reflects the low intensity of Si reflections. After heat treatment, all the calculated values are close to the equilibrium value of 11.7 %. Hence, unlike in the as-built state, the reduced intensity of Si peaks in the annealed alloy is not related to a low Si volume fraction. The widening of Si peaks can be ascribed to the small particle size of Si in the range of tens of nm, which mirrors the results of the microstructural investigation (Fig. 4.2d).

4.3.4 Density and mechanical properties

Density measurements were conducted to analyse the densification effect of HIP treatment. Table 4.5 reports the results obtained in terms of relative density. In the as-built condition, the alloy is almost entirely dense with a relative density of 99.8 %. Conversely, conventional T6 heat treatment reduces the relative density to 97.9 %. These values are considered as the upper and lower thresholds for evaluating the effectiveness of the HIP process. Despite the low temperature employed, annealing reduces the relative density to 99.1 %. Even though their relative densities are lower than that of the as-built sample, all the HIP treated samples show values greater than 99 %, confirming

the densification effect of HIP treatment [11]. Furthermore, there are no significant differences in the relative density when the pressure is changed from 50 to 150 MPa.

Table 4.5. Characteristic impact toughness parameters and Brinell hardness.

	Relative Density [%]	F_P [kN]	E_I [J]	E_P [J]	Hardness [HBW]
as-built	99.8 ± 0.2	6.8 ± 0.07	2.6 ± 0.1	2.1 ± 0.09	125 ± 1
annealed	99.1 ± 0.1	6.9 ± 0.03	7.8 ± 0.10	11.3 ± 0.16	87 ± 1
T6	97.9 ± 0.3	6.4 ± 0.20	2.3 ± 0.35	0.4 ± 0.06	104 ± 1
HIP_{50}	99.5 ± 0.1	5.4 ± 0.14	5.8 ± 0.39	5.0 ± 0.09	79 ± 1
$HPT6_{50}$	99.5 ± 0.1	6.6 ± 0.06	3.3 ± 0.01	1.6 ± 0.14	100 ± 1
HIP_{50} + T6	99.2 ± 0.1	6.6 ± 0.03	3.0 ± 0.08	0.6 ± 0.04	99 ± 2
HIP_{150}	99.4 ± 0.2	5.4 ± 0.22	5.5 ± 0.48	4.6 ± 0.09	83 ± 1
$HPT6_{150}$	99.5 ± 0.2	6.8 ± 0.19	3.4 ± 0.08	1.1 ± 0.09	104 ± 1
HIP_{150} + T6	99.4 ± 0.1	7.2 ± 0.17	3.0 ± 0.54	0.7 ± 0.16	111 ± 1

Table 4.5 also shows the impact parameters calculated from the Charpy force-displacement curves in Fig. 4.14 and the results of Brinell hardness tests. A high impact strength characterises the as-built material: the calculated F_P of ~7 kN is much higher than that previously reported for cast Al-Si-Mg alloys [41] and agrees with an outstanding hardness value of ~125 HBW. Nevertheless, this sample suffers from a low total absorbed energy (4.7 J), which is about equally divided between crack initiation (2.6 J) and propagation (2.1 J) stages. Regardless of the pressure level, HIP application softens the material. It enhances E_I and E_P by a factor 2 when compared to the initial state, but reduces the impact strength by ~20 % to 5.4 kN. Similarly, the hardness of the alloy reduces to ~80 HBW.

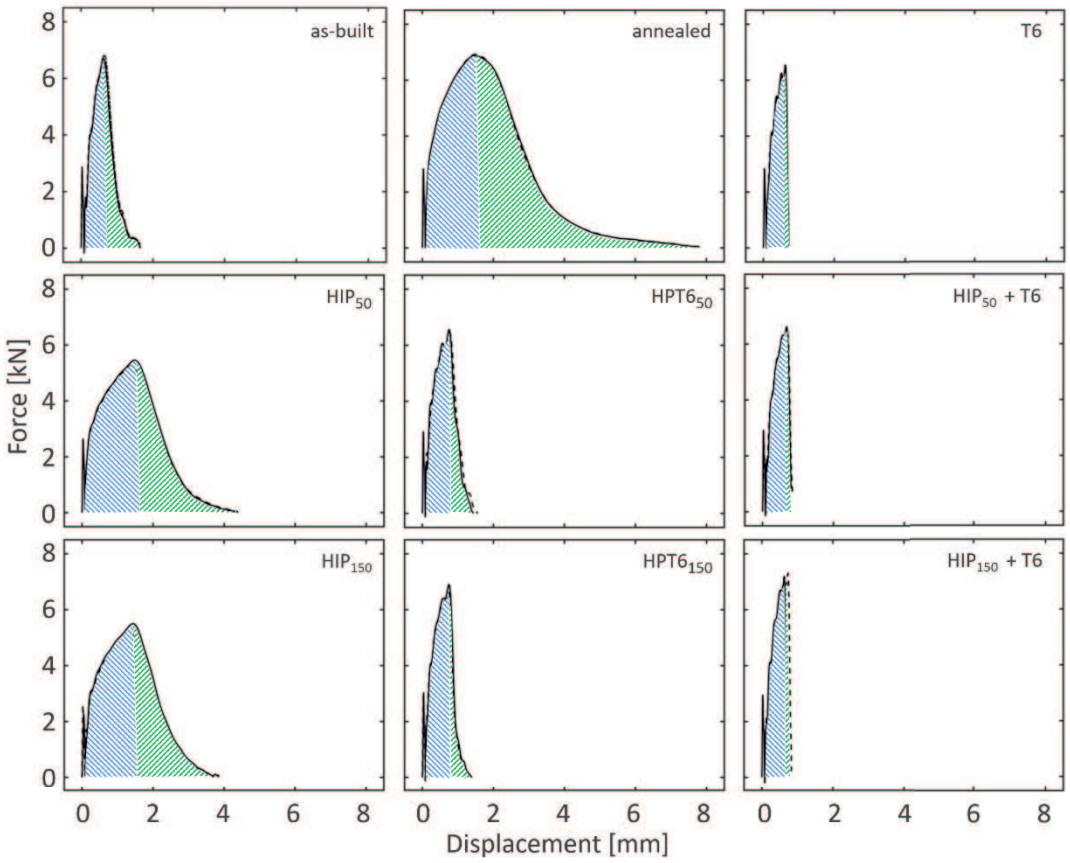

Figure 4.14. Force-displacement curves from Charpy impact tests of the alloy in different heat treatment conditions. Areas marked in blue and green correspond to initiation (E_I) and propagation (E_P) energies, respectively. Solid and dashed lines show the reproducibility of results of different tested samples.

The HPT6 and HIP + T6 samples have F_P and hardness values closer to the as-built state (6.6-7.2 kN and 100-110 HBW, respectively). The absorbed initiation energy E_I is slightly higher (3.0-3.4 J), and this is accompanied by a remarkable drop in E_P (0.6-1.5 J). In addition, this decrease is slightly higher in HIP + T6 samples than in HPT6 ones. The characteristic impact parameters of T6 alloys follow similar trends, but each of them is the lowest in the corresponding category when compared to the rest of the alloys subjected to different ageing-treatment conditions. The enhanced ductility of the annealed alloy increases its E_I and E_P by a factor of 3 and 5, respectively, when compared to the initial state. Interestingly, the impact strength of the annealed alloy matches that of the as-built alloy, whereas its hardness reduces by ~30 % to 87 HBW.

4.3.5 Fractographic investigation

Figure 4.15a depicts the fracture surface of the as-built alloy, in which the semi-circular outlines of melt pool sections are readily detectable and marked by dotted lines. The moderate flatness of the fracture surface at a low magnification suggests a brittle fracture behaviour. Figure 4.15b shows several emerging ridges, mostly elongated radially to the traces of melt pools, along the preferred orientation of grains and cellular dendrites (Fig. 4.1). At higher magnification, it can be observed that these ridges emerge from Al dendrites to form fine irregular dimples, which host continuous stripes of the Si network, marked by arrows in Fig. 4.15c.

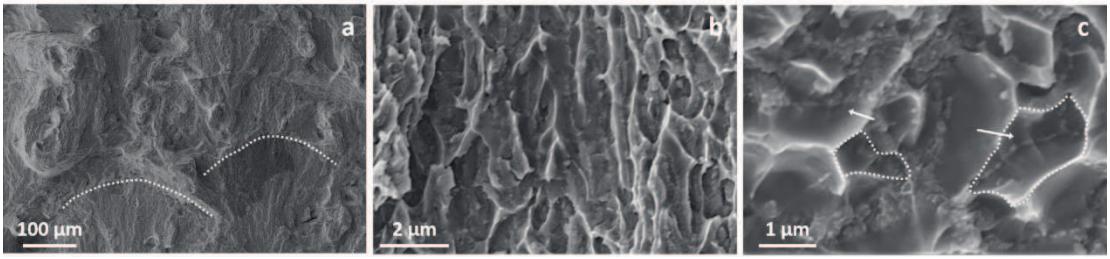

Figure 4.15. Fracture surface of the sample in the as-built condition. (a) Panoramic view of the surface, the dotted lines show traces of the melt pool boundaries. (b) Elongated ridges. (c) Irregular dimples, the arrows point out traces of the Si network.

The SEM images in Fig. 4.16 show details of the fracture surface of the annealed alloy. Footprints of the scan tracks are still detectable, as underlined in Fig. 4.16a by a dotted line. The higher magnification image in Fig. 4.16b indicates the presence of fine equiaxed dimples that could not be observed in the as-built sample. Figure 4.16c shows that each dimple hosts nanometric Si particles.

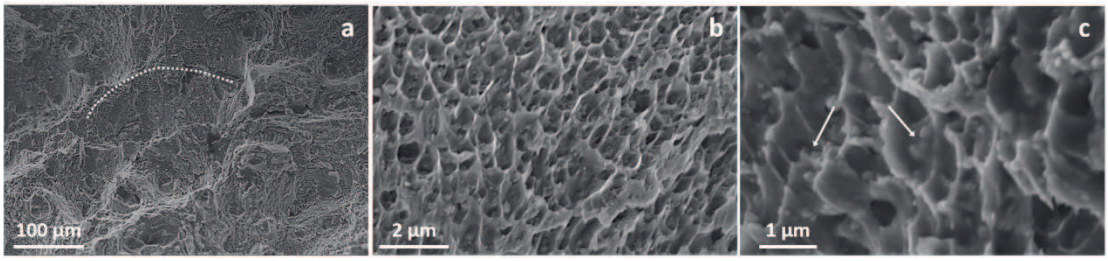

Figure 4.16. Fracture surface of the sample in the annealed condition. (a) Panoramic view of the surface, the dotted line shows traces of the melt pool boundaries. (b) Fine equiaxed dimples. (c) Si particles, marked by arrows, emerging inside the dimples.

Figure 4.17 shows characteristic fracture surfaces of samples heat-treated at a high temperature. Coarse, equiaxed, and deep dimples, several µm in size, appear on the

fracture surfaces of solely HIP treated alloys, as shown in Fig. 4.17a, suggesting a ductile fracture behaviour. Compared to the fine dimples seen in the annealed alloy (Fig. 4.16b), dimples in HIP treated samples are approximately one order of magnitude larger in size. This feature is consistent with the coarsening of Si particles (Fig. 4.3 and Fig. 4.5) during the heat treatment of the alloy at high temperatures. At higher magnifications (Fig. 4.17b), both Si particles and Fe-rich compounds are detected inside the dimples, as confirmed by EDX analysis.

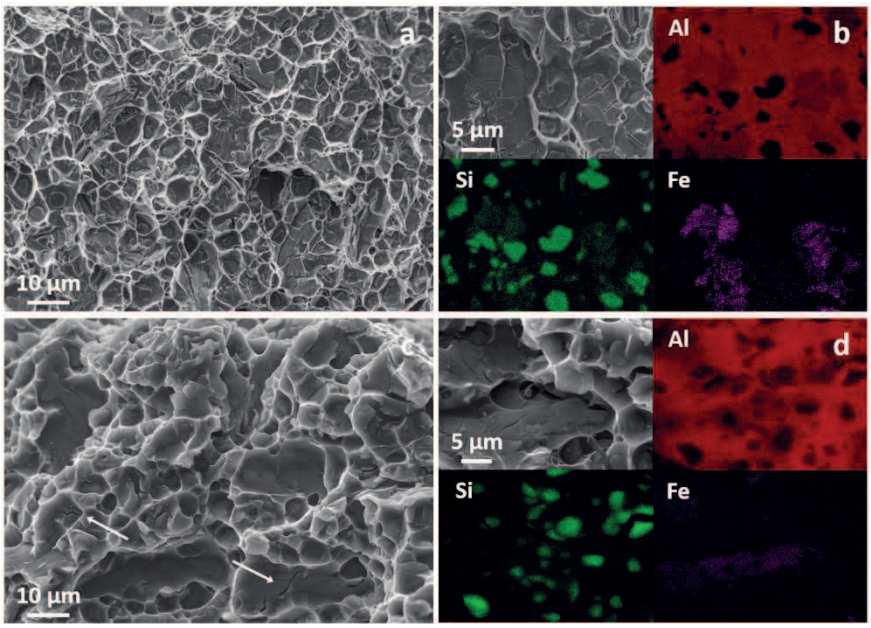

Figure 4.17. Fracture surfaces of samples after high-temperature heat-treatment other than T6. (a-b) Without and (c-d) with the final ageing treatment. (b) and (d) EDX elemental mapping of Al, Si, and Fe from dimples in (a) and (c), respectively. The arrows in (c) mark secondary cracks.

Figure 4.17c depicts a representative fracture surface of the alloys subjected to ageing as the final step of the heat-treatment process. Compared to the solely HIP treated samples, shallow and smaller dimples appear, together with many secondary cracks in brittle secondary phases. These facts account for the less ductile fracture behaviour of the aged alloys compared to the solely HIP treated ones, as expected from the formation of strengthening compounds. The EDX map in Fig. 4.17d highlights the presence of a large number of Si particles and cracked Fe-compounds, similarly to Fig. 4.17b.

Porosity is not detectable on the fracture surfaces of HIP treated samples, which indicates successful densification. However, pores are abundant on the fracture surface of solely T6 samples, as highlighted by Fig. 4.18.

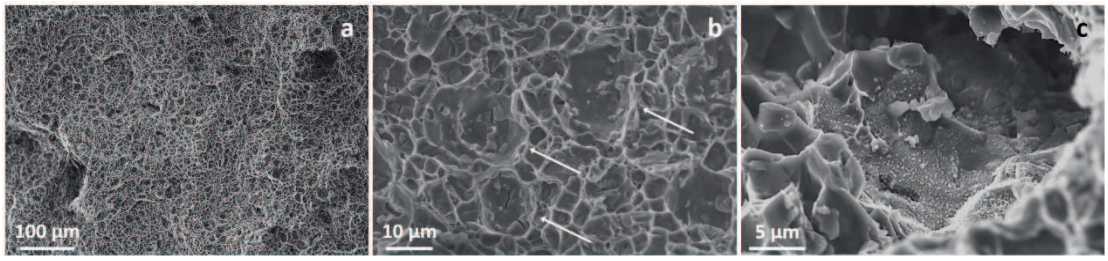

Figure 4.18. Fracture surfaces of the sample after T6 heat-treatment. (a) Panoramic view of the surface with a dimple-like appearance. (b) Coarse dimples, the arrows mark pores. (c) Detailed image of a pore with possible surface oxides.

At low magnification (Fig. 4.18a), the surface exhibits a dimple-like appearance, and several sparse pores ~10-20 µm in size, marked by arrows in Fig. 4.18b, can be observed. The size of pores on the fracture surface well matches the one measured on polished sections (Fig. 4.3c-d). Figure 4.18c is a detailed image from the inner part of a pore, which exhibits fine droplets on its surface. Such sub-micrometric features likely are de-wetted Al-based oxides [42].

4.4 DISCUSSION

4.4 Comparison of as-built and low-temperature heat-treated samples

The as-built sample exhibits a hierarchical microstructure inside the melt pools (Fig. 4.1a), with coarse and elongated grains (Fig. 4.1b) composed of fine Al cellular dendrites surrounded by Si network (Fig. 4.1c-d). XRD results (Fig. 4.13) show that the Si volume fraction is ~9.4 %, which is much lower than the value predicted (11.7 %) from the phase diagram. EDX was conducted at a low accelerating voltage inside the Al dendrites to clarify these results, and it measured an average Si content of ~2.4 wt. % (the average was calculated from 10 readings). This latter is much higher than the equilibrium value reported for Al-Si-Mg alloys (<0.1 %) and stems from the high solidification rate in the L-PBF process [43]. This value was set as the Si content (wt. %) in the Al solid solution and was used to generate the mass-balance equation. The densities of Si and Al phases and the corresponding binary alloy were set at 2.33, 2.7, and 2.68 g/cm^3, respectively, together with a total content of 10.24 wt. % for Si (Table 4.1). From the mass balance, a volume fraction of 9.3 % was calculated for Si, which is similar to the value obtained by Rietveld refinement. The noteworthy mechanical resistance of the as-built alloy, both in terms of impact strength and hardness, is likely related to its fine microstructures and Si

solid solution. On the contrary, the impact toughness is relatively low. As density measurements reveal a highly dense material, potential porosity cannot be held to be responsible for the low absorbed energy. This latter is more reasonably related to the limited deformability of the as-built alloy, as suggested by the flat fracture surface in Fig. 4.15, and to possible residual internal stresses [34], dislocation networks [33], and solid-solution strengthening [44].

Annealing leads to the rupture of the Si network (Fig. 4.2c-d) but does not significantly modify the coarse grains (Fig. 4.2b). XRD analysis revealed that both the Al lattice parameters and Si volume fraction are restored to equilibrium values (Fig. 4.13). The hardness of the alloy decreased to 87 HBW compared to its initial value, but its ductility, as suggested by the absorbed impact energy, increased significantly. This outcome agrees with the ductile dimple-like fracture surface in Fig. 4.16 and with the tensile behaviour reported earlier [1], [30], [43]. Unlike hardness, the impact strengths of the annealed and as-built alloys are similar. The contribution of each microstructural strengthening mechanism to the yield strength (YS) of the as-built and annealed alloys was calculated to elucidate these findings better. Five mechanisms were considered, namely grain boundaries (Hall–Petch), precipitates (Orowan), dislocations (Taylor), solid-solution and load-bearing phase strengthening mechanisms. Table 4.6 shows the corresponding constitutive equations and numerical values and Fig. 4.19 graphically depicts the contribution of each mechanism.

Constant internal friction stress was ascribed to both alloys. The Hall–Petch effect was considered to originate from both Al dendrites and grains in the as-built alloy, while only the grains contributed to this effect in the annealed alloy [30]. The mean widths of the cellular dendrites and grains reported in Section 4.3.1 were used to analyse the observed Hall-Petch relationship. The overall volume fraction of nanometric Si particles was considered to contribute to Orowan strengthening in the annealed alloy, and the calculated ED was used as the particle size. Some studies report the presence of nanometric Si precipitates in Al dendrites in the as-built alloy [33], [45], but they were not detected in the present work (Fig. 4.1d), probably due to differences in the process parameters employed. Therefore, there was no Orowan strengthening in the as-built alloy, as the Si phase was involved either in the eutectic network or in solid-solution strengthening. The amount of Si measured by EDX was used to analyse the solid-

solution reinforcement. The Taylor strengthening mechanism was supposed to be active only in the as-built alloy, assuming that dislocation networks can be recovered by annealing. In the load-bearing phase mechanism, a constant Si/Al interface strength was used.

Table 4.6. Constitutive equations and corresponding parameters for the YS estimation

	Relationship		as-built	annealed
Strengthening mechanism	Internal friction	σ_0	$\sigma_0 = 72\ MPa$ [46]	$\sigma_0 = 72\ MPa$ [46]
	Taylor	$\beta MGb\sqrt{\rho_d}$	$\beta = 0.16$ [33] $M = 3.06$ [47] $G = 27000\ MPa$ $b = 0.286\ nm$ [47] $\rho_d = 1.14 \cdot 10^{14}\ m^{-2}$ [45]	-
	Hall-Petch	$\frac{k}{\sqrt{d_{cell}}} + \frac{k}{\sqrt{d_{grain}}}$	$k = 40\ MPa \cdot \mu m^{0.5}$ [48] $d_{cell} = 0.4\ \mu m$ $d_{grain} = 7.5\ \mu m$	$k = 40\ MPa \cdot \mu m^{0.5}$ [48] $d_{grain} = 7.5\ \mu m$
	Solid solution	KC^N	$K = 13\ MPa \cdot at.\ \%^{-1}$ [49] $C = 2.4\ at.\ \%$ $N = 1$ [49]	$K = 13\ MPa \cdot at.\ \%^{-1}$ [49] $C = 0.5\ at.\ \%$ [50] $N = 1$ [49]
	Orowan	$\frac{\varphi Gb}{d_{Si}} \cdot \left(\frac{6V_{Si}}{\pi}\right)^{1/3}$	-	$\varphi = 0.4$ [51] $d_{Si} = 92\ nm$ $V_{Si} = 0.117$
	Load-bearing phase	$1.5 \cdot \sigma_i \cdot V_{Si}$	$\sigma_i = 240\ MPa$ [52] $V_{Si} = 0.094$	$\sigma_i = 240\ MPa$ [52] $V_{Si} = 0.117$
Estimation of YS	Cahoon [53]	$\left(\frac{HBW}{3}\right)(0.1)^n \cdot 9.81$	$HBW = 125$ $n = 0.2$ [4]	$HBW = 87$ $n = 0.2$ [4]

As shown in Fig. 4.19, the calculated yield strength of the annealed alloy (155 ± 2 MPa) was 35 % lower than that of the as-built alloy (255 ± 8 MPa). For comparison, experimental values of YS from tensile tests of the as-built (251 ± 6 MPa) and annealed (151 ± 6 MPa) samples were taken from previous work [14]. Additionally, YS was also

estimated from hardness measurements according to the relationship proposed by Cahoon *et al.* [53] (Tab. 4.6). A constant value of 0.2 was used for the strain-hardening coefficient n. The estimated values are 258 ± 2 MPa and 180 ± 2 MPa for the as-built and annealed alloys, respectively.

Figure 4.19 compares the experimental values [14], the estimated values and those calculated for different microstructural strengthening mechanisms. It can be noted that there is an excellent agreement between all values related to the as-built alloy. Calculated and experimental values also match for the annealed alloy, whereas the value estimated from hardness is ~25-30 MPa higher. Despite such difference, the strength of the annealed alloy (either calculated, experimental or estimated) is significantly different from that of the as-built alloy. Hence, the numerical results obtained from microstructural observations better agree with hardness and tensile measurements rather than impact tests, where both alloys exhibit a similar strength.

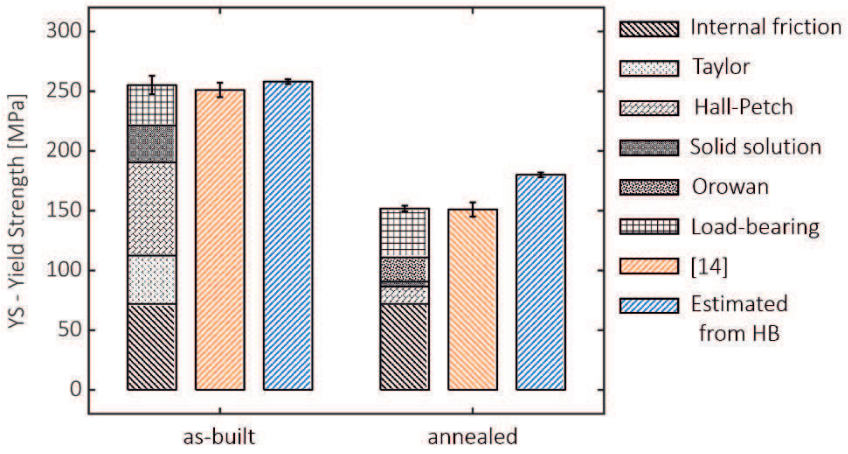

Figure 4.19. Microstructural contributions to yield strength of the as-built and annealed alloys; experimental values from tensile tests [14] and values estimated from hardness tests are shown for comparison.

Such a discrepancy might be attributed to the lack of strain-rate dependency in the constitutive equations in Tab. 4.6. Even though there is not much information available, some authors report a relationship between the microstructure and the corresponding strain-rate sensitivity of the alloy. Das *et al.* [54] showed that steels of different grades display different responses with respect to strain rate. Similarly, Alturk *et al.* [55] verified that strain-rate sensitivity is remarkably high in ferritic and austenitic steels, whereas only a limited difference between quasi-static and high strain-rate tests characterises

dual-phase steels. Millet [56] studied the shock-loading response of a 6061 Al alloy in solution-treated and T6 conditions. As expected, the T6 alloy displayed an increase in strength due to ageing during quasi-static testing as compared to the solution-treated alloy. Conversely, both alloys exhibited a similar response in shock-loading tests, with the material in the T6 state not showing any strain-rate sensitivity. Millet attributed such behaviour to differences in the initial microstructure of the alloys.

Likely, the discrepancy between the as-built and annealed alloys in terms of impact, hardness and tensile strength can be explained similarly. Dislocation movement in the as-built alloy is strongly hindered by the increased solid-solution content and the high number of pre-existing defects, such as grain boundaries and dislocation tangles [45]. Hence, relatively few new dislocations are generated during the deformation process, and consequently, the strain-rate sensitivity is rather low. Conversely, the relatively weak microstructure of the annealed alloy could be easily deformed, with a significant formation and movement of new dislocations. In impact tests, owing to the different strain rat sensitivities, similar impact strengths are observed for the annealed and as-built alloys. However, significant differences in strength are observed from quasi-static hardness and tensile tests. Further TEM investigations regarding microstructural evolution after impact tests are required for a deeper understanding of this phenomenon.

4.4.2 Comparison of HIP and high-temperature heat-treated samples

The T6 heat treatment reduced the relative density of the as-built alloy from 99.8% to 97.8%, due to growth of the pre-existing pores at high temperatures (Fig. 4.3c-d). In the present study, the presence of keyhole and lack-of fusion pores can be considered to be negligible as the process parameters were optimized. However, some small pores (few microns in size) might form during the AM process due to the entrapment of the inert shielding gas or by moisture absorption. At the high temperatures of the T6 heat treatment, the reduced material strength and increased gas pressure allowed the pores to grow significantly, as depicted in Fig. 4.3c-d, which consequently reduced material density and affected mechanical properties.

HIP treatment results in effective densification, regardless of the applied pressure, with the relative density of HIP, HPT6, and HIP + T6 alloys always being higher than

99%. Nonetheless, the exposure to high temperatures coarsened the Si particles and promoted needle-like Fe-rich compounds. Additionally, the absence of a subsequent ageing treatment indicates that strengthening compounds are not formed. These observations align with the limited impact strength (~5.5 kN), and hardness (~80 HBW) of the HIP treated samples and explains their high total absorbed energy (~10 J) and ductile behavior (Fig. 4.17a).

After HIP, HPT6 samples were furtherly subjected to ageing under high pressure, which is expected to affect the precipitation behavior, owing to the low employed temperature. The diffusion coefficient D depends on temperature and pressure, according to [57]:

$$D = D_0 e^{-\left(\frac{\Delta H}{RT}\right)} = D_0 e^{-\left(\frac{\Delta U + P\Delta V}{RT}\right)} \quad (1)$$

where D_0 is a pre-exponential factor, ΔH is the enthalpy change, ΔU is the activation energy of the diffusion process at atmospheric pressure, P is the relative pressure, ΔV is the activation volume. If both D_0 and ΔU are independent of pressure, and assuming a reasonable value of ΔV for strengthening compounds in Al alloys (~10^4 mm^3/mol [57]), the diffusion coefficient during ageing performed at T = 453 K (180 °C) and P = 150 MPa is ~2/3 of the diffusion coefficient at atmospheric pressure. Additionally, the high pressure raises the transformation temperatures of Al alloys with a baric coefficient of ~6-11 °C/100 MPa [58], which should reduce the driving force for precipitation.

The strength contributions of microstructural features of the HPT6 samples were calculated to deepen the microstructure-properties relationship. While SEM images showed similar grains to that of as-built and annealed samples, TEM investigations revealed a complex sub-grain structure. The contrast modulation in BF TEM images (Fig. 4.7a-b) and stretched spots in the DP pattern (Fig. 4.7c) suggest that the sub-grain structure is composed of dislocation boundaries, which reinforce the alloy by the Taylor mechanism. The area of the dislocation boundaries per unit volume ρ_d [m^{-1}] can be estimated as 2/L [30], where L is the mean length of sub-grains, assumed as ~200 nm from TEM investigations (Fig. 4.6 and Fig. 4.7). Using constants listed in Tab. 4.6, the strengthening contribution from dislocation boundaries is ~38 MPa, the Hall-Petch reinforcement from elongated grains (d_{grain} = 7.5 ± 1 μm - Table 4.6) is ~15 MPa, and the

Orowan contribution from Si particles (V_{Si} = 0.117 ± 0.003 - Fig. 5, d_{Si} = 1.2 ± 0.9 μm - § 4.3.1) is negligible (~2 MPa) due to their micrometric size.

TEM investigations also highlighted nanometric compounds (Fig. 4.8, Fig. 4.9, Fig. 4.10), ranging between ~4-10 nm in size (§ 4.3.2). Using constants listed in Table 4.6, their strengthening contribution by the Orowan relationship, assuming a mean diameter of ~7 nm and a typical volumetric fraction of ~1% [39], is ~118 MPa. Additionally, owing to their coherency with the Al lattice (§ 4.3.2), the interface strength should be in the order of ~700-1000 MPa [59], giving a load-bearing reinforcement of ~10-15 MPa. The addition of all contributes reported above to the internal friction (72 MPa - Table 4.6) yields a calculated strength of ~254 MPa. This value reasonably matches the tensile properties of both HPT6 and HIP + T6 samples (252 MPa and 261 MPa, respectively [14]). Furthermore, it agrees with their increased impact strength (~6.6-7.2 kN) and hardness (~100-110 HBW) as compared to the only HIP treated samples. This simplified analysis suggests that, regardless of the higher pressure of the HPT6 treatment, precipitation was prolific and microstructure was comparable in both HPT6 and HIP + T6 alloys, which agrees with their similar impact and hardness properties.

Beside impact strength, HPT6 and HIP+T6 samples also shared limited absorbed energy. Nanometric ageing-induced compounds are associated with a local strain field at the interface owing to lattice misfit with the parent Al matrix [39]. Consequently, resistance to further deformation and fracture propagation is severely affected, especially at high strain rates. Despite this, fracture surfaces still showed a dimples-like appearance (Fig. 4.17c), which indicates the primary role of Si in damage nucleation and fracture behavior. It is worth to note that the exposure to high temperatures also promoted plate-like Fe-based compounds, whose brittleness affects negatively energy absorption and fracture behavior of the alloy. However, the reduced volumetric fraction (~0.66-0.83%, § 4.3.1) and micrometric size reasonably hide their effect as compared to Si particles and strengthening compounds in both HIP- and ageing-treated samples. In this light, they were not considered in the analyses reported above.

Despite the different processing route, HPT6 and HIP+T6 samples showed a similar microstructure. The analysis of strengthening contributions from microstructural features supported this observation in light of static and impact properties, which were comparable for both heat treatment conditions. Further studies considering different

ageing temperatures and soaking times will be performed to verify the current results to be generally applicable. However, the present outcomes satisfactorily demonstrated that the HPT6 treatment could be a suitable candidate for a possible replacement of the conventional HIP + T6 route, thus leading to significant technological advantages.

4.5 CONCLUSION

In this research activity, the impact and microstructural properties of L-PBF produced AlSi10Mg alloys subjected to different heat-treatment conditions were analysed. A new route that combines HIP and ageing under pressure (HPT6) was applied, and the resultant impact behaviour of the alloy was investigated. The impact properties of the same alloy after low-temperature annealing and conventional T6 treatment were also studied for comparison. The following conclusions could be drawn:

- The as-built alloy is characterised by a hierarchical microstructure, which spans over several orders of magnitude. XRD analyses indicate the existence of non-equilibrium conditions due to a large amount of Si retained in the solid solution. This microstructure accounts for the remarkable impact strength of the as-built alloy, but it is also responsible for the low impact toughness of the material.
- Low-temperature annealing completely restored the equilibrium conditions of the alloy. The Si network dissolved and formed nanometric Si particles, while coarse grains were not significantly affected. Changes in the microstructure reduce the static strength of the alloy, as measured by hardness tests. Conversely, impact strength and toughness of this alloy were the best among all the investigated conditions. This is likely due to a different material response in quasi-static or in rapid loading conditions. In this light, low-temperature annealing is a valuable alternative to achieve equilibrium conditions, reasonable static properties and an excellent impact behavior. However, a high-temperature treatment is required to match static and impact properties.
- The HIP before heat treatment results in significant densification of the alloy as compared to T6 heat treatment alone. It is therefore recommended to achieve high-density and defect-free products, especially when high impact and fatigue resistance are required. However, the high HIP temperature strongly affects the microstructure

of the alloy owing to which its hardness and impact strength are reduced. These can be restored by ageing treatment at the expense of ductility and absorbed energy.

- TEM analysis of the HPT6 alloy revealed the inclusion of nanometric precipitates, thus demonstrating that the novel route is capable of inducing precipitation strengthening in the AlSi10Mg alloy. Additionally, it results in a mechanical performance very similar to that of the standard HIP + T6 route, suggesting that HPT6 can possibly replace HIP + T6. The elimination of solution heat treatment will simultaneously cut down the processing duration and cost of production of L-PBF AlSi10Mg alloys.

REFERENCES

[1] L. Zhuo *et al.*, *Effect of post-process heat treatment on microstructure and properties of selective laser melted AlSi10Mg alloy*, Mater. Lett., vol. **234**, pp. 196–200, 2019

[2] J. Fiocchi, A. Tuissi, P. Bassani, and C. A. Biffi, *Low temperature annealing dedicated to AlSi10Mg selective laser melting products*, J. Alloys Compd., vol. **695**, pp. 3402–3409, 2017

[3] I. Rosenthal, R. Shneck, and A. Stern, *Heat treatment effect on the mechanical properties and fracture mechanism in AlSi10Mg fabricated by additive manufacturing selective laser melting process*, Mater. Sci. Eng. A, vol. **729**, no. May, pp. 310–322, 2018

[4] L. Zhou, A. Mehta, E. Schulz, B. McWilliams, K. Cho, and Y. Sohn, *Microstructure, precipitates and hardness of selectively laser melted AlSi10Mg alloy before and after heat treatment*, Mater. Charact., vol. **143**, no. March, pp. 5–17, 2018

[5] N. T. Aboulkhair, I. Maskery, C. Tuck, I. Ashcroft, and N. M. Everitt, *The microstructure and mechanical properties of selectively laser melted AlSi10Mg: The effect of a conventional T6-like heat treatment*, Mater. Sci. Eng. A, vol. **667**, pp. 139–146, 2016

[6] L. F. Wang *et al.*, *Enhancement in mechanical properties of selectively laser-melted AlSi10Mg aluminum alloys by T6-like heat treatment*, Mater. Sci. Eng. A, vol. **734**, no. July, pp. 299–310, 2018

[7] C. B. Finfrock, A. Exil, J. D. Carroll, and L. Deibler, *Effect of Hot Isostatic Pressing and Powder Feedstock on Porosity, Microstructure, and Mechanical Properties of Selective Laser Melted AlSi10Mg*, Metallogr. Microstruct. Anal., vol. **7**, no. 4, pp. 443–456, 2018

[8] N. E. Uzan, R. Shneck, O. Yeheskel, and N. Frage, *Fatigue of AlSi10Mg specimens fabricated by additive manufacturing selective laser melting (AM-SLM)*, Mater. Sci. Eng. A, vol. **704**, no. August, pp. 229–237, 2017

[9] U. Tradowsky, J. White, R. M. Ward, N. Read, W. Reimers, and M. M. Attallah, *Selective laser melting of AlSi10Mg: Influence of post-processing on the microstructural and tensile properties development*, Mater. Des., vol. **105**, pp. 212–222, 2016

[10] T. Hirata, T. Kimura, and T. Nakamoto, *Effects of hot isostatic pressing and internal porosity on the performance of selective laser melted AlSi10Mg alloys*, Mater. Sci. Eng. A, vol. **772**, no. June 2019, p.

138713, 2020

[11] W. H. Kan, Y. Nadot, M. Foley, L. Ridosz, G. Proust, and J. M. Cairney, *Factors that affect the properties of additively-manufactured AlSi10Mg: Porosity versus microstructure*, Addit. Manuf., vol. **29**, no. April, p. 100805, 2019

[12] S. Tammas-Williams, P. J. Withers, I. Todd, and P. B. Prangnell, *Porosity regrowth during heat treatment of hot isostatically pressed additively manufactured titanium components*, Scr. Mater., vol. **122**, pp. 72–76, 2016

[13] S. Hafenstein and E. Werner, *Pressure dependence of age-hardenability of aluminum cast alloys and coarsening of precipitates during hot isostatic pressing*, Mater. Sci. Eng. A, vol. **757**, pp. 62–69, 2019

[14] M. Tocci, A. Pola, M. Gelfi, and G. M. La Vecchia, *Effect of a New High-Pressure Heat Treatment on Additively Manufactured AlSi10Mg Alloy*, Metall. Mater. Trans. A Phys. Metall. Mater. Sci., 2020

[15] E. Padovano, C. Badini, A. Pantarelli, F. Gili, and F. D'Aiuto, *A comparative study of the effects of thermal treatments on AlSi10Mg produced by laser powder bed fusion*, J. Alloys Compd., vol. **831**, p. 154822, 2020

[16] K. Kempen, L. Thijs, J. Van Humbeeck, and J. P. Kruth, *Mechanical Properties of AlSi10Mg Produced by Selective Laser Melting*, Phys. Procedia, vol. **39**, pp. 439–446, 2012

[17] C. A. Schneider, W. S. Rasband, and K. W. Eliceiri, *NIH Image to ImageJ: 25 years of image analysis*, Nat. Methods, vol. **9**, pp. 671–675, 2012

[18] L. Lattanzi, A. Fortini, M. Giovagnoli, and M. Merlin, *Influence of Mg and Ti on both eutectic solidification and modifying efficiency in Sr-modified Al-7Si cast alloys*, Metall. Ital., vol. **110**, no. 2, pp. 5–15, 2018

[19] S. J. Andersen, H. W. Zandbergen, J. Jansen, C. Træholt, U. Tundal, and O. Reiso, *The crystal structure of the β" phase in Al-Mg-Si Alloys*, Acta Mater., vol. **46**, no. 9, pp. 3283–3298, 1998

[20] R. Vissers, M. A. van Huis, J. Jansen, H. W. Zandbergen, C. D. Marioara, and S. J. Andersen, *The crystal structure of the β' phase in Al-Mg-Si alloys*, Acta Mater., vol. **55**, no. 11, pp. 3815–3823, 2007

[21] H. Chen *et al.*, *Atomic scale investigation of the crystal structure and interfaces of the B' precipitate in Al-Mg-Si alloys*, Acta Mater., vol. **185**, pp. 193–203, 2020

[22] S. J. Andersen, C. D. Marioara, R. Vissers, A. Frøseth, and H. W. Zandbergen, *The structural relation between precipitates in Al-Mg-Si alloys, the Al-matrix and diamond silicon, with emphasis on the trigonal phase U1-MgAl2Si2*, Mater. Sci. Eng. A, vol. **444**, no. 1–2, pp. 157–169, 2007

[23] S. J. Andersen, C. D. Marioara, A. Frøseth, R. Vissers, and H. W. Zandbergen, *Crystal structure of the orthorhombic U2-Al4Mg4 Si4 precipitate in the Al-Mg-Si alloy system and its relation to the β' and β" phases*, Mater. Sci. Eng. A, vol. **390**, no. 1–2, pp. 127–138, 2005

[24] K. Matsuda, Y. Ishida, M. I, F. L, and S. Ikeno, *Cube-phase in excess Mg-type Al-Mg-Si alloy studied by EFTEM*, J. Mater. Sci., vol. **41**, pp. 2605–2610, 2006

[25] V. Grillo and E. Rotunno, *STEM_CELL: a software tool for electron microscopy. Part I Simulations*, Ultramicroscopy, vol. **125**, pp. 97–111, 2012

[26] V. Grillo and F. Rossi, *STEM_CELL: A software tool for electron microscopy. Part2 analysis of crystalline materials*, Ultramicroscopy, vol. **125**, pp. 112–129, 2013

[27] L. Lutterotti, H. R. Wenk, and S. Matthies, *MAUD (Material Analysis Using Diffraction): a user friendly Java program for Rietveld Texture Analysis and more*, in *ICOTOM-12.*, 1999, pp. 1599–1604

[28] H. Qin, Q. Dong, V. Fallah, and M. R. Daymond, *Rapid Solidification and Non-equilibrium Phase Constitution in Laser Powder Bed Fusion (LPBF) of AlSi10Mg Alloy: Analysis of Nano-precipitates, Eutectic Phases, and Hardness Evolution*, Metall. Mater. Trans. A Phys. Metall. Mater. Sci., vol. **51**, no. 1, pp. 448–466, 2020

[29] S. Marola *et al.*, *A comparison of Selective Laser Melting with bulk rapid solidification of AlSi10Mg alloy*, J. Alloys Compd., vol. **742**, pp. 271–279, 2018

[30] N. Takata, H. Kodaira, K. Sekizawa, A. Suzuki, and M. Kobashi, *Change in microstructure of selectively laser melted AlSi10Mg alloy with heat treatments*, Mater. Sci. Eng. A, vol. **704**, no. August, pp. 218–228, 2017

[31] M. Fousová, D. Dvorský, A. Michalcová, and D. Vojtěch, *Changes in the microstructure and mechanical properties of additively manufactured AlSi10Mg alloy after exposure to elevated temperatures*, Mater. Charact., vol. **137**, no. December 2017, pp. 119–126, 2018

[32] Y. H. Cho, H. C. Lee, K. H. Oh, and A. K. Dahle, *Effect of strontium and phosphorus on eutectic Al-Si nucleation and formation of β-Al5FeSi in hypoeutectic Al-Si foundry alloys*, Metall. Mater. Trans. A Phys. Metall. Mater. Sci., vol. **39**, no. 10, pp. 2435–2448, 2008

[33] A. Hadadzadeh, B. S. Amirkhiz, and M. Mohammadi, *Contribution of Mg2Si precipitates to the strength of direct metal laser sintered AlSi10Mg*, Mater. Sci. Eng. A, vol. **739**, no. August 2018, pp. 295–300, 2019

[34] A. H. Maamoun, M. Elbestawi, G. K. Dosbaeva, and S. C. Veldhuis, *Thermal post-processing of AlSi10Mg parts produced by Selective Laser Melting using recycled powder*, Addit. Manuf., vol. **21**, no. March, pp. 234–247, 2018

[35] N. T. Aboulkhair, C. Tuck, I. Ashcroft, I. Maskery, and N. M. Everitt, *On the Precipitation Hardening of Selective Laser Melted AlSi10Mg*, Metall. Mater. Trans. A Phys. Metall. Mater. Sci., vol. **46**, no. 8, pp. 3337–3341, 2015

[36] T. Tański and P. Snopiński, *Effect of the Processing Conditions on the Microstructural Features and Mechanical Behavior of Aluminum Alloys*, in *Aluminium Alloys Recent Trends in Processing, Characterization, Mechanical behavior and Applications*, 2017, pp. 137–156

[37] Y. Chen, Y. Tang, H. Zhang, N. Hu, N. Gao, and M. J. Starink, *Microstructures and hardness prediction of an ultrafine-grained al-2024 alloy*, Metals (Basel)., vol. **9**, no. 11, pp. 1–10, 2019

[38] J. Lu, Y. Zhao, Y. Du, W. Zhang, and Y. Zhang, *Microstructure and mechanical properties of a novel titanium alloy with homogeneous (TiHf)5Si3 article-reinforcements*, J. Alloys Compd., vol. **778**, pp. 115–123, 2019

[39] H. W. Zandbergen, S. J. Andersen, and J. Jansen, *Structure determination of Mg5Si6:particles in Al by dynamic electron diffraction studies*, Science (80-.)., vol. **277**, no. 5330, pp. 1221–1225, 1997

[40] J. H. Rao, Y. Zhang, K. Zhang, A. Huang, C. H. J. Davies, and X. Wu, *Multiple precipitation pathways in an Al-7Si-0.6Mg alloy fabricated by selective laser melting*, Scr. Mater., vol. **160**, pp. 66–69, 2019

[41] L. Girelli *et al.*, *Evaluation of the impact behaviour of AlSi10Mg alloy produced using laser additive*

manufacturing, Mater. Sci. Eng. A, vol. **748**, pp. 38–51, 2019

[42] M. Tang and P. C. Pistorius, *Oxides, porosity and fatigue performance of AlSi10Mg parts produced by selective laser melting*, Int. J. Fatigue, vol. **94**, pp. 192–201, 2017

[43] X. P. Li *et al.*, *A selective laser melting and solution heat treatment refined Al-12Si alloy with a controllable ultrafine eutectic microstructure and 25% tensile ductility*, Acta Mater., vol. **95**, no. October, pp. 74–82, 2015

[44] T. Maeshima and K. Oh-ishi, *Solute clustering and supersaturated solid solution of AlSi10Mg alloy fabricated by selective laser melting*, Heliyon, vol. **5**, no. 2, p. e01186, 2019

[45] A. Hadadzadeh, B. Shalchi Amirkhiz, A. Odeshi, J. Li, and M. Mohammadi, *Role of hierarchical microstructure of additively manufactured AlSi10Mg on dynamic loading behavior*, Addit. Manuf., vol. **28**, no. November 2018, pp. 1–13, 2019

[46] E. Ghassemali, M. Riestra, T. Bogdanoff, B. S. Kumar, and S. Seifeddine, *Hall-Petch equation in a hypoeutectic Al-Si cast alloy: Grain size vs. secondary dendrite arm spacing*, Procedia Eng., vol. **207**, pp. 19–24, 2017

[47] B. Chen *et al.*, *Strength and strain hardening of a selective laser melted AlSi10Mg alloy*, Scr. Mater., vol. **141**, pp. 45–49, 2017

[48] N. Hansen, *Hall–Petch relation and boundary strengthening*, Scr. Metall., vol. **51**, pp. 801–806, 2005

[49] Q. Zhao and B. Holmedal, *The effect of silicon on the strengthening and work hardening of aluminum at room temperature*, Mater. Sci. Eng. A, vol. **563**, no. October 2017, pp. 147–151, 2013

[50] V. C. Pierre, B. Anthony, T. Lore, V. H. Brecht, and V. Kim, *Heat treatment optimization via thermo-physical characterization of AlSi7Mg and AlSi10Mg manufactured by laser powder bed fusion (LPBF)*, Euro PM 2018 Congr. Exhib., pp. 1–7, 2020

[51] E. D. Cyr, A. Brahme, M. Mohammadi, R. K. Mishra, and K. Inal, *A new crystal plasticity framework to simulate the large strain behaviour of aluminum alloys at warm temperatures*, Mater. Sci. Eng. A, vol. **727**, pp. 11–28, 2018

[52] S. Xia, Y. Qi, T. Perry, and K. S. Kim, *Strength characterization of Al/Si interfaces: A hybrid method of nanoindentation and finite element analysis*, Acta Mater., vol. **57**, no. 3, pp. 695–707, 2009

[53] J. R. Cahoon, W. H. Broughton, and A. R. Kutzak, *The Determination of Yield Strength from Hardness Measurements*, Metall. Trans., vol. **2**, pp. 1979–1983, 1971

[54] A. Das, P. Biswas, S. Tarafder, D. Chakrabarti, and S. Sivaprasad, *Effect of Strengthening Mechanism on Strain-Rate Related Tensile Properties of Low-Carbon Sheet Steels for Automotive Application*, J. Mater. Eng. Perform., vol. **27**, no. 7, pp. 3709–3722, 2018

[55] R. Alturk, S. Mates, Z. Xu, and F. Abu-Farha, *Effects of microstructure on the strain rate sensitivity of advanced steels*, in *Minerals, Metals and Materials Series*, 2017, vol. **Part F6**, pp. 243–254

[56] J. C. F. Millett, *Modifications of the Response of Materials to Shock Loading by Age Hardening*, Metall. Mater. Trans. A Phys. Metall. Mater. Sci., vol. **46**, no. 10, pp. 4506–4517, 2015

[57] T. Evans and E. Williams, *Effect of pressure on precipitation in an Al-4·3% Cu alloy*, Philos. Mag., vol. **20**, no. 163, pp. 181–194, 1969

[58] T. K. Akopyan, N. A. Belov, A. G. Padalko, N. V. Letyagin, and N. N. Avksent'yeva, *Analysis of the*

Effect of Hydrostatic Pressure on the Nonvariant Eutectic Transformation in Al–Si, Al–Cu, and Al–Cu–Si Systems, Phys. Met. Metallogr., vol. **120**, no. 6, pp. 593–599, 2019

[59] X. P. Li *et al., Selective laser melting of nano-TiB2decorated AlSi10Mg alloy with high fracture strength and ductility*, Acta Mater., vol. **129**, pp. 183–193, 2017

CHAPTER 5

ANISOTROPIC IMPACT BEHAVIOUR WITH DIFFERENT HEAT TREATMENTS

The present chapter deals with the anisotropic high-strain rate behaviour of an L-PBF produced AlSi10Mg alloy as a function of heat treatment. Charpy impact specimens produced in both vertical and horizontal directions, and with different U-notch positions were tested. In this way, the effect of a different microstructural arrangement with respect to the fracture direction was assessed. Besides, several heat treatment routes were considered to evaluate the relationship between anisotropy and heat treatment state. Purposes of this research activity are the assessment of microstructural features affecting isotropy, and suggestion of possible methods to mitigate anisotropy.

5.1 INVESTIGATION ON THE ANISOTROPIC IMPACT BEHAVIOUR

5.1.1 Additional background and purpose of the work

Among the process-related drawbacks, L-PBF produced Al alloys suffer from structural anisotropy [1]–[5], which is a significant limitation in conventional engineering applications that generally require isotropic and consistent mechanical properties. However, anisotropy does not regard just Al alloys [1]–[7] but generally affects metals and alloys processed by AM techniques. While it is generally accepted that it stems from the superimposition of successive layers during the manufacturing process, any attempt to find a microstructural explanation led to somewhat different results.

Carrol *et al.* [8] and Simonelli *et al.* [9] attributed the different ductility of an L-PBF processed Ti-6Al-4V alloy in the longitudinal and transverse directions to the morphological texture of β-grains. Hitzler *et al.* [10] found that the best strength and Young's modulus of an L-PBF produced 316L stainless steel are reached under a 45° offset between the layer and loading direction. Takaichi *et al.* [11] ascribed the mechanical anisotropy of a CrCoMo alloy to a combination of morphological and crystallographic textures of primary columnar grains.

Concerning Al alloys, Hitzler *et al.* [5] showed that the tensile properties of an AM produced AlSi10Mg alloy strongly depend on the specimen orientation. For instance, Young's modulus and tensile strength range between 62.6-72.9 GPa and 314-399 MPa, respectively. Tang *et al.* [3] found that AlSi10Mg specimens exhibit better tensile performances when produced horizontally rather than vertically, and attributed this behaviour to the micro-residual stress resulting from the different thermal expansion of Al matrix and Si network. Di Giovanni *et al.* [1] ascribed the anisotropic high-cycle fatigue crack growth behaviour of the AlSi10Mg alloy in the as-built state to the easy fracture path offered by the melt pool boundaries and residual stresses. After T6 heat treatment, homogenisation of microstructure and reduction of residual stresses mitigate the dependence of the crack growth rate on specimen orientation. De Menezes *et al.* [6] similarly explained differences in fracture toughness of an L-PBF produced A357 alloy, ascribing the microstructural heterogeneities as the leading cause of anisotropy. Conversely, Rao *et al.* [7] suggested that the tensile anisotropy of the A357 alloy stems from crystallographic-dependent strains due to oversaturation of Si in the Al matrix.

The diversity of results reported above states that the orientation dependency of mechanical properties of AM products is not yet fully understood. Additionally, studies about anisotropy of AM produced alloys mainly concern tensile or fatigue performances, whereas little attention is drawn to high-strain rate properties [12]–[14]. Hadadzadeh *et al.* [12] used a split Hopkinson pressure bar apparatus to investigate the compressive impact behaviour of differently oriented AlSi10Mg specimens. Despite microstructural features like grains, Al dendrites, Si precipitates, and dislocation density were different as the building orientation changed, the resulting high-strain rate compressive flow behaviour was almost identical. Conversely, Rosenthal *et al.* [13] found that horizontal samples show a superior high-strain rate tensile behaviour as compared to vertical samples. They attributed this finding to the different interaction of melt pool boundaries with the fracture path.

In light of what is reported above, to date, there is lack of information about the anisotropic high-strain rate response of L-PBF processed Al alloys. Additionally, most of the research work dealt with the alloy in the as-built state, and the effect of different heat treatments has to be assessed. Therefore, the current research activity aims to investigate the anisotropic Charpy impact behaviour of an L-PBF produced AlSi10Mg

alloy in different heat treatment conditions. Three different specimen orientations and several heat treatment routes were employed, and the relationship between microstructural features and anisotropic high-strain rate response was investigated. Specifically, this work provides new insights about the inherent anisotropy of AM processed Al alloys and enables the comprehension of the role of heat treatment on the impact properties.

5.2 MATERIALS AND EXPERIMENTAL PROCEDURE

5.2.1 L-PBF and heat treatment

L-PBF produced impact specimens were realised using an AlSi10Mg alloy powder in both horizontal and vertical orientations to the building platform and then subjected to heat treatment. Details regarding the manufacturing process and different heat treatment routes were previously reported in Chapter 3 (§ 3.2.1) and Chapter 4 (§ 4.2.1), respectively. For short, they will not be repeated here, and just a schematic of the heat treatment routes with the corresponding designations is depicted in Fig. 5.1.

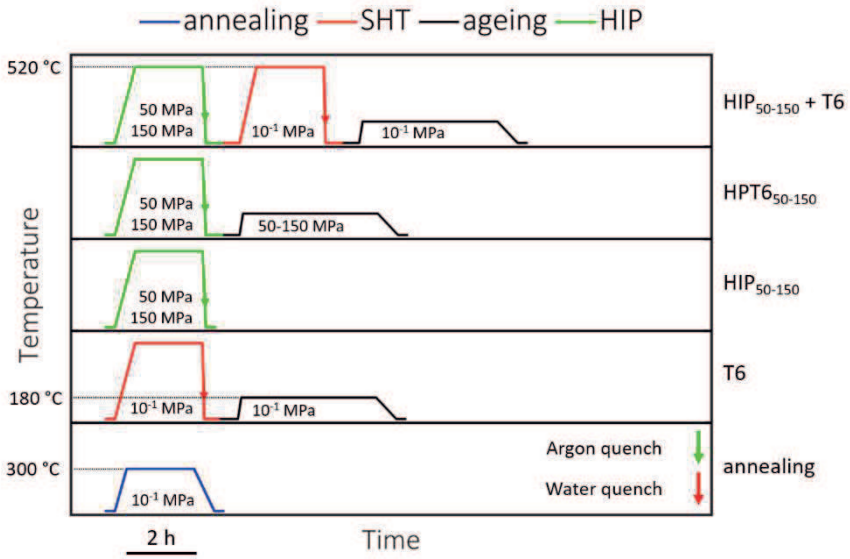

Figure 5.1. Schematic of heat treatments and corresponding designations.

After heat treatments, specimens were machined to the final U-notched Charpy specimen dimension (10×10×55 mm^3) according to the ASTM E23 standard. In the following, different samples will be labelled according to the U-notch position. Horizontal samples are referred to as XZ and XY depending on whether the U-notch was machined on the lateral or top surface of the long side, respectively, and vertical samples

will be referred to as Z. Different specimen orientations with respect to the building platform, U-notch positions and designations are depicted in Fig. 5.2a.

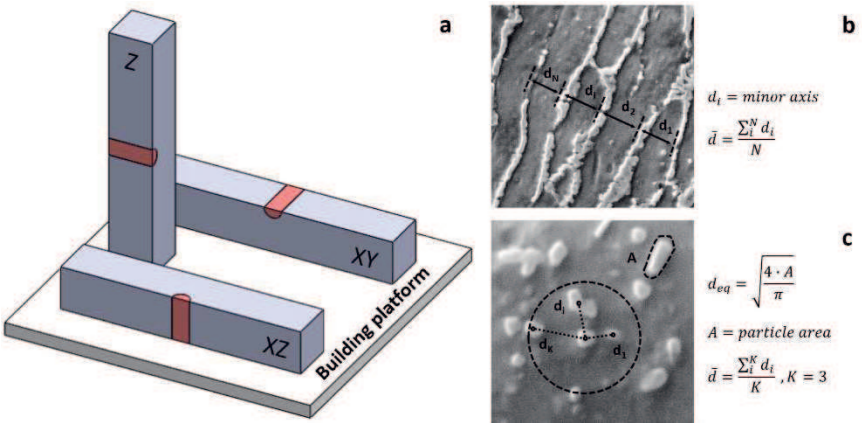

Figure 5.2. (a) Specimens orientation and corresponding U-notch position. (b) Distance between stripes of the Si network measured as the width of cells. (c) Equivalent diameter and distance of Si particles.

In the following, specimens in Fig. 5.2a will be described simply as having different orientations, whereas the actual meaning is that they have a different microstructural arrangement with respect to the fracture direction provided by the U-notch.

5.2.2 Charpy impact tests

All details about the Charpy impact tests were reported in detail in Chapter 3 (§ 3.2.2) and, for the sake of brevity, will not be reported here. At least two specimens were tested for each condition.

5.2.3 Microstructural characterisation

Samples for microstructural observations were cut perpendicularly to the U-notch of fractured Charpy specimens, subjected to standard metallographic preparation and then etched for 10 s with a 0.5 wt. % HF aqueous solution. The characterisation of metallographic samples and fracture surfaces of Charpy specimens was conducted with a Leica DMI 5000M optical microscope (OM) and a Zeiss EVO MA 15 scanning electron microscope (SEM). Quantitative image analysis of grains, Si phase and fracture surfaces was performed using the software ImageJ [15]. Grains were analysed in terms of their length and width. Cellular-like Si was analysed in terms of spacing $\bar{d}$, measured as the width of the cell (Fig. 5.2b). Particle-like Si was analysed in terms of size d_{eq} and spacing

$\bar{d}$, measured as equivalent diameter and 3-nearest neighbour (3NN) distance, respectively (Fig. 5.2c). Dimples spacing on the fracture surface was measured using the 3NN distance.

X-ray diffraction (XRD) tests were conducted using the Bragg-Brentano geometry on a Bruker D8 Advance diffractometer equipped with a Cu filament (Kα, 1.5406 Å). All patterns were acquired in the 2θ range of 20° to 110° with 0.02° of step-size and 1 s of step time. Quantitative texture analysis of the Al phase was performed according to the Harris method [16], [17]. The texture coefficient of the *hkl* reflection C_{hkl} and the degree of preferred orientation σ were measured according to:

$$C_{hkl} = \frac{I_{hkl} / I_{hkl,0}}{\frac{1}{N}\sum^{N} I_{hkl} / I_{hkl,0}} \quad (1)$$

$$\sigma = \sqrt{\frac{\sum^{N} (C_{hkl} - 1)^2}{N}} \quad (2)$$

where I_{hkl} is the integrated intensity of the *hkl* reflection in the experimental pattern, $I_{hkl,0}$ is the integrated intensity of the *hkl* reflection of a completely random (texture-free) specimen, and *N* is the number of reflections considered. When all grains are randomly oriented, C_{hkl} of any reflection equals 1, and σ is 0. Conversely, for entirely oriented grains along the *hkl* direction, C_{hkl} equals *N* for the *hkl* reflection and 0 for the others and σ matches $\sqrt{N-1}$. These represent the lower and upper thresholds for C_{hkl} and σ, and intermediate values are reached for a not-perfect crystallographic texture.

Given the employed 2θ range reported above, *N* = 6 for the Al phase in the present analysis. The 00-004-0787 file from the International Centre for Diffraction Data (ICDD) was used as the reference random Al sample. Experimental XRD patterns were fitted using the Rietveld refinement procedure with the software Maud [18] to isolate the contribution of the Al phase. The integrated intensity of peaks, texture coefficients and degree of preferred orientation were measured using Matlab®.

5.3 RESULTS AND ANALYSES

5.3.1 Microstructural heterogeneities and heat treatment

Figure 5.3 depicts relevant microstructural features of samples in different heat treatment conditions. OM image of the as-built sample (Fig. 5.3a) clearly shows semi-

circular sections of melt pools. These latter are slightly blurred in the annealed sample (Fig. 5.3b) and make room to a homogeneous microstructure after high-temperature heat-treatments (Fig. 5.3c) (for short, HTHT samples in the following). Sections of melt pools are marked by dotted lines in the as-built (Fig. 5.3d) and annealed (Fig. 5.3e) samples. Melt pool boundaries (MPBs) are not discernible after an HTHT, as shown in Fig. 5.3f for the HIP_{50} sample, taken as the reference for all samples heat-treated at high temperatures. However, the radial growth of elongated grains identified by BSE crystallographic contrast recalls the semi-circular shape of the melt pool, whose boundaries are suggested by black markers in Fig.5.3f.

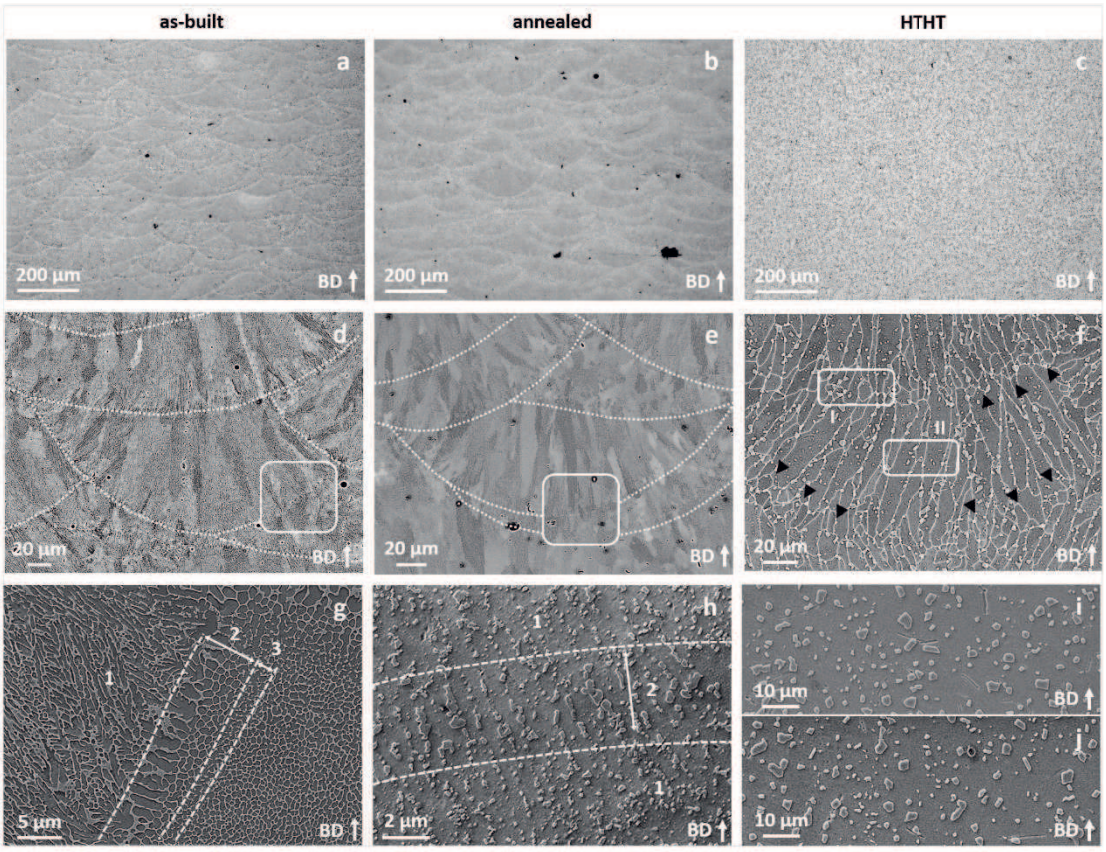

Figure 5.3. Microstructural features in the transverse section of samples in different heat treatment conditions. (a-d-g) as-built. (b-e-h) annealed. (c-f-i-j) HTHT. (a-b-c) OM images. (a-b) Semi-circular melt pools, dotted lines mark the MPBs. (c) Elongated grains, with boundaries marked by fine solid lines; black markers suggest the location of MPBs. (g-h-i-j) Detailed images taken from areas marked by the solid line in (d-e-f), respectively; showing heterogeneous microstructure at the MPB. In (g-h) dotted lines divide 1-fine zone, 2-coarse zone and 3-HAZ. In all images, the white vertical arrow shows the building direction (BD).

Figures 5.3g-h show the morphological evolution of Si phase along the MPBs in the as-built and annealed samples, respectively. Fine cellular Al dendrites and a Si network (zone 1 or fine zone) compose the inner part of the melt pool in the as-built sample (Fig. 5.3g). Al dendrites are coarser in the inner region of the MPB (zone 2 or coarse zone) as compared to zone 1, whereas the Si network breaks into particles in the outer region (zone 3 or HAZ). After annealing, the Si network breaks up to form nanometric Si particles (Fig. 5.3h) whose size is coarse (zone 2) along the MPBs and fine elsewhere (zone 1). In both as-built and annealed samples, the MPB is a few μm thick. Figures 5.3i-j compare the microstructure of regions within the molten pool and at the MPB, respectively, of the HTHT sample. Both exhibit micrometric Si particles embedded in the Al matrix, with no appreciable differences among each other.

5.3.2 XRD analyses

Figure 5.4 shows the XRD patterns of samples in different orientations and heat treatment conditions. Samples for microstructural characterisations were cut perpendicularly to the U-notch of Charpy specimens. Hence, according to Fig. 5.2a, sections parallel to the building direction were analysed for XY and Z samples, whereas a section perpendicular to the building direction contributes to diffraction in XZ samples.

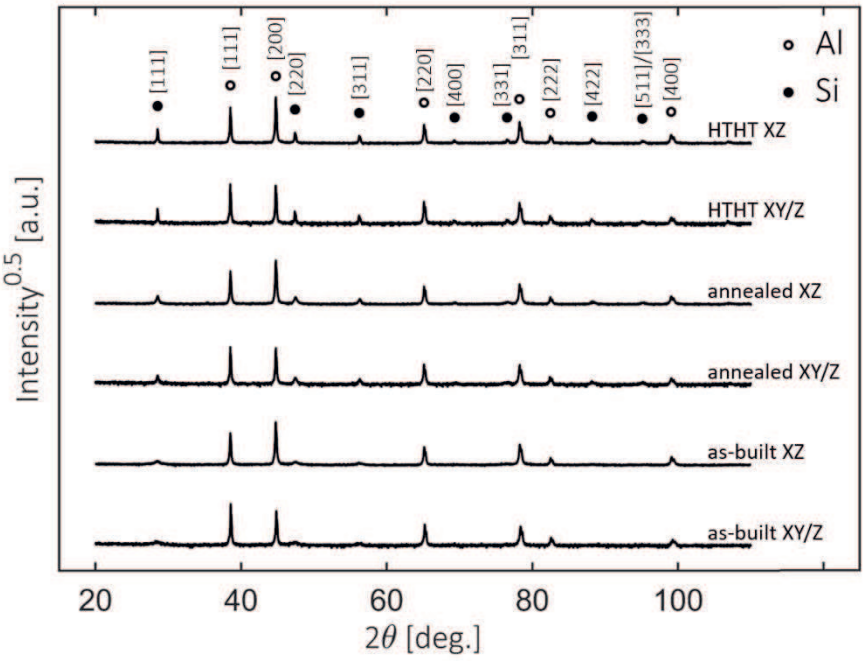

Figure 5.4. XRD patterns of specimens in different orientations and heat treatment conditions.

Since HTHT samples share similar XRD patterns, just the one corresponding to the HIP_{50} sample is depicted in Fig. 5.4 for the sake of simplicity. All patterns show reflections of only Al and Si phases, and the intensity of these latter strongly changes with the heat treatment. Si reflections are barely distinguishable from the background in the as-built samples and progressively increase in intensity after annealing and HTHT. In the previous Chapter 4 (§ 4.3.3) it was shown that the integrated intensity of Si peaks in annealed and HTHT samples is the same, with the differences in the absolute intensity just being determined by the nanometric size of Si particles in the annealed alloy.

Figure 5.4 highlights that relative intensity of Al peaks changes with the specimen orientation. For instance, intensities of $[200]_{Al}$ and $[111]_{Al}$ reflections are similar for the XY and Z specimens, whereas the former is significantly higher for the XZ specimens. In a texture-free sample, the $[111]_{Al}$ reflection should be by far the most intense, which means that a crystallographic texture exists in both sections parallel and perpendicular to the building direction. The higher intensity measured in this latter section well matches with the fibre texture reported for L-PBF produced alloys [19], [20].

5.3.3 Orientation-dependent impact properties

Figure 5.5 shows the Charpy impact parameters as a function of heat treatment and specimen orientation. The as-built samples have a high impact strength, with F_p of ~6.8-6.9 kN independently of the specimen orientation (Fig. 5.5a). Conversely, absorbed energies suffer from significant anisotropy. Both E_i (Fig. 5.5b) and E_p (Fig. 5.5c) progressively decrease for XZ, XY and Z samples, in this order. After annealing, the alloy retains an impact strength comparable to the as-built state, with F_p ranging between 6.6-7.1 kN. Besides, E_i and E_p increase about threefold and fivefold the corresponding values of the as-built samples up to 6-10 J to 8-12 J, respectively. However, the anisotropic impact response is not mitigated after heat treatment: all impact parameters reach the highest and lowest values for the XZ and Z samples, respectively, and XY samples locate in-between them.

After the HIP treatment either at 50 or 150 MPa, F_p reduces to 5.3-5.8 kN, while E_i and E_p reach about 6 J and 5 J respectively. All specimen orientations show similar absorbed

energies, considering the experimental uncertainty, whereas F_p is slightly higher for the Z samples.

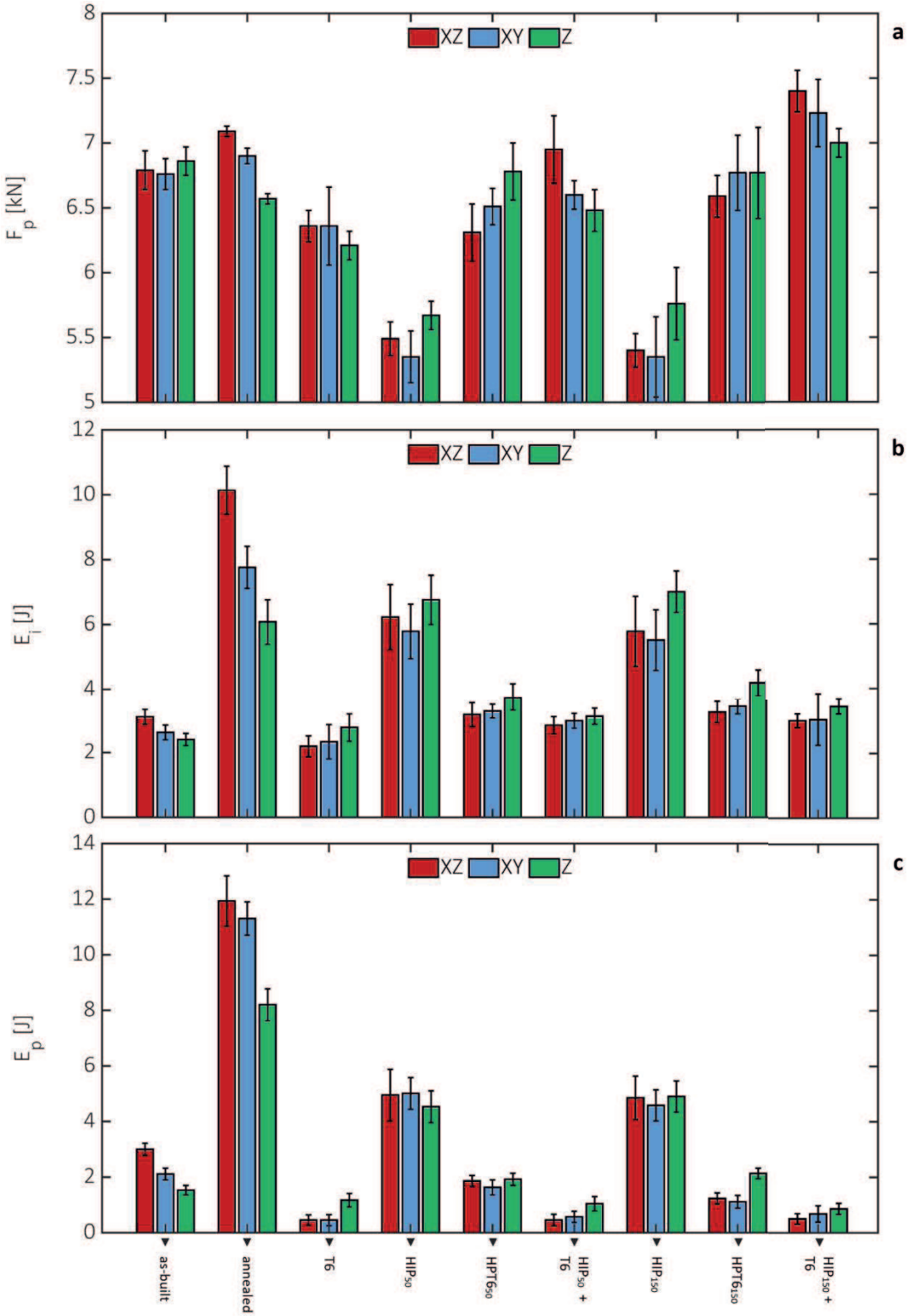

Figure 5.5. Impact parameters from Charpy force-displacement curves of specimens in different heat treatment conditions and orientations. (a) Peak force. (b) Initiation energy. (c) Propagation energy. Standard deviations are shown as error bars.

After microstructure homogenisation, either with SHT or both HIP and SHT, the ageing treatment strengthens the alloy, with F_P of T6, HIP + ageing, and HIP + T6 samples that ranges between 6.5-7.5 kN. As a drawback, E_i and E_P fall to 3-4 J and 0.5-2 J, respectively. Figures 5.5b-c show that there are no significant differences in absorbed energies of samples mentioned above as the specimen orientation changes. Conversely, Fig. 5.5a shows that specimen orientation affects the impact strength of those samples, but the scattering of experimental data prevents conclusive observations.

5.3.4 Micro-scale fracture behaviour

The fracture behaviour of the alloy in different heat treatment conditions was studied over different length scales to explain the anisotropic impact properties. Charpy specimens were cut and polished to the mid-thickness plane in order to analyse the microstructure just beneath the fracture profile, and the primary damage mechanism was investigated. Figures 5.6a-b depict the damage features of the as-built alloy at different magnifications. Irregular voids grow at the Al/Si interface, mainly by decohesion of adjacent phases, and sometimes by rupture of the Si network. A reduced number of voids with a relatively coarse size is generally detected for the as-built alloy.

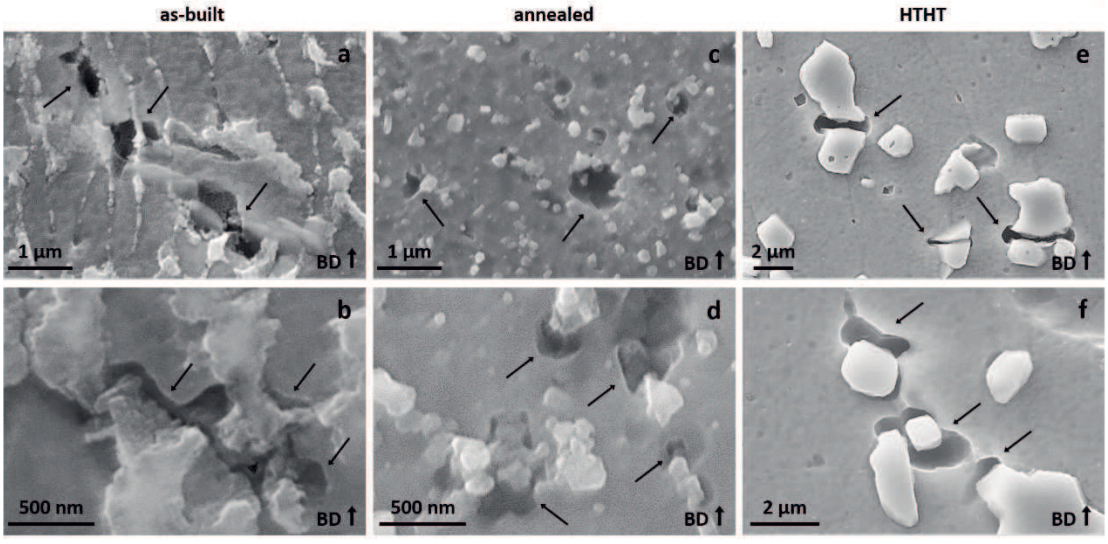

Figure 5.6. Fracture mechanism of specimens in different heat treatment conditions. (a-b) as-built. (c-d) annealed. (e-f) HTHT. Fine arrows mark the nucleation of voids at the Si phase. Vertical arrows in the bottom-right corner mark the building direction (BD).

In the annealed samples (Figs. 5.6c-d), voids with a regular morphology nucleate by decohesion of Si particles from the Al matrix. Damage by breakage of Si particles was not detected but, in light of the nanometric size of Si particles, cannot be ruled out undoubtedly. As compared to as-built samples, the damage is significantly diffuse in annealed samples, with a higher number of voids that nucleates and reaches a smaller size at fracture. Damage nucleates at coarse Si particles also in HTHT samples (Figs. 5.6e-f), either by decohesion from the parent matrix and breakage of Si particles. Figure 5.6f shows that growth and coalescence of adjacent voids is a likely damaging mechanism.

5.3.5 Macro-scale fracture behaviour

The previous section highlights that the Si phase mainly rules the damage nucleation at the micrometric and sub-micrometric scale. In this light, the microstructural heterogeneity of Si phase reported in § 5.3.1 calls for the investigation of fracture behaviour at a broader scale.

Fracture profiles of samples in different orientations and heat treatment conditions are depicted in Fig. 5.7. Different features are discernible in as-built and annealed samples as the specimen orientation changes. Perpendicular sections to the building direction highlight elongated melt pools along the laser scan direction in XZ samples (Figs. 5.7a-b), whereas parallel sections show the semi-circular section of melt pools in XY and Z samples (Figs. 5.7d-e-g-h). In both cases, such features are visible according to a different size and morphology of the Si phase along the MPBs, marked with dotted lines in Fig. 5.7. Melt pools are not discernible in HTHT samples (Figs. 5.7c-f-i), even if MPBs can be suggested according to the radial arrangement of elongated grains in XY and Z samples. In HTHT samples, grain boundaries are marked by superimposing fine solid lines.

In as-built (Fig. 5.7a) and annealed (Fig. 5.7 b) XZ samples, the fracture profile crosses the melt pools transversally, with just limited zones following the MPBs. Rotation of the scan pattern in successive deposition steps sometimes results in a fracture path following the entire MPB. The presence of sole equiaxed grains prevents any detailed interpretation of the fracture path in HTHT XZ samples (Fig. 5.7c). As the specimen orientation changes to XY, the fracture profile still significantly crosses melt pools in as-built (Fig. 5.7d) and annealed (Fig. 5.7e) samples. However, fracture often deviates from its straight path to follow the MPBs, leaving pronounced edges on the profile. MPBs

represent a significant part of fracture profiles of Z samples, both in as-built (Fig. 5.7g) and annealed (Fig. 5.7h) states. Additionally, secondary cracks along the MPBs just beneath the fracture profile (Fig. 5.7g) indicates that they are a favourable fracture path. In HTHT XY (Fig. 5.7f) and Z (Figs. 5.7i), the arrangement of elongated grains suggests that the fracture path is coherent with observations in Figs. 5.7d-e and Figs. 5.7g-h, respectively.

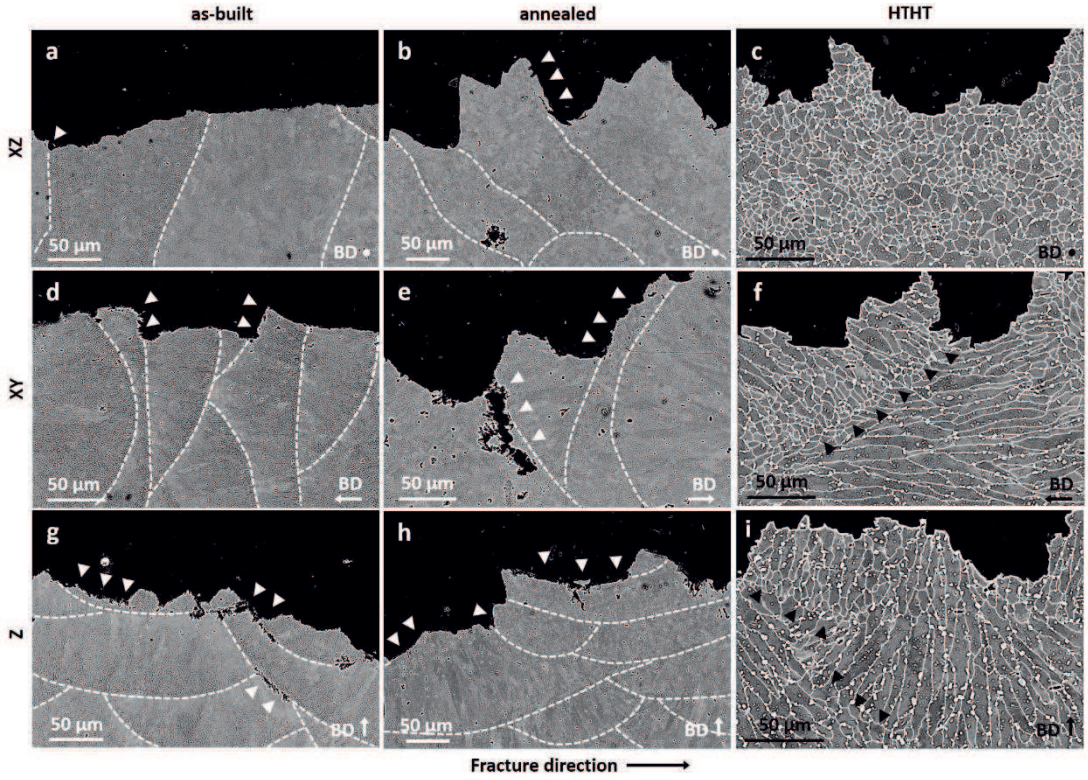

Figure 5.7. Fracture profiles of specimens in different orientations and heat treatment conditions. (a-b-c) XZ. (d-e-f) XY. (g-h-i) Z. (a-d-g) as-built. (b-e-h) annealed. (c-f-i) HTHT. In the as-built annealed samples, a dashed line marks the MPBs, and white markers indicate a fracture along MPBs. In the HTHT specimens, the black markers suggest the MPBs. Arrows and dots in the bottom-right corner mark the building direction (BD).

Figure 5.8 depicts the fracture surfaces of samples with different orientations and heat treatment states and complements the observation of fracture profiles in Fig. 5.7. Semi-circular sections of melt pools are detectable on the fracture surface of the as-built XZ sample (Fig. 5.8a), whereas they are seldom recognisable in the annealed XZ sample (Fig. 5.8b). A very irregular dimple-like surface characterises the HTHT XZ samples (Fig. 5.8c), and no features recall the shape of melt pools. In the as-built XY sample (Fig. 5.8d), semi-circular traces of melt pools are clearly recognisable. A more in-depth analysis

reveals fine elongated dimples in the inner part of the melt pools (Fig. 5.8d'), and coarse elongated dimples along the trace of the MPB (Fig. 5.8d''). This finding matches the microstructural heterogeneities of the Si phase described in Fig. 5.3g and supports the role of Si in damage nucleation reported in Figs. 5.6a-b.

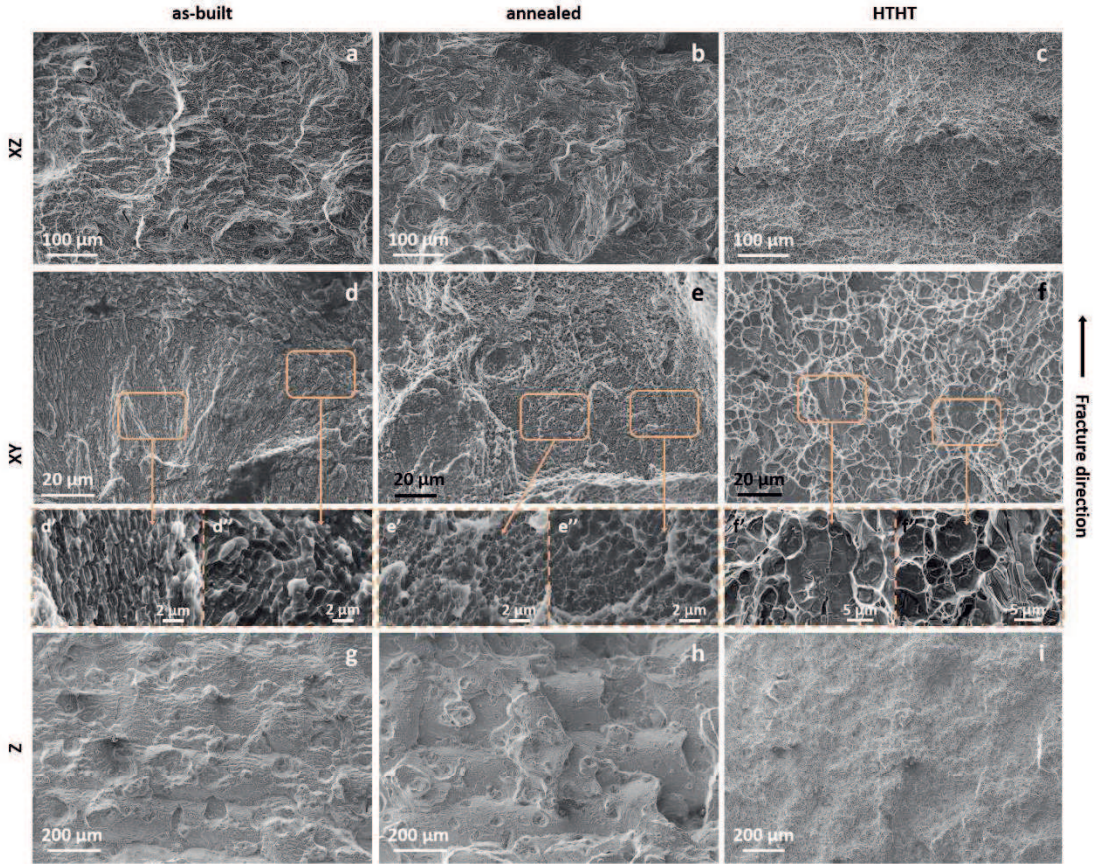

Figure 5.8. Fracture surfaces of specimens in different orientations and heat treatment conditions. (a-b-c) XZ. (d-d'-d''-e-e'-e''-f-f'-f'') XY. (g-h-i) Z. (a-d-d'-d''-g) as-built. (b-e-e'-e''-h) annealed. (c-f-f'-f''-i) HTHT. (d'-d''), (e'-e''), (f'-f'') Detailed images taken from the areas marked by the solid orange line in (d), (e), (f), respectively. (d'-e'), (d''-e'') Detailed images taken from the core and boundary of the melt pools traces, respectively.

Traces of melt pools are still detectable on the fracture surface of the annealed XY sample (Fig. 5.8e). Similarly to the as-built XY sample, equiaxed dimples are small inside the melt pool (Fig. 5.8e') and coarse along the MPB (Fig. 5.8e''), in agreement with Fig. 5.3h. Conversely, the dimple-like appearance of the fracture surface of HTHT samples (Fig. 5.8f) is consistent in size and morphology, as highlighted by the similarity of Fig. 5.8f' and Fig. 5.8f''. Fracture surfaces of as-built (Fig. 5.8g) and annealed (Fig. 5.8h) Z samples clearly show elongated melt pools, and both agree with the fracture path

suggested in Figs. 5.7g-h. These features are no longer detectable in HTHT Z samples (Fig. 5.8i).

5.4 DISCUSSION

5.4.1 Anisotropic impact behaviour with heat treatments

Section § 5.3.3 shows that the orientation-dependency of Charpy impact behaviour depends on the heat treatment state. Strength and absorbed energy of as-built and annealed samples significantly change with specimen orientation, decreasing for XZ, XY and Z samples in this order, whereas impact properties are more consistent after heat treatment at high temperatures. The effect of different heat treatments on the impact behaviour was deepened in the previous Chapter 4, and will not be recalled here. The following sections aim to analyse and discuss the possible sources of anisotropy in light of current experimental investigations.

5.4.2 Role of morphological and crystallographic textures

Among the other features, morphological grains texture possibly induces anisotropy of mechanical properties in AM produced alloys [8], [9], [21]. In this light, the size of grains of samples in different orientations and heat treatment conditions was analysed in terms of width and length, and results are reported in Fig. 5.9 as statistical distributions.

Since the polished surface of XZ samples is perpendicular to the building direction, the transverse section of grains is revealed, and they appear mostly equiaxed (Figs. 5.7a-b-c). This justifies why the width and length of grains in XZ samples are almost the same, regardless of heat treatment. In as-built and annealed samples, the maximum size of grains is ~10 μm, whereas it is slightly higher in HTHT samples, up to 15-20 μm. Grains are cut longitudinally in XY and Z samples, and thus they appear with the elongated shape. Regardless of the heat treatment state, their width ranges between 1-10 μm, confirming results of XZ samples, whereas their length spans over several tens of μm.

Minor differences in statistical distributions in Fig. 5.9 can be ascribed to the different methods employed to measure the grain size: etching sufficiently reveals grain boundaries in HTHT samples, while BSE channelling contrast was used in as-built and annealed samples. In this light, appreciable size differences of grains cannot be detected

as the heat treatment condition changes, even if a slight coarsening is sometimes reported [22], [23]. Most importantly, the elongated shape of grains is fully maintained after heat treatment, which does not recover the morphological texture. Si particles at grain boundaries (Figs. 5.3i-j) likely hinders the movement of grain boundaries themselves, and prevent recrystallisation at high temperatures. Since the elongated shape of grains is retained after heat treatment, whereas this latter significantly levels out the impact properties (Fig. 5.5), grains morphology is unlikely the main reason for anisotropy. Presents results agrees with Xiao et al. [24], who found that a nano-TiB_2-added AlSi10Mg alloy with an equiaxed crystal structure still exhibits anisotropic tensile properties, although anisotropy is reduced as compared to the counterpart with a columnar grains structure. Other studies concerning the anisotropic response of different alloys concluded that grains morphology is a slightly influencing factor [21], [25]. However, the contribution of grains morphology cannot be ruled out completely: their elongated shape yields coarse columnar grains and equiaxed grains on the load-bearing sections of XY/XZ and Z specimens, respectively. This contributes to the anisotropy of as-built and annealed samples and likely accounts for small residual differences of impact data of HTHT samples with different orientations.

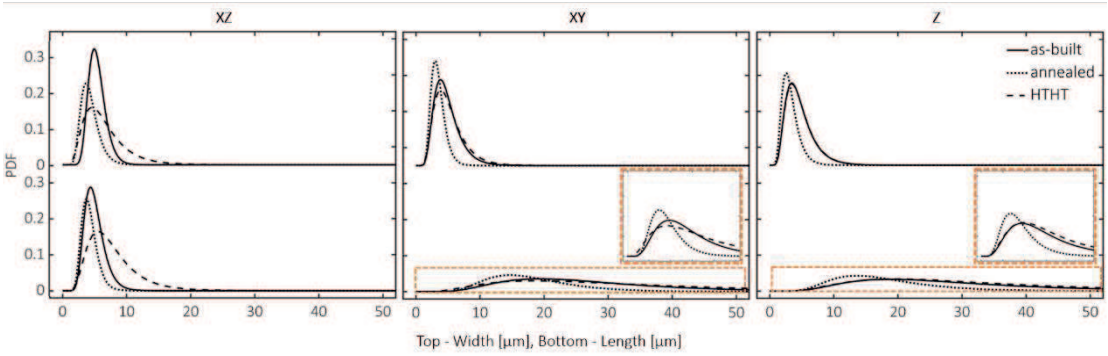

Figure 5.9. Statistical distributions of width and length of grains of samples in different orientations and heat treatment conditions.

Another reported cause of anisotropy of AM processed alloys is crystallographic texture [2], [4], [11]. For the FCC Al phase, deformation preferentially occurs on the {111} plane along the $< \underline{1}10 >$ direction [26]. In a uniaxial tensile state, the shear stress along the slip direction τ_R [MPa] depends on the applied tensile stress σ [MPa] and Schmid factor m according to the Schmid's law [27]:

$$\tau_R = m \cdot \sigma = cos\varphi \cdot \cos\lambda \cdot \sigma \quad (3)$$

where φ is the angle between the loading direction and the normal to the slip plane, and λ is the angle between loading and slip directions. The higher the Schmid factor, the lower the mechanical resistance of the material. The Schmid factor could change with specimen orientation, owing to the existence of a crystallographic texture, and thus determine a different mechanical response.

Figure 5.4 shows that a crystallographic texture of Al phase exists in sections both parallel and perpendicular to the building direction, and it is more pronounced in this latter case, which reasonably indicates a fibre texture [19], [20]. The Harris method was employed to analyse texture from XRD patterns quantitatively, and results are listed in Tab. 5.1.

Table 5.1. Analysis of XRD patterns of specimens in different orientations and heat treatment conditions: normalized intensity to the maximum value (I %), texture coefficients (C_{hkl}) and degree of preferred orientation (σ).

		Al reference 00-004-0787	as-built XY/Z	as-built XZ	annealed XY/Z	annealed XZ	HTHT XY/Z	HTHT Z
I %	[111]	100	100	53.4	95.0	48.5	95.1	52.3
	[200]	47	86.8	100	100	100	100	100
	[220]	22	39.4	24.8	45.6	21.4	44.0	22.6
	[311]	24	47.2	38.5	51.3	34.9	52.6	37.3
	[222]	7	9.4	5.0	8.9	4.5	9.5	5.2
	[400]	2	6.7	7.7	7.7	7.6	8.4	8.4
C_{111}		1	0.53	0.32	0.46	0.31	0.44	0.31
C_{200}		1	0.98	1.28	1.03	1.35	1.00	1.25
C_{220}		1	0.95	0.68	1.00	0.62	0.94	0.61
C_{311}		1	1.04	0.97	1.04	0.92	1.02	0.91
C_{222}		1	0.71	0.43	0.61	0.40	0.64	0.44
C_{400}		1	1.78	2.32	1.86	2.40	1.96	2.48
σ		0	0.39	0.67	0.44	0.72	0.48	0.73

As previously reported (§ 5.3.2), the integrated intensity of $[111]_{Al}$ and $[200]_{Al}$ reflections is similar in XY and Z samples, while a ~1:2 ratio exists in XZ samples,

regardless of heat treatment. Texture coefficient is generally >1 for $[200]_{Al}$, $[311]_{Al}$, $[400]_{Al}$ reflections and <1 for the remaining ones. The calculated degree of preferred orientation σ is always >0, which confirms texture in both sections parallel (XY/Z) and perpendicular (XZ) to the building direction. Additionally, it is much higher for XZ samples, which agrees with the fibre texture. Although σ slightly increases with the heat treatment temperature, the difference in σ between XY/Z and XZ samples is almost the same in as-built, annealed and HTHT samples, which means that crystallographic texture is not recovered during heat treatment. Accordingly, the reduced anisotropy of impact properties with heat treatment cannot be explained by the removal of crystallographic texture. In agreement with present results, Xiong et al. [28] verified limited variations of the Schmid factor with the specimen orientation for the as-built material, showing that crystallographic texture affects isotropy just to a limited extent. Similarly to grains morphology, its partial contribution is retained after heat treatment and possibly justifies the residual anisotropy of HTHT samples.

5.4.3 Role of microstructural heterogeneities

Microstructural heterogeneities possibly affect the impact response of the L-PBF produced AlSi10Mg alloy, resulting in anisotropic properties. SEM investigation shows that the gradient evolution of the microstructure mainly regards the Si phase in as-built and annealed samples (Fig. 5.3d-e), while HTHT samples exhibit a consistent microstructure. Additionally, the analysis of the damage mechanism (Fig. 5.6) highlights the primary role of the Si phase [29]. A quantitative analysis was performed to assess if a relationship between microstructural heterogeneities and fracture behaviour exists. Size and spacing of microstructural and fractographic features of samples in different heat treatment conditions were measured by image analysis. XY samples were selected as the reference since semi-circular traces of melt pools are more easily detectable on their fracture surface. Results are listed in Tab. 5.2.

In the as-built XY sample, dimples spacing matches the width of Al cellular dendrites (spacing of Si network) in both fine and coarse zones of the melt pool, whereas it is similar to the distance between Si particles in the HAZ. Heterogeneous fractographic features are also detected in the annealed XY sample, and their spacing well matches the spacing of nanometric Si particles.

Table 5.2. Analysis of microstructural and fractographic features of XY specimens in different heat treatment conditions: size (d_{eq}) of the Si phase, spacing ($\bar{d}$) of the Si phase and dimples.

		Microstructure		Fracture surfaces
		d_{eq} [μm]	$\bar{d}$ [μm]	$\bar{d}$ [μm]
as-built	1. Fine zone	- *	0.61 ± 0.06	0.59 ± 0.16
	2. Coarse zone (MPB)	- *	0.94 ± 0.09	0.75 ± 0.24
	3. HAZ (MPB)	0.26 ± 0.10	0.50 ± 0.13	0.46 ± 0.10
annealed	1. Fine zone	0.15 ± 0.06	0.30 ± 0.08	0.34 ± 0.10
	2. Coarse zone (MPB)	0.29 ± 0.13	0.45 ± 0.16	0.45 ± 0.11
HTHT	1. Elongated zone	1.2 ± 0.5	2.4 ± 0.8	2.9 ± 1.1 **
	2. Equiaxed zone (MPB)	1.1 ± 0.4	2.2 ± 1.0	

* For the cellular dendritic microstructure just the spacing $\bar{d}$ was measured

** Elongated and equiaxed zones are not discernible on the fracture surface

In the HTHT XY sample, traces of melt pools are discernible on the polished section owing to the different arrangement of grains, but not on the fracture surface. Hence, a single value of dimples spacing is measured. However, it reasonably corresponds to the distance of micrometric Si particles, which is the same in the elongated and equiaxed grained areas. The analysis here reported confirms the primary role of Si in damage nucleation and highlights that microstructural heterogeneities detected in Fig. 5.3 are also present on the fracture surfaces, depending on the heat treatment state.

Heterogeneous microstructure means locally different properties, which affect strength and fracture behaviour. Such differences can be evaluated analysing the strengthening mechanism owned to the Si phase as it changes in size and shape across the microstructure. Several microstructural features contribute to material strength in L-PBF produced Al-Si alloys [20], but just Si contribution will be considered for the sake of comparison and according to its primary role in damage nucleation (Fig. 5.6). The operating strengthening mechanisms of Si and corresponding constitutive equations are reported in Fig. 5.10 as a function of heat treatment. The resulting strength increment $\Delta\sigma_y$ is calculated according to data in Tab. 5.2.

	as-built (fine zone)	as-built (coarse zone)	annealed (fine zone)	as-built (HAZ) annealed (coarse zone)	HTHT
					
$\bar{d}$, d_{eq} [μm]	0.61	0.94	0.15	0.26 ÷ 0.29	1.2
Strengthening mechanism	Si boundary - Hall-Petch - $\frac{k}{\sqrt{\bar{d}}}$		Si particle - Orowan - $\frac{\varphi G b}{d_{eq}} \cdot \left(\frac{6 V_{Si}}{\pi}\right)^{1/3}$		
Constants	$k = 40\ MPa \cdot \mu m^{0.5}$ [20]		$\varphi = 0.4$ [20]		$Gb = 7722$ MPa $\cdot nm$ [20]
$\Delta\sigma_y$ [MPa]	51.1	41.3	12.4	6.4 ÷ 6.7	negligible

Figure 5.10. Strengthening mechanisms of Si phase in different heat treatment conditions.

In as-built samples, Si strengthens the alloy by the Hall-Petch relationship in fine and coarse zones, and by the Orowan relationship in the HAZ, with the resulting $\Delta\sigma_y$ being ~50, ~40 and ~7 MPa. Just the Orowan mechanism operates in the annealed alloys, and $\Delta\sigma_y$ is ~12 and ~6 MPa for fine and coarse zones respectively. The micrometric size of Si particles yields a negligible $\Delta\sigma_y$ in HTHT alloys. It is worth notice that the actual volume fraction of Si measured by XRD was used in the Orowan relationship: it is 0.094 in the as-built samples, owing to the supersaturated solid solution of Si in the Al matrix, and 0.114 and 0.117 in annealed and HTHT samples, respectively (Chapter 4, § 4.3.3). Simplified calculations show that MPBs represent the weakest part of the microstructure in as-built and annealed samples, whereas the homogeneous microstructure yields uniform properties in HTHT samples.

5.4.3 Role of specimen orientation

MPBs were quantitively described as a significant weakness in as-built and annealed samples. It follows that the distribution of MPBs along the deformation and fracture path could affect the material response, possibly causing anisotropic properties. Several fracture profiles as those depicted in Fig. 5.7 were analysed to estimate roughly the amount of MPBs on the fracture path. In agreement with Fig. 5.7, as-built and annealed samples share similar results: the length of the fracture path occupied by MPBs ranges between 8-10 % in XZ samples. It significantly increases to 22-25 % and 42-45 % in XY and Z samples, respectively. Similar measurements were not achievable in HTHT

samples, which do not exhibit MPBs. However, the analysis of Figs. 5.7c-f-i suggests a fracture path similar to as-built and annealed samples as the specimen orientation changes.

Considering the limited strength of MPBs and their distribution along the fracture path as the specimen orientation changes, decreasing impact properties are expected for XZ, XY and Z samples, in this order, both in as-built and annealed samples. On the contrary, a uniform impact behaviour is expected in HTHT samples owing to the homogeneous microstructure. These outcomes well match the analysis of impact properties in Fig. 5.5 elucidating that the mitigation of anisotropic impact behaviour of the alloy is related to the recovery of microstructural heterogeneities.

It is worth to notice that some differences in impact strength of HTHT samples may be suggested from Fig. 5.5a. Such residual anisotropy likely results from the retainment of elongated grains morphology and crystallographic texture after heat treatment. Further heat treatment routes and treatment parameters will be investigated in future work to mitigate the effect of residual sources of anisotropy. However, the current research activity provides useful insights about the anisotropic high-strain rate behaviour of the L-PBF produced AlSi10Mg alloy and lays the foundation for the selection of proper heat treatment parameters to achieve a fully isotropic material. Additionally, it suggests that, when heat treatment cannot be performed for technological or economic purposes, anisotropy has to be mitigated during the manufacturing process, by the modulation of deposition parameters.

5.5 CONCLUSION

The present research activity deals with the anisotropic Charpy impact behaviour of an L-PBF produced AlSi10Mg alloy in different heat treatment conditions. Primary possible sources of anisotropy were investigated to assess the relationship between impact parameters and specimen orientation. The following conclusions can be drawn:

- Significant anisotropy affects the impact behaviour of the alloy in the as-built and annealed conditions. Conversely, the exposure to high temperatures generally yields isotropic properties, which depend just on the given heat treatment route.

- Regardless of heat treatment, the Si phase mainly rules damage nucleation during deformation at a high strain rate. The excellent match between microstructural and fractographic features validates this outcome.
- Microstructural heterogeneities of the Si phase characterise the as-built and annealed samples, whereas samples heat-treated at high temperatures exhibit a uniform microstructure. Since heat treatment does not significantly affect other sources of anisotropy, like elongated shape of grains and crystallographic textures, anisotropy is mainly ascribed to microstructural heterogeneities.
- A simple analysis shows that MPBs represent the weakest microstructural feature, and their distribution along the fracture path affects isotropy, leading the impact behaviour to change with the specimen orientation.

REFERENCES

[1] M. T. Di Giovanni, J. T. O. de Menezes, G. Bolelli, E. Cerri, and E. M. Castrodeza, *Fatigue crack growth behavior of a selective laser melted AlSi10Mg*, Eng. Fract. Mech., vol. **217**, no. March, p. 106564, 2019

[2] Y. Kok *et al.*, *Anisotropy and heterogeneity of microstructure and mechanical properties in metal additive manufacturing: A critical review*, Mater. Des., vol. **139**, pp. 565–586, 2018

[3] M. Tang and P. C. Pistorius, *Anisotropic Mechanical Behavior of AlSi10Mg Parts Produced by Selective Laser Melting*, Jom, vol. **69**, no. 3, pp. 516–522, 2017

[4] D. Herzog, V. Seyda, E. Wycisk, and C. Emmelmann, *Additive manufacturing of metals*, Acta Mater., vol. **117**, pp. 371–392, 2016

[5] L. Hitzler *et al.*, *Direction and location dependency of selective laser melted AlSi10Mg specimens*, J. Mater. Process. Technol., vol. **243**, pp. 48–61, 2017

[6] J. T. Oliveira de Menezes, E. M. Castrodeza, and R. Casati, *Effect of build orientation on fracture and tensile behavior of A357 Al alloy processed by Selective Laser Melting*, Mater. Sci. Eng. A, vol. **766**, no. September, p. 138392, 2019

[7] J. H. Rao, Y. Zhang, K. Zhang, X. Wu, and A. Huang, *Selective laser melted Al-7Si-0.6Mg alloy with in-situ precipitation via platform heating for residual strain removal*, Mater. Des., vol. **182**, p. 108005, 2019

[8] B. E. Carroll, T. A. Palmer, and A. M. Beese, *Anisotropic tensile behavior of Ti-6Al-4V components fabricated with directed energy deposition additive manufacturing*, Acta Mater., vol. **87**, pp. 309–320, 2015

[9] M. Simonelli, Y. Y. Tse, and C. Tuck, *Effect of the build orientation on the mechanical properties and fracture modes of SLM Ti-6Al-4V*, Mater. Sci. Eng. A, vol. **616**, pp. 1–11, 2014

[10] L. Hitzler, J. Hirsch, B. Heine, M. Merkel, W. Hall, and A. Öchsner, *On the anisotropic mechanical*

properties of selective laser-melted stainless steel, Materials (Basel)., vol. **10**, no. 10, 2017

[11] A. Takaichi *et al.*, *Effect of heat treatment on the anisotropic microstructural and mechanical properties of Co–Cr–Mo alloys produced by selective laser melting*, J. Mech. Behav. Biomed. Mater., vol. **102**, no. October 2019, p. 103496, 2020

[12] A. Hadadzadeh, B. S. Amirkhiz, J. Li, A. Odeshi, and M. Mohammadi, *Deformation mechanism during dynamic loading of an additively manufactured AlSi10Mg_200C*, Mater. Sci. Eng. A, vol. **722**, no. March, pp. 263–268, 2018

[13] I. Rosenthal, A. Stern, and N. Frage, *Strain rate sensitivity and fracture mechanism of AlSi10Mg parts produced by Selective Laser Melting*, Mater. Sci. Eng. A, vol. **682**, no. November 2016, pp. 509–517, 2017

[14] T. Maconachie *et al.*, *Effect of build orientation on the quasi-static and dynamic response of SLM AlSi10Mg*, Mater. Sci. Eng. A, vol. **788**, no. December 2019, p. 139445, 2020

[15] C. A. Schneider, W. S. Rasband, and K. W. Eliceiri, *NIH Image to ImageJ: 25 years of image analysis*, Nat. Methods, vol. **9**, pp. 671–675, 2012

[16] V. Consonni, G. Rey, H. Roussel, B. Doisneau, E. Blanquet, and D. Bellet, *Preferential orientation of fluorine-doped SnO 2 thin films: The effects of growth temperature*, Acta Mater., vol. **61**, no. 1, pp. 22–31, 2013

[17] H. R. Moutinho *et al.*, *Investigation of polycrystalline CdTe thin films deposited by physical vapor deposition , closespaced sublimation , and sputtering Investigation of polycrystalline CdTe thin films deposited by physical vapor deposition , close-spaced sublimation , and spu*, vol. **2877**, no. 1995, 2013

[18] L. Lutterotti, H. R. Wenk, and S. Matthies, *MAUD (Material Analysis Using Diffraction): a user friendly Java program for Rietveld Texture Analysis and more*, in *ICOTOM-12.*, 1999, pp. 1599–1604

[19] Y. J. Liu, Z. Liu, Y. Jiang, G. W. Wang, Y. Yang, and L. C. Zhang, *Gradient in microstructure and mechanical property of selective laser melted AlSi10Mg*, J. Alloys Compd., vol. **735**, pp. 1414–1421, 2018

[20] A. Hadadzadeh, B. Shalchi Amirkhiz, A. Odeshi, J. Li, and M. Mohammadi, *Role of hierarchical microstructure of additively manufactured AlSi10Mg on dynamic loading behavior*, Addit. Manuf., vol. **28**, no. November 2018, pp. 1–13, 2019

[21] L. Thijs, M. L. Montero Sistiaga, R. Wauthle, Q. Xie, J. P. Kruth, and J. Van Humbeeck, *Strong morphological and crystallographic texture and resulting yield strength anisotropy in selective laser melted tantalum*, Acta Mater., vol. **61**, no. 12, pp. 4657–4668, 2013

[22] N. Takata, H. Kodaira, K. Sekizawa, A. Suzuki, and M. Kobashi, *Change in microstructure of selectively laser melted AlSi10Mg alloy with heat treatments*, Mater. Sci. Eng. A, vol. **704**, no. August, pp. 218–228, 2017

[23] F. Alghamdi, X. Song, A. Hadadzadeh, B. Shalchi-Amirkhiz, M. Mohammadi, and M. Haghshenas, *Post heat treatment of additive manufactured AlSi10Mg: On silicon morphology, texture and small-scale properties*, Mater. Sci. Eng. A, vol. **783**, no. March, p. 139296, 2020

[24] Y. K. Xiao *et al.*, *Effect of nano-TiB2 particles on the anisotropy in an AlSi10Mg alloy processed by selective laser melting*, J. Alloys Compd., vol. **798**, pp. 644–655, 2019

[25] M. Diehl, J. Niehuesbernd, and E. Bruder, *Quantifying the contribution of crystallographic texture and*

grain morphology on the elastic and plastic anisotropy of bcc steel, Metals (Basel)., vol. **9**, no. 12, pp. 1–21, 2019

[26] W. F. Hosford, *Mechanical behavior of materials*. Cambridge University Press, 2010

[27] E. Schmid and W. Boas, *Plasticity of Crystals With Special Reference to Metals*. F.A. Hughes & Co., 1935

[28] Z. H. Xiong, S. L. Liu, S. F. Li, Y. Shi, Y. F. Yang, and R. D. K. Misra, *Role of melt pool boundary condition in determining the mechanical properties of selective laser melting AlSi10Mg alloy*, Mater. Sci. Eng. A, vol. **740–741**, no. April 2018, pp. 148–156, 2019

[29] L. Zhao, J. G. Santos Macías, L. Ding, H. Idrissi, and A. Simar, *Damage mechanisms in selective laser melted AlSi10Mg under as built and different post-treatment conditions*, Mater. Sci. Eng. A, vol. **764**, pp. 1–25, 2019

CONCLUDING REMARKS AND FUTURE DEVELOPMENTS

The present doctoral thesis investigated the process-microstructure-properties relationship of an L-PBF produced AlSi10Mg alloy. Notably, two main topics were covered: the effect of deposition parameters and reliability of the energy density-based design method, and the effect of heat treatment on microstructural evolution and impact properties. This final section aims at drawing the concluding remarks of each topic and suggesting possible future developments.

CONCLUDING REMARKS

- ***3D printing parameters and reliability of the energy density-based method***

This research activity was performed in collaboration with the industrial partner AMT S.r.l., whose goal was the optimisation of density and tensile properties of the L-PBF produces AlSi10Mg alloy. The reliability of the energy density-based method, typically adopted in the literature, was assessed using suitable combinations of deposition parameters to reproduce a literature-suggested range of volumetric energy density (VED) values. The effect of deposition parameters in this range of VED on microstructure, faultiness and static properties of the alloy was investigated in-depth.

Results showed that, in the adopted processing range, the metastable hierarchical microstructure of the AlSi10Mg alloy was fully maintained. Regardless of the employed parameters, columnar grains, Al cellular dendrites and Si precipitates ranged between ~7-20 μm, ~0.85-1.15 μm and ~60-80 nm in width, respectively. Such features lend the alloy the outstanding UTS and YS of ~550-500 MPa and ~320-300 MPa, respectively, preserving a considerable E_f of ~6 %, which were systematically higher as compared to literature data. This indicates that VED cannot accurately predict the tensile performances of the alloy, since it lacks in considering the effect of process parameters on microstructural features and the resulting strength contributions.

Although not affecting the microstructure appreciably, even a limited change of process parameters was yet deleterious to porosity, which grew up to ~3.5 % and caused a ~20-25 % reduction of all static properties. These results did not match with literature data, which indicate the employed range of VED as suitable to achieve fully dense parts.

Besides tensile properties, the final density of L-PBF products cannot be accurately predicted using VED. This latter merely estimates the effect of deposition parameters on the energy imparted to the powder bed, but considers just a few parameters and does not account for their effect on the actual dynamic of the molten pool.

In conclusion, as currently defined, the use of VED guarantees neither the selection of suitable deposition parameters nor the optimisation of material properties. Hence, it cannot be intended as a reliable design parameter. However, the different sensitivity of microstructure and porosity to printing parameters is an advantage where the process is to be optimised for defect reduction or productivity maximisation since the contribution of microstructural features to strength would not be significantly affected.

- ***Impact behaviour, heat treatment and anisotropy***

This research activity was performed in collaboration with the University of Brescia and the CNR of Bologna and aimed at investigating the high-strain rate properties and anisotropic behaviour of the AlSi10Mg alloy in different heat treatment states. The main goal was to possibly identify alternative heat treatment routes to the conventional ones.

Results showed the remarkable impact strength of the as-built material, which stems from its ultra-fine and metastable microstructure. However, it also suffered from reduced absorbed energy despite the absence of a significant porosity, likely being a consequence of residual process defects. Additionally, impact properties were significantly anisotropic, especially regarding the absorbed energy, with the vertical orientation of the Charpy specimens being the worst condition.

The stress-relieving (annealing) treatment is often suggested in the literature for additively manufactured Al-Si alloys to achieve a compromise between strength and ductility. However, the annealed alloy exhibited an impact strength similar to the as-built material with a ~4-fold total absorbed energy. Similarly to the as-built material, the high-strain rate properties were highly anisotropic, and vertical specimens still displayed the lowest values of impact strength and absorbed energy.

Standard T6 heat treatment is not advisable, since it reduced properties mostly by growth of residual gas pores, which conversely was successfully avoided by the HIP. After HIP, the alloy was softened by microstructural coarsening and lack of strengthening precipitates, and an artificial ageing treatment is necessary to recover an

adequate strength. A novel high-pressure heat treatment was investigated, and it showed comparable results to the HIP + T6 route, suggesting the possible replacement of this latter with a considerable technological advantage.

As a significant benefit, a more consistent high-strain rate behaviour characterised all samples heat-treated at high temperature, with the impact properties being similar for specimens with different orientations. Microstructural investigations ruled out morphological and crystallographic textures as causes of anisotropy. Conversely, heterogeneous features of the Si phase of as-built and annealed samples were recovered after heat treatment at high temperatures. The observation of the primary role of Si in damage nucleation and fractographic investigations suggested that Si heterogeneities mainly determine the anisotropic behaviour, which furtherly elucidates the importance of heat treatment.

In conclusion, the present activity systematically investigated the high-strain rate behaviour of the additively manufactured AlSi10Mg alloy as a function of the heat treatment, filling a significant literature gap. Additionally, it provided experimental results of practical interest in designing and developing new heat treatment methods for L-PBF produced Al alloys.

FUTURE DEVELOPMENTS

Both the main topics covered within the present doctoral thesis make room for further research development.

In light of the 3D printing parameters theme, the research activity is ongoing at present: the first step enabled the optimisation of bulk material, whereas the second step currently aims at studying the effect of contour strategy parameters on superficial faultiness and roughness. Additionally, given the limited reliability of design by the energy density-based approach, new methods need to be established. Promising ones rely on the use of dimensionless parameters to account for the molten pool dynamic more reliably. Similarly, dedicated dimensionless parameters could be determined to assess the effect of processing parameters on microstructural features, thus providing an effective estimation of mechanical properties.

In light of the impact behaviour, several future developments are possible. Within the current research activity, the effectiveness of the novel high-pressure heat treatment was

satisfactorily demonstrated. However, more in-depth analyses to evaluate the effect of pressure on kinetics and thermodynamics of precipitation strengthening is to be performed before industrially substituting the HIP + T6 route with the novel one. Additionally, a single ageing condition was selected in the present study, whereas ageing curves as a function of different times and temperatures need to be investigated. Finally, the annealing treatment showed very promising results in terms of impact properties, whereas it is commonly known to reduce static properties as compared to the as-built material. This result highlights the need for studying the strain rate sensitivity of the alloy as a function of the heat treatment state which, to date, has not been covered at all for additively manufactured metals and alloys.